Doctoral thesis for the Degree of Doctor of Philosophy

Electronic Transport in Normal and Superconducting Nanocontacts

Juan Carlos Cuevas

Departamento de Física Teórica de la Materia Condensada. Facultad de Ciencias. Universidad Autónoma de Madrid. 28049 Madrid, Spain.

Thesis advisors: Alvaro Martín Rodero and Alfredo Levy Yeyati.

Thesis committee: F. Flores
                          C. Urbina
                          F. Sols
                          N. Agraït
                          J.A. Vergés

Madrid, March 1999.

1

Agradecimientos

Cuando echo la vista atrás me doy cuenta de que esta tesis no habría sido posible sin la inestimable ayuda de mucha gente. Espero que estas líneas en forma de agradecimientos sirvan para rendirles un merecido tributo.

En primer lugar me gustaría agradecer a mis directores de tesis Alvaro Martín y Alfredo Levy por iniciarme y guiar mis primeros pasos en el mundo de la ciencia. De ellos he aprendido casi todo lo que sé de física, pero sobre todo he aprendido cómo debe hacerse física. Sólo espero que con mi esfuerzo y entusiasmo les haya devuelto un mínima parte de todo lo que me han aportado.

También me gustaría dar las gracias a toda la gente con la que he tenido el privilegio de colaborar durante la realización de mi tesis. En especial, estoy agradecido a Elke Scheer, Cristian Urbina y Jan van Ruitenbeek por honrarme con su amistad y por recordarme en qué consiste la ciencia en un momento en el que lo necesitaba. También quisiera dar las gracias a Nicolás Agraït, Gabino Rubio, Carlos Untiedt y Bas Ludoph con los que espero compartir en el futuro nuevos descubrimientos científicos.

Una mención especial merecen todos y cada uno de mis compañeros de fatigas del Departamento de Física Teórica de la Materia Condensada. Gracias por haberme honrado con vuestra amistad y ayuda, sin las cuales esto no hubiera salido adelante nunca. Odiaría olvidarme algún nombre, así que permitidme que no haga ninguna mención explícita.

También quisiera agradecer a todos los profesores del Departamento de Física Teórica de la Materia Condensada la ayuda que me han prestado.

Gracias a la Universidad Autónoma de Madrid por confiar en mi a través de una ayuda de tercer ciclo y de un contratado de Profesor Asociado, sin los cuales este trabajo no hubiera sido posible.

A mis (sucesivos y en algún momento simultáneos) compañeros de piso: Ángel, Jesús, Luis, Antonio, Joseba y José Antonio, mil gracias por los momentos compartidos, y espero que en el futuro continuemos pateando algunas frutas [1]. Gracias

---

[1] Ver Tesis Doctorales de Antonio Turiel y Ángel Uranga, Departamento de Física Teórica de la Universidad Autónoma de Madrid.

también al *camarada Cachalote* y a todos mis amigos en general por esos ratos imborrables.

Me gustaría dar las gracias de forma muy especial a Elena y Beatriz, dos mujeres maravillosas con las que he tenido la suerte de compartir experiencias inolvidables en estos años.

Por último, esta tesis está dedicada a mis padres por su amor y apoyo incondicional. A ellos se lo debo todo y sólo espero ser capaz algún día de devolverles al menos una pequeña parte de todo lo que han dado, aunque me temo que eso no es posible. No me gustaría olvidarme de mis hermanos Jesús y Javier, dos espejos en los que siempre me he mirado.

Preface

In this preface we shall briefly describe the contents and structure of this thesis. This work is devoted to the theoretical analysis of the electronic transport in different mesoscopic systems in normal and superconducting state [2], paying special attention to the analysis of metallic atomic-size contacts. The thesis is divided into two almost independent parts. In the first one we shall develop a theoretical description of the electronic transport in *superconducting quantum point contacts* (SQPCs) [3]. In the second part we shall concentrate in the microscopic analysis of the normal transport in metallic atomic-size contacts. Moreover, in this thesis we shall show the connection between the normal transport and the superconducting one in these atomic contacts. The rest of this preface is devoted to summarize the contents that can be found in both parts.

PART I: Electronic transport in mesoscopic superconducting systems.

- ### Chapter 1: Transport in superconducting junctions: Introduction.

  In this first chapter we shall introduce the topic of electronic transport in superconducting junctions. Firstly, we shall do a historical review of this topic, paying special attention to the problems that we shall analyze in this work. Secondly, we shall present our aims for the part I of the thesis and describe the experimental systems in which we are interested.

- ### Chapter 2: Transport in superconducting quantum point contacts.

  This chapter is devoted to the analysis of the electronic transport in a superconducting quantum point contact (SQPC) for arbitrary voltage, temperature and transmission. First, we shall describe our model for a single quantum channel contact based on a Hamiltonian approach in combination with nonequilibrium Green function techniques (section 2.2). In section 2.3 we shall explicitly show

---

[2] We only study traditional superconductor, and we shall not consider high T_C superconductors.

[3] These contacts consist of two superconducting electrodes connected by a constriction whose length is much smaller than the superconducting coherence length of the leads, and whose width is comparable to the Fermi wave length of the system electrons.

the equivalence between our Hamiltonian approach and the scattering formalism for the case of N-N and N-S single channel contacts. The main part of the chapter (section 2.4) is devoted to the analysis of a single channel SQPC, describing in detail the dc and ac Josephson effect: dc current, ac current components and small bias voltage limit. Finally, we shall show that there exists a quantitative agreement between our predictions and the experimental results obtained in superconducting atomic contacts (section 2.5).

- **Chapter 3: Shot noise in superconducting quantum point contacts.**

  In this chapter we shall study the zero-temperature current fluctuations or shot noise in SQPCs. After revising the N-N and N-S cases briefly, we shall show the novel results that our Hamiltonian approach provides for S-S contacts with arbitrary voltage and transmission (section 3.4). In particular, we shall show that in superconducting contacts one can observe the coherent transfer of multiple charges associated to multiple Andreev reflections.

- **Chapter 4: Resonant tunneling and Andreev reflections.**

  In this chapter we shall discuss how the superconducting transport is modified by the presence of a resonant transmission in the system. In particular, we shall analyze two situations: first, we shall study the current through metallic nanoparticles connected to superconducting leads in relation with recent experiments (section 4.3). Secondly, we shall analyze how the subharmonic structure evolves in presence of a resonant transmission (section 4.4). Finally, to conclude this chapter we shall comment something on future works and open problems related to the topics treated in the first part of the thesis.

  PART II: Electronic transport in atomic contacts

- **Chapter 5: Electronic transport in atomic contacts: Introduction.**

  In this chapter we shall introduce the topic of the electrical current through metallic atomic-size contacts in normal state. After a brief historical review of this topic, we shall describe our aims for the second part of the thesis.

- **Chapter 6: Origin of the conducting channels.**

  In this chapter we shall analyze the microscopic origin of the conducting channels in atomic contacts. We shall make use of a Hamiltonian approach in terms of an atomic orbital basis, together with Green function techniques (section 6.2-3). We shall analyze contacts of different metals, covering a broad range of valences and orbital structures (section 6.4), and we shall show how conducting channels arise from the valence orbitals of the corresponding material. In special, we shall show how in an one-atom contact the number and

character of the conducting channels are controlled by the chemical nature of the central atom. Finally, we shall show experimental results which support our picture of the electronic transport in atomic contacts (section 6.5).

- **Chapter 7: Elastic evolution of conducting channels.**

  In this chapter we investigate both experimentally and theoretically the evolution of the conductance in metallic one-atom contacts under elastic deformation. While simple metals like Au exhibit almost constant conductance plateaus, Al and Pb show inclined plateaus with positive and negative slope (section 7.2). It is shown how these behaviors can be understood in terms of the orbital structure of the atoms forming the contact (section 7.3). This analysis provides further insight into the issue of conductance quantization in metallic contacts revealing important aspects of their atomic and electronic structure. We shall end the chapter with some comments about future works and open problems in relation to the topics treated in the second part of the thesis (section 7.5).

APPENDICES

- In order to make easy the reading of this work, in some occasions we explain the most technical details in different appendices. This is the case of appendices B, C and E. On the other hand, Appendix A contains a detailed description of the Keldysh formalism, a technique widely used throughout this thesis. Finally, Appendix D contains a proposal for the direct observation of the Andreev bound states in a Josephson junction by means of the application of microwave radiation to the contact.

Publications

This thesis is based on the following publications:

- *Photoinduced currents in normal and superconducting micro-junctions*, A. Levy Yeyati, J.C. Cuevas and A. Martin-Rodero, in *Photons and Local Probes*, edited by O. Marti and R. Müller (Kluwer Academic, Dordrecht, 1995).

- *The phase-dependent linear conductance of a superconducting quantum point contact*, A. Levy Yeyati, A. Martín-Rodero and J.C. Cuevas, J. Phys.: Condens. Matter **8**, 449 (1996).

- *Microscopic theory of the phase-dependent linear conductance in highly transmissive superconducting quantum point contacts*, A. Martín-Rodero, A. Levy Yeyati and J.C. Cuevas, Physica B **218**, 126 (1996).

- *Hamiltonian approach to the transport properties of superconducting quantum point contacts*, J.C. Cuevas, A. Martín-Rodero and A. Levy Yeyati, Phys. Rev. B **54**, 7366 (1996).

- *Resonant tunneling through a small quantum dot coupled to superconducting leads*, A. Levy Yeyati, J.C. Cuevas, A. López-Dávalos, and A. Martín-Rodero, Phys. Rev. B **55**, R6317 (1997).

- *Microscopic origin of conducting channels in metallic atomic-size contacts*, J.C. Cuevas, A. Levy Yeyati and A. Martín-Rodero, Phys. Rev. Lett. **80**, 1066 (1998).

- *The signature of chemical valence in the electrical conduction through a single-atom contact*, E. Scheer, N. Agraït, J.C. Cuevas, A. Levy Yeyati, B. Ludoph, A. Martín-Rodero, G. Rubio, J.M. van Ruitenbeek and C. Urbina, Nature **394**, 154 (1998).

- *Evolution of conducting channels in metallic atomic contacts under elastic deformation*, J.C. Cuevas, A. Levy Yeyati, A. Martín-Rodero, G. Rubio, C. Untiedt and N. Agraït, Phys. Rev. Lett. **81**, 2990 (1998).

- *Shot noise and coherent multiple charge transfer in superconducting quantum point-contacts*, J.C. Cuevas, A. Martín-Rodero and A. Levy Yeyati, Phys. Rev. Lett. **82**, 4086 (1999).

- *General transport properties of superconducting quantum point contacts: a Green functions approach*, A. Martín-Rodero, A. Levy Yeyati and J.C. Cuevas, to be published in Superlattices and Microstructures.

Contents

List of Figures

15

Part I

Electronic transport in superconducting mesoscopic contacts

Chapter 1

Transport in superconducting junctions: Introduction

1.1 Introduction

The superconductivity was discovered by Kamerlingh Onnes [1] in 1911. In the course of an investigation on the electrical resistance of various metals at liquid helium temperatures, he observed that the resistance of a sample of mercury dropped from 0.08 Ω at above 4 K to less than 3×10^{-6} Ω at about 3 K. Thus, he arrived at the first characteristic property of a superconductor: its electrical resistance is zero below a certain critical temperature.

The superconductivity is a notable example of quantum effects operating in a truly macroscopic scale. In a superconducting material, below certain critical temperature, a finite fraction of the electrons are condensed in a "superfluid" which extends throughout the bulk system and is able to move as a whole. The surprising properties of a superconductors as the vanishing electrical resistance, the perfect diamagnetism (Meissner effect), etc, are related with the peculiar excitation spectrum of this fluid.

In 1957 Bardeen, Cooper y Schrieffer proposed the first microscopic theory of the superconductivity, which is known as BCS theory [2]. In this theory it is explained in an elegant way how the superfluid is formed with pairs of electrons which are bounded by the action of lattice polarization forces. The pairs overlap appreciably in space, and the strong correlations between pairs are responsible for the energy gap in the excitation spectrum of a superconductor, from which most of the properties of a superconductor follow as a consequence.

In this part of the thesis we shall concentrate in the analysis of the electronic transport in superconducting junctions. Since the beginning of this topic in the early sixties until nowadays, the knowledge of how the electrical current flows in

superconducting circuits has evolved greatly. At the present time the *superconducting electronics* is a relatively well-established branch of engineering [3, 4]. There already exist a great amount of applications of this new area of the electronics in themes like the information technology, radiofrequency technology, technology associated with electrical and magnetic measures of high precision or electromedicine.

The most important part of electronics is that related with the semiconductor technology, which has conditioned much our present way of life. What are the advantages of the *superconducting electronics* with respect to the well-established semiconductor electronics? First of all, once the electrical resistance disappears so do the parasitic heat losses which occur in the circuit resistances and connections of semiconductor devices. The frequency limitations of superconductor components are therefore quite exceptionally high. If they are used as sensors their sensitivity limits can be so low as to be set only by Heisenberg uncertainty principle.

On the other hand, superconductor electronics can utilize special effects which do not occur with semiconductors. In particular, most of the applications of the superconducting circuits are based on the Josephson effect, which is a macroscopic quantum phenomenon which takes place in superconducting junctions. The SQUID [1] magnetic field sensors, have their operation based on the direct current Josephson effect. They make the quantization of the magnetic field macroscopically observable and technically utilizable. With the alternating current Josephson effect the quantization of the electromagnetic field energies in the form of photons becomes macroscopically observable. This effect is put to technical use in high precision d.c. voltage standard.

Electronics initiated many years ago a race toward the miniaturization of its different components. Nowadays we are attending to the first steps in the transition from the microelectronics to the definitive nanoelectronics. One of the main problems that one will have to face is that in devices of reduced dimensions the heat losses in the integrated circuits of semiconductors o normal conductors will be appreciable. In this case the superconducting electronics presents its main advantages.

On the other hand, in nanoelectronics there is a crucial aspect which provokes that the electrical current flow takes place in a different way with respect to traditional circuits. When one has a nanometric-size electronic device, the dimensions of the system are comparable to the Fermi wave length of the electrons in the system. Thus, it is obvious that quantum effects will appear in these devices. In these small systems it is possible that the electron maintains the phase coherence along the whole system and the current can be controlled by interference phenomena associated to the phase of the electron wave function. The physics of these quantum systems is known as *Mesoscopic Physics* [5, 6, 7, 8, 9], indicating that the system dimensions involved are somewhere in between the microscopic world of the atoms and the

---

[1]SQUID means superconducting quantum interference device.

macroscopic one. Finally, the mesoscopic superconductivity is the framework of the present work. In short, our aim is the theoretical analysis of the electronic transport through mesoscopic superconducting systems.

This chapter is devoted to an introduction on the electronic transport in superconducting contacts, and we also present the aims for the part I of the thesis. The rest of this chapter is divided into two main sections. In section 1.2 we shall do a brief historical review of this topic paying special attention to the problems and systems which will be analyzed in this work. In section 1.3 we explain our objectives for the part I of the thesis.

1.2 Historical review

1.2.1 Tunnel junctions

The study of the electrical current in superconducting junctions began in the early sixties, just after the appearance of the BCS theory [2]. The first systems experimentally investigated were the *tunnel junctions*. These systems consist of two metallic electrodes, which may be in superconducting state, separated by a thin insulator barrier (see Fig. 1.1). Such barrier has usually a thickness from 10 to 20 Å and it is typically made of an oxide of one of the metals. In these systems the current is due to the passage of electrons via tunnel effect through the potential barrier created by the insulator.

Giaever performed a pioneer experiment in 1960 [10] in which he analyzed an aluminum/aluminum oxide/lead tunnel junction at temperatures between 1.6 K and 4.2 K. At these temperatures Pb is superconducting and Al remains in normal state. The main conclusion of that work is summarized in Fig. 1.2 taken from the original article. This figure shows the ratio between the conductance when Pb is in superconducting state and the corresponding conductance when Pb is in normal state, as a function of bias voltage. In the case of a tunnel junction, where the electrodes are weakly coupled, this ratio is the ratio between the Pb density of states in superconducting state and the corresponding one in normal state [11, 12]. As can be observed in Fig. 1.2, this conductance ratio resembles the BCS density of states with a broadening of the singularity. Thus, Giaever showed the existence of a gap in superconductors and determined it quantitatively.

Some months after the Giaever pioneer work there appeared two new experiments in tunnel junctions analyzing the current in contacts with two superconducting electrodes [13, 14]. Again, the superconductor gap was reflected in the current-voltage (I-V) characteristics and the results were well described within the framework of BCS theory, what was one of the main confirmations of this theory. With the appearance in the following months of a great number of tunneling experiments between
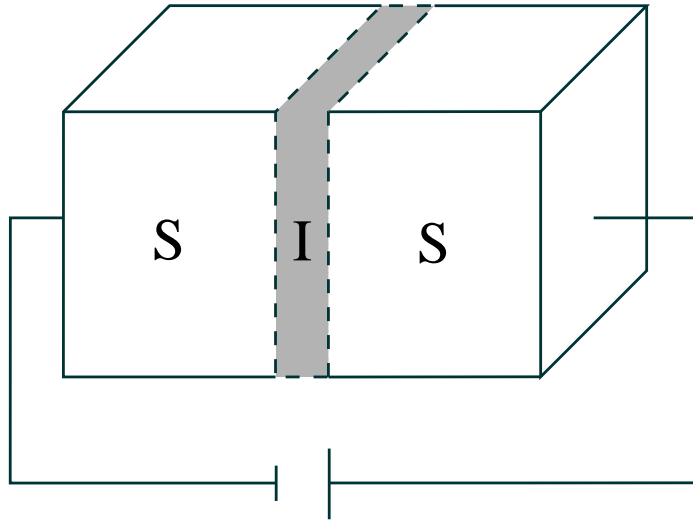
Figure 1.1: Schematical representation of a superconductor-insulator-superconductor tunnel junction.

superconductors [15, 16, 17], tunneling became a very valuable spectroscopy for investigating the electronic properties of these materials.

In 1962 B.D. Josephson predicted the possibility of new effects in the tunneling between superconductors [18]. In his famous paper Josephson predicted the two following effects which received his name:

1. **dc Josephson effect:** in a superconducting junction current can flow at zero voltage due to the phase difference between the superconducting electrodes. This current is due to the coherent tunneling of Cooper pairs through the junction. In short, a nondissipative current or supercurrent can flow through a superconducting contact.

2. **ac Josephson effect:** in a superconducting junction with a constant bias voltage V, apart from a dc current, there appears an alternating current which oscillates with a frequency $\omega_0 = 2eV/\hbar$, referred to as Josephson frequency and whose value is 483.6 $MHz/\mu V$.

Let us pay attention to the quantitative description of these effects, as a reference for later discussions. Josephson calculated the tunnel current in a superconducting junctions making use of the transfer Hamiltonian introduced by Cohen *et al.* [12].
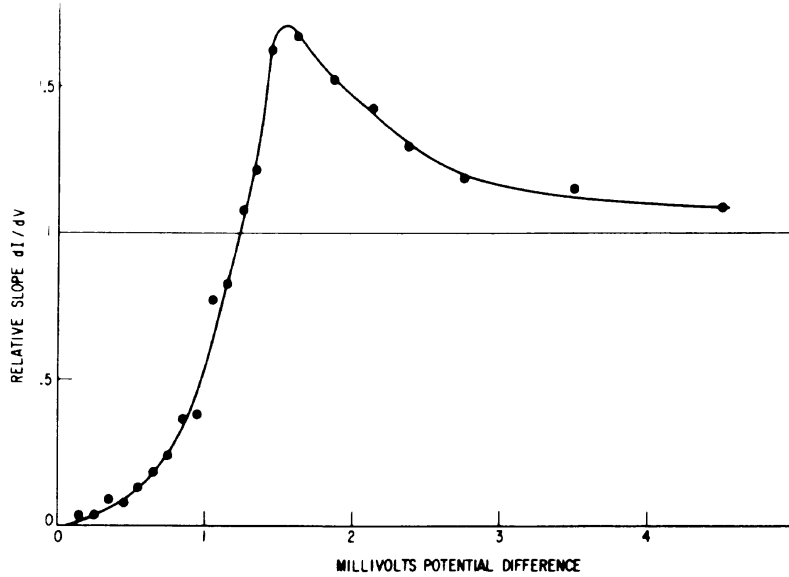
Figure 1.2: Normalized conductance vs voltage in an Al-Pb tunnel junction at 1.6 K [10].

This Hamiltonian consists of three terms: the first two describe the uncoupled electrodes within the framework of BCS theory, and the third one couples states of the electrodes. To be precise, Josephson calculated the current up to first order in the coupling between electrodes, what in principle seems sufficient for the case of a tunnel junction [2]. The result of this microscopic calculation can be summarized in the following expression for the current:

$$I(V, T, t) = I_0(V, T) + I_S(V, T) \sin \phi(t) + I_1(V, T) \cos \phi(t). \qquad (1.1)$$

This expression tell us that the current I flowing through the junction as a function of the voltage V, temperature T and time t can be expressed as a sum of three terms. The first one, I_0, is a time-independent term (dc current component) produced by the tunneling of quasiparticles, in the same way as in a normal contact. The other two terms oscillate with time with the superconducting phase difference between electrodes ϕ, which in the finite voltage case varies linearly as a function of time with the Josephson frequency: $\phi(t) = \phi_0 + 2eVt/\hbar$. Thus, at finite voltage these two terms give rise to the ac Josephson effect, which we defined above. However,

---

[2]As we shall see in Chapter 2, some results are nonperturbative in the coupling and even in the tunnel limit one has to consider the processes up to infinite order to obtain a correct description.

the nature of these two contributions is rather different. The term of I_S is due to the tunneling of Cooper pairs and is non-zero even at $V = 0$, giving rise to the dc Josephson effect. Thus, at $V = 0$ the *supercurrent* is given by $I = I_C \sin \phi_0$, where $I_C \equiv I_S(0, T)$ is the critical current of the junctions, i.e. the maximum current that the junction can support without generating a voltage. The temperature dependence of I_C was calculated by Ambegaokar and Baratoff [19], and for a symmetric [3] junction has the form

$$I_C(T) = \frac{\pi \Delta(T)}{2eR_N} \tanh \left(\frac{\beta \Delta(T)}{2} \right), \tag{1.2}$$

where $\Delta(T)$ is the temperature-dependent superconducting gap, R_N is the resistance of the normal contact and β is the inverse of the temperature.

On the other hand, I_1 is a dissipative term which arises from the interference between quasiparticles and the condensate of Cooper pairs, and whose existence was doubted during a lot of time as we shall comment below.

Fig. 1.3 shows the amplitudes (I_0, I_S, I_1) for the case of a symmetric junction at zero temperature, as obtained from the tunnel theory. As can be observed in this figure, the quasiparticle term, i.e. the dc current component, vanishes inside the gap, as one would expect naively. At $V = 2\Delta$ this term jumps to a finite value given by $I_0(V = 2\Delta) = \pi \Delta / 2eR_N$. On the other hand, the term I_S is finite at $V = 0$ with the value predicted by expression (1.2), and it shows a singularity at $V = 2\Delta/e$ referred to as *Riedel peak* [20]. Finally, I_1 vanishes inside the gap and jumps to a finite and negative value at $eV = 2\Delta$. For a detailed analysis of the tunnel I-V curves see Refs. [21, 22].

The new effects predicted by Josephson were quickly confirmed experimentally. Anderson and Rowell [23] observed for the first time a supercurrent. Later, the magnetic field dependence of the supercurrent predicted by Josephson [24], and its temperature dependence were also confirmed [25, 26]. The ac Josephson effect was also detected, in a indirect way by Shapiro [27], and in a direct way by Giaever [28] and Yanson *et al.* [29].

The intensive investigations of the tunnel junctions gave rise to the discovery of a great deal of new effects. Next, we shall describe two phenomena which will be analyzed in this thesis: the subharmonic gap structure and the $\cos \phi$ problem.

Subharmonic gap structure

We shall explain in detail this phenomenon which is the core of this thesis and which has remained without a totally satisfactory explanation during the last thirty years.

---

[3]We shall use the term *symmetric junction* to indicate that the junction is formed by two electrode of the same material.
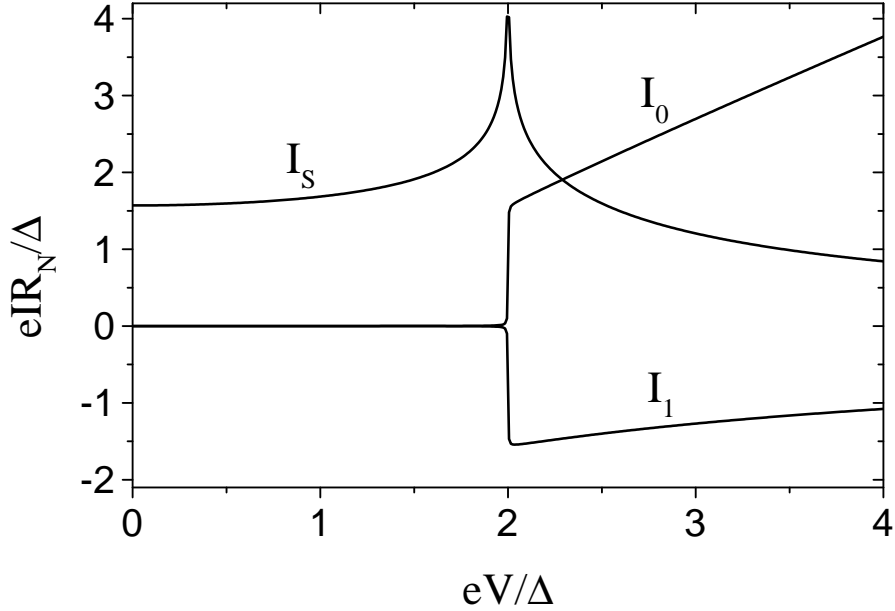
Figure 1.3: Amplitudes of the tunnel current terms as a function of voltage at zero temperature for a symmetric junction (see Eq. (1.1)).

We do here our first approach to this phenomenon and we shall come back to it below.

If a tunnel junction, formed by two superconductors S_1 and S_2 separated by an insulator barrier I, is cooled below the critical temperatures of both superconductors, then the current which flows at a voltage $V \ll (\Delta_1 + \Delta_2)$, where Δ_i is the gap of S_i, should be very small in comparison with the one which flows at $V > \Delta_1 + \Delta_2$. For example, in Pb at 1 K the number of quasiparticles excited above the gap Δ (1.39 meV) is $\sim N_0 exp(-\Delta/kT) \sim 10^{-7} N_0$. The tunnel current in a Pb-I-Pb junction at 1 K for small voltages should be exclusively due to these excited quasiparticles. Thus, in a such a junction at 1 K, the current (I_{SS}) for $V \ll 2\Delta$ should be $\sim 10^{-7}$ times the corresponding to the normal case (I_{NN}). In practise, currents much greater than this have been observed, typically from 10^{-5} to $I_{NN}/2$.

The first measurements of these excess currents for $eV < 2\Delta$ were done by Taylor and Burstein [30], and independently by Adkins [31]. They observed that in certain junctions of Sn-I-Sn and Pb-I-Pb the current increased abruptly at voltages Δ_{Sn} or Δ_{Pb}. The size of this increase was $\sim 10^{-4}$ times that of $2\Delta_{Sn}$ or $2\Delta_{Pb}$ (see left panel

in Fig. 1.4). Later, Yanson *et al.* [32] and Marcus [33] observed that there were not only an abrupt increase at $eV = \Delta$, but also a series of jumps located at $eV = 2\Delta/n$ with n integer (for a symmetric junction), as can be observed in Fig.1.4 (right panel). This series of current jumps is known as **subharmonic gap structure** due to its localization in voltages.
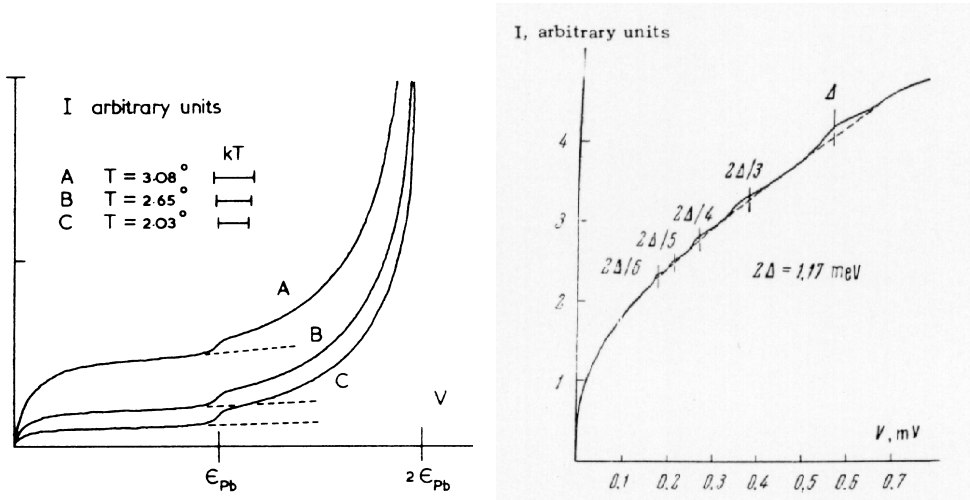
Figure 1.4: First observations of the subharmonic gap structure. Left: I-V characteristics in a Pb-Pb tunnel junction [31]. Notice the structure at $eV = \Delta$, as well as its temperature dependence. Right: I-V characteristics in a Sn-SnO$_2$-Sn tunnel junction at T=1.61 K [32]. Notice the structure at voltages $eV = 2\Delta/n$ with integer n.

In the sixties two theories were developed to explain the subharmonic structure. The first one was presented by Schrieffer and Wilkins and is referred to as *multiparticle tunneling theory* (MPT) [34]. This theory was specially developed to explain the current step at $eV = \Delta$ in the experiments of Taylor and Burstein [30]. For this purpose they calculated the dc current up to second order in the coupling between electrodes in the transfer Hamiltonian. This second order shows the possibility of a process in which the transfer of two quasiparticle takes place, creating a Cooper pair in the other electrode. This process has a threshold voltage $eV = \Delta$ (for a symmetric junction), explaining qualitatively the experiment of Ref. [30]. Within the MPT the explanation of the structure at voltages $eV = 2\Delta/n$ would come from the possibility of multiple processes in which n quasiparticles cross the barrier. This theory presents some problems, and in those years an important defect was pointed out. The probability of a process which involves the passage of n quasiparticle through the barrier is

proportional to T^n, where T is the transmission through the insulator barrier. Taking into account that $T \sim 10^{-10}$ in a tunnel junction, it is difficult to believe that this could be the explanation for the whole series which appears for instance in Fig. 1.4 (right panel) [4]. On the other hand, MPT presents a theoretical problem. For instance, the second order calculated by Schrieffer and Wilkins diverges at $eV = 2\Delta$ due to the divergence of the BCS density of states. In higher order terms, similar divergencies appear [5].

A second theory for the explanation of the subharmonic gap structure was proposed by Werthamer in 1966 and is referred to as *self-coupling of Josephson radiation* [36]. This author claimed that the quasiparticle tunneling could be coupled to the Josephson radiation coming from the ac current present in the tunnel junction. If a quasiparticle process took place while simultaneously a photon is absorbed from the Josephson radiation, an increase of the tunnel probability would occur at $eV + \hbar\omega = 2\Delta$, i.e. at $2\Delta/3$ since $\hbar\omega = 2eV$ for the Josephson radiation. The inclusion of multiphotonic processes gives structure in $2\Delta/(2n+1)$, i.e. for odd values of the denominator. One can obtain the even terms of the series by including the absorption of the Josephson radiation by the electrodes, generating thus quasiparticles at $n\hbar\omega = 2\Delta$. The main problem of this explanation is that it invokes two different mechanisms for the odd and even terms, while the experimental current jumps are identical for both series. Moreover, it was pointed out by Rowell and Feldmann [35] that this theory does not reproduce the series of jumps which appears in an asymmetric junction.

The $\cos \phi$ problem

This is a problem that one can find in several textbooks [21, 22, 37] and it was one of the most important failures of the tunnel theory. After years of great attention this problem was abandoned and we recover it in this thesis proposing what we believe it is the solution of this long-standing problem.

The current through a tunnel junction with a constant bias voltage is given by the expression (1.1), which can be rewritten as

$$I(V, T, t) = I_S(V, T) \sin \phi(t) + \sigma_0(V, T) \left[1 + \epsilon(V, T) \cos \phi(t)\right] V, \qquad (1.3)$$

where

---

[4]Indeed, nowadays it is clear that the presence of subharmonic structure in tunnel junctions is due to the existence of microbridge or pinholes that make that some of the conducting channels have a not so small transmission, giving rise to the presence of the excess current inside the gap [35].

[5]As we shall show in Chapter 2, this kind of divergencies disappear when one solves the problem up to infinite order.

$$\epsilon(V, T) = \frac{\sigma_1(V, T)}{\sigma_0(V, T)} \tag{1.4}$$

is the conductance ratio between the cosine term and the quasiparticle one. Thus, we can see that the dissipative current contains a phase-dependent term, the so called $\cos \phi$ *term*. This term was simply ignored for years. The first observation of the $\cos \phi$ term was performed by Pedersen *et al.* [38] in the course of a study of the magnetic field dependence of the Josephson plasmon resonance frequency in a Pb tunnel junction. In this experiment they found that the $\cos \phi$ term had approximately the magnitude predicted by the tunnel theory, but the sign was the opposite. Let us remember that the tunnel theory, within the BCS scheme, predicts that when $T \to 0$ and $V \to 0$, the conductance ratio $\epsilon \to 1$ [21]. In the experiment of Pedersen and coworkers a ratio $\epsilon \sim -1$ was found in this limit. Later experiments making use of different techniques [39, 40, 41, 42, 43] showed similar results, arising thus the so called $\cos \phi$ **problem**.

Here, we shall remark the result obtained by Rifkin and Deaver [42] in which by means of a measure of the inductance of a ring-shape junction as a function of the superconducting phase difference ϕ through the contact, they were able to extract the phase-dependent linear conductance, $G(\phi)$, which in the tunnel theory adopts the form

$$G(\phi) = G_0 \left(1 + \epsilon \cos \phi\right). \tag{1.5}$$

The result which they obtained is shown in Fig. 1.5, where it is quite clear that the measurement is more compatible with a value of -1 for ϵ. Moreover, $G(\phi)$ differs from a cosine shape what complicated even more the $\cos \phi$ problem [6].

Several theories tried to explain this discrepancy by introducing phenomenologically a finite relaxation time associated with an inelastic interaction [44, 45]. Some of them showed the possibility of having $\epsilon \sim -1$, but with unrealistic values of the relaxation time, and furthermore none could explain the deviation of the conductance from a cosine-type shape. After more than one hundred papers in the seventies, this problem was forgotten and we have recovered it in this work (see Chapter 2).

So far we have revised only a small part of the rich phenomenology of the electronic transport in superconducting tunnel junctions. For those who want to profound into this topic there are several monographs [46, 47] and excellent review articles [24, 48, 49, 50].

---

[6]We should say that the experiment of Rifkin and Deaver was done in a point contact, where it is not clear that the tunnel theory holds.
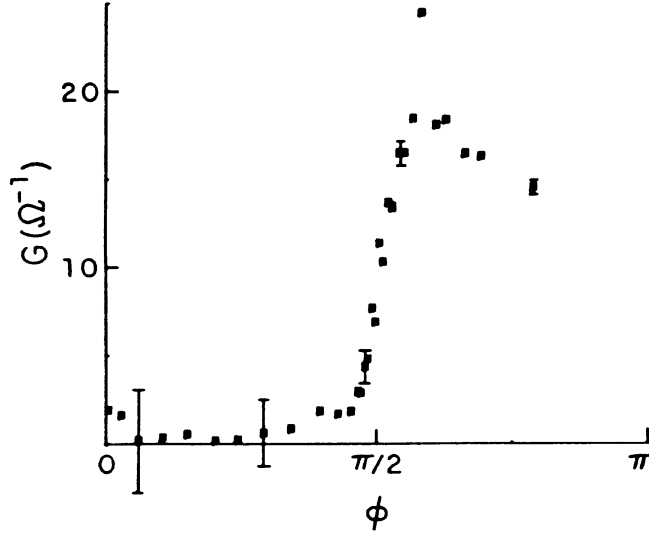
Figure 1.5: Experimental results by Rifkin and Deaver [42] for the linear conductance G of a superconducting point contact as a function of the phase ϕ.

1.2.2   Weak Links

Although the tunnel junctions played a crucial role in the investigation of the Josephson effect, since 1964 with the work by Anderson and Dayem [51] it was clear that this effect also took place in a great variety of systems known as **weak links**. A weak link is a junction between two electrodes where the current flow takes place in direct way, and not via tunnel effect through an insulating layer as in the tunnel junctions. The Josephson effect appears in these systems when the weak link has reduced dimensions, i.e. when the distance between electrodes and the cross section of the weak link are small. The critical current in these systems is much smaller than in the electrodes giving rise to the term, *weak superconductivity*.

Next, we shall briefly describe some of the more important weak links (see Ref. [49]). A type of junction related with the tunnel junctions is that in which the oxide barrier is replaced by a non-superconducting metal. A finite supercurrent can flow through such a junction due to the proximity effect [52]. This effect lies in the fact that if a metal and a superconductor are put in contact, some Cooper pairs penetrate in the metal giving rise to a non zero order parameter, which decays exponentially inside the metal over a distance of the order of the normal coherence length. Thus, if the length of normal region is not very large, the order parameter will be non-zero

throughout the metal and a supercurrent may flow.

Another type of weak link consists of a superconductor with a very small section which links two macroscopic superconductors [51]. In these contacts, known as *Dayem bridges*, the supercurrent flows through the weak link in a similar way as it does in the superconductor bulk, and there is no tunneling process.

An additional group of junctions is the one known as *point contact*, which is made pressing a superconducting tip over a surface [53]. These systems have barriers that are not very well defined and whose properties can vary between the ones of a tunnel junction and the ones of microbridges adjusting the pressure over the tip.

As we commented above, these contacts exhibit Josephson effect, but in a different way with respect to the tunnel junctions. Before going on, we should say what we understand by Josephson effect in these systems. For instance, by dc Josephson effect we mean that the supercurrent is a periodic function of the phase difference, although it may be different from the sinusoidal relation of the tunnel junctions. With respect to the ac Josephson effect, the relation between the voltage and frequency, $\omega_0 = 2eV/\hbar$, still holds because it does not depend on the details of the barrier, but it manifests in a different way in the different contacts, so for instance their I-V characteristics are different.

In the weak links there exist different length scales which determine the current through the system. An important length scale in this problem is the length L of the constriction which separates the superconducting electrodes. One can classify the different weak links according to the comparison between the length L and the characteristic lengths of the material which formed the weak link, like the superconducting coherence length ξ and the mean free path l. The junctions where $L \ll \xi$ are called *short junctions*, and *long* those in which $L \geq \xi$. Even in the case of short junctions, the processes may differ depending on the mean free path l. We shall call *dirty* to those structures in which $l \ll L$, and *clean* to those in which $l \geq L$.

As an example of that the Josephson effect which takes place in a weak link is in general different from that of tunnel junctions, we shall mention here the prediction of Kulik and Omelyanchuk [54] for the supercurrent in short and clean weak links ($L < l, \xi$):

$$I_S = \frac{\pi \Delta(T)}{eR_N} \sin(\phi/2) \tanh\left(\frac{\beta \Delta(T) \cos(\phi/2)}{2}\right). \qquad (1.6)$$

In this expression Δ is the gap, R_N is the resistance of the normal contact, ϕ the superconducting phase and β the inverse of temperature. As one can see, this expression differs from the sinusoidal behavior of a tunnel junction [7].

---

[7]For those who want to profound in how the different characteristic lengths give rise to different manifestations of the Josephson effect, we recommend the excellent review article of Likharev [55].

At the beginning of the eighties the situation was the following. While for the case of tunnel junctions there existed since the sixties a suitable theoretical description for almost all phenomena, in the case of weak links there was only a limited knowledge. Concentrating ourselves in the I-V curves, since it is the topic that we shall analyze in detail in this thesis, among the different characteristics which remained without a satisfactory explanation there were two outstanding ones: the above mentioned *subharmonic structure*, which appears more clearly in weak links [56, 57, 58, 59], and the *excess current*, which we explain next. One would expect that at voltages much greater than the gap, the current through a weak link reached the same value as in the normal case, as it happens in tunnel junctions. However, different experiments in point contacts and microbridges [60, 61] show that the current in the high voltage limit is linear but does not extrapolate to zero as the voltage vanishes. The difference at voltages much larger than the gap between the current in the superconducting case and the corresponding one in the normal case is referred to as **excess current**.

In the eighties new theories for the description of the superconducting I-V curves appeared. Among them we shall review two of special interest. The first one is known as KBT model and provided the basis for a definitive understanding of transport phenomena in these systems. It identified the processes which control the current and allowed an unified analysis of tunnel junctions and weak links. The second theory was developed by Arnold and it was orientated to a more microscopic and quantitative description of the superconducting transport. In the following two subsections we shall briefly revise these theories and their predictions.

KBT Model

In a set of papers in 1982 and 1983, Klapwijk, Blonder, Tinkham and in one of them Octavio developed a model based on the scattering formalism to describe N-S and S-S contacts [8] [62, 63, 64]. In their model the excitations of a clean superconductor are described by the Bogoliubov-de Gennes equations [66]. In order to simulate the scattering that takes place in the junctions they used a δ-like potential located in the interfase between electrodes, whose strength is controlled by a parameter Z [9]. The central idea of the model consists of connecting the wave functions of the electrodes through the barrier to obtain the probability of each process and finally its contribution to the total current.

As it is explained in detail in Ref. [63], these authors carried out this scheme completely for the case of a N-S junction. They obtained the current as a function of Z, ranging from the case of a tunnel barrier, where they recovered the results

---

[8]We shall use the notation N-N, N-S, S-S, etc, to refer to contacts made of normal metal-normal metal, normal metal-superconductor, superconductor-superconductor, etc.

[9]The parameter Z is related to the normal transmission coefficient T through the potential barrier by the expression $T = 1/(1 + Z^2)$. Thus for instance, $Z = 0$ means no barrier at all.

of the traditional tunnel theory, to the case in which there is no scattering in the interfase. They showed that both the current inside the gap and the excess current for voltages $eV \gg \Delta$ which appear in these junctions are due to the contribution of a process called *Andreev reflection* [65].

When at least one of the electrodes is superconducting, apart from the quasi-particle tunneling, there exists the possibility of having Andreev reflections. In a N-S junction the Andreev reflection is a process in which an electron coming from the normal metal is reflected as a hole in the interfase, giving rise to the transfer of a Cooper pair to the superconducting electrode (see Fig. 1.6). Due to the energy conservation, the hole has the same energy, measured from the Fermi level, as the incoming electron, i.e. this hole corresponds to the time-reversal state of the original electron. This process produces a charge transfer equal to $2e$, which becomes super-current in the superconducting electrode. The Andreev reflection is an fundamental mechanism in nature since it is the way in which a dissipative current in the normal metal is converted in a supercurrent in the superconductor.
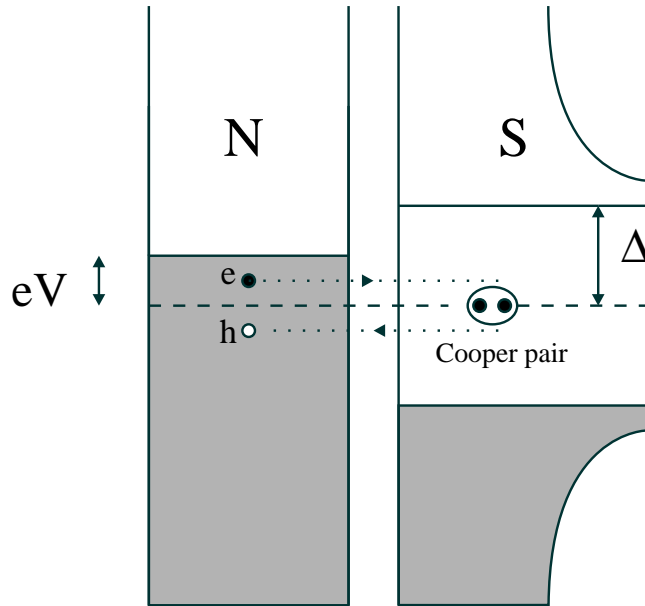
Figure 1.6: Schematical representation of an Andreev reflection in a N-S contact. In this process an electron is reflected as a hole by creating a Cooper pair in the superconducting electrode.

Two of the authors, Blonder and Tinkham [67], showed experimentally that the BTK model describe quantitatively the I-V curves of an N-S contact. To be concrete, they analyzed the current through Cu-Nb point contacts. The special features of the point contacts allowed them to analyze the transition from a tunnel junction to a weak link. The notable agreement indicated the importance of the Andreev reflections in the correct description of the superconducting transport.

The case of a contact with two superconducting electrodes is much more complex. In these contacts it is possible the occurrence of multiple Andreev reflections (MAR), which take place in the following way (see Fig. 2.7 in Chapter 2). When an electron [10] is reflected as a hole, such a hole can undergo a similar process in the other electrode giving rise thus to a reflected electron. This new electron can undergo a new reflection and so on. Thus, when an electron cross the barrier it gains a energy equal to eV, and in the return journey the hole do the same. So, a process in which the quasiparticles cross the interfase n times can be seen as a process in which a quasiparticle gains energy reflection after reflection until it finally gains a energy equal to neV. This multiple process ends when the quasiparticle finds an empty state in an electrode, what happens (at zero temperature) when the minimum condition $neV = 2\Delta$ is fulfilled. Thus, at zero temperature every time $eV = 2\Delta/n$ (n integer) a new multiple Andreev reflection is possible giving a new contribution to the current and explaining in a natural way the subharmonic gap structure. In the case of an asymmetric contact, the subharmonic structure can be explaining using the same argument and taking into account the relation between the gaps.

The scheme developed for the N-S case is difficult to carry out for the S-S or S-N-S case and the authors only did it in the limit of a contact with perfect transmission [62]. In its place, the authors proposed a semiclassical model (OTBK model) based on the Boltzmann equation, which allowed them to analyze the I-V curves for arbitrary transmission [64]. In this model the nonequilibrium distribution functions are determined by means of boundary conditions in the N-S interfases, which are determined by the different processes that take place in such interfases. In some sense, in this model an S-N-S junction is considered as two N-S junction in series. For instance, the probability of a multiple Andreev reflection is given by the product of the probabilities of the elementary processes which form it, neglecting so the interferences between these processes [11].

Fig. 1.7 shows results obtained with the OTBK model for both the current and the differential resistance in a S-S contact. The subharmonic structure can be

---

[10]Strictly speaking the excitations of a superconductor are a combination of electrons and holes. However, for the sake of simplicity we shall speak about electrons instead of quasielectrons, and about holes instead of quasiholes.

[11]As we shall show in Chapter 2, this is probably the main limitation of this model for describing a mesoscopic system.
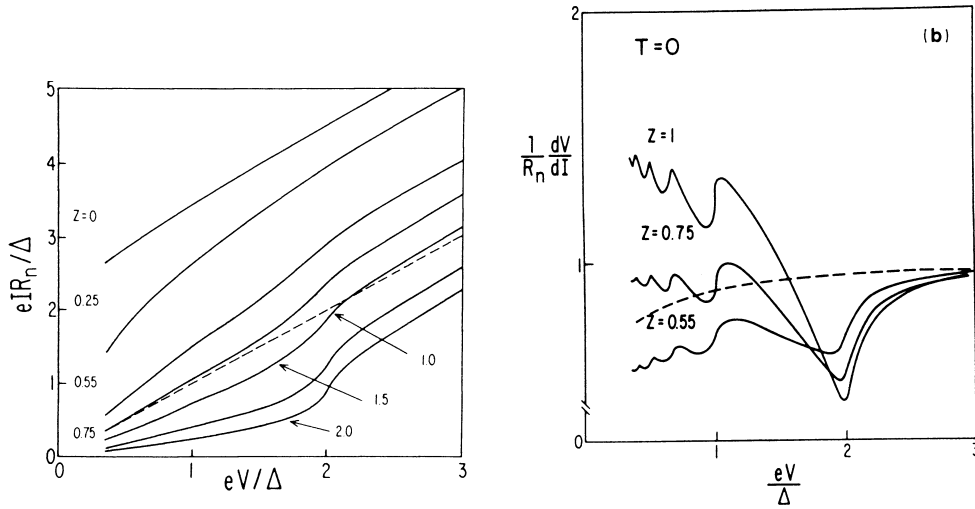
Figure 1.7: Predictions of the OTBK model [68]. Left panel: zero-temperature I-V characteristics of an S-S contact for different transmissions. Right panel: zero-temperature differential resistance for a S-S contact with different transmissions.

observed specially in the differential resistance which exhibits maxima at voltages $eV_n = 2\Delta/n$ with n integer.

Arnold theory.

In the mid eighties Arnold developed a theory for analyzing superconducting junctions with arbitrary transmission through the insulator barrier [69, 70, 71]. His theory is based on nonequilibrium Green function techniques. The idea that he worked out is that of calculating the Green functions for the uncouped electrodes and finally connect them in the interfase by means of suitable boundary conditions. His theory is adequate for treating different junctions as N-I-S, S-I-S, etc.

We remark here the results obtained for the current in a S-I-S junction. Fig. 1.8 (left panel) shows the I-V curves for different values of the transmission coefficient. In this figure the subharmonic structure can be observed, which is more clearly seen in the differential resistance (see Fig. 1.8, right panel). As it was stressed by the author, the subgap structure is due to Andreev reflections in agreement with the KBT model. As can be seen the main difference with this latter model is that the subharmonic structure is more pronounced.
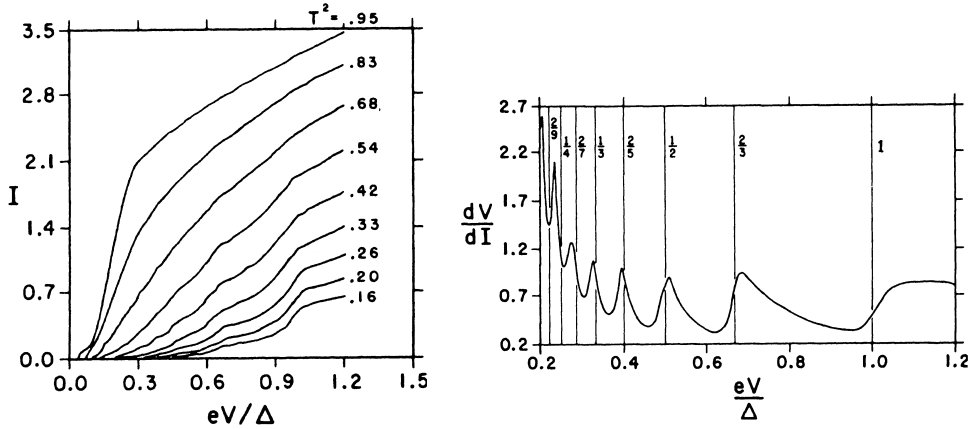
Figure 1.8: Current and differential resistance in the Arnold model. Left panel: zero-temperature I-V characteristics of a S-I-S contact with different transmissions. Right panel: zero-temperature differential resistance for a S-I-S contact with transmission 0.42 [71].

1.2.3 Mesoscopic Superconductivity

With the advance of the microfabrication techniques, nowadays the design of nanometric-size devices is possible. In these systems the characteristic dimensions are comparable to the Fermi wave length (λ_F) of the electrons, thus a purely quantum-mechanical description of their transport properties is indispensable. An example of this kind of systems is a two dimensional electron gas (2DEG) created in semiconductor heterostructures [72]. In this system the electrons are confined in a plane, where the low electronic density implies a large λ_F (typically 40 nm) which is comparable to the dimensions of these structures. Moreover, the mean free path can be as large as (> 1 μm).

Other examples of nanometric-size systems are the metallic atomic-size contacts. These contacts are fabricated with the Scanning Tunneling Microscope (STM) [73] or with the technique of the *mechanically controllable breakjunctions* (MCB) [74]. The current in these atomic contacts flows through a few atoms, thus the system has a minimum width comparable to λ_F, which in the metals is of the order of interatomic distances. Below, we shall describe in detail these contacts which play a fundamental role throughout this thesis.

In these nanometric-size systems the electron phase coherence can be kept over distances of several microns at low temperatures (< 1 K), i.e. almost macroscopic distances. The reason is that the elastic scattering with impurities does not destroy

the phase coherence, what can provoke a modification of the conductivity due to interference phenomena. The physics of these systems is known as **Mesoscopic Physics** [5, 6, 7, 8, 9] to indicate that the length scales involved are between the microscopic world of atoms and the macroscopic world.

In these systems the technological interest coincides with the interest in the investigation of the fundamental principles of the Quantum Mechanics (those related with the concept of the wave function phase). In fact, these solid state devices have become ideal systems where to examine such principles. In the study of electronic transport in the quantum regime one finds certain surprises associated with the mentioned interference phenomena. For instance, the usual rule for connecting resistances in parallel or in series may break down in the quantum regime. Also, the resistance may be nonlocal in the sense that what is measured between a given pair of points may depend on things connected further away.

In the last two decades the mesoscopic systems have given rise to the appearance of a great number of new phenomena that now play a central role in Condensed Matter Physics. For instance, we can mention the Aharanov-Bohm effect, the quantum Hall effect, universal conductance fluctuations, the conductance quantization, Coulomb blockade, etc (see Ref. [72] and references therein). The combination of the mesoscopic physics with the superconductivity has given rise to a new branch known as **Mesoscopic Superconductivity** [75, 76, 77, 78, 79], which is the framework of this first part of the thesis. The rest of this section is devoted to a review of some of well-known superconducting mesoscopic systems which are the aim of our analysis in this thesis.
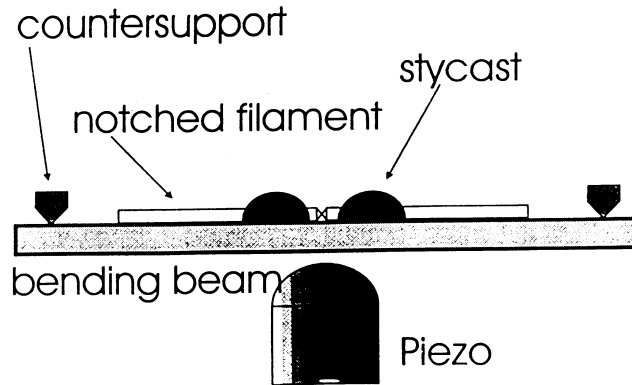
Figure 1.9: Representation of the experimental set-up used for fabricating a breakjunction. A notched filament is mounted over a flexible substrate (bending beam) which is bent in a controllable way making use of a piezo [80].

Let us start by describing the atomic contacts known as *mechanically controllable breakjunctions* (MCB). These contacts initially designed by Moreland *et al.* [81] and improved by Muller *et al.* [74] are formed in the following way. As can be seen in Fig. 1.9, a metallic wire of the material under investigation is glued in a flexible substrate which is broken by bending in a controllable way such substrate. Breaking the wire at low temperatures and at high vacuum guarantees two clean atomic surfaces. The distance between surfaces is controlled by a piezoelectric. This system has a great stability (better than 10^{-13} m), what permits to create contacts of just a few atoms (even one-atom contacts [82]). The great advantage of these systems is that one can vary the contact from the tunnel regimen, with normal resistances $R_N \gg h/2e^2 \sim 12.9$ $k\Omega$, to form a weak link with a few Ohms. Therefore, they are ideal systems for studying the transport in different regimes.
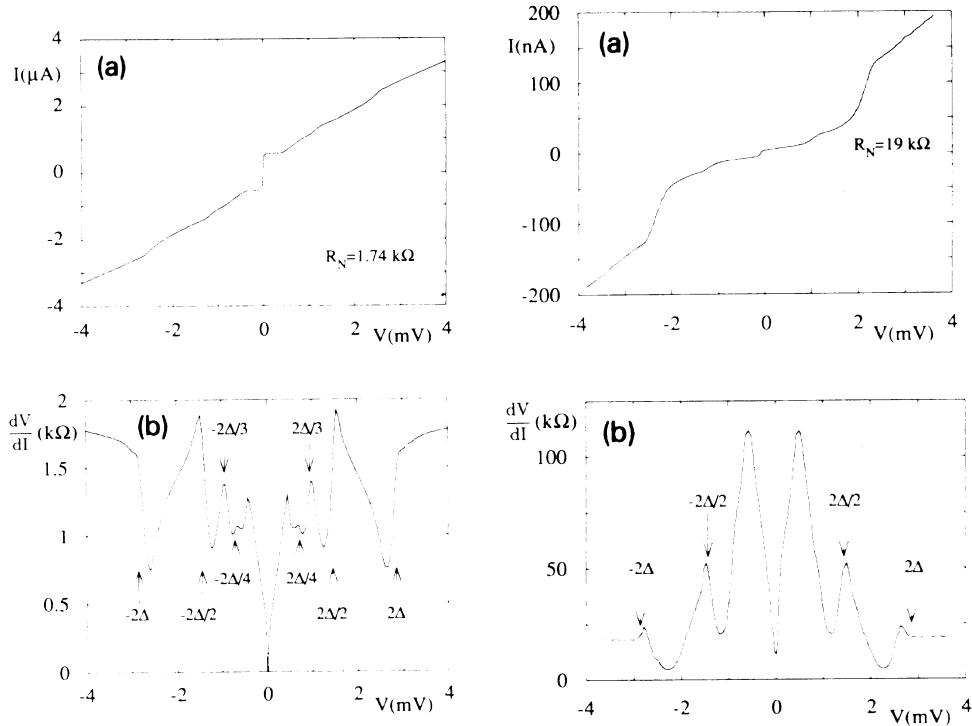
Figure 1.10: I-V characteristics (a) and differential resistance (b) of a Nb breakjunction with 1.74 $k\Omega$ (left panel) and 19 $k\Omega$ (right panel). Notice in both cases the clear subharmonic structure [74].

In the last years this technique has allowed the detailed study of different trans-

port phenomena. For instance, in the breakjunctions a phenomenon similar to the conductance quantization in semiconductor devices has been observed, and something similar for the supercurrent [83, 84]. On the other hand, due to the control in the contact characteristics it has been possible to study the evolution of the supercurrent and the I-V curves from tunnel regime to contact regime. As an example we show here the subharmonic structure which appears clearly in these contacts [74, 85, 86]. Fig.1.10 shows the I-V curves and the differential resistance of two Nb breakjunctions with different normal resistance after Ref. [74]. Notice the pronounced subharmonic gap structure, which is clearly visible even in the current.
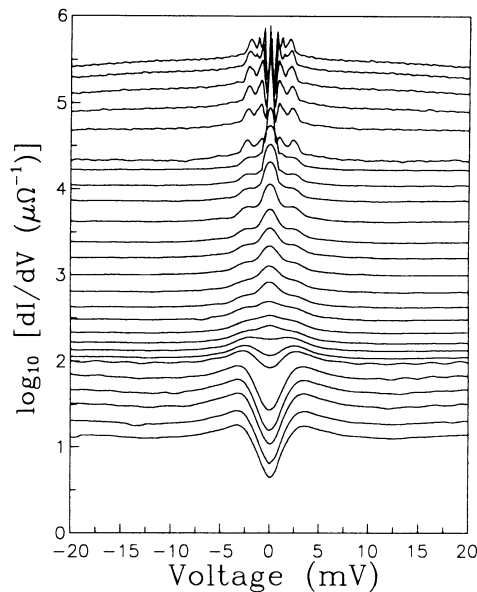
Figure 1.11: Differential conductance in a Pb-Pb superconducting atomic contact created with the STM [88]. The resistance varies from tunnel regimen to contact regime where the subharmonic structure is visible.

Another method to fabricate metallic atomic-size contacts is provided by the Scanning Tunneling Microscope (STM) [73]. This microscope deviced in the early eighties has provided great information about the electronic properties of superconducting materials. For instance, it has been used as planar junctions, point contacts and other geometries for determining the density of states of a superconductor, as well as its phonon spectrum [22]. The STM shares with the breakjunctions all its advantages, and moreover it has the possibility of lateral movement. Due to this movement it is possible to characterize very well the barrier between electrodes,

what provides a better knowledge of the contacts. As in the case of MCB's, one can vary the junction from tunnel to contact [87, 88], what permits to take a whole family of curves ranging the resistance as it is illustrated in Fig. 1.11.

In the above described atomic-size contacts the current finally pass through a few number of atoms, or in other words, the current is controlled by reduced number of conducting channels. This fact converts them in ideal these systems in order to do a quantitative comparison with theory. In this thesis we shall show an exhaustive comparison between our theoretical results and the experimental results obtained with these types of atomic contacts.

The first quantum point contacts arose in the context of the two dimensional electron gases (2DEG) fabricated in semiconductor heterostructures. In these systems was firstly observed the phenomenon of conductance quantization [89, 90]. In principle, the main difficulty to fabricate a superconducting point contact with a 2DEG lies in incorporating the superconducting electrodes. This difficulty has been recently overcome by Takayanagi *et al.* [91]. These authors deviced a superconductor-2DEG-superconductor point contact as the one illustrated in Fig. 1.12 (left panel). Furthermore, they incorporated a "split gate" whose width L_W can be controlled by means of a gate voltage. Thus, they could control the number of conducting channels which contribute to the current through the 2DEG. With this ingenious device they could investigated the quantization of the critical current as it is illustrated in Fig. 1.12 (right panel).

Finally, we mention a system that although it has not the typical profile of a mesoscopic system, it has a renewed interest: the tunnel junctions. These junctions in their modern version, almost always making use of the Nb technology, could serve as X rays detectors [92, 93, 94]. These tunnel junctions exhibit a clear subharmonic structure (see for instance Ref. [94]). Typically this subharmonic gap structure is superimposed to a notable excess current inside the gap, taking into account that they are tunnel junctions. The explanation is that the insulator barriers are not perfect and present pinholes which provoke the mentioned excess current inside the gap [94].

In the last years there has been a great advance in the knowledge of the transport properties of mesoscopic systems in which superconducting elements are involved. From the theoretical point of view there are two important approaches. Firstly, the scattering formalism [95] has provided a very intuitive picture of the superconducting transport in mesoscopic systems [96, 97, 98, 75, 99]. It is also remarkable the so called *nonequiblibrium superconductivity theory* [100, 101, 102, 103, 79]. This theory, based on semiclassical Green function techniques, is specially well adapted for dealing with situations where the elastic scattering with impurities is essential. Furthermore, it provides a suitable framework for treating interactions like electron-electron interaction, electron-phonon interactions, spin-flip processes, etc. Nowadays, it is believed
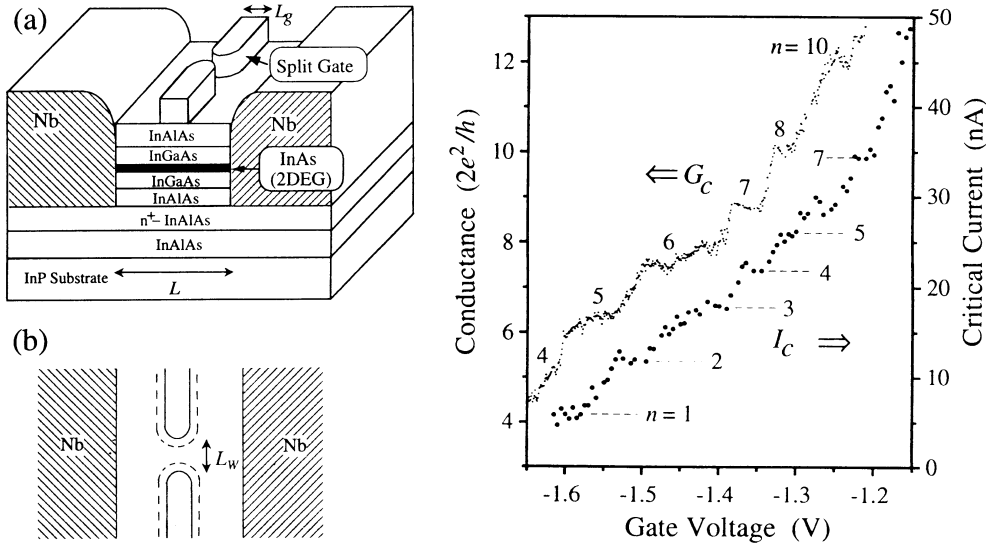
Figure 1.12: Superconducting point contact created by means of a 2DEG [91]. Left: (a) cross sectional view of the point contact. (b) Upper view of the contact. An applied voltage generates a *gate* defining a constriction of width L_W in the 2DEG. Right: critical current I_C and normal conductance G_C of the junction as a function of the gate voltage V_g.

that this theory can explain all proximity effect experiments in N-S structures (see Ref. [104]). In fact, it has achieved such a refinement that there even exists a circuit theory [105], which consists of simple rules, in the same way as the Kirchoff rules, which in principle permit to solve any N-S circuit.

1.3   Objective of the part I

In spite of the notable and numerous successes of the scattering formalism and of the nonequilibrium superconductivity theory, at the beginning of this thesis it was quite clear that there was still a very elementary situation for which there did not exist a satisfactory description. We are referring to the case of superconducting contacts with a finite applied voltage. Although the existent theories seemed to contain part of the physics which governs the electronic transport in superconducting junctions, it was by no means clear that they could quantitatively describe even the simplest situations. At the beginning of this thesis the debate about which theory (multiparticle tunneling theory, self-coupling of the Josephson radiation or

the theories based on multiple Andreev reflections) gave a better description still went on [92, 106, 93, 94, 87]. By analyzing the experiments of the previous references it was rather clear that none of the mentioned theories gave a completely satisfactory explanation for the different situations.

Historically it has been very difficult to do a quantitative comparison between experiment and theory. The main reason lies in that in the traditional experiments, with planar tunnel junctions, there exists a great uncertainty about the crucial junction parameters like the thickness, contact area, transmission, composition and dimensionality of the insulator barrier. However, with the modern microfabrication techniques which have given rise to systems like the STM, 2DEGs and the breakjunctions, these problems have disappeared to a great extent. Thus, our aim at the beginning of this thesis was *to develop a theory which quantitatively describes the electronic transport in superconducting contacts.* The following paragraphs are devoted to concrete this aim.

As it is clear from the historical review, the description of the electronic transport in S-S contacts is very complex, even in the simplest situations. Thus, we shall concentrate in the description of *short* contacts known as *superconducting quantum point contacts* (SQPC). Next we shall explain what we mean by an SQPC and for ending this chapter we shall mention the experimental systems which fit in the profile of these contacts.
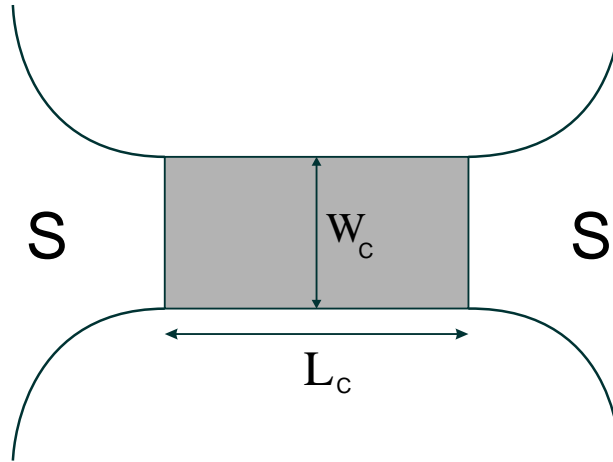
Figure 1.13: Schematical representation of a SPQC.

By an SQPC we mean a superconducting contact like the one depicted in Fig.

1.13. In this contact the constriction which links both electrodes has a length L_C much smaller than the superconducting coherence length ξ of the electrodes. As we shall comment in the Chapter 2, this feature allows us to do some hypothesis which simplify the problem considerably. On the other hand, in a SQPC the constriction width is comparable to the Fermi wave length λ_F of the system electrons, what implies that the junctions only sustains a reduced number of conducting channels [12].

The different mesoscopic systems that we described in the previous section fit in the definition of a SQPC, in special the metallic atomic-size contacts and the S-2DEG-S point contacts. Thus for instance, in the metallic contacts, created with the STM o with the breakjunction technique, have a minimum width of the order of a few atoms, that is, comparable to the λ_F of the metals. On the other hand, the superconducting coherence length ($\xi \sim 10^2 - 10^3$ nm) is much greater than the contact atomic neck length.

Thus, systems of undoubted interest fit the definition of a SQPC. Finally, we conclude this chapter by reminding our aim for the part I of the thesis:

> To develop a theory which describes the dc an ac transport in SQPCs quantitatively.

---

[12]This assumption is not fundamental in the theory that we will develop, but of course the experimental comparison will be more accessible if this condition holds.

Chapter 2

Transport in superconducting quantum point contacts

2.1 Introduction

Traditionally, quantum transport in microelectronic devices has been mainly addressed by three different approaches: one is based in the scattering formalism, first introduced by Landauer [95] and generalized by Bütikker [107], in which the transport properties are expressed in terms of the scattering matrix of the system [1]. In this picture one converts a transport problem in a scattering problem by replacing the device by an appropriate scattering matrix. The natural extension of this formalism to the superconducting case was provided by the already mentioned KBT model [62].

Another widely used technique is that of the semiclassical Green functions [100, 101, 102, 103, 79]. In this case the problem consists of determining the Green functions for the uncoupled electrodes and finally connect them in the interfases by means of suitable boundary conditions. As we explained in the previous chapter, this point of view has produced great results, specially in the context of N-S systems.

Finally, a different point of view arises when the problem is analyzed starting from a microscopic Hamiltonian. We shall very generally call *Hamiltonian approach* to the theories which take this starting point. The origin of this approach can be traced back to the work by Bardeen who introduced the tunnel Hamiltonian [2] approximation for describing a tunnel junction [11]. Most of the calculations based on this tunnel Hamiltonian were restricted to the lowest order transport processes like in the calculation of the Josephson current in a S-I-S junction [18, 19]. Multi-particle

---

[1] As general references about the scattering formalism we recommend the textbooks [7, 9].

[2] Also known as *transfer Hamiltonian*.

tunneling was first discussed by Schrieffer and Wilkins [34] in their *multiparticle tunneling theory*, as a possible explanation for the observed subgap structure in superconducting tunnel junctions. The contributions of these higher order processes were found to be divergent, which has led to the quite extended belief that the Hamiltonian approach is pathological except for describing the lowest order tunneling processes.

We shall make use of this last point of view and we shall show the equivalence between the scattering formalism and the Hamiltonian approach. As will be shown below, the inclusion of higher order processes up to infinite order eliminates the pathologies associated with finite order perturbation theory.

On the other hand, the Hamiltonian approach in combination with non-equilibrium Green function techniques presents certain advantages. For instance, this approach can be generalized for dealing with situations where self-consistency of the superconducting order parameter is needed [108, 109]. Moreover, the formulation in terms of Green functions is specially well suited for dealing with correlation effects when strong electron-electron interactions are present [110]. Furthermore, with respect to the semiclassical Green functions the Hamiltonian approach has the following advantage. If a system is described by a Hamiltonian, one has not to worry about boundary conditions, since one has a natural prescription to connect Green functions in the interfases. Of course, the Hamiltonian approach has also certain disadvantages. One may think that the scattering formalism is more transparent from the physical point of view, in comparison with the apparent complexity of the Green functions. On the other hand, it is obvious that the semiclassical Green functions are better adapted for dealing with situations like disordered systems.

This chapter, based on our works [111, 112], is organized as follows. In section 2.2 we shall start describing our Hamiltonian approach to study the transport properties of a single channel SQPC, as well as the method used for solving such a model. In section 2.3 we shall analyze the case of single channel N-N and N-S contacts in order to show explicitly the equivalence with the scattering formalism. Section 2.4 is devoted to the detailed analysis of single channel S-S contacts, emphasizing the novel results that our model provides. In section 2.5 we show an exhaustive comparison between experimental results obtained in superconducting atomic contacts and the predictions of our theory. In section 2.6 we shall summarize the main conclusions of this chapter and we postpone some comments about future works and open problems until the end of Chapter 4.

2.2 Hamiltonian approach for SQPCs

For the general description of a superconducting system we take as a starting point a grand canonical Hamiltonian with an attractive delta-type electron-electron inter-

action ($U > 0$), which written in second quantization language has the form

$$
\begin{aligned}
\hat{H} &= \hat{H}_0 + \hat{H}_{int} \\
\hat{H}_0 &= \int d\vec{r} \sum_{\sigma} \hat{\Psi}_{\sigma}^{\dagger}(\vec{r}) \, H_0 \, \hat{\Psi}_{\sigma}(\vec{r}) \\
\hat{H}_{int} &= -\frac{1}{2} \int d\vec{r} \sum_{\sigma,\sigma'} U(\vec{r}) \hat{\Psi}_{\sigma}^{\dagger}(\vec{r}) \hat{\Psi}_{\sigma'}^{\dagger}(\vec{r}) \hat{\Psi}_{\sigma'}(\vec{r}) \hat{\Psi}_{\sigma}(\vec{r}),
\end{aligned}
\tag{2.1}
$$

where $\hat{\Psi}_{\sigma}(\vec{r})$ is the field operator which destroys an electron with spin σ located in $\vec{r}$. H_0 is the single-particle Hamiltonian given by $H_0 = (1/2m)\left(\vec{p} - (e/c)\vec{A}\right)^2 + V_0(\vec{r}) - \mu(\vec{r})$. In this latter expression $\vec{A}$ is the vector potential associated with the corresponding magnetic field, $V_0(\vec{r})$ is an arbitrary external potential which may represent an electrostatic potential or an impurity potential, and finally μ is the chemical potential of the system.

Within the BCS approximation the Hamiltonian (2.1) is analyzed in a mean field approximation or generalized Hartree-Fock approximation [113, 66, 114]. This is equivalent to approximate the four operator term in $\hat{H}_{int}$, using the Wick theorem, by sums of products in which two operator terms are replaced by their mean values. This lead us to an effective Hamiltonian [66] [3]

$$
\hat{H} = \int d\vec{r} \left\{ \hat{\Psi}_{\sigma}^{\dagger}(\vec{r}) \, H_0' \, \hat{\Psi}_{\sigma}(\vec{r}) \; + \; \Delta^*(\vec{r}) \hat{\Psi}_{\downarrow}^{\dagger}(\vec{r}) \hat{\Psi}_{\uparrow}^{\dagger}(\vec{r}) \; + \; \Delta(\vec{r}) \hat{\Psi}_{\uparrow}(\vec{r}) \hat{\Psi}_{\downarrow}(\vec{r}) \right\},
\tag{2.2}
$$

where $H_0'(\vec{r}) = H_0(\vec{r}) + V(\vec{r})$, being $V(\vec{r})$ the Hartree potential, which only renormalizes the single-particle spectrum, given by $V(\vec{r}) = -U(\vec{r})\langle \hat{\Psi}_{\uparrow}^{\dagger}(\vec{r}) \hat{\Psi}_{\uparrow}(\vec{r}) \rangle$. On the other hand, the order parameter $\Delta(\vec{r})$ is given by $\Delta(\vec{r}) = -U(\vec{r})\langle \hat{\Psi}_{\downarrow}^{\dagger}(\vec{r}) \hat{\Psi}_{\uparrow}^{\dagger}(\vec{r}) \rangle$.

As it is well-known, one may diagonalize this effective Hamiltonian by defining new fermion operators by means of a Bogoliobuv transformation [115]. Because of the pair-potential Δ the creation operators of these new fermions quasiparticles will consist of a coherent sum of an old quasiparticle and its time-reversed counterpart. The equations which describe the dynamics of the two-component wave functions of the superconductor quasiparticles are called Bogoliubov-de Gennes (BdeG) equations, and they have the form of a Schrödinger equation in the space of electrons and holes:

---

[3]Notice that we have considered that expectation values as $\langle \hat{\Psi}_{\uparrow}^{\dagger} \hat{\Psi}_{\downarrow} \rangle$ vanish, because we shall not consider magnetic situations. Moreover, we only consider s pairing for the order parameter, according with our aim of analyzing traditional superconductors.

$$\left(\begin{array}{cc} H_0'(\vec{r}) & \Delta(\vec{r}) \\ \Delta^*(\vec{r}) & -H_0'^*(\vec{r}) \end{array} \right) \left(\begin{array}{c} u \\ v \end{array} \right) = i\hbar \frac{d}{dt} \left(\begin{array}{c} u \\ v \end{array} \right). \qquad (2.3)$$

The solution of these equations is simple in the case of a homogeneous system in absence of impurities, where quasiparticle wave functions are simply plane waves. However, in more complex situations, where for instance one has a space-dependent order parameter, to solve the BdeG equations is rather difficult. In these cases, it is more convenient the use of Green functions, which is the approach that we shall follow. Moreover, instead of working in real space, we believe that the use of a local basis has certain advantages, as we shall show below. For this reason, we first transform the Hamiltonian (2.2) to a site representation. The change of basis is given by the relation between operators in both basis:

$$\hat{\Psi}_\sigma(\vec{r}) = \sum_i \phi_i(\vec{r}) \, \hat{c}_{i\sigma}, \qquad (2.4)$$

where $\{\phi_i(\vec{r})\}$ is a orthonormal local basis, as for instance an atomic orbital basis [4], whose wave functions are localized around the different system sites. On the other hand, $\hat{c}_{i\sigma}$ is the annihilation operator in the site i. In this new basis the effective Hamiltonian in absence of magnetic field adopts the form

$$\hat{H} = \sum_{i,\sigma} (\epsilon_i - \mu_i) c_{i\sigma}^\dagger c_{i\sigma} + \sum_{i \neq j,\sigma} t_{ij} c_i^\dagger c_j + \sum_i (\Delta_i^* c_{i\downarrow}^\dagger c_{i\uparrow}^\dagger + \Delta_i c_{i\uparrow} c_{i\downarrow}), \qquad (2.5)$$

where i, j run over the sites used to represent the system [5]. The different parameters of the Hamiltonian are: the on-site energies ϵ_i, the chemical potential μ_i in each site, the hoppings t_{ij} which couple the different sites and the local complex order parameter Δ_i. By choosing appropriately the different parameters one can simulate a superconducting contact with arbitrary geometry. In general, one has to complement the previous Hamiltonian with the self-consistency condition for the order parameter in each site:

$$\Delta_i = -U_i \langle c_{i\downarrow}^\dagger c_{i\uparrow}^\dagger \rangle, \qquad (2.6)$$

where U_i is the attractive electron-electron interaction in each site.

In previous works of our group this approach based on a site representation has been used for describing the electronic and transport properties of superconducting contacts [116, 108, 109]. This representation can be view either as a tight-binding description of the electronic states or as a discretization of the BdeG equations. The

---

[4]In part II of the thesis we shall use an atomic orbital basis for describing the electronic transport in metallic atomic-size contacts.

[5]Usually we shall assume that there is only one "orbital" per site.

first case would be more suitable for describing systems like an atomic-size contact (Fig. 2.1(a)), while the second could be used to represent constrictions involving a 2DEG in semiconductor heterostructures (Fig.2.1(b)).
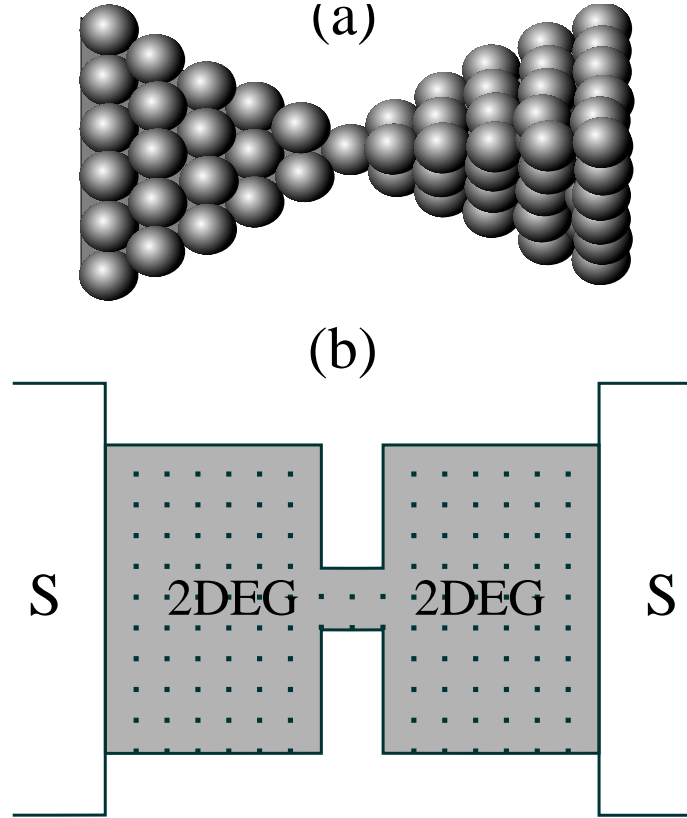
Figure 2.1: Schematical representation of two types of SQPC: (a) atomic contact and (b) two-dimensional electron gas.

In Refs. [108, 109] the dc Josephson effect has been analyzed for the case of a constriction of arbitrary length. The self-consistent description carried out in these works is very difficult to generalize to the case of a finite bias voltage. Thus, as we stated at the end of Chapter 1, we shall restrict ourselves to the study of a SQPC. Let us remember that these contacts consist of two wide (3D or 2D) electrodes connected by a narrow constriction (see Fig. 1.13). The constriction length, L_C, is assumed to be much smaller than the superconducting coherence length and its width, W_C, comparable to the Fermi wavelength, λ_F. As we commented in the

previous chapter, there are a lot of systems that fit the SQPC definition. For instance, the atomic contacts created by the break-junction technique [85, 86] or with the STM [87, 88], and the split-gate S-2DEG-S of Takayanagi [91]. These two situations are schematically represented in Fig. 2.1.

In the case of a short constriction ($L_C \ll \xi$), as the SQPC case, the detailed form of the self-consistent order parameter and the electrostatic potential in the region between the electrodes become irrelevant, allowing us to represent them by simple step functions. The validity of this hypothesis has been discussed in detail by several authors [55, 108, 109] and its justification is explained as follows:

1. If the width W_C of the junction is small compared to the coherence length, the non-uniformities in Δ extend only over a distance of the order W_C from the junction. Since non-uniformities on length scales $\ll \xi$ do not affect the dynamics of the quasiparticles, these can be neglected and the step-function model holds. In fact, if the length and width of the junction are $\ll \xi$, it is irrelevant whether it is made of a normal metal or of a superconductor. In particular, the atomic-size contacts correspond to this case.

2. Alternatively, the step-function hypothesis works if the resistance of the junction is much bigger than the resistance of the bulk superconductor. This condition has been formulated precisely by Kupriyanov *et al.* [117]. A superconductor-semiconductor-superconductor junction typically belongs to this second case.

With the previous hypothesis we need not to determine the exact profile of the potentials and the problem is thus simplify greatly. Anyway, in order to simplify the problem as much as possible, we start analyzing the case of a single quantum channel contact. Below, in section 2.5 we shall indicate how to generalize the results to the case of a SQPC with an arbitrary number of channels. A single channel model can be built up in a simple way within the approach represented by Hamiltonian (2.5), we just need to connect only one site of each electrode (this situation is schematically represented in Fig. 2.2). Thus, taking the complex order parameter and the electrostatic potentials as constants on the left and right electrodes [denoted by (Δ_L, μ_L) and (Δ_R, μ_R), respectively], the case of a single channel connecting both electrodes can be described by the following Hamiltonian

$$\hat{H} = \hat{H}_L + \hat{H}_R + \sum_\sigma (t c^\dagger_{L\sigma} c_{R\sigma} + t^* c^\dagger_{R\sigma} c_{L\sigma}) - \mu_L \hat{N}_L - \mu_R \hat{N}_R, \qquad (2.7)$$

where $\hat{H}_L$ and $\hat{H}_R$ are the BCS Hamiltonians, written in a local basis, which describe the uncoupled electrodes. The third term is the coupling term which describes the electron transfer processes between the outermost sites on both electrodes, denoted as L and R. Finally, $\hat{N}_{L,R}$ are the particle number operator of each electrode.

We would like to stress that, although this is a very simple model Hamiltonian (formally equivalent to a tunnel Hamiltonian), it contains the relevant physics of a quantum point contact which depends essentially on the contact normal transmission coefficient. In our model this transmission can vary between ~ 0 (tunnel limit) and ~ 1 (ballistic regime) as a function of the coupling parameter t. This will be discussed in section 2.3.
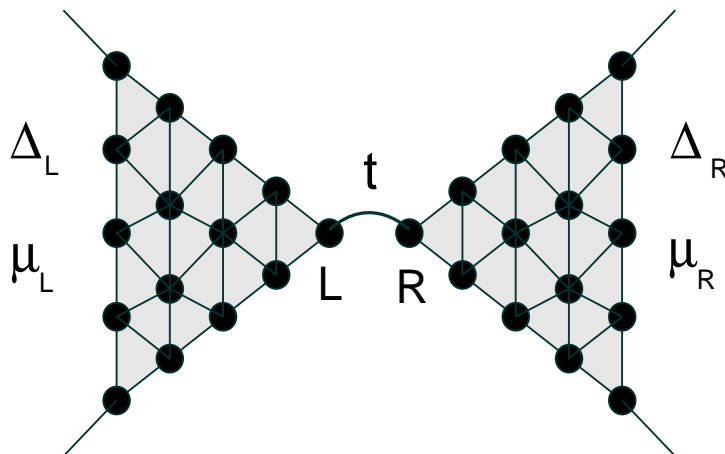
Figure 2.2: Representation of a superconducting contact with only one conducting channel described in a site representation.

We shall study the case of a symmetric contact with constant bias voltage $eV = \mu_L - \mu_R$ [6]. In order to analyze this case it is convenient to perform a gauge transformation [118] by means of which the Hamiltonian (2.7) adopts the following time-dependent form [7]

$$\hat{H}(\tau) = \hat{H}_L + \hat{H}_R + \sum_{\sigma} \left(t e^{i\phi(\tau)/2} c_{L\sigma}^{\dagger} c_{R\sigma} + t^* e^{-i\phi(\tau)/2} c_{R\sigma}^{\dagger} c_{L\sigma} \right), \qquad (2.8)$$

where the superconducting phase, $\phi(\tau)$, is given by the Josephson relation $\phi(\tau) = \phi_0 + 2eV\tau/\hbar$ and appears as a phase factor in the hopping elements.

Within the previously introduced model, the average total current through the contact evaluated between both electrodes is given by

---

[6]In order to keep constant the voltage in the system, it is necessary that impedance of the junction (of the order of h/e^2) be greater than the characteristic impedance of the external circuit. This is a condition that is experimentally achieved, unless the voltage is very small ($eV \ll \Delta$).

[7]We denote the time as τ to distinguish it from the hopping t.

$$I(\tau) = \frac{ie}{\hbar} \sum_{\sigma} (t < c_{L\sigma}^{\dagger}(\tau) c_{R\sigma}(\tau) > - t^* < c_{R\sigma}^{\dagger}(\tau) c_{L\sigma}(\tau) >), \qquad (2.9)$$

where, depending on the gauge choice, t can include a time dependent phase like in Eq. (2.8). Thus, our problem consists of determining the expectation values appearing in the current expression. These average quantities are evaluated over non-equilibrium states whose dynamics is controlled by Hamiltonian (2.8). In order to determine these type of expectation values it is convenient to use the Keldysh formalism [119] that we describe in detail in Appendix A. Moreover, for the superconducting state it is also convenient to introduce the (2×2) matrix Nambu representation [120], where the field operators in a local representation are defined as

$$\hat{\psi}_i = \begin{pmatrix} c_{i\uparrow} \\ c_{i\downarrow}^{\dagger} \end{pmatrix}, \quad \hat{\psi}_i^{\dagger} = \begin{pmatrix} c_{i\uparrow}^{\dagger} & c_{i\downarrow} \end{pmatrix}. \qquad (2.10)$$

The different correlation functions which appear in the Keldysh formalism adopt the following form

$$\hat{G}_{i,j}^{\alpha,\beta}(t_\alpha, t_\beta') = -i \langle \hat{T}_c \left[\hat{\psi}_i(t_\alpha) \hat{\psi}_j^{\dagger}(t_\beta') \right] \rangle, \qquad (2.11)$$

where $\hat{T}_c$ is the time-ordering operator along the Keldysh time contour. The indexes α and β indicate the branch in such a contour ($\alpha, \beta = \pm$) (see Appendix A). On the other hand, i, j indicate the sites. Thus for instance, the Green functions $\hat{G}_{i,j}^{+,-}$, which give us information on the non-equilibrium distribution function, are given by a (2×2) matrix

$$\hat{G}_{i,j}^{+-}(\tau, \tau') = i \begin{pmatrix} < c_{j\uparrow}^{\dagger}(\tau') c_{i\uparrow}(\tau) > & < c_{j\downarrow}(\tau') c_{i\uparrow}(\tau) > \\ < c_{j\uparrow}^{\dagger}(\tau') c_{i\downarrow}^{\dagger}(\tau) > & < c_{j\downarrow}(\tau') c_{i\downarrow}^{\dagger}(\tau) > \end{pmatrix}. \qquad (2.12)$$

In terms of these Green functions, the current can be expressed as

$$I(\tau) = \frac{e}{\hbar} \, \mathrm{Tr} \left[\hat{\sigma}_z \left(\hat{t} \hat{G}_{RL}^{+-}(\tau, \tau) - \hat{t}^{\dagger} \hat{G}_{LR}^{+-}(\tau, \tau) \right) \right], \qquad (2.13)$$

where $\hat{\sigma}_z$ is the corresponding Pauli matrix, Tr denotes the trace in Nambu space and $\hat{t}$ is the hopping that in the Nambu matrix representation is written as

$$\hat{t} = \begin{pmatrix} t & 0 \\ 0 & -t^* \end{pmatrix}. \qquad (2.14)$$

In absence of magnetic field, the spin symmetry allows us to simplify the current expression and work only in the electron space:

$$I(\tau) = \frac{2e}{\hbar} \left[\hat{t}\hat{G}_{RL}^{+-}(\tau,\tau) - \hat{t}^*\hat{G}_{LR}^{+-}(\tau,\tau) \right]_{11},\qquad(2.15)$$

where $(1,1)$ indicates the corresponding matrix element in the Nambu representation.

The problem has been then reduced to the determination of these Green functions. We shall calculate them within the perturbative scheme of the Keldysh formalism, treating the coupling term in Hamiltonian (2.8) as a perturbation. The unperturbed Green functions correspond to the uncoupled electrodes in equilibrium, each one with its corresponding chemical potential. For a symmetric contact, and neglecting finite bandwidth effects, the uncoupled retarded and advanced Green functions of the outermost sites of each electrode (L, R) can be expressed as [8]

$$\hat{g}_{LL}^{r,a}(\omega) = \hat{g}_{RR}^{r,a}(\omega) = \frac{1}{W\sqrt{\Delta^2 - (\omega \pm i\eta)^2}} \begin{pmatrix} -\omega \pm i\eta & \Delta \\ \Delta & -\omega \pm i\eta \end{pmatrix},\qquad(2.16)$$

where W is an energy scale related to the normal density of states at the Fermi level (taken as zero) by $\rho(\epsilon_F) \sim 1/(\pi W)$. On the other hand, η is a small energy relaxation rate that takes into account the damping of the quasi-particle states due to inelastic processes inside the electrodes. A typical value of η for the traditional superconductors is $\eta/\Delta < 10^{-2}$ (see for instance Ref. [121]). Thus, in general η is the smallest energy scale and can be usually considered as zero [9]. However, as we shall see below, η play an important role in the small bias voltage limit ($eV \ll \Delta$).

The Green functions (2.16) are the typical BCS Green functions for a bulk superconductor. One can obtain this expression, within a tight-binding representation, calculating the Green functions of the last site of a linear chain or a Bethe lattice (see Ref. [122]). The exact electrode geometry is irrelevant because we are only interested in a small range of energies around the Fermi level, which is the relevant energy interval for the transport properties. In this energy range, and due to the fact that the superconducting gap is much smaller than the band-width, the Green functions of any superconducting electrode have the form given by Eq. (2.16).

On the other hand, the unperturbed functions $\hat{g}^{+-}(\omega)$ satisfy the relation

$$\hat{g}^{+-}(\omega) = 2\pi i\hat{\rho}(\omega)n_F(\omega),\qquad(2.17)$$

where $\hat{\rho}(\omega) = (1/\pi)\text{Im}[\hat{g}^a(\omega)]$ and $n_F(\omega)$ is the Fermi function.

Within the Keldysh formalism the functions $\hat{G}_{i,j}^{+-}$ of the coupled (perturbed) system can be obtained by means of the integral equation (see Appendix A) [10]

---

[8]We assume electron-hole symmetry in the leads.

[9]In most of the calculations we shall take $\eta = 0$, except we say explicitly the contrary.

[10]In Eq. (2.18) we have used the fact that the self-energies $\hat{\Sigma}_{ij}^{+,-} = 0$ in this model, because the coupling term is a one-body perturbation.

$$
\begin{aligned}
\hat{G}^{+-}(\tau, \tau') \;=\; & \int d\tau_1 d\tau_2 \left[\hat{I}\delta(\tau - \tau_1) + \hat{G}^r(\tau, \tau_1)\hat{\Sigma}^r(\tau_1) \right] \hat{g}^{+-}(\tau_1 - \tau_2) \times \\
& \left[\hat{I}\delta(\tau_2 - \tau') + \hat{\Sigma}^a(\tau_2)\hat{G}^a(\tau_2, \tau') \right],
\end{aligned}
\tag{2.18}
$$

where $\hat{G}^{r,a}$ satisfy the Dyson equations

$$
\hat{G}^{r,a}(\tau, \tau') = \hat{g}^{r,a}(\tau - \tau') + \int d\tau_1 \; \hat{g}^{r,a}(\tau - \tau_1)\hat{\Sigma}^{r,a}(\tau_1)\hat{G}^{r,a}(\tau_1, \tau'),
\tag{2.19}
$$

$\hat{g}^{r,a}$ being the Green functions of the uncoupled electrodes given by Eq. (2.16). In the previous expressions the self-energies of this model take the simple form $\hat{\Sigma}^{r,a}_{LL} = \hat{\Sigma}^{r,a}_{RR} = 0$ and $\hat{\Sigma}^{r,a}_{LR} = (\hat{\Sigma}^{r,a}_{RL})^* = \hat{t}$. The knowledge of the self-energies allows to solve the model exactly, i.e. up to infinite order. However, in spite of the apparent simplicity of the model its solving in the general case of a S-S junction is not trivial at all. Thus, we shall start analyzing it in the case of N-N and N-S contacts to gain some insight.

2.3   N-N and N-S single channel contacts

In this section we discuss the N-N and N-S cases within our single channel model. The analysis of the N-N case allows us to define the normal transmission coefficient of the contact in term of the microscopic parameters of the model. Thus, it will permit us to make contact with the scattering formalism. On the other hand, in the N-S case we shall compare our results with the ones of the BTK model [63], to show explicitly the equivalence between the scattering formalism and our Hamiltonian approach in the case where at least a superconducting electrode is involved. For the sake of clarity, all the technical calculations are explained in Appendix B, and here we are mainly concerned with the results.

In these two cases the problem admits a stationary (time-independent) solution, so it is convenient to adopt a time-independent formulation based on Hamiltonian (2.7). In this case the Green functions depend on the difference of their temporal arguments and the integral equations (2.18-19) become simple algebraic equations when Fourier transformed with respect to the difference of times. Then, we have

$$
\hat{G}^{r,a}(\omega) = \hat{g}^{r,a}(\omega) + \hat{g}^{r,a}(\omega)\hat{\Sigma}^{r,a}(\omega)\hat{G}^{r,a}(\omega),
\tag{2.20}
$$

$$
\hat{G}^{(+-),(-+)}(\omega) = \left[\hat{I} + \hat{G}^r(\omega)\hat{\Sigma}^r(\omega) \right] \hat{g}^{(+-),(-+)}(\omega) \left[\hat{I} + \hat{\Sigma}^a(\omega)\hat{G}^a(\omega) \right],
\tag{2.21}
$$

where $\hat{g}^{-+}(\omega) = -2\pi i \hat{\rho}(\omega)[1 - n_F(\omega)]$. On the other hand, it is convenient to rewrite expression (2.15) for the current as (see Appendix B)

$$I = \frac{2e}{h} t^2 \int_{-\infty}^{\infty} d\omega \left[g_{LL,11}^{+-}(\omega) G_{RR,11}^{-+}(\omega) - g_{LL,11}^{-+}(\omega) G_{RR,11}^{+-}(\omega) \right], \qquad (2.22)$$

where we have assumed that the left (L) electrode is in normal state, while the right one can be either normal or superconducting.

Let us first analyze the case where both electrodes are in the normal state (the details of the calculation of the N-N current can be found in Appendix B). As in the scattering approach, the current can be written as [123]

$$I = \frac{2e}{h} \int_{-\infty}^{\infty} T(\omega, V) \left[n_F(\omega - eV) - n_F(\omega) \right] d\omega, \qquad (2.23)$$

where $T(\omega, V)$ is an energy and voltage dependent transmission coefficient which is given by [11]

$$T(\omega, V) = \frac{4\pi^2 t^2 \rho_{LL}(\omega - eV) \rho_{RR}(\omega)}{|1 - t^2 g_{LL}(\omega - eV) g_{RR}(\omega)|^2}. \qquad (2.24)$$

Notice that in the tunnel limit (first order in the coupling term) this transmission coefficient adopts the form $T(\omega, V) \sim 4\pi^2 t^2 \rho_{LL}(\omega - eV) \rho_{RR}(\omega)$, which lead us to the usual expression for the current in this limit. The exact expression of $T(\omega, V)$ is a consequence of the sum of all possible processes, up to infinite order, that take place in the junction.

Eq. (2.24) adopts a simpler form in the small bias limit where the normal system exhibits an Ohmic response. This regime is valid for a bias voltage range much smaller than the typical energy scale for the variation of the normal density of states around the Fermi level. This condition certainly holds for the case we are interested in ($eV \sim \Delta$) and is consistent with the assumptions leading to Eq. (2.16). In this limit the coefficient $T(\omega, V)$ becomes a constant, which we denote as α for convenience in the notation, given by

$$T(\omega, V) \simeq \frac{4t^2/W^2}{(1 + t^2/W^2)^2} \equiv \alpha. \qquad (2.25)$$

The zero-temperature normal conductance of this normal single-mode contact is given by $G_{NN} = (2e^2/h)\alpha$, which is nothing but the Landauer formula for the single-channel case. Notice that α can vary between zero and one as a function of t. The $\alpha \to 0$ limit is reached both for $t/W \ll 1$ and for $t/W \gg 1$, while the ballistic limit, i.e. $\alpha \sim 1$, is reached when $t/W \sim 1$.

---

[11] In Eq. (2.24) we have suppressed the Nambu indexes because we are in the normal case.
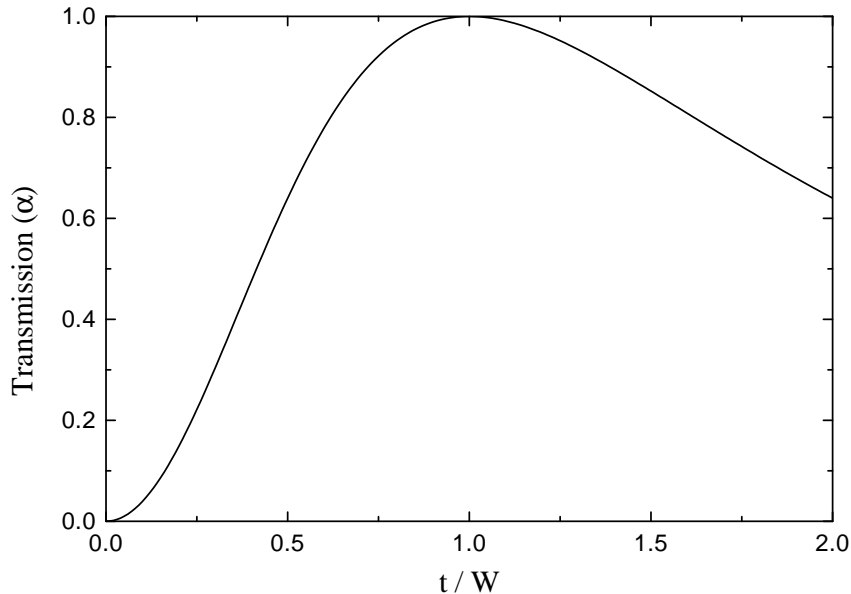
Figure 2.3: Normal transmission α in the linear regime as a function of the ratio t/W (see Eq. (2.25)).

It is worth to further clarify the role of the hybridization parameter t within our point contact model. Although in the context of the tunnel Hamiltonian approach it has been customary to identify $\sim t^2$ with the transmission probability, this strictly holds for the tunnel regime (lowest order perturbation theory in t). However, the actual expression for the contact transparency (Eq. (2.25)), including all order processes is a non-linear function of t^2. While the ballistic condition is achieved for $t^2/W^2 \sim 1$, the way in which α approaches unity is completely different from $\sim t^2/W^2$ [12].

---

[12]In Ref. [124] a detailed discussion on the derivation of Eq. (2.25) by a different perturbative formalism and its range of validity can be found. As stated in this reference, finite order perturbation in the coupling t/W is only valid for $t/W < 1$, while for $t/W > 1$ finite order perturbation theory breaks down together with the appearance of bound states outside the metallic band. This fact could lead to the conclusion that Eq. (2.25) is not valid for $t/W > 1$. However, being the result of the summation of the complete infinite series, Eq. (2.25) is actually a nonperturbative result valid even for the somewhat academic case $t/W > 1$. In fact, by comparing this expression with the normal transmission coefficient of the δ-like scattering potential model used by BTK, the equivalence of both models arises by identifying $Z = [1 - (t/W)^2]/(2t/W)$, where Z is the parameter controlling the barrier strength. Thus, one can associate the case $t/W < 1$ with a repulsive barrier ($Z > 0$), and the case $t/W > 1$ with an attractive δ-like potential ($Z < 0$), which certainly would lead to a

In the N-S case ($\Delta_L = 0$, $\Delta_R = \Delta$) starting from Eqs. (2.20-22) after some simple algebra (see Appendix B for details) we obtain the following expression for the current as the sum of four different contributions $I = I_1 + I_2 + I_3 + I_A$, where

$$
\begin{aligned}
I_1 &= \frac{8e}{h}\pi^2 t^2 \int_{-\infty}^{\infty} d\omega \, |1 + tG^r_{RL,11}(\omega)|^2 \times \\
&\qquad \rho_{LL,11}(\omega - eV)\rho_{RR,11}(\omega) \left[n_F(\omega - eV) - n_F(\omega) \right] \\
I_2 &= -\frac{16e}{h}\pi^2 t^2 \int_{-\infty}^{\infty} d\omega \, \mathrm{Re}\left\{ tG^a_{LR,21}(\omega) \left[1 + tG^r_{RL,11}(\omega) \right] \right\} \times \\
&\qquad \rho_{LL,11}(\omega - eV)\rho_{RR,12}(\omega) \left[n_F(\omega - eV) - n_F(\omega) \right] \\
I_3 &= \frac{8e}{h}\pi^2 t^4 \int_{-\infty}^{\infty} d\omega \, |G_{RL,12}(\omega)|^2 \rho_{LL,11}(\omega - eV)\rho_{RR,22}(\omega) \left[n_F(\omega - eV) - n_F(\omega) \right] \\
I_A &= \frac{8e}{h}\pi^2 t^4 \int_{-\infty}^{\infty} d\omega \, |G_{RR,12}(\omega)|^2 \times \\
&\qquad \rho_{LL,11}(\omega - eV)\rho_{LL,22}(\omega + eV) \left[n_F(\omega - eV) - n_F(\omega + eV) \right]. \quad (2.26)
\end{aligned}
$$

Written in this form, each contribution has a clear interpretation in terms of elementary processes that an electron may undergo in the interfase [13]. For this purpose, we must inspect the spectral densities involved in each case. Thus, I_1 corresponds to normal electron transfer between the electrodes, and reduces to Eq. (2.23) in the N-N case. I_2 corresponds also to a net transfer of a single electron with creation or annihilation of pairs as an intermediate state. On the other hand, I_3 arises from processes where an electron in the normal electrode is converted into a hole in the superconducting side, i.e. processes with "branch crossing" in the BTK language [63], or an Andreev transmission process [125]. Finally, I_A arises from Andreev reflection processes in which an electron (with an associated spectral weight $\rho_{LL,11}(\omega - eV)$) is transmited from the left to the right electrode with a hole reflecting backwards into the normal electrode (with an associated spectral weight $\rho_{LL,22}(\omega + eV)$) while a Cooper pair is created in the superconducting side with a probability proportional to $|G_{RR,12}(\omega)|^2$ [14].

The current I_{NS} can be expressed in a simple form as follows. We group together the first three terms, which corresponds to the transfer of one electronic charge. So, the current is given by

---

transmission lower than 1 and the presence of bound states.

[13]Eq. (2.26) is written in the electron space. So, we will only speak about the processes that an electron undergoes. A hole undergoes similar processes.

[14]We have only spoken about the processes that an incoming electron from the normal side undergoes. Of course, a quasiparticle coming from the superconducting side would undergo complementary processes, and finally each contribution to the current is given by the balance between the current in both senses.

$$I_{NS} \;=\; \frac{2e}{h} \int_0^\infty d\omega \; \{T_N(\omega)[n_F(\omega - eV) - n_F(\omega)] +$$

$$2\,R(\omega)[n_F(\omega - eV) - n_F(\omega + eV)]\}\,, \qquad (2.27)$$

where $T_N(\omega)$ is the transmission probability of an electron at the corresponding energy, given by the sum of the first three terms. On the other hand, $R(\omega)$ is the Andreev reflection probability. The previous expression has a very appealing form and tell us that the current is given by the sum of the probabilities of the different processes weighted by their corresponding charges.

With the same simplifying assumptions leading to Eq. (2.25), i.e. assuming a constant normal density of states around the Fermi level, the coefficients T_N and R adopt the following form in terms of the normal transmission coefficient α:

$$T_N(\omega) = \begin{cases} 0 & \text{if } |\omega| \leq \Delta \\ 2\alpha \dfrac{\alpha(1-\Delta^2/\omega^2)+(2-\alpha)\sqrt{1-\Delta^2/\omega^2}}{\left[\alpha+(2-\alpha)\sqrt{1-\Delta^2/\omega^2}\right]^2} & \text{if } |\omega| \geq \Delta \end{cases}$$

$$R(\omega) = \begin{cases} \dfrac{\alpha^2}{(2-\alpha)^2-4(1-\alpha)(\omega/\Delta)^2} & \text{if } |\omega| \leq \Delta \\ \dfrac{\alpha^2(\Delta/\omega)^2}{\left[\alpha+(2-\alpha)\sqrt{1-\Delta^2/\omega^2}\right]^2} & \text{if } |\omega| \geq \Delta. \end{cases} \qquad (2.28)$$

Therefore, we have a non-linear differential conductance that at zero temperature is given by $G_{NS}(V) = (2e^2/h)\,[T_N(V) + 2R(V)]$, which adopts the form

$$G_{NS}(V) \;=\; \frac{4e^2}{h} \frac{\alpha^2}{(2-\alpha)^2 - 4(1-\alpha)(\frac{eV}{\Delta})^2} \qquad \text{if } eV \leq \Delta$$

$$G_{NS}(V) \;=\; \frac{4e^2}{h} \frac{\alpha}{\alpha + (2-\alpha)\sqrt{1-(\frac{\Delta}{eV})^2}} \qquad \text{if } eV > \Delta. \qquad (2.29)$$

This expression is equivalent to the one obtained with the BTK model [63] with the correspondence $Z = [1 - (t/W)^2]/(2t/W)$ commented above. Thus, it is now clearer the equivalence between the scattering formalism and the Hamiltonian approach.

Fig. 2.4(a) shows the conductance G_{NS} (Eq. (2.29)) for different values of the normal transmission. Such conductance rises from $(4e^2/h)\alpha^2/(2-\alpha)^2$ at $V = 0$ to the value $4e^2/h$ at $eV = \Delta$, and finally tends to the normal value at $eV \gg \Delta$. It is worth noticing that the conductance value at $eV = \Delta$ is independent of the transmission. This is a result which cannot be obtained by finite perturbation theory and requires to sum up the processes up to infinite order. In particular, the traditional tunnel
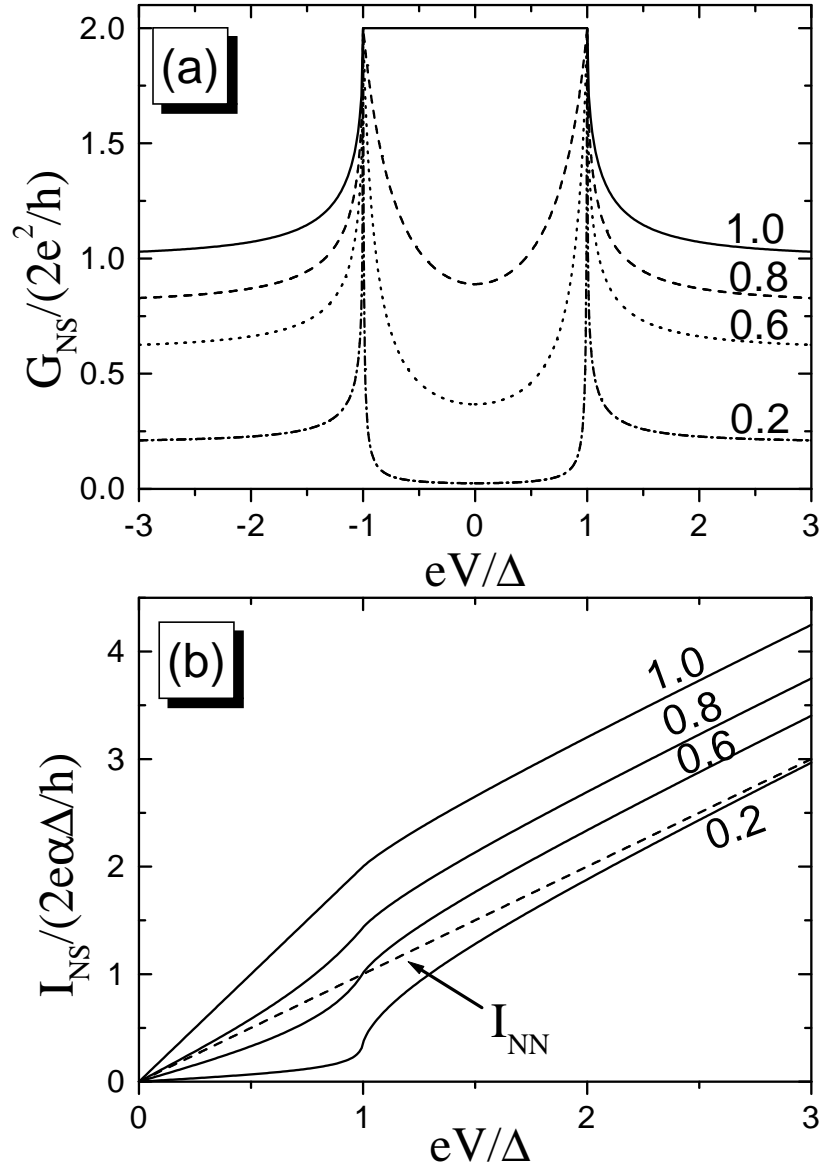
Figure 2.4: Zero-temperature differential conductance (a) and current (b) in a single-channel N-S contact as a function of voltage for different normal transmissions.

theory predicts a conductance G_{NS} proportional to the BCS density of states, i.e.

59

a conductance that strictly diverges at $eV = \Delta$. Usually the disappearance of this divergence in the experiments has been attributed to the fact that the BCS divergence is rounded off by an inelastic mechanism. However, as we have shown above, this divergence is not even present within the BCS framework. These type of nonperturbative results are specially important in the S-S case [126], as we shall show below.

It is also possible to obtain an analytical expression for the zero-temperature current. Such expression has the form

$$I_{NS}(V) = \frac{e\Delta}{h}\frac{\alpha^2}{(2-\alpha)\sqrt{1-\alpha}}\ln\left(\frac{2-\alpha+2(eV/\Delta)\sqrt{1-\alpha}}{2-\alpha-2(eV/\Delta)\sqrt{1-\alpha}}\right) \qquad \text{si } eV \leq \Delta$$

$$I_{NS}(V) = \frac{e\alpha\Delta}{h}\left\{\frac{\alpha}{(2-\alpha)\sqrt{1-\alpha}}\ln\left(\frac{2-\alpha+2\sqrt{1-\alpha}}{2-\alpha-2\sqrt{1-\alpha}}\right) + \right.$$

$$\frac{\alpha(x-1)+(2-\alpha)\sqrt{1-x^2}}{x(1-\alpha)} +$$

$$\left.\frac{\alpha(2-\alpha)}{2(1-\alpha)^{3/2}}\ln\left(\frac{\left[x\sqrt{1-\alpha}+(1+\sqrt{1-x^2})\right]\left[-1+\sqrt{1-\alpha}\right]}{\left[x\sqrt{1-\alpha}+(1-\sqrt{1-x^2})\right]\left[1+\sqrt{1-\alpha}\right]}\right)\right\} \quad \text{si } eV \geq \Delta, \text{ (2.30)}$$

where $x = \Delta/eV$. Fig. 2.4(b) shows this function for different transmissions. One of the remarkable features of the current is the presence of an *excess current* at voltages $eV \gg \Delta$ with respect to the normal case (I_{NN}). Eq. (2.30) permit us to analyze in detail this excess current defined as $I_{exc} = \lim_{V\to\infty}(I_{NS} - I_{NN})$, as a function of the contact transmission. We find the following expression at zero temperature:

$$I_{exc} = \frac{e\Delta}{h}\frac{\alpha^2}{1-\alpha}\left[1 - \frac{\alpha^2}{2(2-\alpha)\sqrt{1-\alpha}}\ln\left(\frac{1+\sqrt{1-\alpha}}{1-\sqrt{1-\alpha}}\right)\right]. \qquad (2.31)$$

Fig. 2.5 shows this function. As can be seen, the excess current is positive for any transmission, however it can be difficult to measure it for two reason. The first one is that for voltages greater than the gap, heating effects can distort the I-V curves [58]. The second one is that the excess current is defined as an asymphotic limit, and therefore in order to measure it one has to investigate sufficiently large voltages. On the other hand, for $\alpha = 1$ the well-known result for the ballistic contact $I_{exc} = (8/3)e\Delta/h$ is recovered [62, 127].
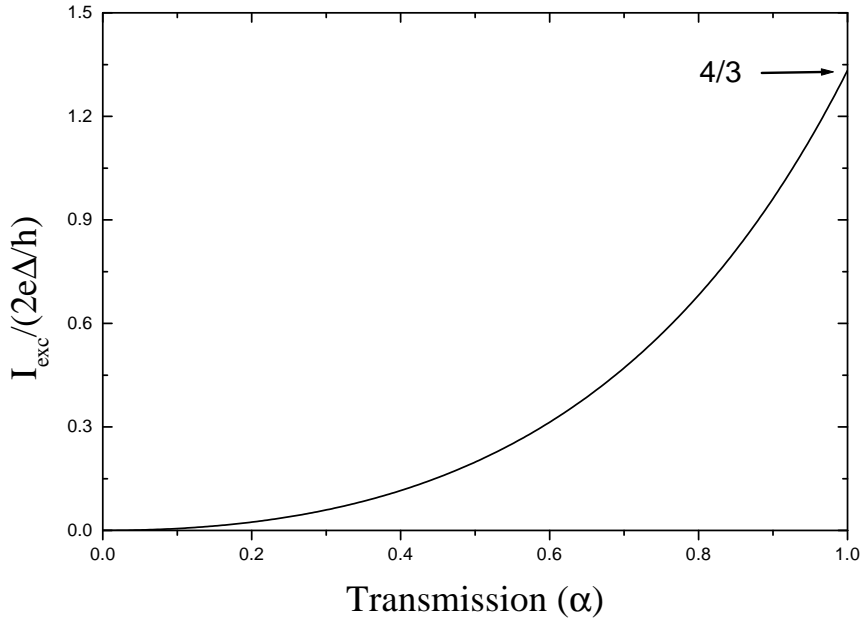
Figure 2.5: Zero-temperature excess current for a N-S junction as a function of transmission.

2.4 Single channel superconducting quantum point contact

In this section we shall analyze in detail the case of a single channel S-S contact with arbitrary constant bias voltage. So far we have shown that with our model we recover classical results of the scattering theory. Let us see now the novel results that our Hamiltonian approach provides.

In the S-S case the problem does not admit a stationary solution, and the Green functions depend on two temporal arguments, making the problem very complex. Let us see how to solve it.

For the case of a S-S contact with finite bias voltage it is convenient to start from the Hamiltonian (2.8) in which the applied bias is taken into account through a time-dependent phase factor in the hopping element, which in the Nambu representation has the form

$$\hat{t} = \begin{pmatrix} te^{i\phi(\tau)/2} & 0 \\ 0 & -te^{-i\phi(\tau)/2} \end{pmatrix},$$ (2.32)

where $\phi(\tau) = \phi_0 + 2eV\tau/\hbar$ is the time-dependent superconducting phase difference.

This explicit time dependence implies, as we shall show below, that all dynamic quantities can be expanded as a Fourier series in all possible harmonics of the fundamental frequency $\omega_0 = 2eV/\hbar$. In particular, the current can be expressed as

$$I(\tau) = \sum_{m=-\infty}^{\infty} I_m e^{im\phi(\tau)}. \qquad (2.33)$$

This is the general expression of the Josephson effect in a superconducting quantum point contact, which indicates that in a SQPC with a constant bias voltage there appear alternating components which oscillate not only with the Josephson frequency ω_0, as in the case of a tunnel junction, but also with all its harmonics. When the voltage tends to zero all the harmonics sum up to yield the supercurrent.

Let us see how the previous expression arises and how every Fourier component, I_m, can be expressed in terms of the Green functions. Due to the time dependence of $\hat{t}$, which is the self-energy in our model, it is easy to realize that the solutions of Eqs. (2.18-19) are Green functions, $\hat{G}$, which admit a Fourier expansion of the form [128]

$$\hat{G}(\tau, \tau') = \frac{1}{2\pi} \sum_n e^{in\phi(\tau')/2} \int d\omega \, e^{-i\omega(\tau-\tau')} \hat{G}(\omega, \omega + n\omega_0/2). \qquad (2.34)$$

This relation indicates that the two frequencies of a Green function are not independent. Introducing this expression in Eq. (2.15), we can see that the time-dependent current admit an expansion as in Eq. (2.33) [15]. On the other hand, it is important to stress that the current components I_m are now independent of the superconducting phase.

Hereafter we shall use the notation $\hat{G}_{nm}(\omega) \equiv \hat{G}(\omega + n\omega_0/2, \omega + m\omega_0/2)$ for the different Fourier components. From this definition it is evident that different Fourier components are related by $\hat{G}_{nm}(\omega) = \hat{G}_{n-m,0}(\omega + m\omega_0/2)$.

At this point the problem is to determine the different Fourier components of the current in terms of the different quantities of the model. Within a perturbative scheme one can follow two different paths. Either one can "dress" the propagators, as we did in the N-N and N-S cases, or one can "dress" the perturbation, as in the case of the RPA approximation for an electron gas. We shall follow the latter approach and dress the perturbative potential, which in our case is simply $\hat{t}$. The dressed or renormalized hoppings, $\hat{T}$, are defined in terms of the Green functions in the following way

---

[15]In principle, it seems that in Eq. (2.33) also half-integer harmonics of the frequency ω_0 should appear. However, one can show that these components vanish.

$$
\begin{aligned}
\hat{T}^{a,r}_{LR}(\tau,\tau') &= \hat{t}(\tau)\delta(\tau-\tau') + \hat{t}(\tau)\,\hat{G}^{a,r}_{RL}(\tau,\tau')\,\hat{t}(\tau') \\
\hat{T}^{a,r}_{RL}(\tau,\tau') &= \hat{t}(\tau)^{\dagger}\delta(\tau-\tau') + \hat{t}^{\dagger}(\tau)\,\hat{G}^{a,r}_{LR}(\tau,\tau')\,\hat{t}^{\dagger}(\tau').
\end{aligned}
\tag{2.35}
$$

These renormalized hoppings, $\hat{T}$, have a simple physical interpretation. Basically they are probability amplitudes for the different processes, depending on their Nambu components. Moreover, these quantities verify their own Dyson equations, thus for instance

$$
\hat{T}^{a,r}_{LR}(\tau,\tau') = \hat{t}(\tau)\delta(\tau-\tau') + \int d\tau_1 d\tau_2\,\hat{t}(\tau)\hat{g}^{a,r}_{RR}(\tau-\tau_1)\hat{t}^{\dagger}(\tau_1)\hat{g}^{a,r}_{LL}(\tau_1-\tau_2)\hat{T}^{a,r}_{LR}(\tau_2,\tau').
\tag{2.36}
$$

After some algebra, see Appendix C for details, we get the following expression for the current harmonics I_m in terms of the renormalized hoppings $\hat{T}^{a,r}_{nm}(\omega)$

$$
\begin{aligned}
I_m &= \frac{2e}{h}\int d\omega \sum_n \Big[\hat{T}^r_{LR,0n}\hat{g}^{+-}_{RR,nn}\hat{T}^a_{RL,nm}\hat{g}^a_{LL,mm} - \hat{g}^r_{LL,00}\hat{T}^r_{LR,0n}\hat{g}^{+-}_{RR,nn}\hat{T}^a_{RL,nm} \\
&\quad + \hat{g}^r_{RR,00}\hat{T}^r_{RL,0n}\hat{g}^{+-}_{LL,nn}\hat{T}^a_{LR,nm} - \hat{T}^r_{RL,0n}\hat{g}^{+-}_{LL,nn}\hat{T}^a_{LR,nm}\hat{g}^a_{RR,mm} \Big]_{11}.
\end{aligned}
\tag{2.37}
$$

One can show that there exists the general relation $\hat{T}^{a,r}_{RL,nm}(\omega) = \hat{T}^{r,a\dagger}_{LR,mn}(\omega)$. Thus, we shall express the current only in terms of the hoppings $\hat{T}^{a,r}_{LR,nm}$, which hereafter we denote as $\hat{T}^{a,r}_{nm}$. In terms of these latter hoppings the current for a symmetric junction can be written as

$$
\begin{aligned}
I_m &= \frac{2e}{h}\int d\omega \sum_n \Big[\hat{T}^r_{0n}\hat{g}^{+-}_{nn}\hat{T}^{r\dagger}_{mn}\hat{g}^a_{mm} - \hat{g}^r_{00}\hat{T}^r_{0n}\hat{g}^{+-}_{nn}\hat{T}^{r\dagger}_{mn} \\
&\quad + \hat{g}^r_{00}\hat{T}^{a\dagger}_{n0}\hat{g}^{+-}_{nn}\hat{T}^a_{nm} - \hat{T}^{a\dagger}_{n0}\hat{g}^{+-}_{nn}\hat{T}^a_{nm}\hat{g}^a_{mm} \Big]_{11},
\end{aligned}
\tag{2.38}
$$

where we have suppressed the site indexes L and R in the Green functions of the uncoupled electrodes.

The problem is now reduced to the evaluation of the components $\hat{T}_{nm}$. From Eq. (2.36) it can be seen that these (advanced and retarded) components satisfy a set of linear equations of the form

$$
\hat{T}_{nm} = \hat{t}_{nm} + \hat{\epsilon}_n\hat{T}_{nm} + \hat{V}_{n,n-2}\hat{T}_{n-2,m} + \hat{V}_{n,n+2}\hat{T}_{n+2,m}.
\tag{2.39}
$$

These equations are mathematically equivalent to those describing the motion of electrons in a tight-binding linear chain with "site energies", $\hat{\epsilon}_n$, and "nearest-neighbor couplings", $\hat{V}_{n,n-2}$ and $\hat{V}_{n,n+2}$. The detailed expressions of $\hat{\epsilon}_n$ and $\hat{V}_{n,m}$ in

terms of the unperturbed Green functions are given in Appendix C. This analogy allows us to obtain the Fourier coefficients $\hat{T}_{nm}$ using standard recursion techniques. In particular, one can show that the following recursive relation holds

$$\begin{cases} \hat{T}_{n+2,m}(\omega) = \hat{z}^+ \left[\omega + (n-1)\omega_0\right] \hat{T}_{nm}(\omega) & , n \geq 1 \\ \hat{T}_{n-2,m}(\omega) = \hat{z}^- \left[\omega + (n+1)\omega_0\right] \hat{T}_{nm}(\omega) & , n \leq -1, \end{cases} \tag{2.40}$$

where the transfer matrix $\hat{z}^\pm$ satisfies the equation

$$\hat{z}^\pm(\omega) = \left[\hat{I} - \hat{\epsilon}_{\pm 3} - \hat{V}_{\pm 3, \pm 5}\hat{z}^\pm(\omega \pm \omega_0)\right]^{-1}. \tag{2.41}$$

Clearly, as the transfer matrix $\hat{z}^\pm$ connects consecutive harmonics of $\hat{T}$, it can be viewed as a generating function which introduces the effect of a unitary Andreev reflection process. The problem has been reduced to the calculation of only two matrix coefficients like, for instance, $\hat{T}_{1,0}$ and $\hat{T}_{-1,0}$ as a starting point for generating the rest of the components.

In summary, the basic mathematical difficulty lies in the evaluation of the transfer matrix functions $\hat{z}^\pm$ from Eq. (2.41). In principle, this equation gives rise to an infinite system that cannot be solved analytically for arbitrary voltages. We shall show analytical results for the cases of $eV/\Delta \to 0$ and $eV/\Delta \to \infty$. For intermediate voltages, an accurate numerical solution of Eq. (2.41) can be obtained.

The rest of this section is organized as follows. Next we shall analyze in detail the dc current component. Then, we shall study the ac current components, and finally we shall investigate the interesting small bias voltage limit.

2.4.1 Dc current

This section is devoted to the analysis of the dc current in a single-channel SQPC. The overall features of the I-V characteristics have been calculated by different authors: Octavio *et al.* [64], Zaitsev [127] and Arnold [71]. Recently, more quantitative and detailed analysis are being reported. In particular, Bratus *et al.* [129] have analyzed the tunnel limit and Averin and Bardas [130] have analyzed the case of arbitrary transmission using the scattering formalism. We shall comment below the comparison of our results with the different theories.

Fig. 2.6 shows the numerical result [16] for the zero-temperature dc current in a symmetric junction, together with the corresponding differential conductance $G = dI/dV$. As can be observed in Fig. 2-6(a), the current for $eV < 2\Delta$ is a highly non-linear function of the voltage. In particular, there appears some structure at voltages $eV \sim 2\Delta/n$ (n integer), known as subharmonic gap structure (SGS), which is more pronounced in the tunnel limit ($\alpha \ll 1$) where becomes a series of steps

---

[16]The results of Fig. 2.6 were obtained for $\eta = 0$.
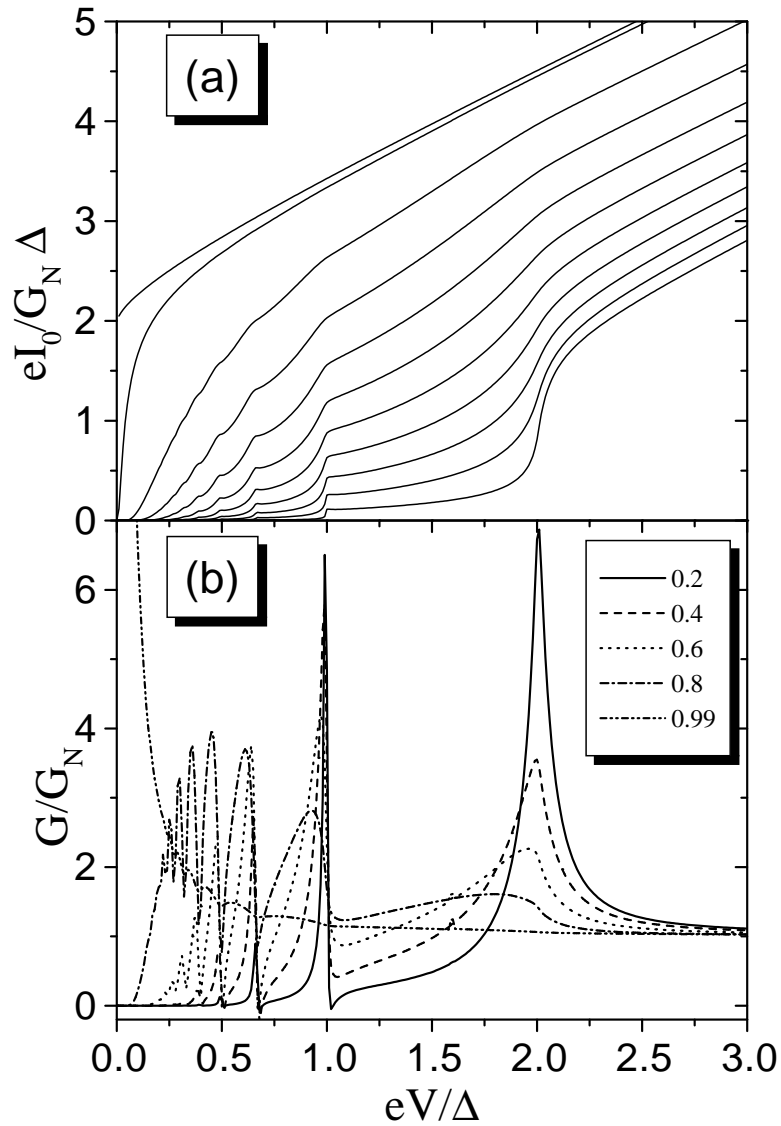
Figure 2.6: Zero-temperature dc current (a) and differential conductance (b) as a function of voltage for different transmissions in a single channel S-S contact. In the case of the current (a) the transmission from bottom to top are $\alpha = 0.1, 0.2, 0.3, 0.4, 0.5, 0.6, 0.7, 0.8, 0.9, 0.99, 1.0$. G_N is the normal conductance of the single channel given by $G_N = (2e^2/h)\alpha$.

at such voltages. In the contrary, as the transmission increases the subharmonic structure is smoothed and is completely washed out for $\alpha \to 0$. The SGS is already clear in the I-V curves, but we can see it more clearly in the conductance (see Fig. 2.6(b)). As can be observed, there are conductance maxima at $eV \sim 2\Delta/n$. It is also worth noticing the presence of $G < 0$ in some subharmonic gap current steps. Other interesting features are the huge conductance near zero voltage for transmissions close to 1 and a finite value of the dc current at $V = 0$ for $\alpha = 1$. On the other hand, at voltages much greater than the gap the contact exhibits an excess current with respect to the normal case. Next, we shall analyze the origin of all these features.

In order to understand the nature of the subharmonic gap structure we first analyze the tunnel limit ($\alpha \ll 1$). Before showing some analytical results in this limit, let us explain qualitatively the origin of such a structure. As it has been pointed out by several authors [62, 64, 71], this structure is due to the occurrence of multiple processes, known as Multiple Andreev Reflections (MAR), in the junction. We shall explain the nature of these processes and the origin of the current steps at $eV \sim 2\Delta/n$ using the schematical representation of Fig. 2.7. Let us assume zero temperature. As it is indicated in the upper panel of this figure, as the voltage reaches the gap ($eV = 2\Delta$) quasiparticle tunneling can occur, giving rise to the current step at this voltage. Of course, this process gives a contribution to the current proportional to the transmission α and dominates the current in the tunnel limit for $eV > 2\Delta$.

When $eV = \Delta$ a simple Andreev reflection can take place (see second panel in Fig. 2.7). This Andreev reflection is quite similar to the one that takes place in a N-S contact and gives rise to the current step at $eV = \Delta$. In this process an electron is reflected as a hole (its corresponding time-reverse state), transferring a Cooper pair to the other electrode. In this process both the electron and the hole gain an energy equal to eV every time they cross the interfase. Thus, this process ends when the hole finds an empty state in the initial electrode, what can only happen when $eV \geq \Delta$, which gives rise to the current step at $eV = \Delta$. In this simple Andreev reflection a Cooper pair is transferred, it gives a contribution proportional to α^2 and in the tunnel limit it is the main contribution for voltages $\Delta < eV < 2\Delta$.

When the voltage reaches $eV = 2\Delta/3$ a triple process known as a multiple Andreev reflection can take place. As can be seen in the third panel of Fig. 2.7, this process takes place as follows: when an electron approaches the interfase can be Andreev reflected, the corresponding reflected hole has not enough energy to reach an empty state in the initial electrode. However, this hole can also be Andreev reflected transmitting a Cooper pair of holes to the initial electrode and giving rise to a new electron that now has enough energy to reach an empty state in the second electrode. The contribution of this process is proportional to α^3, needs a voltage $eV > 2\Delta/3$ and gives rise to the transfer of a Cooper pair plus a quasiparticle. This

Single quasiparticle
process

2Δ e   eV

I

2Δ V

Andreev Reflection

2Δ h

e   eV

I

Δ V

Multiple Andreev
Reflection
(MAR) 2Δ

eV

I

$2\Delta/3$ V

(MAR)

2Δ

eV

I

$2\Delta/n$

V
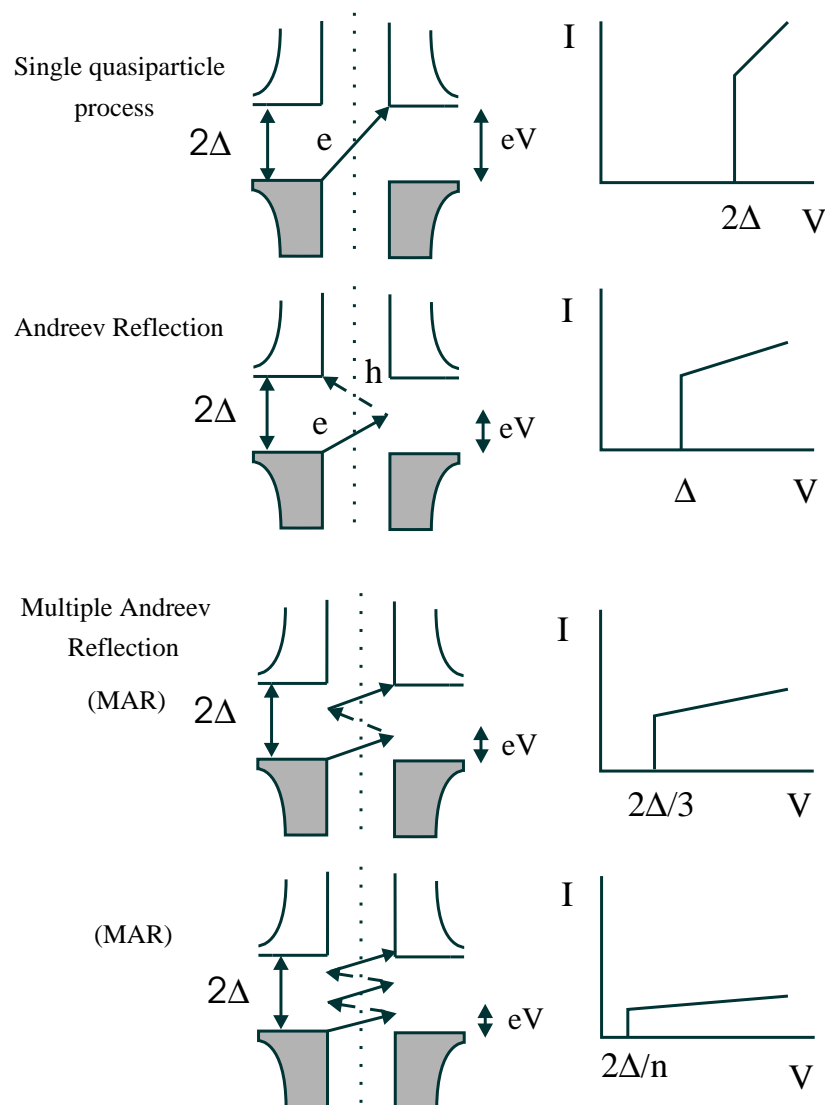
Figure 2.7: Schematical representation of the multiple Andreev reflections in the
tunnel limit. In the left hand side we show the energy trajectories of the different
processes and in the right hand side their contributions to the current.

process gives the main contribution for voltages $2\Delta/3 < eV < \Delta$ in the tunnel limit.

It is now easy to understand how the complete series of current steps arises. In general, a n-order multiple Andreev reflection, like the one depicted in the lower panel of Fig. 2.7, consists of a cascade of reflections in which n quasiparticles cross the barrier until one finds an available state in one of the electrodes. In order to have this n-order process a minimum voltage $eV = 2\Delta/n$ is needed. This process gives a contribution proportional to α^n and in the tunnel limit is the main contribution for $2\Delta/n < eV < 2\Delta/(n+1)$. Finally, notice that there is a difference between the even-order and odd-order Andreev reflections. While the even-order reflections end with the transmission of a hole, odd-order ones end with the transmission of an electron. The electron-hole symmetry that we have assumed implies that there is no difference between both series of current steps. So in summary, the subharmonic gap structure is due to the opening of multiple Andreev reflections at voltages $eV_n = 2\Delta/n$.

This picture about the origin of the subharmonic structure in the tunnel limit is supported by analytical results that we now describe. In the tunnel limit one can describe the transport by means of a sequential picture in which one identifies the probability R_n of a n-order multiple Andreev reflection [17]:

$$R_n(\omega, V) = \frac{\pi^2 \alpha^{\mathbf{n}}}{4^{n-1}} \left[\prod_{i=1}^{n-1} P(\omega - ieV) \right] \rho(\omega - neV)\rho(\omega) \quad ; \; \omega \in [\Delta, neV - \Delta], \quad (2.42)$$

where $\rho(w) = |\omega|/\sqrt{\omega^2 - \Delta^2}$ is the dimensionless BCS density of states and $P(\omega) \sim \Delta^2/(\Delta^2 - \omega^2)$ is the probability of creating a Cooper pair at energy ω. Before giving the exact expression of $P(\omega)$, notice that these probabilities have a simple interpretation in the framework of a sequential picture. Simply, R_n is proportional to the probability of crossing n times the barrier (α^n), proportional to the probability of creating $n-1$ Cooper pairs and proportional to the initial and final density of states. Notice that in order to have a non-zero probability R_n the voltage must be $eV \geq 2\Delta/n$.

In the previous expression, the probability of creating a Cooper pair has the form: $P(\omega) = |f(\omega)/D(\omega)|^2$, where $f(\omega) = \Delta/\sqrt{\Delta^2 - \omega^2}$ is the dimensionless anomalous BCS Green function for the uncoupled electrodes. On the other hand, the denominator is equal to $D(\omega) = 1 - (\alpha/4)g(\omega)(g_1(\omega) + g_{-1}(\omega)) - (\alpha^2/16)g_1(\omega)g_{-1}(\omega)$, where $g_i(\omega) \equiv g(\omega + ieV)$ is the dimensionless Green function given by $g(\omega) = -\omega/\sqrt{\Delta^2 - \omega^2}$. Moreover, the term $n = 1$ in Eq. (2.42) corresponds to the quasiparticle term and should be understood as

$$R_1(\omega, V) = \frac{\pi^2 \alpha}{|D(\omega)|^2} \rho(\omega - eV)\rho(\omega) \quad ; \; \omega \in [\Delta, eV - \Delta]. \quad (2.43)$$

---

[17]In this expression we have used explicitly the electron-hole symmetry.

It is important to remark that, although R_n is proportional to the BCS density of states, it does not diverge at all (it is truly a probability bounded between 0 and 1). Indeed, Eq. (2.42) is a nonperturbative result in which the divergencies appearing in the perturbative expansion have been renormalized in a natural way.

In terms of the R_n the current in the tunnel limit can be written in a very simple form

$$I_0(V) = \frac{2e}{h} \int d\omega \sum_{n=1}^{\infty} n R_n(\omega, V).$$ (2.44)

This expression indicates that the current can be written as a sum of the Andreev reflection probabilities weighted by their corresponding charges [18]. Fig. 2.8 shows the comparison between the tunnel result of Eq. (2.44) and the exact numerical result.

The expression for the tunnel current allows us to understand better several things. For instance, as one can see in Fig. 2.6, the subharmonic structure consists of a series of abrupt steps only in the tunnel regime and it is progressively washed out as the transmission increases. Eq. (2.42) for the R_n indicates that a multiple Andreev reflection probability is proportional to initial and final quasiparticle densities of states. Moreover, in the tunnel limit these densities are truly BCS densities of states and thus diverge at the gap edges. This implies that when the opening of a n-order Andreev reflection takes place at a voltage $eV = 2\Delta/n$, its probability reaches a maximum because at this voltage the process starts and ends at the gap edges, giving a finite contribution since its opening. For increasing transmissions the SGS disappears because the lead density of states is no longer a BCS one, due to to the finite coupling between the superconductors. In this case, the density of states has not singularities and the contribution of the Andreev reflections is small at their openings.

On the other hand, with the tunnel expression one can understand the appearance in this limit of negative differential conductance near some steps (see Fig. 2.6(b) and Fig. 2.8). When $eV = 2\Delta/n$ a n-order Andreev reflection start contributing and its probability reaches a maximum precisely at this voltage because the process begins and ends at the gap edges. As the voltage is increased it is no longer possible that the process takes place between both gap edges. Thus, the current diminishes slightly giving rise to a negative differential conductance. As we keep on increasing the voltage the current increases again because we are increasing the energy window in which the reflection can take place. For larger transmissions a negative conductance is not observed because the density of states is rounded off due to a finite coupling between the superconducting electrodes.

---

[18]In the next chapter we shall analyze the charge of Andreev reflections by means of the analysis of the current fluctuations.
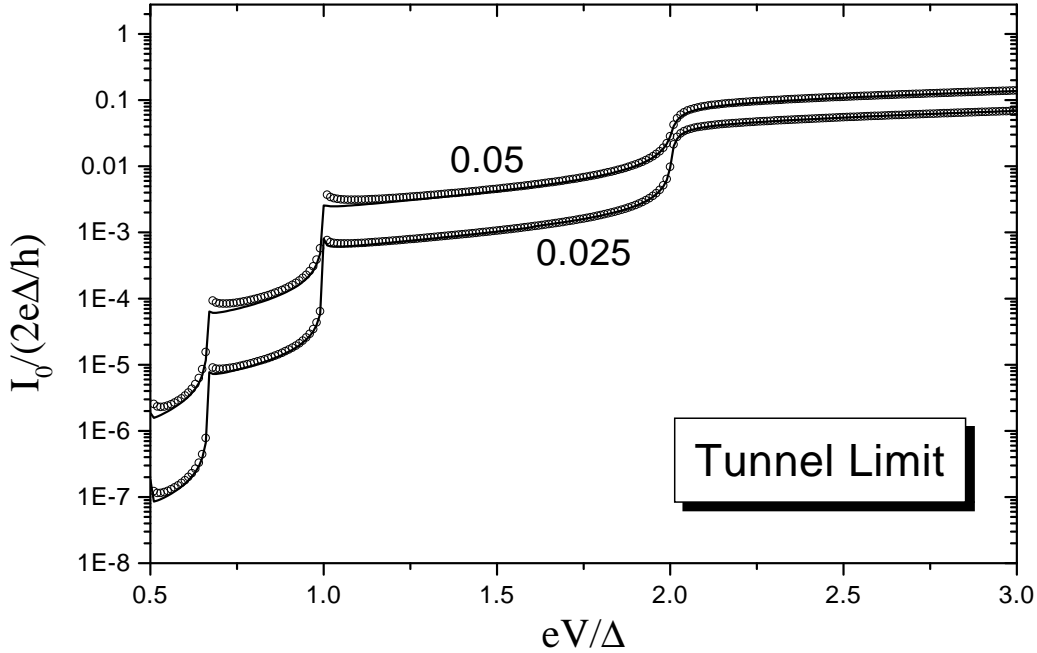
Figure 2.8: Comparison between the tunnel expression (2.44) (open circles) and the exact result (solid lines) for two transmissions. Notice the logarithmic scale.

Another important information that we can obtain from the tunnel current expression is the value of the current steps, $I_0^{(n)}$, at voltages $eV_n = 2\Delta/n$ in the small transparency limit. For this purpose we have to evaluate the current that a n-order MAR provides just at a voltage $eV = 2\Delta/n$, i.e.

$$\delta I_0^{(n)} = \lim_{eV \to 2\Delta^+/n} \frac{2e}{h} \int_{-\infty}^{\infty} d\omega \, n R_n(\omega, V). \qquad (2.45)$$

An appropriate way of estimating these current steps as the transmission tends to zero is to approximate the denominators in Eq. (2.42) as 1, i.e. $D(\omega) \sim 1$. Thus, the result for the steps coincides with the one obtained with a perturbative expansion, like in the multiple-particle tunneling theory [34, 126]. The result of the integrals yields

$$\delta I_0^{(n)} = \frac{e\Delta\alpha^n}{\hbar} \left(\frac{2n}{4^{2n-1}}\right) \left(\frac{n^n}{n!}\right)^2.$$ (2.46)

As we see, the magnitude of the n-step is proportional to α^n because it is due
to the opening of a n-order MAR. This result coincides with the one obtained in
Ref. [129]. In particular, Eq. (2.46) for $n = 1$ yields the well-known quasiparticle
step $\delta I_0^{(1)} = \pi e\Delta\alpha/h = \pi\Delta/2eR_N$, for $eV = 2\Delta$. Moreover, Eq. (2.46) indicates
that the ratio between consecutive current steps is proportional to the transmission,
something which has been confirmed experimentally by Post et $al.$ [85].

When the transmission increases the sequential picture, represented by Eq. (2.44),
breaks down due to the interference between the different processes forming a multi-
ple Andreev reflection. As we commented above, the subharmonic structure progres-
sively disappears due to the disappearance of the divergencies of the density of states.
The analysis of the current for intermediate transmissions is thus rather complicated
and analytical results cannot be obtained. However, in the perfect transmission case
the absence of backscattering (no normal reflection) in the contact simplifies the
analysis. In this case ($\alpha = 1$) it can be shown, see Appendix C for details, that the
dc current adopts the following form for arbitrary temperature

$$I_0 = \frac{2e}{h} \int_{-\infty}^{\infty} d\omega \sum_{m=0}^{\infty} \left[\prod_{j=1}^{m} |a_j|^2\right] \left(1 - |a_0|^2|a_{m+1}|^2\right) \{n_F(\omega) - n_F(\omega + (m+1)eV)\},$$

(2.47)

where $a_j \equiv a(\omega + jeV)$ and $a(\omega)$ is the amplitude of an Andreev reflection in a N-S
interfase with perfect transmission, and is given by

$$a(\omega) = \frac{1}{\Delta} \left\{ \begin{array}{ll} \omega + i\sqrt{\Delta^2 - \omega^2} & |\omega| \leq \Delta \\ \omega - sign(\omega)\sqrt{\omega^2 - \Delta^2} & |\omega| \geq \Delta. \end{array} \right.$$ (2.48)

This formula allows us to understand why the SGS disappears in the perfect trans-
parency case. When a new Andreev process is opened (m-th term in Eq. (2.47)), its
probability increases slowly starting from zero. Thus, the opening of a new Andreev
reflection does not give rise to a current step like in the tunnel regime.

The previous expression also permits to study another interesting feature of the
dc current, namely, the finite current value at zero voltage for perfect transmission
(see Fig. 2.6). From Eq. (2.47) it is deduced that the zero-temperature dc current
saturates at a value $I_0 = (4e/h)\Delta$ when $V \to 0$. This result has been obtained by
different authors [131, 130, 132]. We stress that this finite value of the current at
zero voltage comes from the contributions of Andreev reflections whose orders tend
to infinity as $2\Delta/eV$. These contributions are finite due to the perfect transmission.
It is evident that in this extreme case any inelastic interaction giving rise to a finite

relaxation energy η will play a relevant role in the determination of the current.
When the voltage is smaller than this energy η, this latter becomes the natural cut-
off of the Andreev reflections. To be concrete, when a reflection needs a time greater
than $\hbar/\eta$ to take place, the inelastic interaction will damp the Andreev reflection.
This implies that in a real contact, where η is non-zero, the dc current vanishes at
zero voltage. The detailed analysis of the complex $V \rightarrow 0$ limit will be carried out
in section 2.4.3.
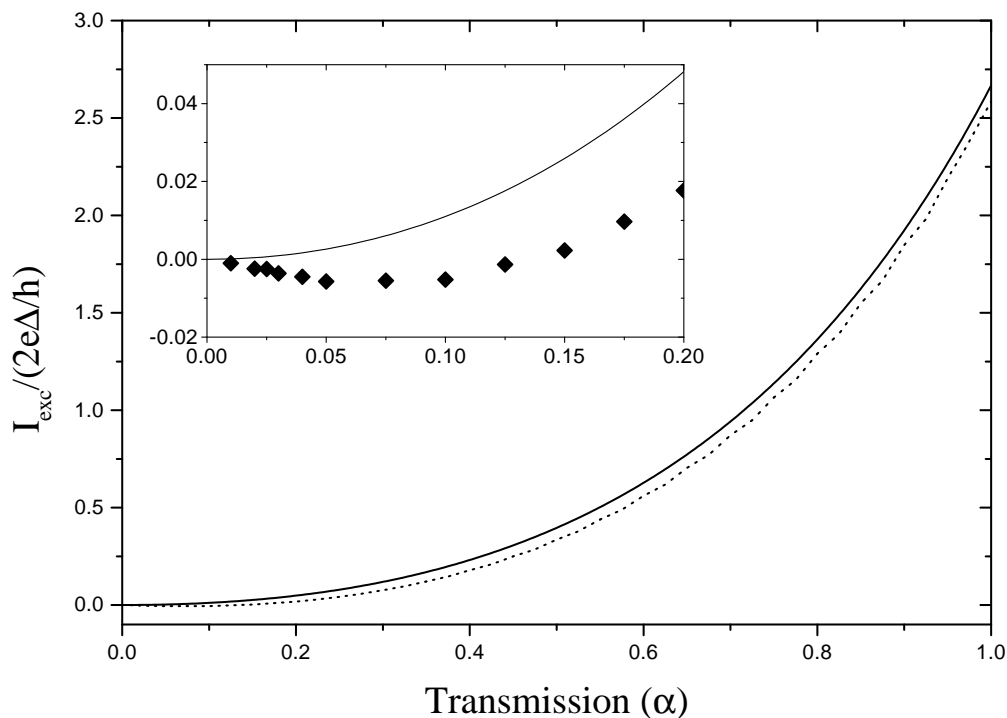
Figure 2.9: Zero-temperature excess current in a single channel S-S contact as a
function of transmission. The solid line represents the exact result defined as an
assymptotic limit. The dotted line corresponds to the excess current obtained nu-
merically at $eV = 6\Delta$. The inset shows the small transparency region, where the
numerical results (diamonds) shows a defect current as the transmission goes to zero.

Another relevant feature of the dc current is, as in the N-S case, the large voltage
excess current, which can be analytically evaluated within our model for any trans-
mission value. The main simplification in this limit comes from the fact that only the
lowest order Andreev reflection process gives a significant contribution to the excess

current [64]. This implies that one can truncate the system of equations (2.39) for
harmonic indexes $n > 1$, the resulting simplified system can then be solved explicitly
for $\hat{T}_{1,0}(\omega)$ and $\hat{T}_{-1,0}(\omega)$ (see Appendix C for details). As shown in this Appendix,
the simple result $I_{exc}^{SS} = 2I_{exc}^{NS}$ is obtained for any value of the transmission. This
result reduces in the ballistic limit ($\alpha = 1$) to the result obtained in Refs. [127, 62].
Moreover, some authors have reported the existence of a negative excess current for
low transmissions [68], which seems to be in contradiction with the above result.
However, one should notice that the excess current as defined above is an asymp-
totic quantity (only valid in the $eV/\Delta \to \infty$ limit). When corrections of order Δ/eV
are taken into account one actually can have a defect instead of an excess current
for sufficiently low transmission. Thus for instance, Fig. 2.9 shows the comparison
between the excess current given by the exact formula and the numerical result for
$eV = 6\Delta$. As can be observed in the inset, there is a defect for $\alpha \ll 1$.

So far we have analyzed the subharmonic structure at zero temperature. Next,
we shall briefly comment how this structure is modified by a finite temperature. Fig.
2.10 shows the evolution of the SGS with temperature in reduced units for different
transmissions. In panel (a) we see that the temperature progressively smoothes the
SGS and increases the current for low transmissions. This is a simple consequence
of the thermal excitation of quasiparticles. On the other hand, for intermediate
transmissions the structure inside the gap is only slightly modified by the effect
of temperature (see panel (b) and (c)). For perfect transmission the temperature
reduces slightly the current, specially at small voltages (see panel (d)). This is due
to the fact that the multiple Andreev reflected quasiparticles reach states that would
be empty at zero temperature, but at finite temperature there is certain probability
of being occupied, giving rise to a reduction of the current. Finally, in Ref. [132]
a detailed analysis of the finite temperature SGS for perfect transmission of an
asymmetric S-S contact can be found.

Due to the experimental interest of the dc current, we shall devoted the rest of
this subsection to a comparison of our results with other theories. As commented
above, there are several works analyzing the I-V curves for arbitrary transmission.
Probably, the most important model is the OTBK one [64] commented in the pre-
vious chapter. Fig. 2.11 shows the dc current obtained with the OTBK model [68]
and our results for different transmissions. As can be observed, there are clear dif-
ferences in the current and we do not need to show the differential conductance. In
general, the SGS obtained with our model is more pronounced. Both models only
coincide for the perfect transmission case. In our opinion, the discrepancies are due
to the fact that in the OTBK model a S-N-S is treated as two N-S contacts in series,
in the sense that the probability of a multiple process is given by the product of
the processes that take place in the interfases, neglecting the possibility of that a
quasiparticle interferes with itself. This is only valid in the absence of normal reflec-
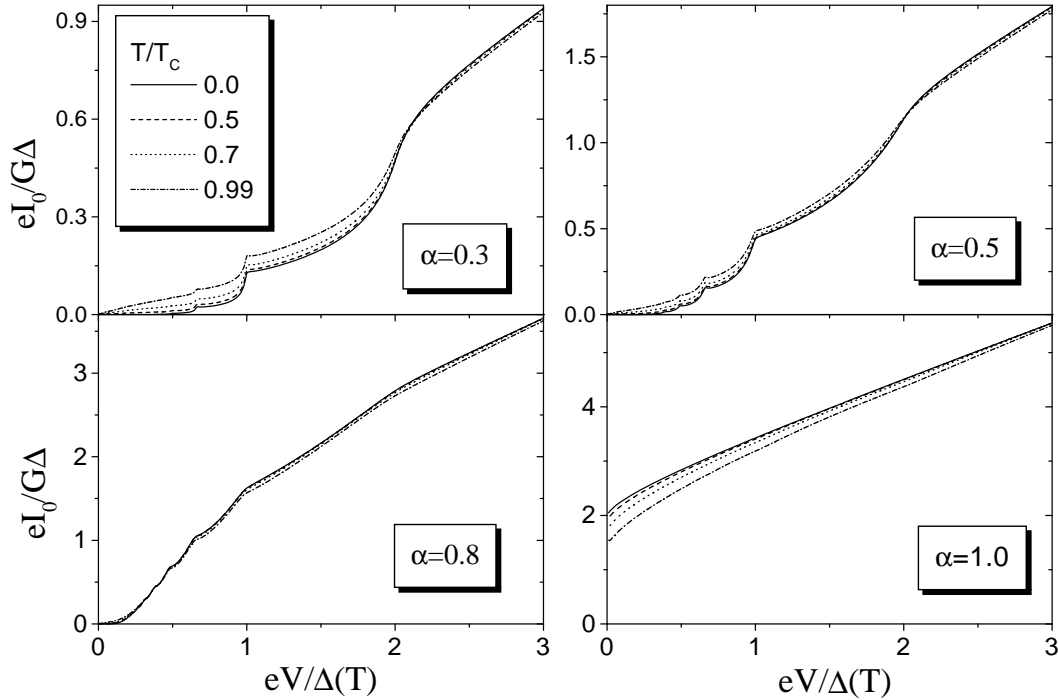
Figure 2.10: Finite temperature I-V characteristics for four transmissions. The temperature is in unit of the critical temperature and the voltage is normalized to the temperature dependent gap.

tion of the contact, explaining that both models only coincide quantitatively in the case of perfect transparency. Thus, the main conclusion of this comparison is that for describing properly the electronic transport in a SQPC a *coherence and purely quantum-mechanical description* is needed.

Another remarkable theory is the one developed by Arnold [71] and commented in Chapter 1. A comparison between Figs. 1.8 and 2.6 shows the qualitative agreement between both theories.

Finally, we discuss the results obtained by Averin and Bardas [130] using the scattering formalism. These authors carried out independently a description of the ac Josephson effect in a single channel contact. Fig. 2.12 shows the dc current for both theories for different transmissions. As can be observed, both models give quantitatively the same description for the transport in a SQPC, as one would expect taking into account that both models share the same physical ingredients. Moreover,
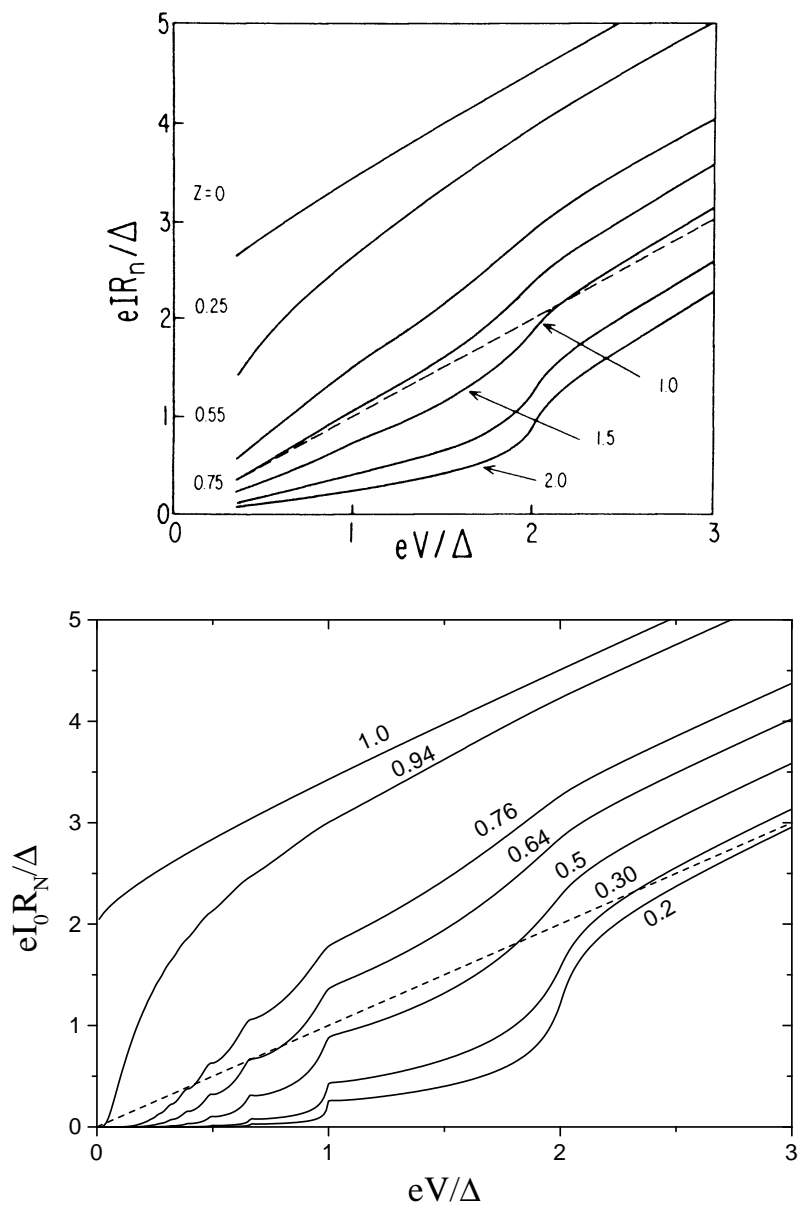
Figure 2.11: Zero-temperature I-V characteristics in the OTBK model (upper panel)
[68] and in our theory (lower panel) for different transmissions. In both cases the
dashed line indicates the normal case.
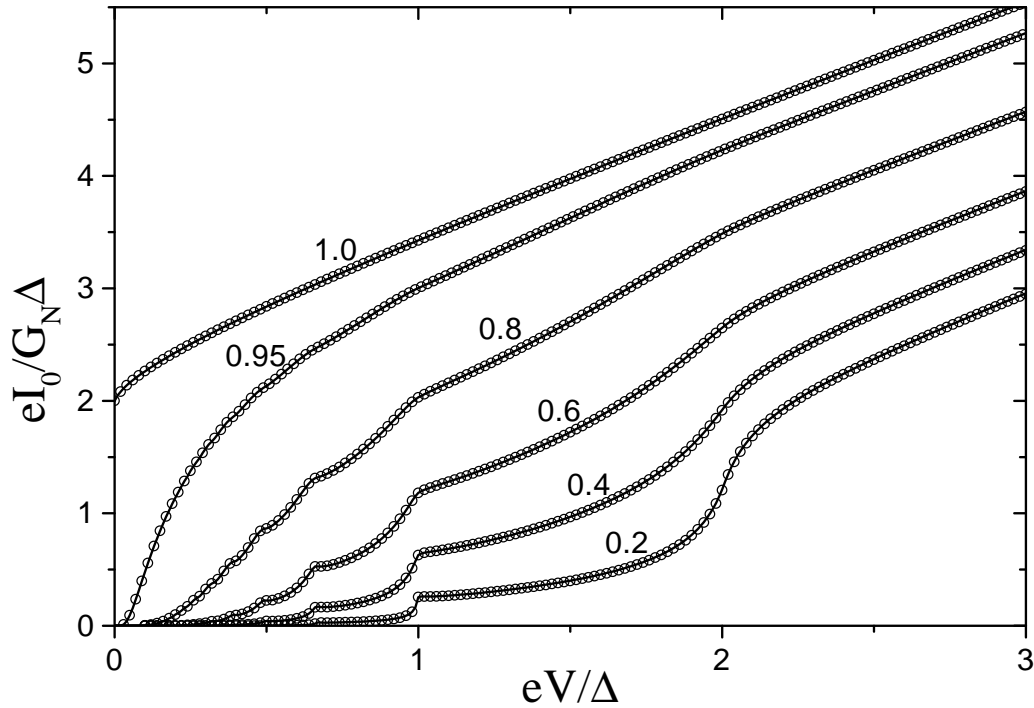
Figure 2.12: Zero-temperature I-V curves for our model (solid lines) and the model
of Averin and Bardas [130] (open circles) for different transmissions.

the I-V curves has been lately obtained by Bratus *et al.* [133] using also the scattering
formalism.

2.4.2 Ac current components

This section is devoted to the analysis of the ac current components. The algorithm
described in section 2.4 allows an efficient evaluation of the higher order ac compo-
nents of the current. For the following analysis we decompose the ac current, Eq.
(2.33), into its dissipative I_D and non-dissipative I_S contributions given respectively
by

$$I_D = I_0 + \sum_{m=1}^{\infty} I_m^D \cos m\phi(\tau) \tag{2.49}$$

and

$$I_S = \sum_{m=1}^{\infty} I_m^S \sin m\phi(\tau), \qquad (2.50)$$

where $I_m^D = 2\mathrm{Re}(I_m)$ and $I_m^S = -2\mathrm{Im}(I_m)$.

Due to the inclusion in the current of multiple processes there appear all the harmonics of the Josephson frequency. It is easy to show that the lowest order contribution of the m-th current component goes like α^m. The results obtained for the three components I_m^D and I_m^S are shown in Figs. 2.13 and 2.14. As can be seen, these components also exhibit a pronounced subgap structure. Moreover, these components become exponentially small for bias voltages larger than Δ/n. On the contrary, when $eV < \Delta/n$ the decay of the ac components with increasing n becomes slower. The analysis of the higher order components reveals a decay for $eV < \Delta/n$ close to a inverse power law. As a consequence of this slow decay, one is forced to take an increasing number of ac components into account in order to adequately describe the behavior at small bias. This will be the subject of the next subsection.

Let us say a few words about the observability of these alternating components. Due to their fast oscillation, it is difficult to observe them in a direct measurement of the I-V characteristics. However, they manifest in a direct way in the case of $eV \to 0$, both in the supercurrent (sinusoidal components) or in the linear conductance (cosinusoidal components), as we shall show below. Traditionally, the ac current components have been investigated by means of the application of a radiation to the contact. As it is well-known, the dc current is modified by the application of a laser radiation, appearing the well-known Shapiro steps [27, 21]. In a superconducting tunnel junction, when the condition $\omega_0 = m\omega_r$ is satisfied, where $\omega_0 = 2eV/\hbar$ is the Josephson frequency, ω_r is the radiation frequency and m is a integer number, then a new step in the dc current appears. The Shapiro step heights depend on the ac current components [21], which in the case of a tunnel junction reduce to the first harmonic. In the case of a transmissive point contact, the application of a radiation would provoke the appearance of a greater number of steps, according to the relation $\omega_0 = (m/n)\omega_r$ with m, n integers, and their heights will depend on the explicit form of the ac current components. This would be an appropriate way of testing our predictions for the ac current components.

2.4.3   Small bias regime ($eV \ll \Delta$)

In this subsection we concentrate in the $eV/\Delta \to 0$ case, which turns out to exhibit a remarkable variety of different regimes according to the values of the parameters $\alpha\Delta$ and the inelastic scattering rate η. As $eV \to 0$, the ac components oscillate more slowly, and at zero voltage these components give rise to the supercurrent. There are a lot of questions that naturally arise when one analyzes this limit: how does the
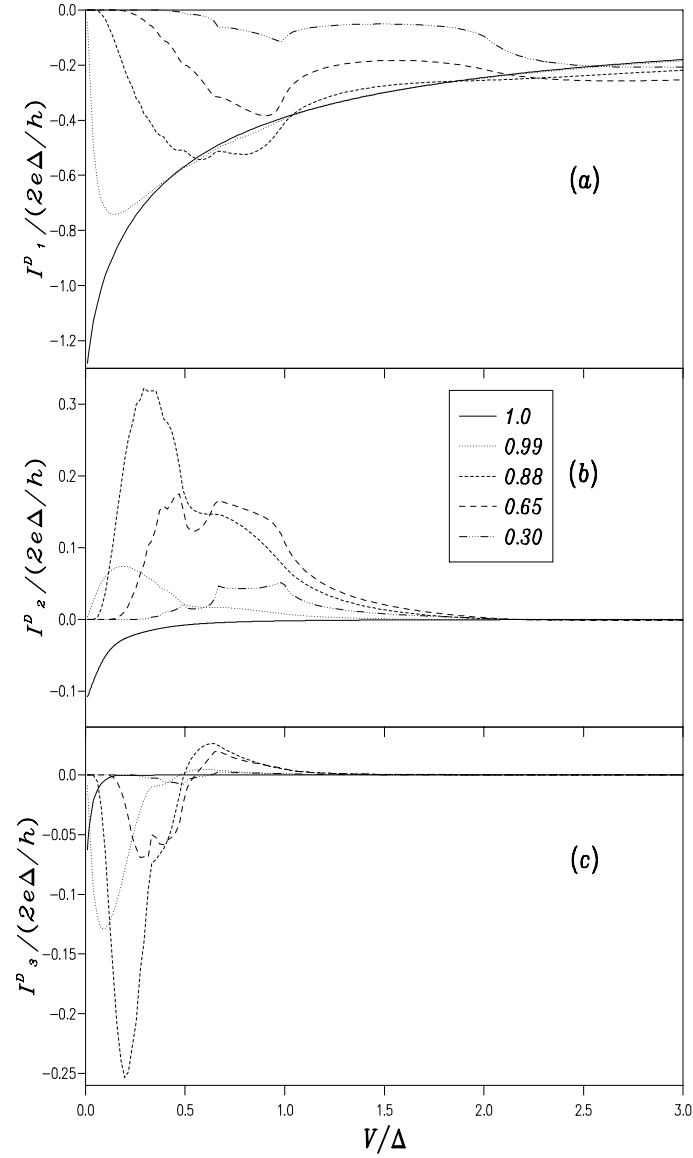
Figure 2.13: The first three ac components of the dissipative current for different values of the normal transmission at zero temperature.
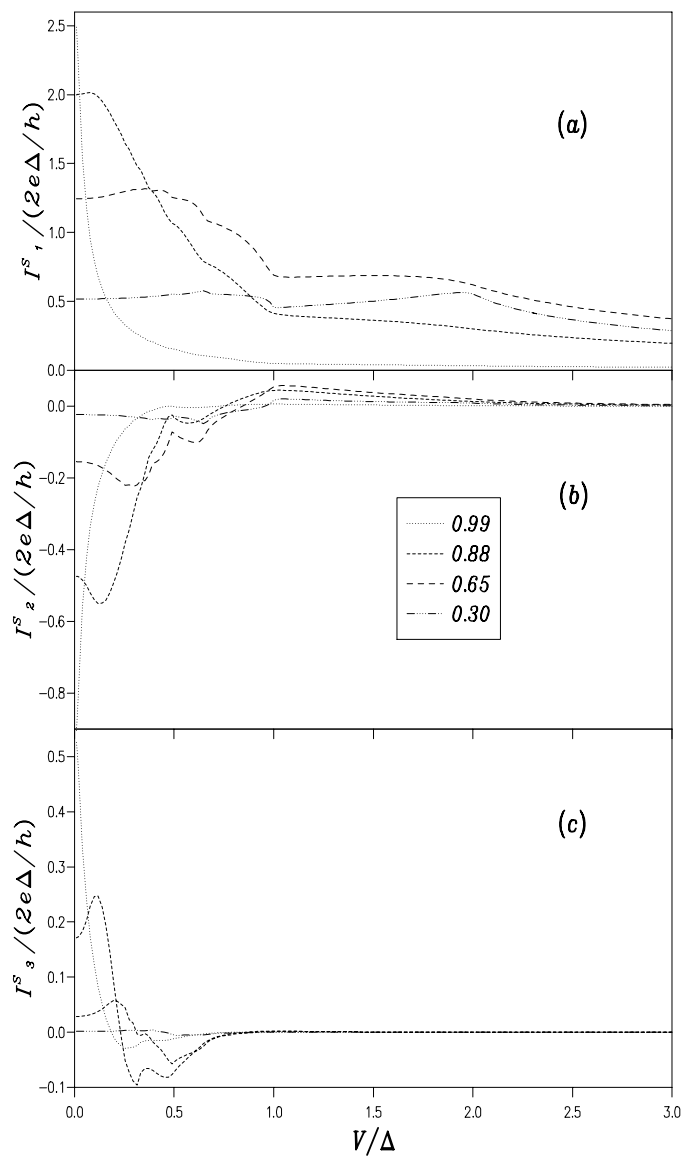
Figure 2.14: The first three ac components of the nondissipative current for different
values of the normal transmission at zero temperature.

current pass form its dissipative branch (I_0) to the supercurrent branch at $V = 0$?, does it cross a linear regime?, if it does, how does the linear conductance vary as a function of the superconducting phase?, does it take place like in the tunnel theory?, what can we say about the long-standing "$\cos\phi$ problem"? (see Chapter 1). We shall try to answer some of these questions during the analysis of the small bias regime.

As we commented above, the main difficulty for obtaining quantitative results in this limit lies in the fact that the order of the Andreev reflections that contribute to the current grows with decreasing V as $\sim \Delta/eV$. Furthermore, the amplitudes of these multiple processes do not decay when $(V, \eta) \to 0$ leading to the appearance of divergencies in the perturbative expansion in the coupling $\hat{t}$. Again, a complete summation of the perturbative series is needed in order to regularize these divergencies. An additional difficulty arises, as will be discussed below, from the fact that the limits $V \to 0$ and $\eta \to 0$ do not actually commute.

When the order of a multiple Andreev reflection increases there are two possible cut-offs for these processes, apart from of course the contact transmission. One is the bias voltage and the other is the energy relaxation rate η associated to inelastic scattering mechanisms. When the voltage is large enough a MAR ends outside the gap and its probability reduces greatly. Another cause for the MARs decay is the occurrence of inelastic processes inside the leads. If the time elapsed for the occurrence of a MAR is greater than $\hbar/\eta$, then the MAR will be damped or killed. Depending on the effective damping mechanism we can have two regimes: the case of $(eV/\Delta \to 0)$ with finite η, analyzed in our works [111]; and the case of $(eV/\Delta \to 0)$ with negligible η analyzed by Averin and Bardas [130]. In this subsection we shall analyze in detail the main results for both regimes and the conditions for their observability in a actual SQPC.

Linear regime

In the case of $eV/\Delta \to 0$ with $\eta > eV$, the energy relaxation rates becomes the damping mechanism that controls the MARs. In this case, one can linearize the current expression (2.38) with respect to voltage, separated in its dissipative and nondissipative components. The linear expression can be obtained by expanding the Fermi functions appearing in the functions $g^{+,-}$ up to first order in eV. Doing this and after some algebra (see Appendix C for details) we obtain [19]

$$I_0 = \frac{2e^2}{h}\beta V \int_{-\infty}^{\infty} d\omega \, \text{sech}^2(\frac{\beta\omega}{2}) \sum_{n=odd>0} n\text{Re}\left\{\text{Tr}\left(\hat{\sigma}_z \hat{T}_n^{a\dagger}(\hat{g}_0^a - \hat{g}_0^r)\hat{T}_n^a \hat{g}_0^a\right)\right\}$$

---

[19]Notice that now we express the current only in terms of the advanced hoppings.

$$I_m^D = \frac{2e^2}{h}\beta V \int_{-\infty}^{\infty} d\omega \, \text{sech}^2(\frac{\beta\omega}{2}) \sum_{n=odd>0} n\text{Re}\left\{ \text{Tr}\left(\hat{\sigma}_z \left[\hat{T}_{n+m}^{a\dagger} + \hat{T}_{n-m}^{a\dagger} \right] (\hat{g}_0^a - \hat{g}_0^r)\hat{T}_n^a \hat{g}_0^a \right) \right\}$$

$$I_m^S = \frac{8e}{h} \int_{-\infty}^{\infty} d\omega \, n_F(\omega) \sum_{n=odd>0} \text{Im}\left\{ \text{Tr}\left(\hat{\sigma}_z \left[\hat{T}_{n+m}^{a\dagger} - \hat{T}_{n-m}^{a\dagger} \right] (\hat{g}_0^a - \hat{g}_0^r)\hat{T}_n^a \hat{g}_0^a \right) \right\}, \quad (2.51)$$

where $\beta = 1/k_B T$, we have again simplified the notation: $\hat{T}_n \equiv \hat{T}_{n0}$ and now the
Green functions for the uncoupled electrodes and the renormalized hoppings are
evaluated at zero voltage. Thus, the previous expression indicates that the current
in the linear regime adopts the form: $I(\tau) = I_S(\phi) + G(\phi)V$, where $I_S(\phi)$ is the
supercurrent at $V = 0$ and $G(\phi)$ is the conductance in this linear regime. Let us
recall that in the standard tunnel theory (see Chapter 1), the conductance has the
form $G(\phi) = (1 + \epsilon \cos \phi)$. The aim is to obtain analytical expressions for these two
terms.

As we shall comment below, according to the value of η and the normal trans-
mission α, one can identify two subregimes within the linear regime: the weakly
damped regime (WDR) for $\eta \ll \alpha\Delta$, an the strongly damped regime (SDR), where
$\eta \gg \alpha\Delta$. For the interesting WDR one can show that the perturbative series for the
current is formed by terms that diverge more and more strongly in the $eV \to 0$ limit.
It is easy to show that the contribution to the current of order t^{2n}, $n \geq 2$, diverges
like $\sim t^{2n}/\eta^{n-1}$ (in comparison with the tunnel case where it does like $t^2 \ln \eta$). This
result is a consequence of the increasing contribution coming from the gap edges.
Therefore, *a correct answer can only be obtained by means of infinite perturbative
expansion.*

Within our formalism, analytical results in the small bias limit become feasible
since the transfer matrix $\hat{z}^{\pm}(\omega)$ (see Eq. (2.41)) tends to a scalar quantity having
the form of a simple phase factor inside the gap region. As shown in Appendix C
for $(\eta, V) \to 0$ we find

$$\hat{z}^{\pm}(\omega) = z(\omega)e^{i\varphi(\omega)} \ , \qquad \Delta\sqrt{1-\alpha} \leq |\omega| \leq \Delta, \qquad (2.52)$$

where

$$\varphi(\omega) = \arcsin\left(\frac{2}{\alpha\Delta^2}\sqrt{\Delta^2 - \omega^2}\sqrt{\omega^2 - (1-\alpha)\Delta^2} \right). \qquad (2.53)$$

As the multiple Andreev processes are generated by successive applications of
$\hat{z}(\omega)$, Eq. (2.40) indicates that these processes do not decay in this limit inside the
gap region. This infinite series of MAR gives rise to the well-known bound states
spectrum of a current-carrying SQPC at zero bias voltage [54, 134, 97]. As shown
in Appendix C, the positions of these bound states are determined by the condition
$\varphi(\omega) = \phi$, thus appearing inside the gap in positions ω_s given by [54, 134, 97]

$$\omega_s = \pm \Delta \sqrt{1 - \alpha \sin^2(\phi/2)}. \tag{2.54}$$

As we commented above, within this linear regime one can identify two different sub-regimes according to the ratio $\eta/\alpha\Delta$. The case $\eta/\alpha\Delta \ll 1$ corresponds to a situation where MARs are very weakly damped and give the dominant contribution to the current. This is the usual case, except for $\alpha \ll 1$. In order to illustrate the dominant contribution of the processes inside the gap in the WDR, we show in Fig. 2.15 the current density corresponding to the dc component I_0 for three values of the transmission. Three important features of this linear regime are displayed in this figure: firstly, the current density inside the gap increases as $\sim 1/\eta$ therefore giving the dominant contribution in the weakly damped case; secondly, there is a region inside the gap of width $2\Delta\sqrt{1-\alpha}$ in which the current density vanishes. This is the forbidden energy region for bound states at a given transmission. Finally, in Fig. 2.15(c) one can observe that the contribution of the continuum outside the gap becomes important as $\alpha < \eta/\Delta$. In the limit $\eta/\alpha\Delta \gg 1$ a second sub-regime is reached where the contributions of MAR are heavily damped and the current is dominated by single quasi-particle tunneling processes. Below, we shall analyze the transition between these two sub-regimes.

In order to identify the actual sub-regime for a real SQPC an estimation of the order of magnitude of η is needed. In Ref. [121] η is estimated from the electron-phonon interaction to be a small fraction of the gap for traditional superconductors. Thus, our theory predicts that a real SQPC would generally fall into the weakly damped case except for extremely low transmissions.

In the most interesting case of WDR, one can show that the sum of all harmonics gives rise to the Andreev bound states (ω_s) inside the gap, and that they carry all the current. As it is shown in Appendix C, after hard algebra, one obtains the following expression for the supercurrent $I_S(\phi)$ and the linear conductance $G(\phi)$ as a function of temperature and contact transmission

$$I_S(\phi) = \frac{e\Delta}{2\hbar} \frac{\alpha \sin\phi}{\sqrt{1 - \alpha \sin^2(\phi/2)}} \tanh(\frac{\beta|\omega_s|}{2}) \tag{2.55}$$

and

$$G(\phi) = \frac{2e^2}{h} \frac{\pi}{16\eta} \left[\frac{\Delta \alpha \sin\phi}{\sqrt{1 - \alpha \sin^2(\phi/2)}} \operatorname{sech}(\frac{\beta|\omega_s|}{2}) \right]^2 \beta V, \tag{2.56}$$

where ω_s is the position of the bound states inside the gap and $\beta = 1/k_B T$.

Let us start commenting the expression for the supercurrent as a function of the superconducting phase $I_S(\phi)$. In Eq. (2.55) we recover the well-known result for the supercurrent. This expression interpoles between the results of Ambegaokar-Baratoff
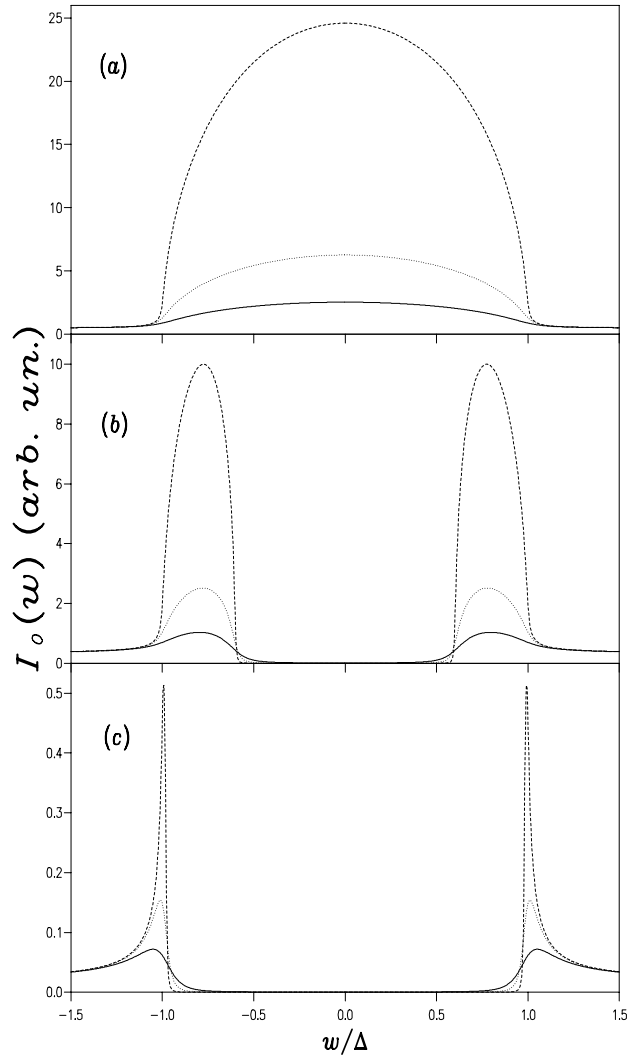
Figure 2.15: Current density for the dc component I_0 within the linear regime. (a),
(b) and (c) correspond to transmissions $\alpha = 1, 0.65$ and 0.04, respectively. In all
cases the full line corresponds to $\eta/\Delta = 1/10$, the dotted line to $\eta/\Delta = 1/25$ and
the broken line to $\eta/\Delta = 1/100$. The thermal factor $\mathrm{sech}^2(\beta\omega/2)$ (see Eq. (2.51))
has been extracted from the current density.

[19] for tunnel limit (see Eq. (1.2)) and the Kulik-Omelyanchuk one for the ballistic case ($\alpha = 1$) [54] (see Eq. (1.6)). The general case of arbitrary transmission was obtained for the first time by Haberkorn *et al.* [135] and lately for different authors [70, 136, 134, 137, 108]. Beenakker generalized this result to the case of an arbitrary number channels [97]. In Fig. 2.16 we show this result $I_S(\phi)$ for different normal transmissions of the contact.
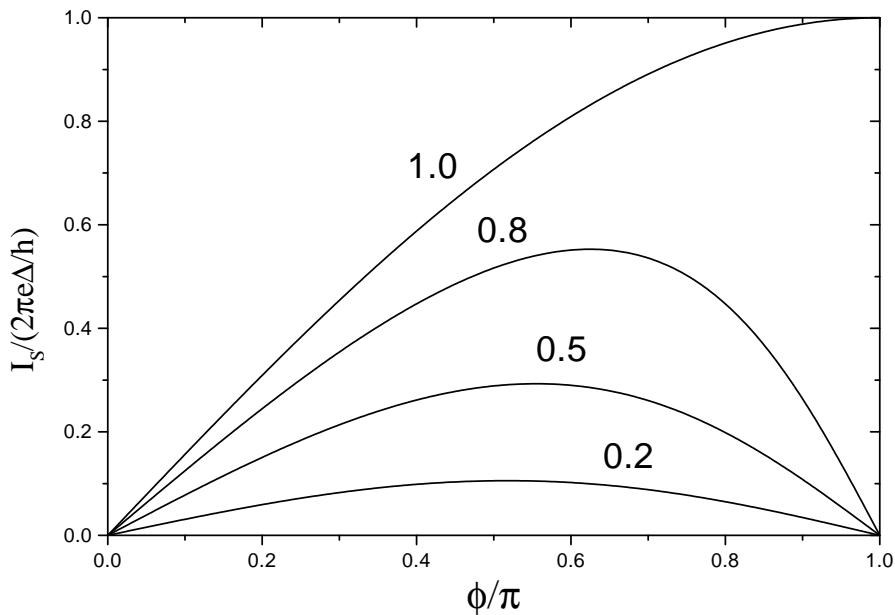
Figure 2.16: Zero-temperature supercurrent-phase relation in a S-S contact for different transmissions. The current is normalized to the critical current $I_C = e\Delta/\hbar$.

As can be seen in Fig. 2.16, when the transmission increases, $I_S(\phi)$ deviates from the sine-like shape of tunnel limit. Although, this is a result known since certain time ago, the first observation of a non-sinusoidal supercurrent-phase relation took place recently. In an excellent experiment, using atomic contacts created with the breakjunction technique, Koops *et al.* [138] measured the current-phase characteristic in a ring-shape junction. Their results showed at low temperatures a clear nonsinusoidal behavior with an extremum at phase differences between $\pi/2$ and π. However, they observed certain deviations with respect to the theory. The discrepancies can be mainly due to the fact that for any quantitative comparison between theory and experiment, a detailed knowledge of the transmission distribution is needed. They compared their experimental results with the theory for the ballis-

tic regime, but it hard to believe that every channel transmit perfectly in an atomic
contact (as we discuss in the part II of this thesis). In this sense we believe that the
study of the supercurrent-phase relation in SQPCs deserves further investigation.

In the previous calculations we have shown how to obtain the dc Josephson effect
starting from the finite voltage case. Thus, we have shown how this effect arises from
the infinite sum of Andreev reflection at zero voltage. In this sense, one could say
that the dc Josephson effect is simply another manifestation of the multiple Andreev
reflections.

Let us now comment the novel result of Eq. (2.56) for the linear conductance
$G(\phi)$. First, the linear conductance depends on η as $1/\eta$, i.e. is proportional to
the number of MAR taking place before the quasiparticles are inelastically scattered
(roughly given by $\alpha\Delta/\eta$). This is the expected dependence, $G \sim \tau_{in}$, where $\tau_{in} \equiv
\hbar/\eta$, as in the Drude model, and at variance with tunnel divergency $(ln(\eta/eV))$.
Moreover, the α^2 dependence in Eq. (2.56) indicates that the MARs dominate over
the quasiparticle processes.

Our theory yields a phase-dependent linear conductance which strongly deviates
from the tunnel theory result. In the limit of low barrier transparency, Eq. (2.56)
predicts $G(\phi) \sim 1 - \cos(2\phi)$ instead of $G(\phi) \sim 1 + \epsilon \cos \phi$ of standard tunnel theory
(see Chapter 1). Therefore, the tunnel theory linear conductance can never be
recovered in the weakly damped regime. On the other hand, with increasing values
of η MARs are progressively damped (the function $z(\omega)$ is no longer a phase factor,
decaying exponentially with η); eventually, when $\eta \gg \alpha\Delta$ only the lowest-order
processes contribute to the current and the tunnel theory expression is recovered.
The Figs. 2.17(a) and 2.17(b) illustrate in an explicit way the transition from the
weakly to the strongly damped regimes, allowing to establish precisely the range of
validity of our Eq. (2.56) for $G(\phi)$. In Fig. 2.17(a) the ratio between the exact linear
conductance, obtained numerically, and the analytical expression of Eq. (2.56), is
plotted as a function of η/Δ for increasing values of α. As can be observed, this ratio
tends to unity for η/Δ sufficiently small, within a range $\eta < \alpha\Delta$. On the other hand,
the validity of standard tunnel theory in the strongly damped regime is illustrated
in Fig. 2.17(b), where the ratio between the exact numerical conductance and the
tunnel theory $(O(t^2))$ conductance is represented against η/Δ. From this figure it
is clear that tunnel theory becomes valid only for sufficiently small α, provided that
$\alpha \ll \eta/\Delta$. In a real contact, where the inelastic scattering rate η can be expected
to be a small fraction of Δ, our expression for $G(\phi)$ will be valid provided that the
transparency is not extremely low.

It is worth mentioning that the strong sensitivity of the dissipative current on a
phenomenological inelastic scattering rate was pointed out by several authors during
the 1970s. This fact was used for trying to meet an agreement between the stan-
dard tunnel theory conductance and the experimental results (for a review on the
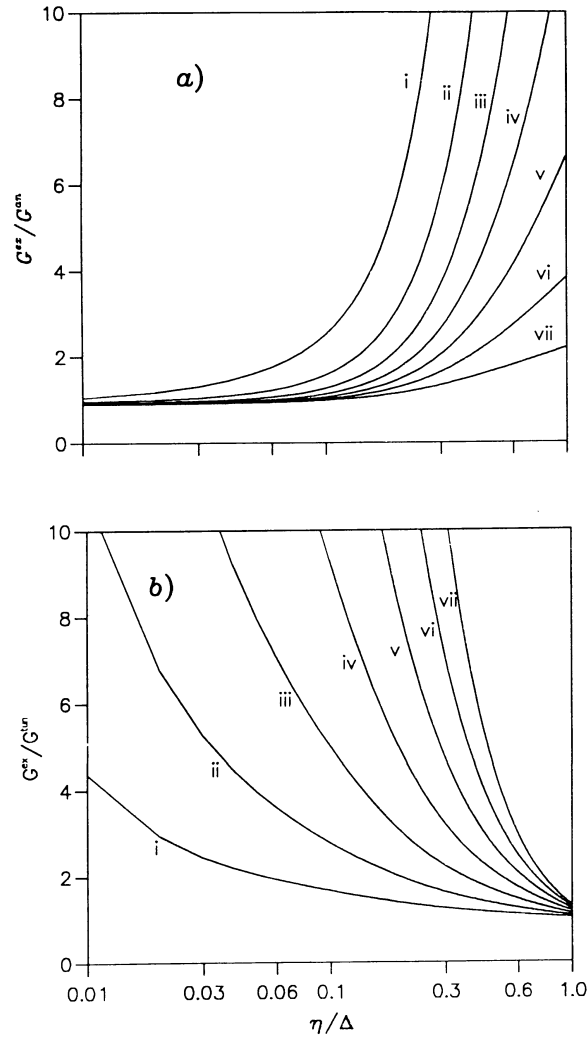
Figure 2.17: Transition between the weakly and strongly damped regimes. The ratio between the exact numerical conductance and: (a) the analytical expression given in Eq. (2.56); and (b) the tunnel theory ($O(t^2)$) conductance, plotted against η/Δ. The values of α considered are: i) 0.15, ii) 0.48, iii) 0.64, iv) 0.78, v) 0.88, vi) 0.95 and vii) 0.99. In all cases the phase is the one corresponding to the maximum supercurrent.

discrepancy between standard tunnel theory and experiments, usually referred to as the "cos(ϕ)-problem", see Chapter 1 and Ref. [21]). However, as shown above, when the condition $\eta < \alpha\Delta$ holds, the standard tunnel theory can *never* give the correct

result.

Another interesting limiting case of Eq. (2.56) corresponds to the ballistic regime. In this case and for $T \sim T_C$, $G(\phi)$ behaves approximately as $(1 - \cos \phi)$, in agreement with the result given by Zaitsev [127]. However, the most unusual phase-dependence of $G(\phi)$ appears for high values of the transmission and low temperatures ($k_B T < \Delta$). This is illustrated in Fig. 2.18, where $G(\phi)$ is plotted for two different temperatures and increasing values of the transmission.

The only experiment where the full phase dependence of $G(\phi)$ was measured is, to our knowledge, that of Rifkin and Deaver [42]. Their measured $G(\phi)$ strongly deviates from a $\cos \phi$-like form (see Fig. 1.7), being almost negligible for small values of ϕ and exhibiting a large increase around $\phi \sim \pi/2$. In Fig. 2.19 we have tried to do a comparison between the experimental results of Rifkin and Deaver and our theoretical results. As the experiment was performed in a point contact with many channels, we have included curves with different transmissions. In both cases $G(\phi)$ shows an asymmetry around $\phi = \pi/2$, at variance with the form $\cos(\phi)$ of the standard tunnel theory.

The fluctuation-dissipation theorem [139] states that the conductance G in the linear regime is related to the thermal fluctuations of the supercurrent, S, through the expression $S = 4k_B T G$. This relation has been confirmed in an independent calculation of the thermal noise carried out by our group [140].

On the other hand, it is interesting to point out the existence of an analogy between our expression for $G(\phi)$ and the conductance of a normal mesoscopic loop threaded by a magnetic flux [142]. The reason for this analogy lies in the fact that in both systems the current is mainly carried by two-phase dependent discrete levels.

Finally, let us say a few words about the observability of the linear conductance. The main problem is the difficulty for fixing the voltage when $eV \ll \Delta$. Thus, our theory could be not directly applicable to this limit. In this case one should solve the equation of the circuit taking into account the influence of the different circuit elements. This has been carried out successfully by Vion *et al.* [141] for the case of a tunnel junction. These authors determined the influence of the *environment* in the value of the current at which the jump to the dissipative regime takes place, known as *switching current*, which in general is different from the critical current. In the case of a transmissive contact the linear conductance ($G(\phi)$) influences the dynamics of the superconducting phase and should be reflected in the switching current. Thus, one would expect that a similar analysis to the one of Ref. [141] for the case of transmissive contacts reveals the linear conductance dependence on the transmission, phase and temperature.
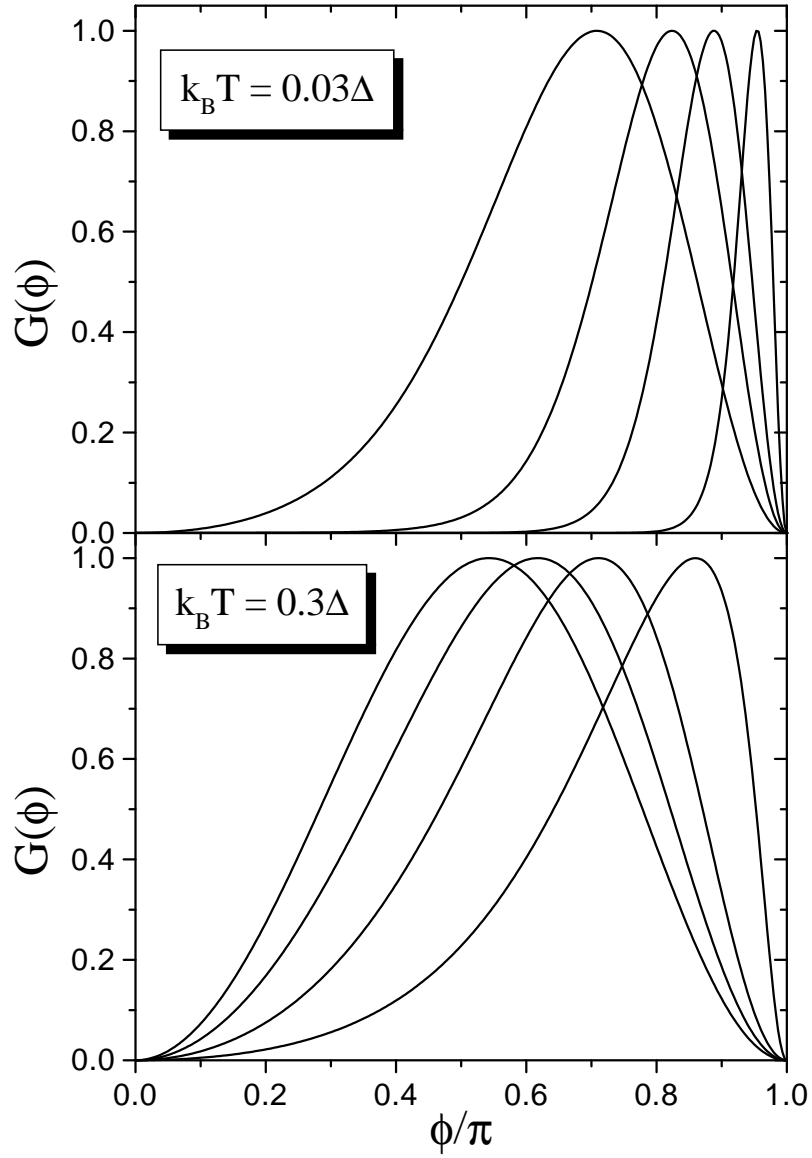
Figure 2.18: Phase dependence of the linear conductance given by Eq. (2.56) for two
different temperatures and increasing values of the normal transmission coefficient,
from left to right: 0.2, 0.5, 0.8 y 0.99. The conductance is normalized to its maximum
value for every transmission.
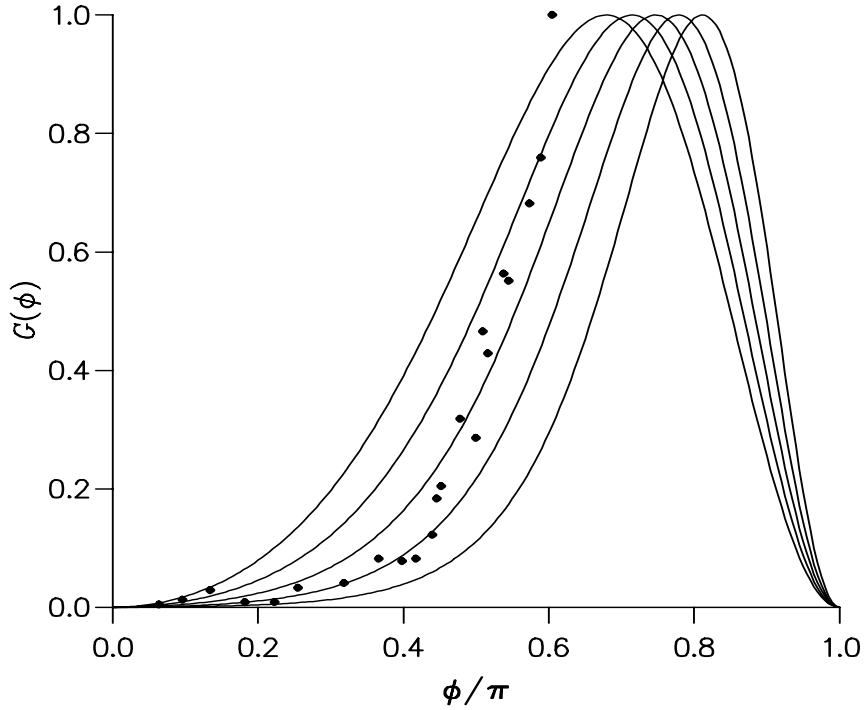
Figure 2.19: Phase-dependent linear conductance normalized to its maximum value for different values of the transmission (from left to right $\alpha = 0.4, 0.5, 0.6, 0.7, 0.8$) and $k_B T = 0.1\Delta$. The dots represent the data from Ref. [42].

Non-linear regimen $(eV > \eta)$

Averin and Bardas [130] described the non-linear regime as $eV \to 0$ for $\eta = 0$. When the truncation of the infinite series of MAR is caused by a finite V (with negligible η), analytical results have only been obtained in the quasi-ballistic limit, i.e. $\alpha \to 1$. A closer inspection of the $I - V$ curves in the small bias region and for $\alpha \sim 1$ reveals that the supercurrent components decay exponentially from its value at $V = 0$ with a collapsing width $\sim (1 - \alpha)\Delta$. This is illustrated in Fig. 2.20(a) where a blow up of the behavior of I_1^S for small bias voltages and quasi-ballistic transmissions is shown. In the limit $\alpha \to 1$ the supercurrent becomes a delta function at $V = 0$. On the contrary, the dissipative components in this same limit tend to a finite value outside the region of width $\sim (1 - \alpha)\Delta$. This behavior is shown in Fig. 2.20(b) where I_1^D is plotted in the same magnified scale as I_1^S. The summation of these dissipative
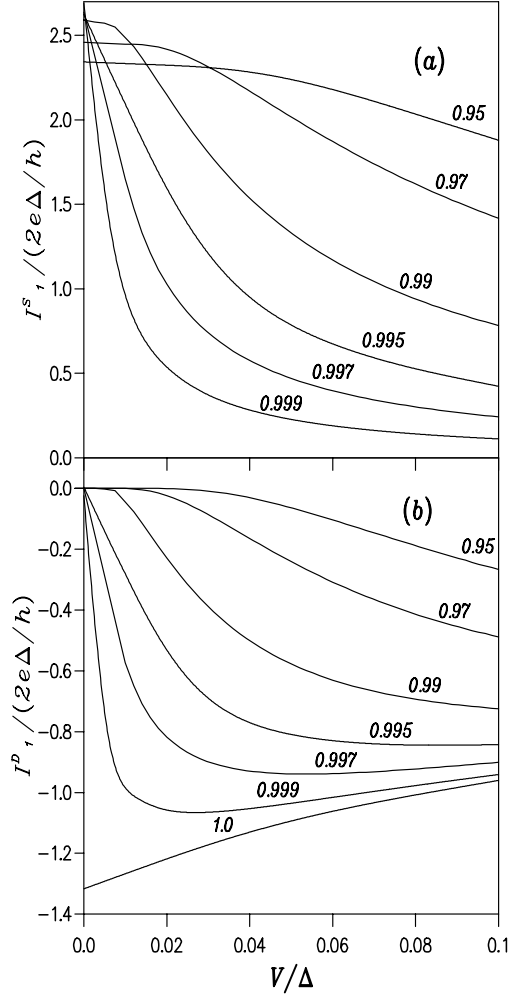
Figure 2.20: Behavior of the first non-dissipative (a) and dissipative (b) ac components in the very small voltage range close to ballistic conditions. These results have been obtained for negligible η: non-linear regime.

components for $\alpha = 1$ and very small V yields (see Appendix C)

$$I_D(\phi) = \frac{e\Delta}{\hbar} \tanh\left(\frac{\beta\Delta}{2}\right) |\sin(\phi/2)|\text{sign}V, \qquad (2.57)$$

in agreement with the result derived by Averin and Bardas [130]. This current ex-

pression differs from the usual one at V=0 (see Eq. (2.55)). The existence of a region of decreasing width $V \sim (1 - \alpha)\Delta$ in which this crossover from supercurrent to dissipative current takes place can be associated with the collapse of the forbidden region for MAR inside the superconducting gap taking place when $\alpha \to 1$. In this way, when V is small compared to the width of the forbidden region the excitation of quasi-particles from states at $\omega < -\Delta\sqrt{1 - \alpha}$ into states at $\omega > \Delta\sqrt{1 - \alpha}$ is negligible and there is no appreciable dissipative current; whereas the opposite situation holds for $V > \sqrt{1 - \alpha}\Delta$. Averin and Bardas [130] have described this crossover as a Landau-Zener transition in which the non-dissipative and the dissipative components scale with α and V as $(1 - p)$ and p respectively, where $p = \exp[-\pi(1 - \alpha)\Delta/eV]$. The numerical results for sufficiently small eV/Δ and $(1 - \alpha)$ are well fitted by these scaling laws. However, a careful analysis reveals that their range of validity around $V = 0$ and $\alpha = 1$ decreases strongly when increasing the component number.

Comment on the observability of both small voltages regimes

In summary, in this small bias limit one can identify four different sub-regimes depending on the relative values of parameters η, $\alpha\Delta$ and eV. The prediction of the actual behavior of a real SQPC in this limit would therefore require a careful estimation of all these parameters. In this respect, one should keep in mind that while eV and α can be varied experimentally in a rather controlled way, the inelastic scattering rate η is an intrinsic property of the superconducting electrodes much more difficult to control. The unavoidable presence of some degree of inelastic scattering can prevent the actual observability of the crossover from non-dissipative to dissipative behavior described after Eq. (2.57). The requirement of $eV \sim (1 - \alpha)\Delta$ together with that of $\alpha \sim 1$ can actually imply $eV < \eta$ which would rather correspond to the linear regime.

2.5 Experimental comparison

2.5.1 Introduction

Since the first observation of the subharmonic structure done by Taylor and Burstein [30] in 1963, many authors have reported experimental data about such structure (see Chapter 1). As we commented in Chapter 1, historically it has been difficult to do a quantitative comparison between theory and experiment, due to uncertainties in the crucial parameter of the superconducting junctions, in tunnel junctions or weak links [92, 106, 93, 94]. But with the modern microfabrication techniques this problem has disappeared in a great extent. In particular, the atomic contacts, designed with the technique of *mechanically controllable breakjunctions* [74, 85, 86] or with the STM [88], are ideal systems for investigating the transport properties of a SQPC.

This section is devoted to an exhaustive comparison between experimental results obtained in atomic contacts and the predictions of our model, concentrating ourselves in the I-V characteristics (dc current).

As a first example toward a quantitative comparison it is worth mentioning the work done by van der Post *et al.* [85], in which they studied the I-V characteristics of breakjuntions of Nb and Pb in the tunnel regime. In this work the authors showed that the height of the successive current steps in the SGS is proportional to increasing powers of the transmission, revealing the role of multiple Andreev reflections.

Recently, in an excellent experiment Scheer *et al.* [143] analyzed the I-V characteristics in Al atomic-size contacts using microfabricated MCBs (see Ref. [143] for details). In this experiment, after breaking the contact, the electrodes are brought back into contact to form a point contact with a resistance of a few ohms. Pushing again on the substrate leads to a controlled opening of the contact, while the sample is maintained at $T < 100$ mK. As found in previous experiments at higher temperatures, the normal conductance G decreases in steps of the order of $G_0 = 2e^2/h$, their exact sequence changing from opening to opening. Between two jumps, G generally tends to increase when pulling the contact. The last conductance value before the contacts breaks is usually between $0.5G_0$ and $1.5G_0$. In this last plateau one could think naively that when $G < G_0$ only one conducting channel contributes to the conductance. Therefore, in this case we can carry out the direct comparison between our single channel theory and this experimental situation.

Fig. 2.21 shows the comparison between different experimental curves for Al last conductance plateau [143] and some theoretical curves obtained with our single channel theory at zero temperature [20]. There are several remarkable features in this figure. First, paying attention to the experimental curves, in spite of the three curves correspond to very similar normal conductance ($G \sim 0.8G_0$) [21], they are very different. Moreover, as can be observed, these curves show a clear subharmonic structure at the predicted voltages. However, when one compares them with the theoretical single channel curves, one finds that they are similar, but there is no a quantitative agreement. What is the origin of this discrepancy? The simplest assumption is that even in the case of $G < G_0$, there are several channels contributing to the current in the case of Al. This leads us to a remaining question: how are the theoretical results obtained so far generalized to the case of an arbitrary number of channels? The following subsection is devoted to the answer of this question.

---

[20]Let us recall that the experiment was performed at $T < 100$ mK. Therefore, the effect of a finite temperature is negligible.

[21]The normal conductance is measured at voltages $V \geq 5\Delta/e$, where the characteristics are perfectly linear.
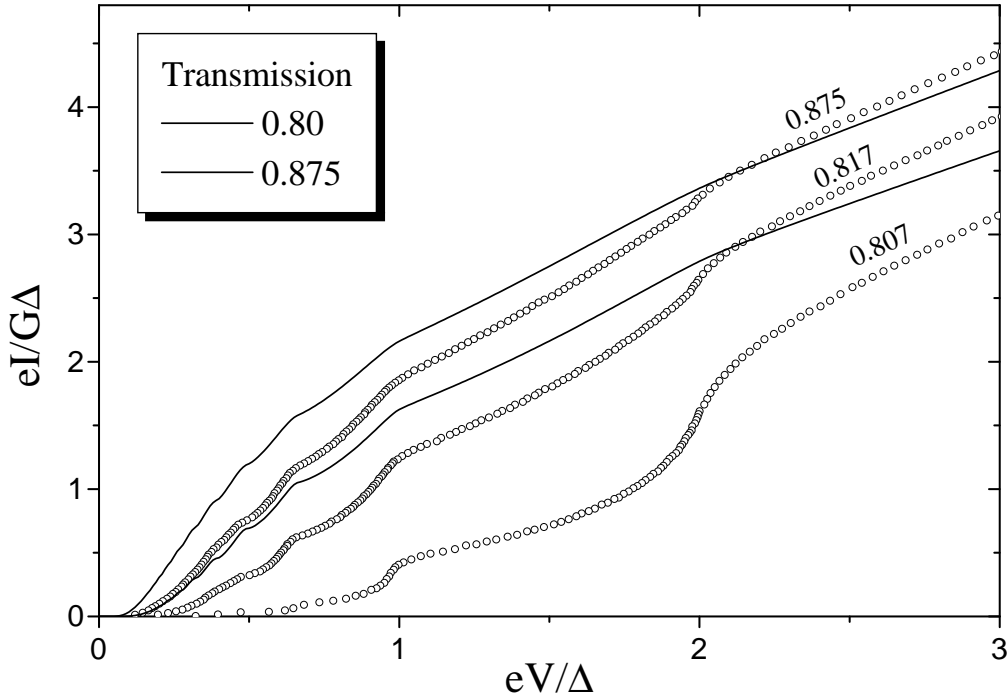
Figure 2.21: Comparison between the I-V curves in a superconducting atomic contact of Al [143] and our single channel theory. The experimental results (open circles), courtesy of Elke Scheer, correspond to the last conductance plateau and the total transmission is indicated in each case. The theoretical curves correspond to the solid lines whose transmissions are indicated in the inset.

2.5.2 Superconducting quantum point contact with an arbitrary number of channels

In the case of a normal mesoscopic conductor it is well-known that the current in the linear regime can be expressed as a superposition of independent contributions. This result is contained in the Landauer formula for the zero-temperature linear conductance [95]

$$G = \frac{2e^2}{h} \text{Tr} \left\{ \hat{t}^\dagger \hat{t} \right\}_{E_F} = \frac{2e^2}{h} \sum_{i=1}^{N} \alpha_i, \tag{2.58}$$

where Tr denotes trace, $\hat{t}$ is the transmission matrix of the system and α_i are the eigenvalues of $\hat{t}^\dagger \hat{t}$ evaluated at the Fermi level E_F. In short, as long as the transmis-

sion coefficients are energy independent in an intervale of the order of the voltage
around the Fermi energy, we are in the linear regime and one can find a basis which
diagonalizes the problem, in the sense that every transport property can be expressed
as a sum of independent channel contributions.

As we know, in the case of superconducting contacts the transport properties are
determined by inelastic processes: the Andreev reflections. In this sense one could
think that in this case the conducting modes are mixed. However, we have to bear in
mind that in an Andreev reflection an electron is reflected as its time-reverse state
(its corresponding hole). In particular, if the transmission coefficients are energy
independent, the hole has the same transmission as the electron and basically comes
back for the same channel, i.e. *an Andreev reflection does not mix the conducting
channels*. Thus, also in the superconducting case the transport properties can be
expressed as a sum of independent contributions. On the other hand, as the Andreev
reflection does not mix the conducting modes, an obvious consequence is that *the
conducting channels in the normal and in the superconducting case are the same*.

The rigorous demonstration of these conclusions can be found for the case of
the supercurrent in a S-S contact in Refs. [97, 75], for the N-S case in Ref. [99].
Recently, Bardas and Averin have generalized these ideas to the case of a SQPC at
finite voltage [144] [22].

In summary, the main conclusion of this discussion is that the transport in SQPC
with arbitrary number of channels can be analyzed with our single channel model,
just summing the contribution of each mode with its corresponding transmission.
This is true, as we stated above, as long as the transmission coefficients are energy
independent in the voltage range we are interested in. In particular, this is true for
the metallic atomic-size contacts for the voltage range ($eV \sim \Delta$), i.e. a few meV.
Thus, the current is the result of the contribution of N independent channels:

$$I(V) = \sum_{i=1}^{N} I_i(\alpha_i, V). \qquad (2.59)$$

Let us emphasize that all the results obtained in this chapter (supercurrent, linear
conductance, excess current, ac current components, etc.) are simply generalized by
summing up the independent contributions of the different modes.

Finally, let us say that this generalization allows us to analyze in an unified way
different physical situations, with the knowledge of the transmission distribution
of the corresponding system. Thus, we can use the results of our single channel
theory for studying atomic contacts, tunnel junctions or S-N-S contacts with diffusive
normal regions [144], as long as the constriction length is much smaller than the
superconducting coherence length of the leads.

---

[22] The demonstration of these properties can also done within our Hamiltonian approach, but we
shall not include it to do not do very dense this work.

2.5.3 Definitive comparison for an atomic contact

Now, we are ready to test the conjecture that we did in the introduction of this section about the contribution of several channels in the last conductance plateau of Al contacts. Fig. 2.22 shows the same experimental curves as in the previous figure, together with the best theoretical fits assuming the superposition of channels. The fits were done using the number of contributing channels and their transmissions as free parameters (see Ref. [143] for details on the fit procedure). As can be observed, the agreement is quantitative, what confirms not only the conjecture about the superposition of channels, but also our theory of the superconducting transport [23]. Refs. [143, 145, 146] show many examples of the comparison for the case of Al, varying a broad range of transmissions. In all cases the quantitative agreement is remarkable, mainly due to the fact that Al is the best example of a BCS superconductor.

The fact that several channels contribute to the current in the case of Al even when $G < G_0$ is in principle surprising. Many questions naturally arise from these results, but all can be summarized in the following one: what determines the number and transmission of conducting channels in atomic contacts? The part II of the thesis is mainly devoted to the answer of this question. In part II we shall show that the number and transmission of conducting channels in an atomic contact depend on its geometry and its electronic orbital structure. In particular, in an one-atom contact [24] the number of channels is controlled by the number of valence orbitals of such atom. For instance, in the last conductance plateau of Al contacts typically three channels were found. This is due to the fact that the Al is a trivalent metal where the s and p orbitals contribute to the current. For a detailed explanation of these questions we recommend the reading of the part II of the thesis and Refs. [146, 147, 148].

The comparison with the theoretical I-V characteristics has been also done for other metals. Atomic contacts of different metals were investigated in a collaboration between different experimental groups [146]. Fig. 2.23 shows a typical example of the fits for the case of a Pb contact created with the STM. As can be seen, the agreement is again quantitative for different transmissions. The number of channels needed for obtaining a good fit coincides with the one of the Al case because both are sp-like metals with similar electronic structures [147].

In the above mentioned work was also study the case of a transition metal like Nb. Fig. 2.24 shows an example of the fit for the last conductance plateau. As can be observed, 5 channels were necessary to get a good fit, what is due to the fact that

---

[23]Someone may think that it is not strange to obtain a quantitative agreement by introducing a greater number of parameter. However, as it is explained in Ref. [143], the highly non-linear subgap structure in the I-V curves provokes that slight deviations in the transmission of the individual channels lead to great differences in the total current.

[24]As we shall discuss in the part II of the thesis, the last conductance plateau of a metallic contact corresponds to the case of an one-atom contact.
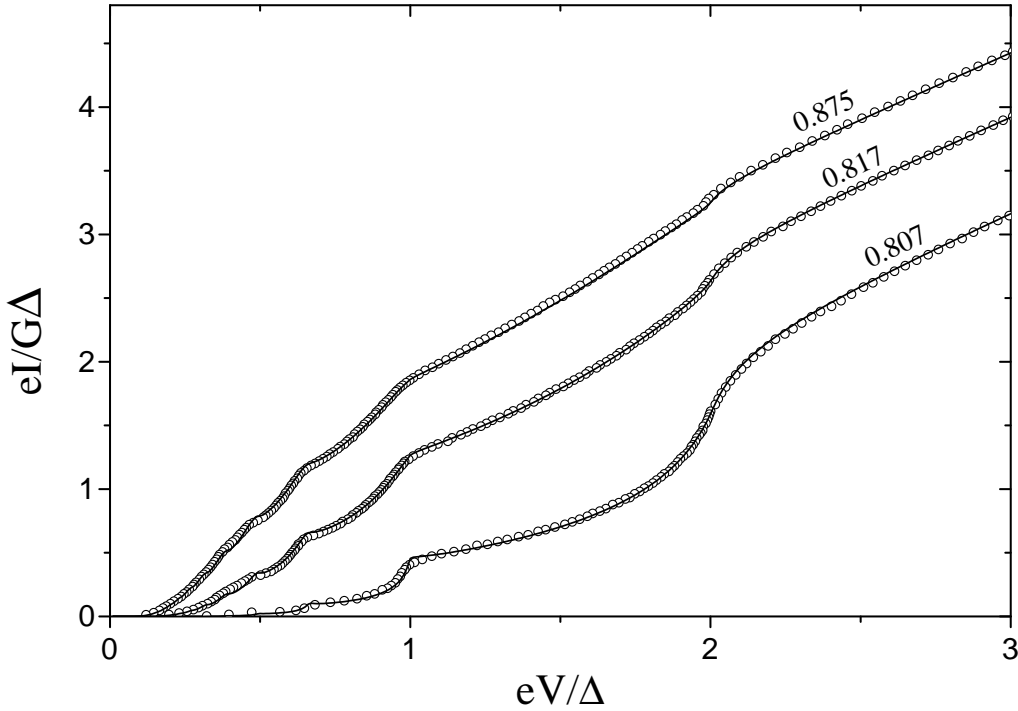
Figure 2.22: Fits of the experimental curves of Fig. 2.21 using the single channel theory together with the superposition of the channels. For the curve of total transmission $\alpha = 0.875$ were necessary two channels with $\alpha_1 = 0.80$ and $\alpha_2 = 0.075$. For the curve with $\alpha = 0.817$ we needed three channels with $\alpha_1 = 0.682$, $\alpha_2 = 0.12$ and $\alpha_3 = 0.015$. For the curve with $\alpha = 0.807$ we needed three channels with $\alpha_1 = 0.399$, $\alpha_2 = 0.254$ and $\alpha_3 = 0.154$.

in a transition metal the d orbitals contribute to the current providing additional channels (see Ref. [147]). Notice that in this case the fit is not so good, mainly due to the following effect. In the inset of Fig. 2.24 can be shown an example of the tunnel current in this Nb contact. There is a strange structure around $eV = 2\Delta$, what seems an effect of the destruction of superconductivity due to proximity effects.

The main conclusion of the previous experiments with respect to the superconducting transport is that our model describe quantitatively the superconducting I-V characteristics of atomic contacts. Although, the comparison has been restricted to the dc current, we expect that a similar agreement can be found for other transport properties.

On the other hand, due to the agreement between experiment and theory, the
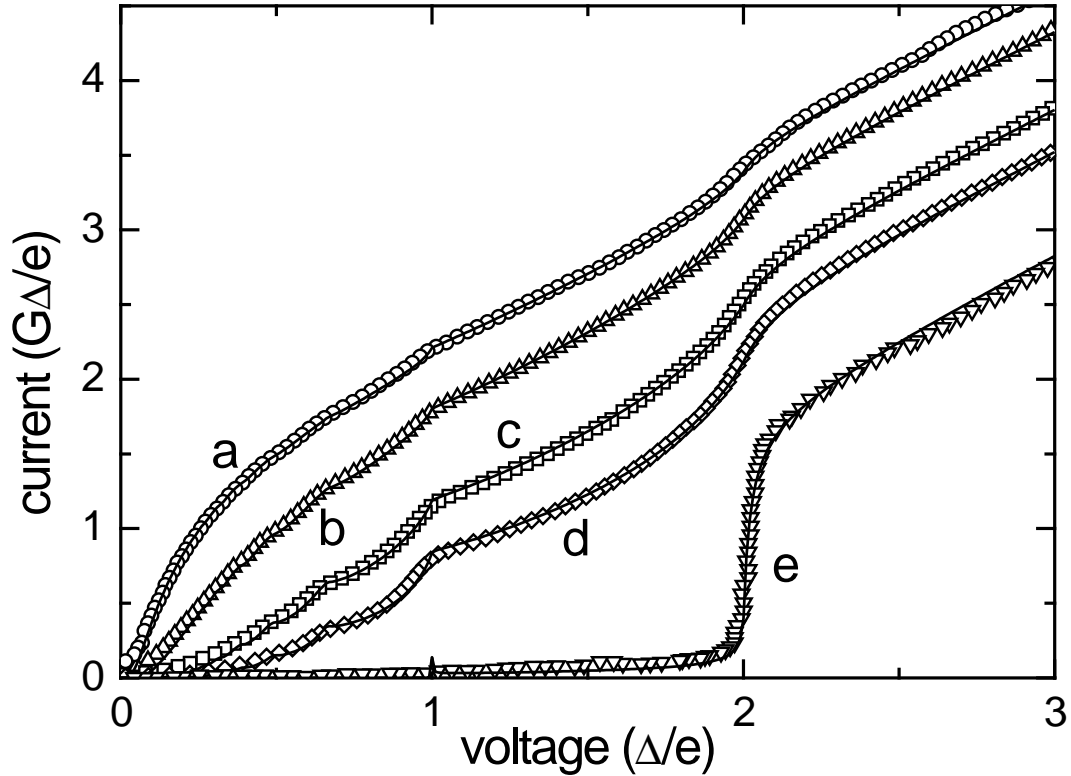
Figure 2.23: Experimental I-V characteristics (symbols) of five configurations of a sample of Pb at 1.5 K using the STM, and the best numerical fits (solid lines). The curves a-d have a similar total transmission, around 1.4; the curve e has been taken in tunnel regime. The transmissions of the individual channels obtained from the fits are: curve a: $\alpha_1 = 0.955$, $\alpha_2 = 0.355$, $\alpha_3 = 0.085$, $\alpha_4 = 0.005$; curve b: $\alpha_1 = 0.89$, $\alpha_2 = 0.36$, $\alpha_3 = 0.145$, $\alpha_4 = 0.005$; curve c: $\alpha_1 = 0.76$, $\alpha_2 = 0.34$, $\alpha_3 = 0.27$, $\alpha_4 = 0.02$; curve d: $\alpha_1 = 0.65$, $\alpha_2 = 0.34$, $\alpha_3 = 0.29$, $\alpha_4 = 0.12$; curve e: $\alpha = 0.026$. The voltage and the current are in reduced units. The measured gap for Pb is $\Delta/e = 1.37$ mV.

superconducting I-V characteristics permit us to obtain information on the normal system, due to the correspondence between normal and superconducting channels. In particular, they give us information on the number and transmission of the conducting channels in these atomic contacts. In this sense, the fits that we have shown have given rise to what we can call a *channel spectroscopy*, permitting a qualitative advance in the understanding of how the electrical current flows in metallic atomic-
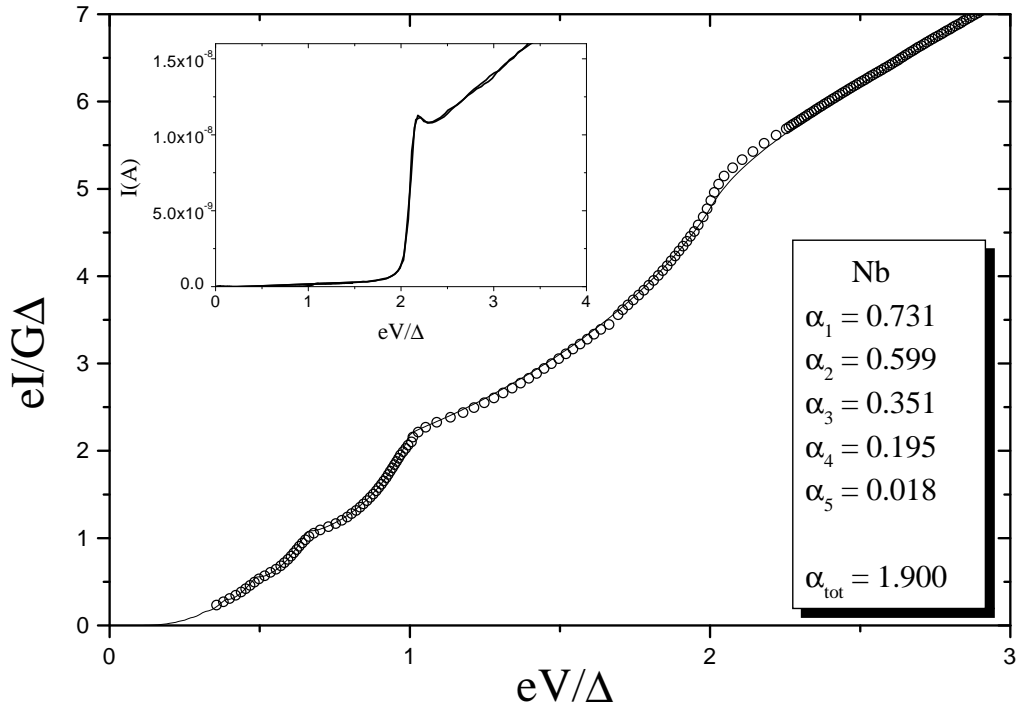
Figure 2.24: Experimental I-V characteristic (open circles) taken in the last conductance plateau of an atomic contact of Nb, courtesy of Bas Ludoph, and the best fit (solid line) obtained with five channels. The inset shows an example of the current in the tunnel regime for a total transmission of 0.047. Notice the anomalous structure around 2Δ.

size contacts [146]. This is finally the link between the two parts of this thesis, devoted in principle to two slightly different topics. The consequences that can be extracted about the normal transport from these experiments will be analyzed in detail in the second part of the thesis.

The next section is devoted to the conclusions of this chapter and we postpone some comments about future works and open problems until the end of the part I (section 4.6).

2.6   Conclusions

This final section is devoted to summarize the main conclusions of this chapter:

- Our model describes quantitatively the I-V characteristics in superconducting atomic contacts [143, 145, 146]. The experimental comparison has been restricted to the dc current, but we expect that a similar agreement can be found for other quantities: supercurrent, linear conductance, ac current components, etc.

- Definitively, the I-V characteristics of superconducting quantum point contacts, and in particular the subharmonic structure, are controlled by multiple Andreev reflections, thus ruling out other mechanisms (see Chapter 1).

- From the theoretical point of view it is clear that one needs a coherence and purely quantum description for determining the electronic transport in superconducting quantum point contacts.

- We have shown the equivalence between the scattering formalism and our Hamiltonian approach. Morevover, we have shown that the pathologies of the Hamiltonian approach disappear in a natural way when one works in a local basis and analyzes the processes up to infinite order.

- Usually the multiparticle tunneling theory (MPT) [34] and the ones based on multiple Andreev reflections [62, 71] have been viewed as opposite, but indeed they contain the same physics, although they usually consider different regimes. The divergencies appearing in the MPT disappear when one sum the processes up to infinite order.

- With respect to the small voltage regime, we have shown the importance of an energy relaxation rate η associated to inelastic scattering. Depending on the value of the different contact parameters: $\alpha\Delta$, eV and η one can find several regimes. In particular, we have analyzed in detail the linear regime and we have shown that the linear conductance (Eq. (2.56)) strongly differs from the results of the standard tunnel theory, what can be the solution of the long-standing $cos\phi$ problem.

- If a normal point contact is in the linear regime, the electronic transport in the corresponding superconducting system can be described as a superposition of independent channels. Thus, one can describe different systems in a unified way: atomic contacts, tunnel junctions, diffusive constrictions, etc.

- The remarkable agreement between experiment and theory in atomic contacts allows us to use the superconducting I-V characteristics to obtain the transmission distribution in these contacts [143, 145, 146]. This has permitted to investigate in detail the normal electronic transport in these atomic contacts

[146], and will permit in the next future the precise analysis of superconducting transport properties like the supercurrent.

Chapter 3

Shot noise and coherent multiple charge transfer in superconducting quantum point contacts

In the previous chapter we were interested in the analysis of the current in superconducting contacts. Nevertheless, the current is not the only quantity which can help us to understand the transport properties of these systems. In the last few years special attention has been paid to the study of shot noise in mesoscopic systems [149]. These time-dependent current fluctuations are a consequence of the discreteness of the carriers charge and their measurement can provide information not available in usual conductance experiments. For this reason this chapter is devoted to the study of shot noise in superconducting quantum point contacts.

Since 1918 we know thanks to Schottky [150] that in electrical circuits there are two intrinsic sources of noise in the electrical current. The first type of noise is known as *thermal noise* o Johnson-Nyquist noise. These fluctuations are due to the thermal movement of electrons and take place in every conductor. The second type of noise is known as *shot noise* and, as commented above, are due to the discreteness of the charge of the current carriers. Not all the conductors exhibit shot noise.

The noise is characterized by its spectral density or power spectrum $S(\omega)$, which is simply the Fourier transform at frequency ω of the current-current correlation function:

$$S(\omega, \tau) = \hbar \int d\tau' \, e^{iw\tau'} < \delta\hat{I}(\tau + \tau')\delta\hat{I}(\tau) + \delta\hat{I}(\tau)\delta\hat{I}(\tau + \tau') >, \qquad (3.1)$$

where $\delta\hat{I}(\tau) = \hat{I}(\tau) - < \hat{I}(\tau) >$ are the fluctuations in the current. Typically the

noise is white, which means that its power spectrum is independent of ω for wide frequency range. For this reason we shall only speak about noise at zero frequency in this chapter.

What is the information provided by the noise analysis? The thermal noise, which takes place at zero voltage and finite temperature, is related with the conductance G by the fluctuation-dissipation theorem [139]:

$$S = 4k_B T G \qquad (3.2)$$

whereas $\hbar\omega \ll k_B T$. In this sense, thermal noise does not provide additional information with respect to conductance.

On the other hand, the shot noise, which takes place at zero temperature and finite voltage, is more interesting because it provides us information on the correlations, statistic and charge of the current carriers. In particular, in a situation where a current I is due to the flow of uncorrelated carriers of charge q, shot noise reaches its maximum $S = 2qI = S_{Poisson}$. This result has been recently used for detecting the fractional charge $e/3$ charge carriers by measuring the ratio $S/2I$ in the fractional quantum Hall regime [151, 152]. One of the aims of this chapter is to use this result for extracting information on the transmitted charges in multiple processes which take place in superconducting contacts.

The shot noise in N-S junction has been analyzed by different authors [153, 154, 155, 156, 157]. In particular, in low transmissive structures a doubling of the normal Poisson noise-current ratio has been predicted due to Andreev processes where twice the electron charge is transmitted. In S-N-S or S-I-S structures the situation is far more complex. As shown in Chapter 2, the main processes contributing to the current for subgap bias voltage are multiple Andreev reflections (MAR). At a given subgap voltage V the current is mainly carried by MAR processes of order $n \sim 2\Delta/eV$, in which a net charge of ne is transferred. One would then expect an increase of the noise-current ratio roughly as $1/V$ for decreasing bias. This qualitative behavior has been recently confirmed experimentally by Dieleman et al. [158] for a S-I-S tunnel junction. Within the semiclassical theory of Ref. [62], these authors give an explanation of the observed shot noise enhancement due in terms of MAR processes through pinholes present in theses junctions.

As commented in previous chapters, a quantitative comparison between experiments and theory in macroscopic tunnel junctions, like the ones of Ref. [158], is rather complicated due to unavoidable uncertainties in the junction characteristics. However, as we shown in the previous chapter, such a comparison is possible in the case of quantum point contacts with a few number of conducting channels, like the metallic atomic-size contacts. As was extensively commented in Chapter 2, in order to describe properly the electronic transport in SQPCs a purely quantum mechanical description is needed. Within the framework of these microscopic theories analytical

results for a single quantum channel have been only obtained for some particular cases. For instance, the excess noise ($eV \gg 2\Delta$) for a perfect transparent channel has been obtained in Ref. [159]. The noise has also been analyzed for zero voltage and arbitrary transmission in Ref. [140], while the perfect transmission and finite voltage case has been addressed in Ref. [160].

The aim of this chapter is to analyze the shot noise for the whole range of transmissions and voltages within the same microscopic model used for the calculation of the current in Chapter 2. We shall paid special attention to the information which the shot noise provides on the charge of the multiple Andreev reflections. We find that the shot noise in a SQPC can be much large than the Poisson noise ($S_{Poisson} = 2eI$) and exhibits as a function of voltage a pronounced subgap structure. Furthermore, we shall explicitly show that in the tunnel limit the effective charge, defined as $S/2I$, tends to *integer multiples* of the electron charge $n = 1 + \text{Int}\,[2\Delta/eV]$.

We shall consider the case of a superconducting quantum point contact like the ones described in previous chapter, with a constant applied bias voltage V. For the range of voltages ($eV \sim \Delta$) one can neglect the energy dependence of the transmission coefficients and all transport properties, in particular the zero frequency shot noise, can be expressed as a superposition of independent contributions, i.e.

$$S = \sum_i S_i(\alpha_i, V). \tag{3.3}$$

Thus, we shall concentrate in analyzing the single channel model introduced in section 2.2. Let us recall that within this model the current operator can be expressed as [see Eq. (2.9)]

$$\hat{I}(\tau) = \frac{ie}{\hbar} \sum_\sigma \left(t e^{i\phi(\tau)/2} c_{L\sigma}^\dagger(\tau) c_{R\sigma}(\tau) - t^* e^{-i\phi(\tau)/2} c_{R\sigma}^\dagger(\tau) c_{L\sigma}(\tau) \right), \tag{3.4}$$

where $\phi(\tau) = \phi_0 + 2eV\tau/\hbar$ is the time-dependent superconducting phase difference.

Our aim is to determine the noise defined as

$$S(\omega, \tau) = \hbar \int d\tau'\, e^{iw\tau'} < \delta\hat{I}(\tau+\tau')\delta\hat{I}(\tau) + \delta\hat{I}(\tau)\delta\hat{I}(\tau+\tau') > \equiv \hbar \int d\tau'\, e^{iw\tau'}\, K(\tau,\tau'), \tag{3.5}$$

where $\delta\hat{I}(\tau) = \hat{I}(\tau) - < \hat{I}(\tau) >$. As we did for the current, we shall express the noise in terms of the nonequilibrium Keldysh Green functions. In particular, we can write the kernel $K(\tau,\tau')$ appearing in the noise spectral density in terms of the functions $\hat{G}_{ij}^{+-}(\tau,\tau')$ and $\hat{G}_{ij}^{-+}(\tau,\tau')$ as follows

$$< \hat{I}(\tau) > = \frac{e}{\hbar} \text{Tr} \left[\hat{\sigma}_z \left(\hat{t}(\tau) \hat{G}_{RL}^{+-}(\tau,\tau) - \hat{t}^\dagger(\tau) \hat{G}_{LR}^{+-}(\tau,\tau) \right) \right]$$

$$
\begin{aligned}
K(\tau, \tau') \;\; = \;\; & \frac{e^2}{\hbar^2} \Big\{ \mathrm{Tr} \Big[\hat{t}^\dagger(\tau) \hat{G}_{LL}^{+,-}(\tau, \tau') \hat{t}(\tau') \hat{G}_{RR}^{-,+}(\tau', \tau) + \\
& \hat{t}(\tau) \hat{G}_{RR}^{+,-}(\tau, \tau') \hat{t}^\dagger(\tau') \hat{G}_{LL}^{-,+}(\tau', \tau) - \\
& \hat{t}^\dagger(\tau) \hat{G}_{LR}^{+,-}(\tau, \tau') \hat{t}^\dagger(\tau') \hat{G}_{LR}^{-,+}(\tau', \tau) - \\
& \hat{t}(\tau) \hat{G}_{RL}^{+,-}(\tau, \tau') \hat{t}(\tau') \hat{G}_{RL}^{-,+}(\tau', \tau) \Big] + (\tau \to \tau') \Big\},
\end{aligned}
\tag{3.6}
$$

where $\hat{\sigma}_z$ is the Pauli matrix, Tr denotes the trace in the Nambu space and $\hat{t}$ is the hopping in this representation. To arrive at this expression for the kernel we have factorized the two body correlation functions following a mean field decoupling scheme consistent with the BCS theory [140].

As in the case of the current, it is easy to show that for a superconducting contact the noise contains not only a dc components but also all the harmonics of the Josephson frequency. This means that the noise oscillates as a function of time as

$$
S(\omega, \tau) = \sum_m S_m(\omega) e^{im\phi(\tau)},
\tag{3.7}
$$

The problem of evaluating the noise Fourier components S_m can be reduced to the calculation of the Fourier components of the Keldysh Green functions. For this calculation we use the algorithm described in the previous chapter. Thus, in this chapter we shall concentrate in the analysis of the results. Finally, we shall restrict our attention to the zero-frequency dc component of the noise: $S \equiv S_0(0, \tau)$.

The rest of the chapter is organized as follows: in section 3.2 we briefly study the elementary case of a single channel N-N contact. Section 3.3 is devoted to the analysis of the N-S case. Finally, in section 3.4 we shall present the novel results on the shot noise in SQPCs.

3.1   Shot noise in a N-N contact

In this section we analyze the well known case of a N-N contact. The main aim of this analysis is to introduce a simple argument which allows to understand the noise results better, specially in the superconducting case. As stated in the introduction, we assume that the normal contact is in the linear regime. With this assumption it is easy to carry out the calculation of the noise starting from Eq. (3.6) because this problem admits a stationary solution.

As stated in the introduction, the thermal noise $(V = 0, T \neq 0)$ is given by the fluctuation-dissipation theorem and for the single channel case adopts the following form

$$S = \frac{8e^2}{h}k_BT\alpha = (4k_BT)\,G, \tag{3.8}$$

where G is the conductance of this channel.

On the other hand, the shot noise ($V \neq 0, T = 0$) is given by

$$S = \frac{4e^2}{h}eV\,\alpha(1-\alpha)\ =\ 2eI\,(1-\alpha). \tag{3.9}$$

This result was obtained for the single channel case by Khlus [153], Lesovik [161] and Yurke and Kochanski [162] and generalized to the multichannel case by Büttiker [163].

As can be seen in Eq. (3.9), the shot noise vanishes for $\alpha = 1$, what can be easily understood. At zero temperature the lead occupations do not fluctuate, this together with the perfect transmission make that the electron flow be noiseless. For intermediate transmissions the noise is reduced in comparison with the Poisson limit because the electron are correlated due to the Pauli principle. In the tunnel limit ($\alpha \ll 1$) the transmitted electrons are uncorrelated in time and the Poisson noise ($S_{Poisson} = 2eI$) is recovered.

For the general case of finite voltage and temperature the noise is a mixture of thermal and shot noise which is given by

$$S = \frac{4e^2}{h}\left\{2k_BT\alpha^2\ +\ \alpha(1-\alpha)eV\coth(\frac{eV}{2k_BT})\right\}. \tag{3.10}$$

This result has been obtained in Refs. [153, 164, 165].

Now, we introduce a simple handwaving argument which will help us to understand better the noise results. Everybody knows how the electronic transport takes place in a N-N contact. The current is due to transfer of electrons through the interfase, whose statistic and charge are very well known. When an electron approach the interfase two things can happen: either the electron crosses the barrier, with probability α, or the electron does not cross the barrier, with probability $1 - \alpha$. In this sense, one can see the current as a random variable which has a binomial distribution. With this idea in mind we shall obtain the current fluctuations.

First of all, let us remember a well-known result. Every conducting channel sustains a current density per spin equal to (e/h). This is a consequence of the cancellation between the group velocity and the density of states of the system (see Ref. [72] pag. 105). On the other hand, the total current is the difference between the current in both directions (see fig. 3.1):

$$\hat{I} = \hat{I}_{L\to R} - \hat{I}_{R\to L}. \tag{3.11}$$
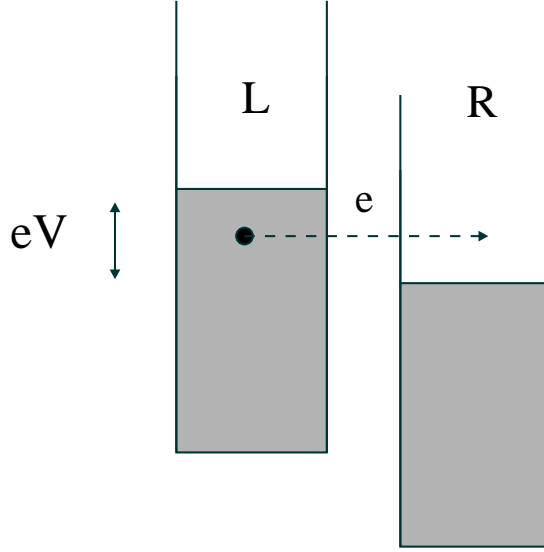
Figure 3.1: Schematical representation of tunnel processes in N-N contacts.

With the argument of the previous paragraph, both currents can be considered as random variables with binomial distributions. To be concrete, the current densities per spin $dI/d\omega$ are distributed as follows

$$\frac{d\hat{I}_{L \to R}}{d\omega} = \begin{cases} e/h & \text{with probability} \quad \alpha f_L(1 - f_R) \\ 0 & \text{with probability} \quad 1 - \alpha f_L(1 - f_R) \end{cases} \qquad (3.12)$$

$$\frac{d\hat{I}_{R \to L}}{d\omega} = \begin{cases} e/h & \text{with probability} \quad \alpha f_R(1 - f_L) \\ 0 & \text{with probability} \quad 1 - \alpha f_R(1 - f_L) \end{cases} , \qquad (3.13)$$

where $f_{L,R}$ are the Fermi functions of the reservoirs [1].

As we are interested in the analysis of the shot noise, we shall concentrate in the zero temperature case, thus $\hat{I}_{R \to L} = 0$. The current is then the mean value of the distribution (3.12) summed over the energies involved, i.e.

---

[1] The origin of these distributions can be easily understood. For instance, the distribution $\frac{d\hat{I}_{L \to R}}{d\omega}$ can be understood as follows. An electron approaching the interfase from the left electrode gives a contribution to the current density equal to e/h with a probability equal to the product of the probability of this state being occupied (f_L), the probability of crossing the barrier (α) and the probability of finding an empty state in the right electrode ($1 - f_R$).

$$< \hat{I} > = \int_{E_F}^{E_F + eV} d\omega \; \langle \frac{d\hat{I}_{L \to R}}{d\omega} \rangle = \frac{2e\alpha}{h} V, \qquad (3.14)$$

where the factor 2 comes from the sum of spins.

In the same way, the shot noise, which is basically the second distribution moment, will be the variance of a binomial random variable:

$$< \hat{I}^2 > - < \hat{I} >^2 = \int_{E_F}^{E_F + eV} d\omega \; \langle \frac{d\hat{I}_{L \to R}^2}{d\omega} \rangle - \langle \frac{d\hat{I}_{L \to R}}{d\omega} \rangle^2 = \frac{4e^2}{h} eV \, \alpha(1 - \alpha). \quad (3.15)$$

Result in agreement with Eq. (3.9).

This simple argument allow us to understand a little better the shot noise expression. Indeed, we have learnt that such expression is due to the fact that the electrons are fermions and there is only a type of current carriers. As we shall see below, in the superconducting case the situation is more complex because there exist the possibility of transfer multiple charges. Finally, this handwaving argument also gives the general result of Eq. (3.10) for finite temperatures. The rigorous derivation of the transmitted charge distribution function in a normal conductor can be found in Ref. [166].

3.2 Shot noise in a N-S contact

As in a N-N contact, in this case the noise given by Eq. (3.6) is time independent. In this section we shall concentrate in the results for zero temperature. The aim of this section is to study this simple case where there is a superconducting electrode involved, which allow us to gain some insight into the general S-S case.

As commented in section 2.3, in the N-S there are two types of processes contributing to the current (see Fig. 3.2): quasiparticle processes in which an electronic charge e is transmitted and can only take place at voltages $eV \geq \Delta$ (for zero temperature). On the other hand, also Andreev reflections occur where a Cooper pair is transmitted. This latter process can take place at any voltage. The shot noise can be expressed in terms of the probabilities of these processes, T_N and R, whose expressions are given by Eq. (2.27). The shot noise for arbitrary bias voltage adopts the form

$$S = \frac{4e^2}{h} \int_0^{eV} d\omega \; \{4R(\omega)(1 - R(\omega)) + T_N(\omega)(1 - T_N(\omega)) - 4R(\omega)T_N(\omega)\} . \quad (3.16)$$

This result is in agreement with Refs. [153, 156]. Fig. 3.3 shows the shot noise as a function of voltage for several normal transmissions. For comparison the current
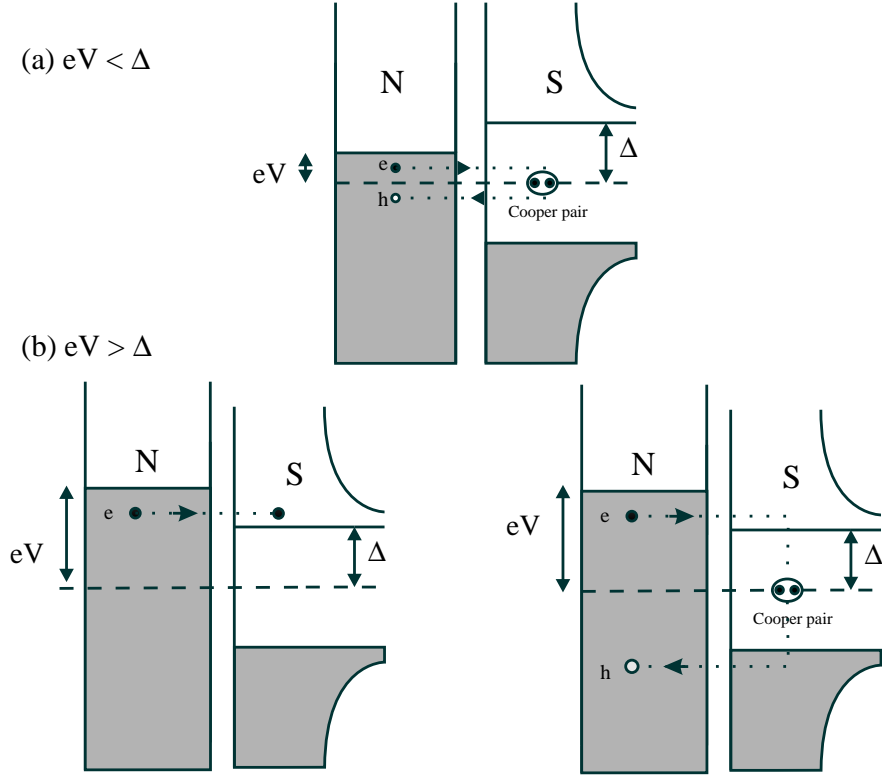
Figure 3.2: Current processes in a N-S contact. Panel (a) shows the Andreev reflection, which is the only process for subgap voltages at zero temperature. For $eV \geq \Delta$ single quasiparticle processes can also take place (left panel (b)).

for the same transmissions is also shown in this figure. Before commenting the main features of this figure we shall analyze analytically some limiting cases.

For subgap voltages ($eV < \Delta$) the only process which contributes to the current is the Andreev reflection, thus Eq. (3.16) reduces in this case to

$$S = \frac{16e^2}{h} \int_0^{eV} d\omega \; R(\omega)(1 - R(\omega)) \; ; \; eV \leq \Delta. \tag{3.17}$$

This expression can be written explicitly in terms of the normal transmission coefficient α as

$$S = \frac{64e^2}{h} \Delta \frac{\alpha^2(1-\alpha)}{(2-\alpha)^4} \int_0^{eV/\Delta} dz \; \frac{1-z^2}{\left[1 - \frac{4(1-\alpha)}{(2-\alpha)^2}z^2\right]^2}. \tag{3.18}$$
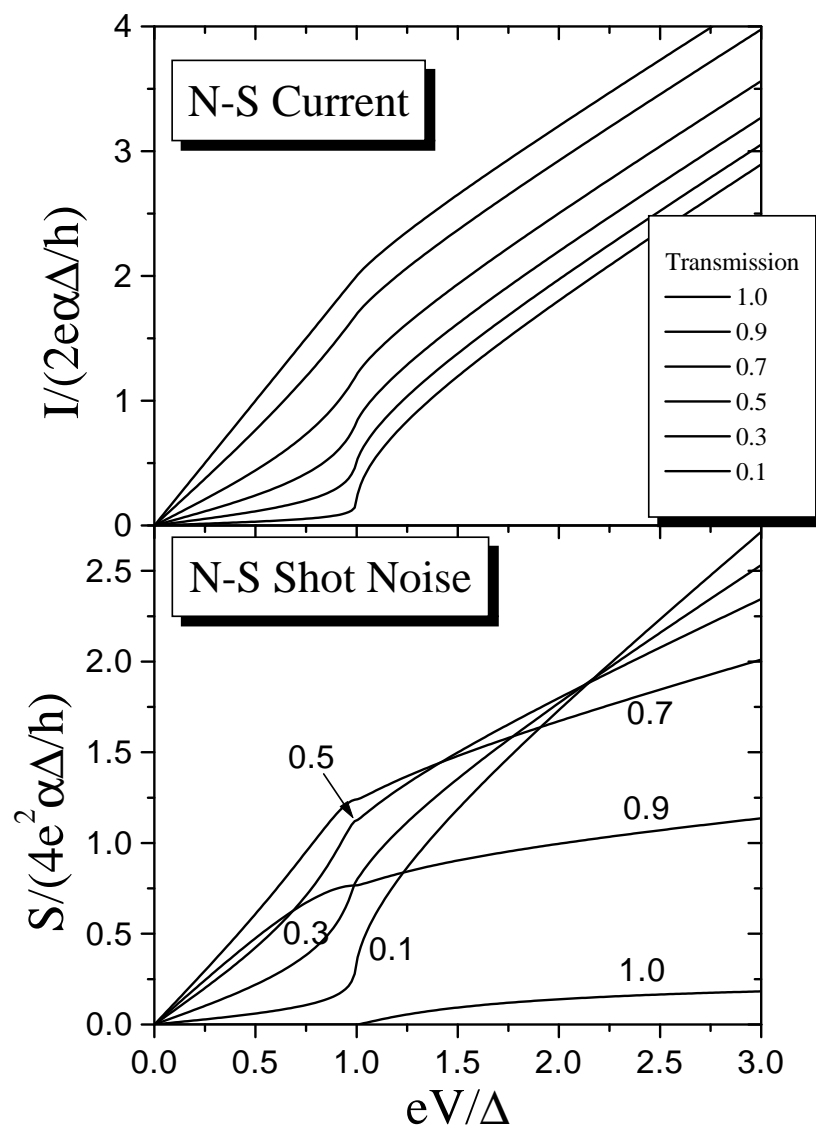
Figure 3.3: Shot noise and current in a N-S contact at zero temperature as a function of the voltage for several transmissions.

In the linear regime ($eV \ll \Delta$) this expression yields

$$S = \frac{64e^2}{h} \frac{\alpha^2(1-\alpha)}{(2-\alpha)^4} V. \tag{3.19}$$

This result has been obtained in Ref. [154] for the multichannel case [2].

For voltages $eV \geq \Delta$, both quasiparticle and Andreev processes contribute to the current and the shot noise is given by the full Eq. (3.16). The contribution of energies outside the gap can be written explicitly in terms of the normal transmission as

$$S_{out} = \frac{8e^2}{h} \alpha \Delta \int_1^{eV/\Delta} dz\, \frac{(2-\alpha)z\sqrt{z^2-1} - \alpha(z^2-1)}{\left[\alpha z + (2-\alpha)\sqrt{z^2-1}\right]^2}. \tag{3.20}$$

Another interesting feature showed by the noise is the *excess noise* which appears at large voltages ($eV \gg \Delta$), i.e at voltages much larger than the gap the N-S noise adopts the expression

$$S(eV \gg \Delta) = \frac{4e^2}{h} eV \alpha(1-\alpha) + S_{exc}, \tag{3.21}$$

where S_{exc} is a function of the normal transmission illustrated in Fig. 3.4. As can be observed is a non-monotonous function. In particular, when $\alpha = 1$ the excess noise reaches the value $(2/5)eI_{exc}$.

Once we have shown different analytical limits, we go back and remarking some of the shot noise features which appear in Fig. 3.3. In particular, we shall pay special attention to two characteristics: first, as can be observed, in the tunnel limit the shot noise is similar to the current. This is due to that in this case we are in the Poissonian limit and the shot noise is simply proportional to the current, being the carriers charge the proportionality constant (we shall show below this charge). Second, notice that the shot noise for perfect transmission vanishes inside the gap, while this does not happen outside. This can be understood as follows. Inside the gap the Andreev reflection is the only contributing process (see Eq. (3.17)). For $\alpha = 1$ one has $R = 1$ and the shot noise vanishes as a consequence of Pauli principle. However, for $eV > \Delta$ There are two processes contributing whose probabilities sum one ($T_N + R = 1$) for $\alpha = 1$. The shot noise expression then reduces to

$$S = \frac{4e^2}{h} \int_\Delta^{eV} d\omega\, R(\omega)(1 - R(\omega)), \tag{3.22}$$

---

[2]It is easy to calculate the integral appearing in Eq. (3.18) for arbitrary subgap voltage, but the analytical result is awful looking and we do not write it here.
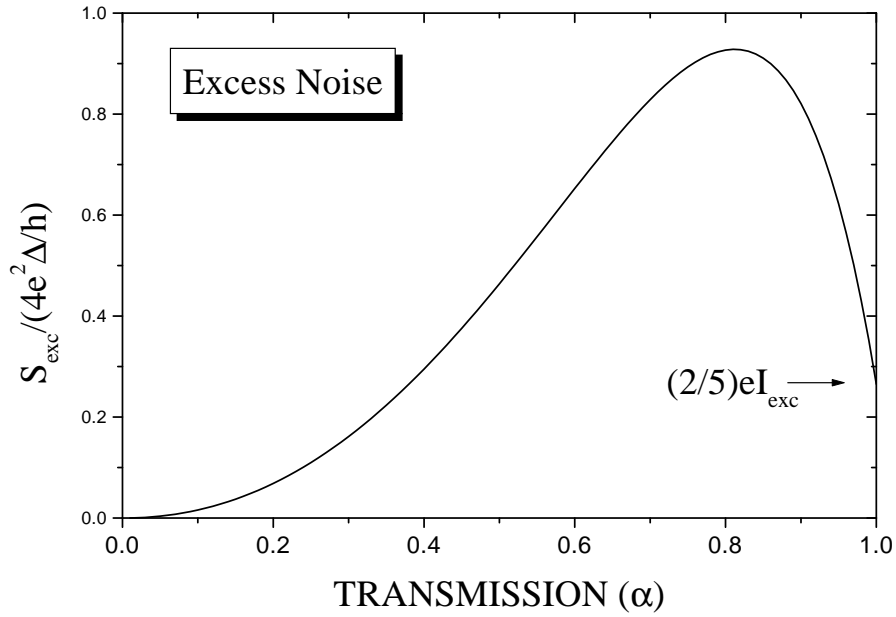
Figure 3.4: Zero temperature excess noise as a function of transmission in a N-S contact.

which does not vanishes because Andreev reflection has a probability less than one outside the gap.

As commented in the introduction, the shot noise provides information on the charge of the electrical current carriers. In particular, in the Poisson or tunnel limit the noise is proportional to the current $S_{Poisson} = 2qI$, where q is the charge of the uncorrelated carriers. Fig. 3.5 shows the effective charge, defined as $q = S/2eI$, as a function of voltage for different transmissions. It is worth noticing that in the tunnel limit (see curve $\alpha = 0.1$) this charge is equal to $2e$ inside the gap and equal to e for voltages greater than Δ. This is due to the fact that in an Andreev reflection a Cooper pair is really transmitted and that for $eV \geq \Delta$ the transport is dominated by single electron processes. As can be seen, for intermediate transmissions the effective charge is not well defined.

We finish this section generalizing the handwaving argument introduced in the previous section. At zero temperature the current distribution given by Eq. (3.12) can now be expressed as

111
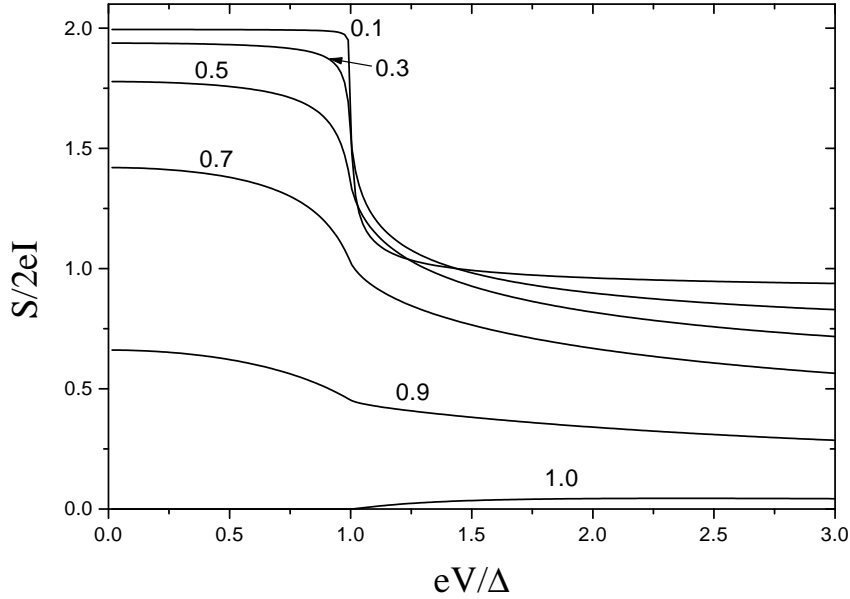
Figure 3.5: N-S zero temperature effective charge $q = S/2I$ in units of the electron charge as a function of voltage for different transmissions.

$$\frac{d\hat{I}_{L \to R}}{d\omega} = \begin{cases} 2e/h & \text{with probability } R; \ \omega \in [0, eV] \\ e/h & \text{with probability } T_N; \ \omega \in [\Delta, eV] \\ 0 & \text{with probability } 1 - R - T_N; \omega \in [0, eV], \end{cases} \qquad (3.23)$$

This expression indicates that the current is distributed binomially inside the gap, with carriers of charge $2e$, while it has a trinomial distribution outside the gap with carriers of both charges $2e$ and e. We can calculate the fluctuations with this distribution in a similar way we did in the N-N case, which leads to the general expression (3.16) for the shot noise. The rigorous calculation of the transmitted charge distribution function in a N-S contact was carried out by Muzykantskii and Khmelnitskii [155].

3.3   Shot noise and transfer of multiple charges in SQPCs

In this section we show the novel results of our work on the shot noise in a SQPC. We analyze how correlations among the multiple processes in a superconducting quantum

point contact are reflected in the noise. In particular, we pay special attention to the study of the charges transmitted in multiple Andreev reflections. From the analysis carried out in Chapter 2, it seems natural to infer that in MARs multiple charges are transferred. However, by no means it is obvious how these processes are reflected in the shot noise, since there no exist excitations of multiple charge in a superconductor. The question is whether we are going to observe correlations between Cooper pairs or if really the coherent transport of multiple charges takes place.

Fig. 3.6 illustrates the behavior of the the zero frequency dc component of the shot noise, S, as a function of V for different values of the normal transmission α. For comparison, the dc component of the current is also shown. As can be observed, the more noticeable features in the shot noise are:

1. The presence of a strongly pronounced subgap ($eV < 2\Delta$) structure, which persists up to transmissions close to one.

2. In the low transparency limit the shot noise subgap structure consists of a series of steps at voltages $eV_n = 2\Delta/n$ (n integer) as in the case of the dc current.

3. For higher transmissions there is a steep increase in the noise at low voltages.

4. For perfect transmission the shot noise is greatly reduced.

5. In the large voltage limit ($eV \gg 2\Delta$) there is an excess noise with respect to the normal case.

Before analyzing in detail the main features of the shot noise, let us have a look to the effective charge, $q(V) = S/2I$, with the aim of answering the question on the transmitted charge in a MAR. Fig. 3.7(a) shows the effective as a function of voltage for different transmissions. As can be seen, inside the gap ($eV < 2\Delta$) the shot noise can be much larger than the Poisson noise ($S_{Poisson} = 2eI$). As will be commented below, this is due to the occurrence of multiple Andreev reflections. In particular, we can see that as the tunnel limit is approached the effective charge tends to exhibit a step-like behavior and integer multiples of the electron charge can be identified. For larger transmissions $q(V)$ increases when the voltage decreases more smoothly and diverges as $1/V$ for small voltages.

Let us start by analyzing the low transmission regime. In this case we can make use of the sequential tunneling picture that we introduced to study the dc current in section 2.4. As was stated there, in the tunnel limit one can identify the probability R_n of the n-order MAR which gives the main contribution to the dc current when $2\Delta/n \leq eV \leq 2\Delta/(n-1)$. Let us recall that the dc current can be written in terms of these probabilities, given by Eq. (2.42), as
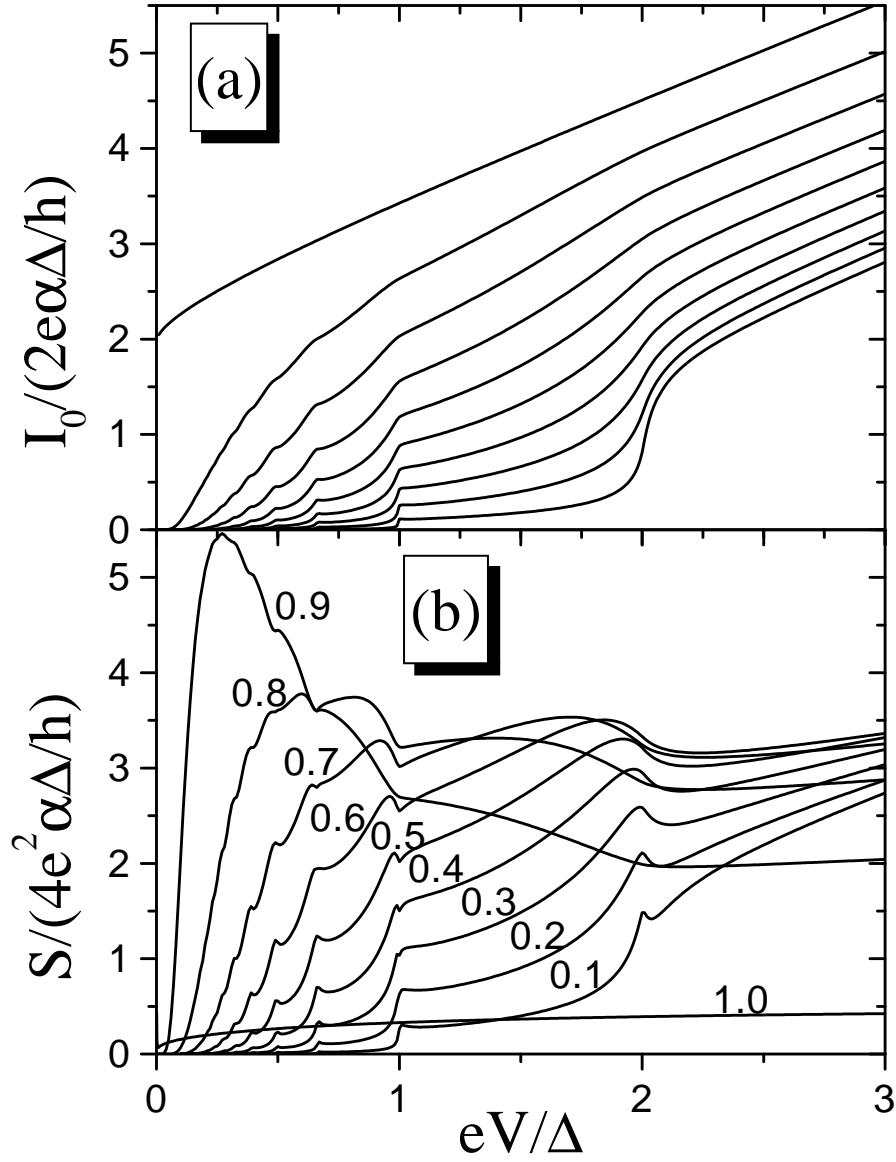
Figure 3.6: (b) Zero-frequency shot noise in a S-S contact as a function of voltage for different transmissions. (a) Dc current for the same transmissions as in the shot noise.
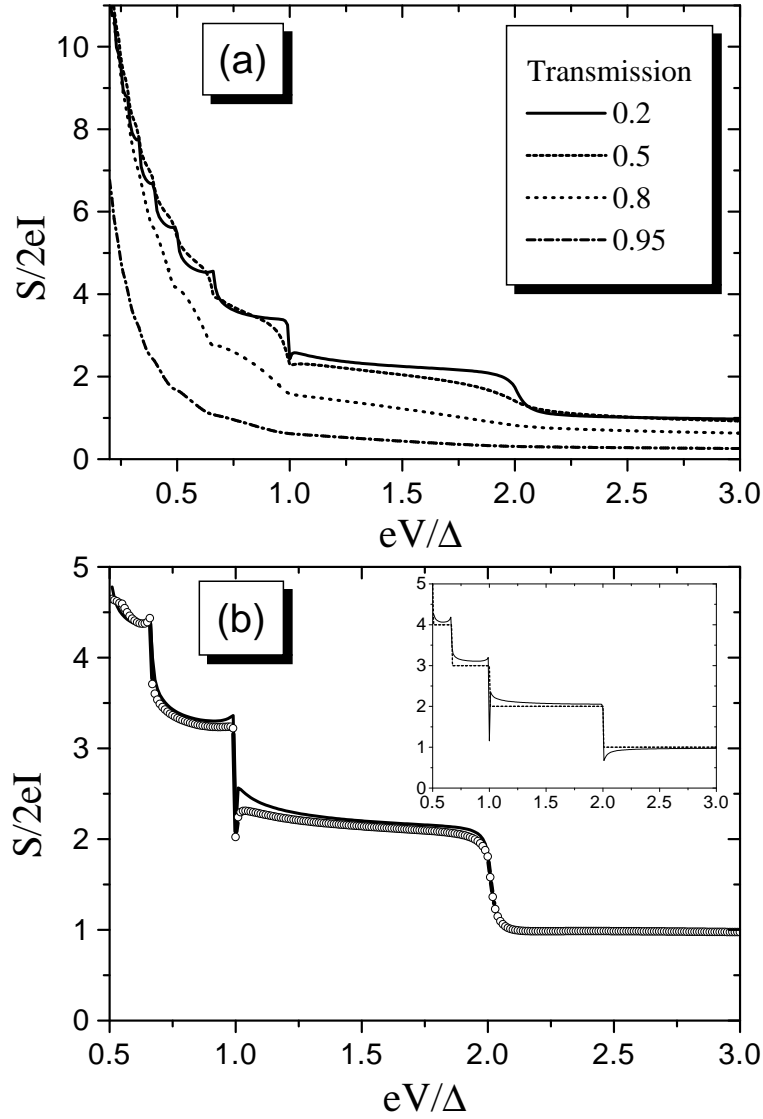
Figure 3.7: (a) Effective charge as a function of voltage for different transmissions in a S-S contact at zero temperature. (b) Comparison between the exact result (full line) and the tunnel approximation (open circles) given by Eqs. (3.24-25) for $\alpha = 0.1$. The inset shows the exact result (full line) for $\alpha = 0.01$ and the step-like function (dashed line) corresponding to the $\alpha \to 0$ limit.

$$I_0(V) = \frac{2e}{h} \int d\omega \sum_{n=1}^{\infty} n R_n(\omega, V). \qquad (3.24)$$

In terms of these R_n the shot noise in the tunnel limit can be expressed as

$$S = \frac{4e^2}{h} \int d\omega \left\{ \sum_{n=1}^{\infty} n^2 R_n - \left(\sum_{n=1}^{\infty} n R_n \right)^2 \right\}. \qquad (3.25)$$

This expression is easily understood with the handwaving argument which we introduced in previous sections. Indeed, the previous expression corresponds to the fluctuations of a random variable (the current) having a multinomial distribution. This indicates that in a S-S contact at a given voltage several MARs coexist transferring charges ne with a probability equal to R_n.

Eqs. (3.24-25) permit us to analyze the effective charge in the tunnel regime. As the transmission goes to zero the main contribution to the current at a given voltages comes from the lowest order Andreev reflection with non-zero probability. As can be shown from Eqs. (3.24-25), this implies that the effective charge show a step-like behavior described by the formula

$$\lim_{\alpha \to 0} q/e = 1 + Integer \left[\frac{2\Delta}{eV} \right]. \qquad (3.26)$$

This means that in the tunnel limit the charge is transferred in integer multiples of the electron charge, i.e. the charge is quantized. Thus, the previous result tell us that *in the tunnel regime one can isolate the n-order MAR, being its charge equal to ne*. Then, in this regime one has coherent tunneling of uncorrelated carriers with multiple charges.

The inset in figure 3.7(b) shows the effective charge for $\alpha = 0.01$ together with the step-like function of Eq. (3.26). It is also shown in this figure the comparison between the tunnel approximation given by Eqs. (3.24-25) and the exact result for a transmission $\alpha = 0.1$. Notice that even for this small transmission value there are deviations from the simple step-like behavior which are increasingly pronounced when the voltage is reduced. These deviations are produced by the contribution of more than one MAR process at a given voltage.

As commented in Chapter 2, as the transmission increases the sequential tunneling picture breaks down due to the interference between different processes which form a MAR. The charge quantization found in the tunnel regime progressively disappears and is eventually washed out when approaching perfect transmission. This is illustrated in Fig. 3.7(a).

The structure of the shot noise for intermediate transmission is a consequence of the competition between the noise reduction due to the Pauli principle and the

116

contribution of a increasing number of MARs with different charges, which tends to enhance the noise. Furthermore, there is an additional factor which complicates the analysis of the noise. As we know, in a S-S contact one has all the harmonics of the Josephson frequency in the current. These ac components also fluctuate in time and give a contribution to the dc component of the shot noise. This contribution is negligible in the tunnel limit but becomes more and more important when the transmission increases, specially at small voltages [3].

On the other hand, in the perfect transmission limit, the analysis is again simplified due to the absence of backscattering. Within our theory one obtains a simple expression for the shot noise in this limit

$$S = \frac{8e^2}{h} \int d\omega \left[\sum_{n=0}^{\infty} R_n (1 - R_n) \right] \left[1 + 2 \sum_{k=1}^{\infty} \prod_{l=1}^{k} |a(\omega + leV)|^2 \right], \qquad (3.27)$$

where R_n are the multiple Andreev reflection probabilities for perfect transparency given by $R_n(\omega) = \prod_{m=0}^{n} |a(\omega - meV)|^2$; $\omega \in [neV, (n+1)eV]$, where $a(\omega)$ is the Andreev reflection amplitude at an N-S interface given by Eq. (2.48). This expression can be shown to be equivalent to the result of Averin and Iman in Ref. [160]. The great reduction of noise that can be observed in Fig. 3.6 for perfect transmission is a consequence of having Andreev reflection probability equal to one inside the gap.

It is also interesting to analyze the large voltage limit. As in the N-S, the shot noise exhibits a excess noise with respect to the normal case,

$$S(eV \gg 2\Delta) = \frac{4e^2}{h} \alpha (1 - \alpha) V + S_{exc}, \qquad (3.28)$$

i.e. the shot noise of a normal contact with transmission α plus an excess noise S_{exc}. This excess has the same physical origin as the excess current (I_{exc}), which arises from the contribution of the lowest order Andreev process. One should remark that the approach to the asymptotic value is much slower for the shot noise than for the current. We obtain that at zero temperature S_{exc} is twice the excess noise of a N-S contact with the same transmission. Thus, the transmission dependence of the excess noise can be observed in Fig. 3.4. In particular, this relation yields $S_{exc} = (2/5)eI_{exc}$ for the perfect ballistic case in agreement with Ref. [159].

A word of caution should be said about the validity of this theory in the limit of extremely small bias voltage ($eV \ll \Delta$). As we explained in the previous chapter, in this limit the inelastic relaxation rate η plays also a role. This finite relaxation rate introduces a cut-off in the MAR processes which determines the behavior of current and noise when the voltage is smaller than η. The effect of this energy on the shot

---

[3]It is important to remark that in the results shown for the dc component of the shot noise we have computed all the contributions, no matter where they come from.

noise is specially important near perfect transmission. In order to illustrate its effect we show in Fig. 3.8 the shot noise for $\alpha = 1$ and different values of η in the small bias voltage limit. As can be observed, its effect is more important than in the case of the current and indicates that one has to take into account this relaxation energy for the correct determination of the transport properties at small voltages.
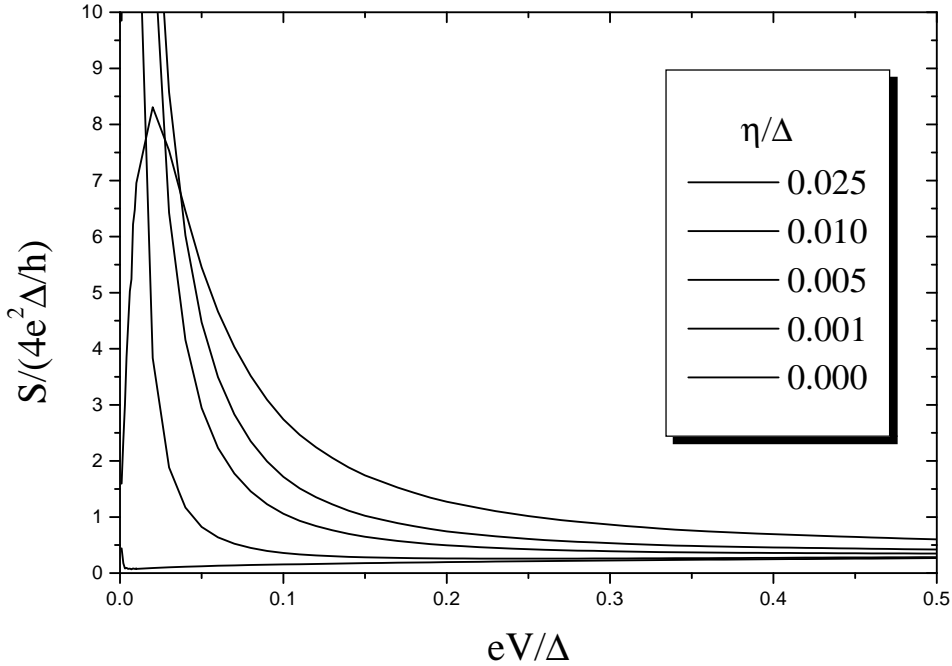
Figure 3.8: Shot noise for $\alpha = 1$ and different values of the energy relaxation rate η at small voltages. η increases from bottom to top.

In a recent experiment Dieleman *et al.* [158] observed for the first time a shot noise much larger than the Poisson noise in a S-I-S tunnel junction (NbN/MgO/NbN). The appearance of subharmonic gap structure in these tunnel junctions is due to the presence of pinholes in the oxide barrier which make that some channels have appreciable transmissions. As stated in the introduction, a detailed comparison between their experimental results and our theory is not possible because we unknow the distribution transmission. In the experimental results shown in Ref. [158] a mean transmission of $\alpha = 0.17$. If one compares the results for the shot noise and effective charge for these transmissions (see Figs. 3.6 and 3.7) with Figs. 4 and 5 of Ref. [158], a qualitative agreement can be observed. In particular, we reproduce the structure around $eV = 2\Delta$ in the shot noise and the continuous increase of the

effective charge as the voltage decreases. Although, the agreement is satisfactory, in order to investigate the experimental evolution of the shot noise with transmission it would be desirable to use more controllable systems like the atomic-size contacts of Refs. [143, 146]. Furthermore, the shot noise could be used to extract information on the transmission distribution of atomic contacts, in the same way it was done with the current [143].

In conclusion, we have analyzed theoretically the shot noise in a superconducting quantum point contact for arbitrary transmission and voltage. We have shown that:

- The shot noise can be much larger than the Poisson noise ($S_{Poisson} = 2eI$) due to the occurrence of multiple Andreev reflections in which multiple charges are transferred.

- The shot noise exhibits a subgap structure ($eV < 2\Delta$) which persists up to transmissions close to one.

- In the tunnel regime the subgap structure consists of a series of steps at voltages $eV_n = 2\Delta/n$ (with n integer), i.e. like in the current.

- In the tunnel regime the effective charge $q(V) = S/2I$ shows a step-like behavior where one can identified integer multiples of the electron charge. **In this limit one can isolate a n-order Andreev reflection and measuring its charge, being the result equal to ne.**

- For larger transmissions the charge is not well defined due to the mixture of MARs which transfer different charges.

- For $\alpha = 1$ the shot noise is greatly reduced because the Andreev reflections have probability equal to one inside the gap.

- Our theoretical results reproduce qualitatively the experimental results of Ref. [158]. However, a more quantitative comparison would require to do new experiments in more controllable systems like the atomic-size contacts, where a similar agreement as the one obtained for the current is expected.

119

Chapter 4

Resonant tunneling and Andreev reflections

4.1 Introduction

In the last decade the advances of the fabrication techniques in microelectronics have allowed the design of nanometric-size systems, in which the density of states is composed by a set of discrete levels whose mean spacing permits that they can be resolved. Examples of these systems are the semiconductor quantum dots (see [167] and references therein) and the metallic particles or islands [168, 169].

This chapter, based on Ref. [170], is devoted to the study of resonant tunneling through these kind of systems coupled to superconducting electrodes. The motivation for this analysis is double. First, we want to analyze how the superconducting transport studied so far is modified by the presence of a resonant transmission. On the other hand, this work will be a starting point for the understanding of several correlation phenomena in combination with superconducting transport. Thus, we intend to study Coulomb blockade and Kondo effect in various situation like quantum dots, impurities and metallic island with superconducting leads.

In the last years much attention has been paid to the analysis of charging effects in superconducting island where the gap is much greater than the mean level spacing [171, 172, 173, 174, 175, 176, 177, 178, 179]. Less attention has been paid to the case where the individual levels can be resolved [180, 181, 182]. In this chapter we shall concentrate in the latter situation where both leads are superconducting.

When one analyzes the superconducting transport through nanosystems as the ones mentioned before, there are many energy scales playing a role: superconducting gap, mean level spacing, charging energy, temperature, voltage, tunneling rates, etc. We shall analyze two cases where the mean level spacing is much greater than the superconducting gap. The following paragraphes are devoted to the description of

both situations.

In first place, we study the case of a recent experiment done by Ralph *et al.* [168]. In this work the authors could resolve the individual electronic states in the tunneling through nanometric Al particles weakly coupled to superconducting leads made also of Al (see Fig. 4.1(a)). In these particles of diameter $< 10\, nm$, the mean spacing of the single-particle levels, δ, is much greater than the superconducting gap Δ [1]. Moreover, the charging energy E_C is the greatest energy scale. As we shall show below, the theoretical analysis of this case is quite simple because of the huge charging energy together with the weak coupling with the leads make that only the quasiparticles processes contribute to the current.

In second place, we shall analyze the case of a larger coupling with the leads and smaller charging energies, where multiple Andreev reflections contribute to the transport. To be precise, we shall study how the subharmonic gap structure is modified by the presence of a resonant transmission. An ideal setup for exploring these effects would be one in which both the resonant level position and the coupling to the leads could be modified in a controlled way as in a normal artificial atom [167]. This situation is represented schematically in Fig. 4.1(b).

The rest of this chapter is organized as follows. In section 4.2 we present the model for analyzing resonant tunneling as well as the method used for solving it. In section 4.3 we analyze the electronic transport through metallic particles. Section 4.4 is devoted to the study of the subgap structure in the presence of a resonant transmission. In section 4.5 we summarize the conclusions of this chapter. Finally, in section 4.6 we make some comments on the future work and open problems related with the first part of the thesis.

4.2 Model for a resonant system

As stated in the introduction, a small quantum dot [2] connected to superconducting leads is characterized by the interplay of many different energy scales. In order to analyze in detail the basic phenomena that can be observed in the case of large mean level spacing $\delta \gg \Delta$, we shall restrict the present theoretical discussion to the simplest case where transport takes place through a single resonant level (we shall indicate below how to generalize the results to the multilevel case). For describing this physical situation we use a natural extension of the Hamiltonian formalism describe in Chapter 2. We shall describe the tunneling through a resonant level using the following model Hamiltonian

---

[1] Because $\delta \gg \Delta$, these Al particles do not show any feature of superconductivity.

[2] We use the term quantum dot for referring systems like semiconductor quantum dots, metallic islands, etc.

a)

b)
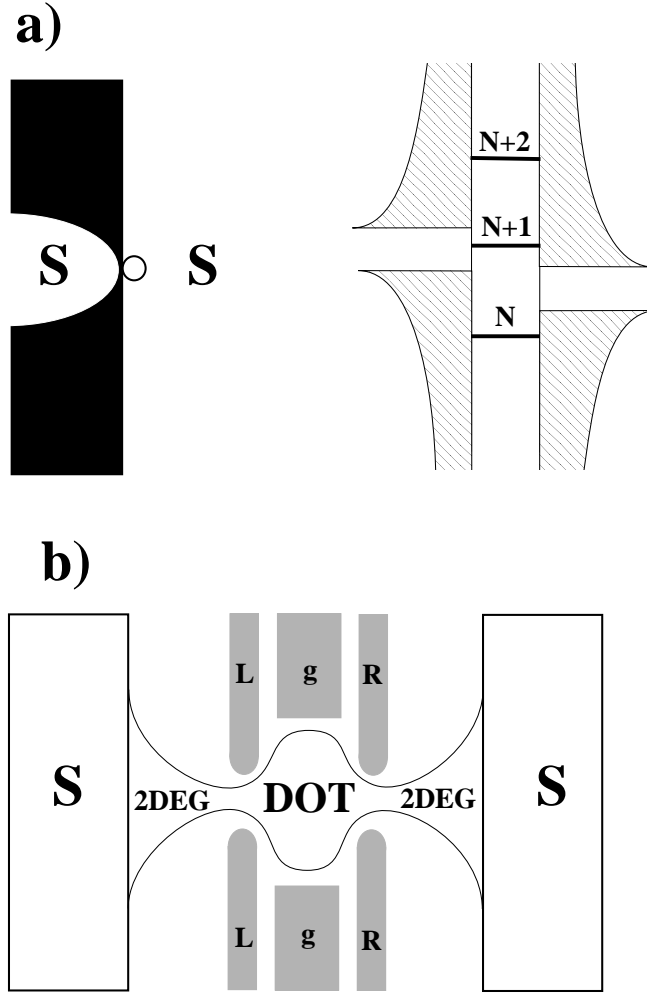
Figure 4.1: Schematical representation of the two situations studied in this chapter. (a) Tunneling through a metallic particle weakly coupled to superconducting leads. (b) Quantum dot defined in a 2DEG and coupled to superconducting leads. In the upper right hand side a typical scheme of the density of states in these systems is shown.

$$\hat{H} = \hat{H}_L + \hat{H}_R + \sum_{\nu,\sigma}(t_\nu \hat{c}^\dagger_{\nu\sigma}\hat{c}_{0\sigma} + t^\dagger_\nu \hat{c}^\dagger_{0\sigma}\hat{c}_{\nu\sigma}) + \sum_\sigma \epsilon_0 \hat{n}_{0\sigma} + U\hat{n}_{0\uparrow}\hat{n}_{0\downarrow}, \qquad (4.1)$$

where $\hat{H}_L$ and $\hat{H}_R$ are BCS Hamiltonians describing the left and right superconducting leads, characterized by a gap parameter $\Delta_L = \Delta_R = \Delta$; ϵ_0 is the bare resonant

level position, t_ν with $\nu = L, R$ are hopping parameters which connect the level to the left and right leads, and the U term describe the intralevel Coulomb repulsion in the quantum dot. This parameter is basically the dot charging energy, E_C, and is related to the total capacitance C by $U \sim e^2/2C$. On the other hand, for the subsequent discussion it is convenient to introduce the normal elastic tunneling rates $\Gamma_\nu = \pi|t_\nu|^2\rho_\nu(\mu)$, where $\rho_\nu(\mu)$ are the normal lead density of states at the Fermi level.

The Hamiltonian (4.1) is nothing but the Anderson Hamiltonian [183] which has been extensively used for studying the case of dots coupled to normal leads [184, 185, 110, 186]. This Hamiltonian together with Green functions techniques provide a suitable framework for analyzing the correlation due to electron-electron interaction in the quantum dot, which gives rise to phenomena like Coulomb blockade or Kondo effect. However, in the two situations that we are going to study in this chapter the correlation effects associated with the U term can either be neglected or taken into account in a simple way. The experimental situation of Ref. [168] corresponds to a case where $U \gg \Delta \gg \Gamma_{L,R}$. In this case double occupancy of the dot level is very unlike and this situation can be simply simulated by replacing the isolated dot Hamiltonian by a single nondegenerate effective level. The second situation that we shall analyze corresponds to a case where the coupling with the leads are not extremely small and the dot capacitance is large enough to smear out the Coulomb blockade effect ($\Gamma_{L,R} \sim U$). In this case the system behaves as if there were a single spin-degenerate resonant level at $\epsilon \simeq \epsilon_0 + U < n_0 >$, i.e. a restricted Hartree approximation on the U term would be reasonable.

With this mean field approximation the problem becomes an one-electron problem very similar to the one analyzed in Chapter 2. As we did in that chapter, in order to solve the model we shall use nonequilibrium Green functions techniques based on the Keldysh formalism. As it was shown in Chapter 2, these techniques allow us to obtain non-perturbative results valid for arbitrary coupling, so we can analyzed the two mentioned situations in an unified way. Due to the resemblance with the problem treated in Chapter 2 is not necessary to give further details on the formalism. Finally, as in the S-S case, the average current $I(\tau)$ contains all the harmonics of the Josephson frequency $\omega_0 = 2eV/\hbar$. In this chapter we shall concentrate in its dc part I_0.

4.3   Transport through metallic nanoparticles

Let us start reviewing the experimental results of Ralph *et al.* [168]. These authors studied the tunneling through Al particles of diameter < 10 nm coupled to superconducting electrodes. Fig. 4.2 (upper panel) shows the results for the current vs voltage for the case of a particle in which a charging energy $E_C \sim 6$ meV was

estimated, a mean level spacing $\delta \sim 0.7 \; meV$ and the resistances of the interfases with the electrodes were several $M\Omega$. In this situation the charging energy is much greater than the gap ($\Delta_{Al} = 0.18 \; meV$), moreover $\delta > \Delta$ and the levels can be resolved at a temperature $T \leq 2 \; K$ (the experiment was done at 320 mK). Finally, the estimated resistances indicate that $\Gamma_{L,R} \ll \Delta$.
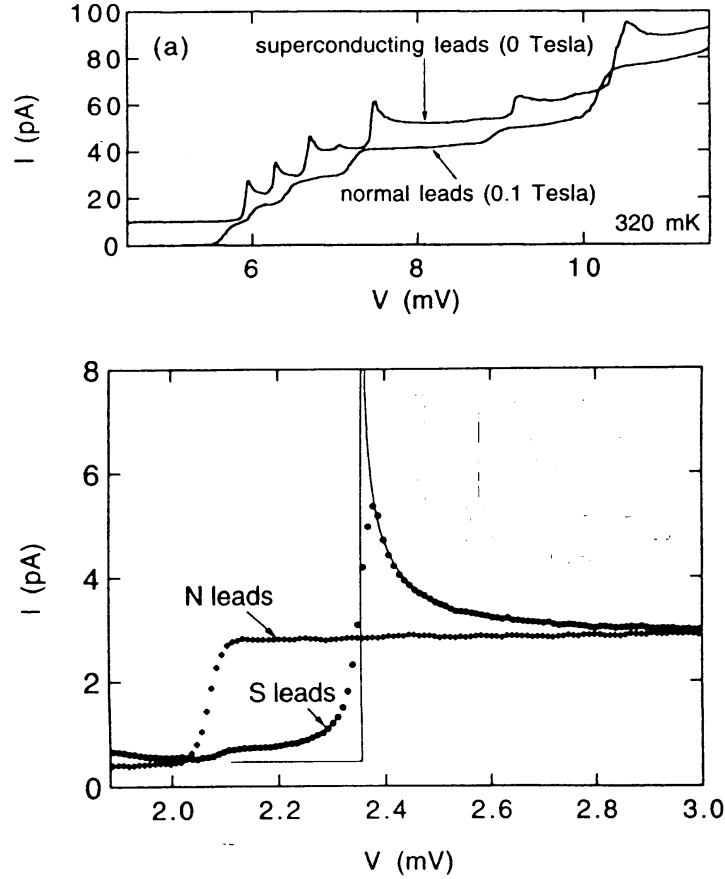
Figure 4.2: Upper panel: current through an Al particle coupled to normal and superconducting leads ($T = 320$ mK). The superconducting curve has been displaced 10 pA. Lower panel: current through a single electronic state at $T = 30$ mK.

Fig. 4.2 (upper panel) shows results for the cases in which the Al electrodes are in normal and superconducting states. In the normal case the current consists of a series of steps known as *Coulomb stair*, as expected in the tunneling via the electronic levels of the particle [187]. As the leads are in superconducting state the

I-V characteristics change dramatically. Each step moves at higher voltages with respect to the normal case and has a shape which reminds the BCS density of states. The detailed shape of these steps can be better observed in Fig. 4.2 (lower panel), where the tunneling through a single level in normal and superconducting cases is shown.

The theoretical analysis of this case is quite simple. Due to the huge charging energy ($E_C \gg \Delta$) and the weak coupling with the electrodes ($\Gamma_{L,R} \ll \Delta$), only the quasiparticle processes contribute to the current. This can be understood as follows. The weak coupling provokes that the probability of an Andreev reflection be very small. On the other hand, the charging energy destroys the Andreev reflection in two ways: first, the charging energy creates an additional gap between electrons and holes of the order of E_C, making that in this case the Andreev reflection be very unlike. Secondly, the charging energy provokes that the current vanishes until the voltage reaches $eV \sim E_C$, i.e. for voltages $eV \gg \Delta$, where the Andreev reflections give a negligible contribution. Thus, the dc current is given exclusively by the quasiparticle term which adopts the form of a resonant-tunneling-like expression

$$I_0(V) = \frac{4e}{h} \int_{-\infty}^{\infty} d\omega \, \frac{\Gamma_L^S(\omega - eV) \, \Gamma_R^S(\omega)}{(\omega - \epsilon)^2 + \left[\Gamma_L^S(\omega - eV) + \Gamma_R^S(\omega)\right]^2} \, \left[n_F(\omega - eV) - n_F(\omega)\right],$$

(4.2)

where $\Gamma_{L,R}^S$ are the superconducting tunneling rates defined as $\Gamma_{L,R}^S(\omega) = \Gamma_{L,R}\tilde{\rho}^S(\omega)$, being $\tilde{\rho}^S$ the corresponding dimensionless BCS density of states given by $\tilde{\rho}^S = |\omega|/\sqrt{\omega^2 - \Delta^2}$, and $n_F(\omega)$ is the Fermi function. In this expression ϵ is the effective resonant level position in which the charging effects have been included, i.e. $\epsilon = \epsilon_0 + E_C + \eta V$. This expression means that the effective level is renormalized by the charging energy. Moreover, this level moves with the voltage depending on the voltage drop in both junctions. In the previous expression η is the relative voltage drop which takes place in the left hand side junction: $\eta \equiv V_L/V = C_R/(C_R + C_L)$, where $C_{L,R}$ are the capacitances of both junctions.

In Fig. 4.3 is shown the dc current $I_0(V)$ given by Eq. (4.2) for decreasing coupling to the leads. The current has been normalized by $I_N = (4e\pi/h)\Gamma_L\Gamma_R/[\Gamma_L + \Gamma_R]$, which is the normal current at very large voltages. In this figure it is also shown the normal case corresponding to the superconducting case represented by the full line. This is the case that we have estimated corresponds to the experimental result of Fig. 4.2 (lower panel). As can be observed, there is a good quantitative agreement with that result. Moreover, notice that the line shape progressively resembles a BCS density of states. Another interesting feature is that the threshold voltage in the superconducting case is shifted with respect to the normal case. This is a simple consequence of that in order to have a non-zero current in the superconducting case, the voltage have to provoke that the lower edge of the left superconductor reaches
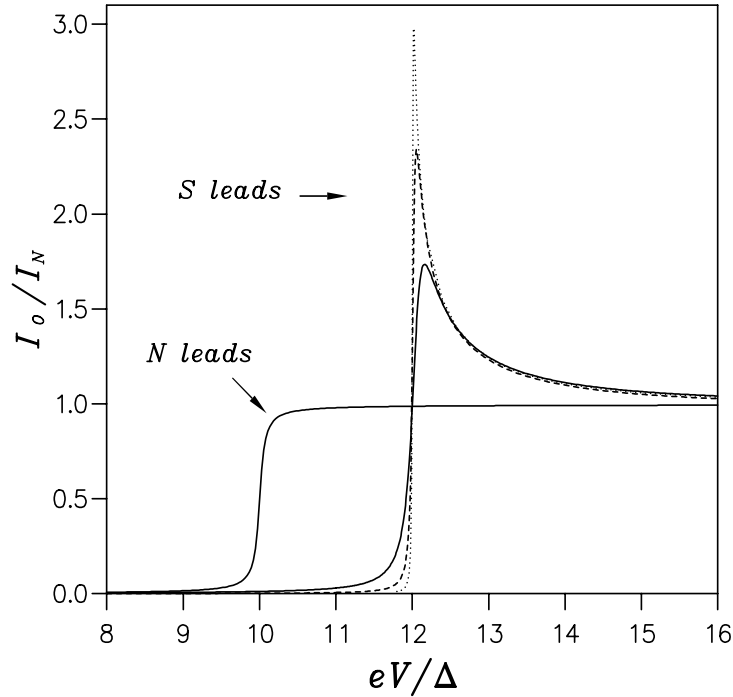
Figure 4.3: Zero-temperature I-V characteristics corresponding to the case of a metallic particle weakly coupled to superconducting leads (Eq. (4.2)). Full line: $\Gamma_L = 5 \times 10^{-3}\Delta$, dashed line: $\Gamma_L = 10^{-3}\Delta$ and dotted line: $\Gamma_L = 2 \times 10^{-4}\Delta$. In all cases $\Gamma_R = 4\Gamma_L$ y $\epsilon = 5\Delta$.

the resonant level [3].

In Ref. [168] special attention was paid to the behavior of the I-V characteristics near the threshold voltage, in particular to the broadening and reduced amplitude with respect to a BCS spectral density. In fact, our theory predicts a finite height and width of these resonances without having to resort to the introduction of any phenomenological broadening parameter. This is a simple consequence of having a small but finite coupling to the leads. Eq. (4.2) in the limit of vanishing coupling reduces to

---

[3]In Fig. 4.3 the superconducting threshold voltage is the normal one plus 2Δ because we have assumed that the voltage drops symmetrically in both interfases.

$$I_0(V) = \frac{4e\pi}{h} \frac{\Gamma_L^S(\epsilon)\Gamma_R^S(\epsilon)}{\Gamma_L^S(\epsilon) + \Gamma_R^S(\epsilon)}, \tag{4.3}$$

which coincides with the result one would expect from a sequential tunneling picture [188]. Thus, the coherent processes taken into account in Eq. (4.2) are responsible for the rounding off of the resonant peaks.

Let us also notice that in the case where $eV \gg \Delta$ the tunneling rate of the right junction reduces to the one of the normal case, what simplifies the expressions (4.2-3). It is also worth noticing that the expression (4.3) for the sequential tunneling limit is only valid for extremely small couplings.

For ending this section, let us make some comments about the generalization of our results for the transport in the multilevel case. Indeed, this generalization is quite simple. Several authors have developed a theory, referred to as *orthodox theory*, which describes the transport through quantum dots taking into account the charging effects by means of a simple classical argument [188, 189]. The description of the current is based on a sequential picture of the electronic transport, where the current is governed by a set of master equations. The generalization of this theory to the superconducting case is trivial. One has only to replace the normal scattering rates by the superconducting ones defined as in Eq. (4.2). This scheme has been recently carried out by Whan and Orlando [190] and we recommend to the reader to consult this reference for further details.

4.4   Resonant tunneling and Andreev reflections

In this section we concentrate in a case where the coupling is not so weak ($U \sim \Gamma_{L,R}$), so that the Coulomb blockade effects are absent. As discussed above, this case can be described by a single spin-degenerate effective level. In contrast to the previous case, now the effect of MAR's becomes crucial and the full formalism is needed for the calculation of the current.

To illustrate how the subharmonic gap structure (SGS) is modified by the resonant transmission we show in Fig. 4.4 the I-V curves for a symmetric case where the level position is fixed at $\epsilon = 0$, while $\Gamma = \Gamma_L = \Gamma_R$ varies between $\Gamma \gg \Delta$ and $\Gamma < \Delta$. As can be observed, in the limit $\Gamma \gg \Delta$ the case of a ballistic S-S junction is recovered (see chapter 2), where the main features are the absence of SGS and the saturation of the current for $V \to 0$ given by $I_0 \sim 4e\Delta/h$. The departure from the S-S behavior becomes apparent for decreasing Γ, where a progressively pronounced SGS appears. Notice that, in contrast to what is found in S-N-S structures with a continuum of states in the central region, in the present case the $I_0(V)$ curve *itself* exhibits oscillations with the concomitant appearance of negative differential con-
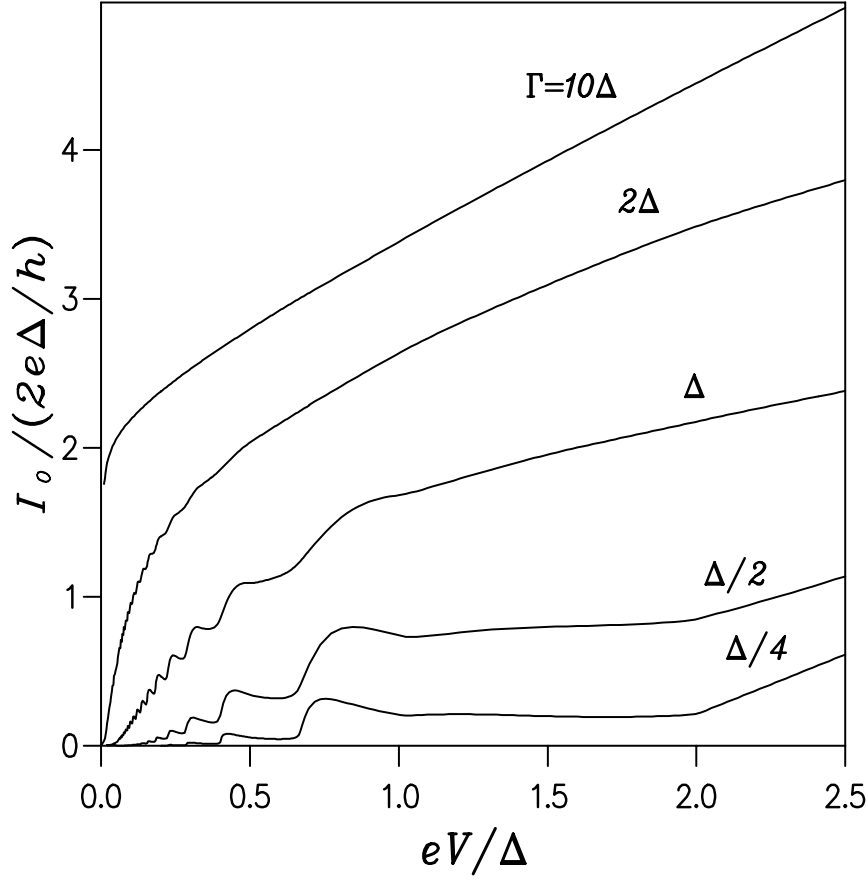
Figure 4.4: Zero-temperature I-V characteristics corresponding to the case where Coulomb blockade is absent for different values of $\Gamma = \Gamma_L = \Gamma_R$. The effective resonant level is fixed at $\epsilon = 0$.

ductance. It is also noticeable the disappearance of the subharmonic structure at voltages $eV = 2\Delta/n$ with even n.

The SGS found in this system is controlled by the resonant transmission. In fact, in the limit of $\Gamma \ll \Delta$ the position and shape of the subgap current peaks can be understood by means of the following simple picture. When $eV < 2\Delta$, current between the superconducting leads can flow due to MAR processes. As in the case of S-S or S-N-S junctions, there appear jumps in the subgap I-V characteristics at voltages corresponding to the opening of a new Andreev channel. However, the

amplitude of these subgap process is greatly modified by the presence of a resonant level between the leads, in such a way that only those MAR *trajectories* that connect the resonant level to the lead spectral densities give a significant contribution to the current. The inset in Fig. 4.5 illustrates the second order Andreev trajectory which gives the dominant contribution to the current when $2\Delta/3 < eV < \Delta$. As eV decreases towards $2\Delta/3$, the energies of the initial and final states on this trajectory approach the gap edges, which results in a BCS density-of-states-like shape of the current peak at $eV = 2\Delta/3$ (see Fig. 4.5(a)).
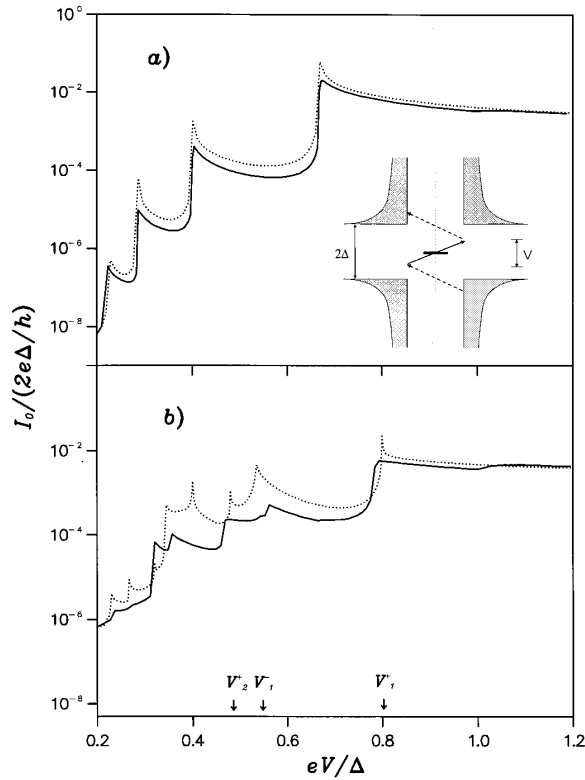
Figure 4.5: Detail of the subgap structure for $\Gamma = 5 \times 10^{-2}\Delta$ with $\epsilon = 0$ (a) and $\epsilon = 0.2\Delta$ (b). Full line: complete numerical calculation; dotted line: sequential approximation discussed in the text. The inset represents a typical resonant trajectory mediated by two Andreev reflections. The arrows indicate the position of the first resonances for $\epsilon = 0.2\Delta$.

This simple picture enables us to evaluate the SGS at $\Gamma \ll \Delta$ analytically. For this purpose we shall generalize the sequential picture for the multiple processes

introduced in Chapter 2. The first step is to identy the generalized tunneling rates $\Gamma_n^{(in)}(\omega)$ and $\Gamma_n^{(out)}(\omega)$ associated with the nth order Andreev process connecting the dot to the leads. Here the $\Gamma_n^{(in)}$ give the probability of an electron or a hole to get into the dot as an electron, while the $\Gamma_n^{(out)}$ correspond to the complementary processes where one electron leaves the dot and reaches the leads as an electron or as a hole. Within the sequential picture of these processes, the rates adopt for a symmetrical case $\Gamma = \Gamma_L = \Gamma_R$ the following expressions:

$$\Gamma_n^{(out,in)}(\omega) = \Gamma^{2n+1}\tilde{\rho}^S(\omega \pm (2n+1)eV/2) \prod_{j=1}^{n} \left| \frac{f(\omega \pm (2j-1)eV/2)}{\omega - (-1)^j\epsilon \pm jeV} \right|^2, \qquad (4.4)$$

where $f(\omega)$ is the dimensionless BCS pairing amplitude of the uncoupled leads defined as $f(\omega) = \Delta/\pi\sqrt{\Delta^2 - \omega^2}$. This expression can be understood as follows. First, $\Gamma^2|f(\omega)|^2$ is the Andreev reflection probability at the lowest order in Γ, while the denominator in Eq. (4.4) is related to the transmission probability through the dot. So that, the rates are simply the product of the probabilities of the elementary processes which form an multiple Andreev reflections. The total current can be then computed as the sum of the contributions due to all possible combinations of *in* and *out* processes. Every contribution must be weighted by the total charge which is transferred in the combined process. For instance, the process depicted as an inset in Fig. 4.5 is a combination of two processes of the first order and has an associated charge of $3e$. The resulting expression for the current is

$$I_0(V) = \frac{8e\pi}{h} \sum_{n,m} (n + m + 1) \frac{\Gamma_n^{(in)}(\epsilon)\Gamma_m^{(out)}(\epsilon)}{\Gamma_n^{(in)}(\epsilon) + \Gamma_m^{(out)}(\epsilon)}. \qquad (4.5)$$

Fig. 4.5 illustrates in further detail the SGS of the I-V curves for $\Gamma \ll \Delta$. For comparison the results given by Eq. (4.5) are also shown. As can be observed, this simple approximation fairly reproduces the exact numerical results in this small Γ limit. The rounding off of the peaks which is observed for increasing Γ in Fig. 4.4 is due to off-resonant processes as discussed for the case of large charging energy. In the limit $\Gamma \sim \Delta$ the sequential tunneling picture breaks down due to the interference among the different multiple processes.

For the general case with $\epsilon \neq 0$, the SGS becomes more complex due to the appearance of additional resonances. This is illustrated in Fig. 4.5(b) for the case $\epsilon = 0.2\Delta$ and $\Gamma = 5 \times 10^{-2}\Delta$. As can be deduced from the sequential formulae of Eq. (4.5), resonances appear both at $eV_n^+ = 2(\Delta+\epsilon)/(2n+1)$ and $eV_n^- = 2(\Delta-\epsilon)/(2n+1)$ corresponding to processes in which the initial or final states are at the gap edges (notice the disappearance of the even series in the SGS). The sequential picture also predicts the appearance of resonances at $jeV = 2\epsilon$ due to resonant coupling between

electron and hole states. In the exact numerical results the resonances are somewhat shifted with respect to these predictions and some of them are difficult to resolve. Nevertheless, it should be stressed that the main qualitative features of the exact SGS are already contained in Eq. (4.5).
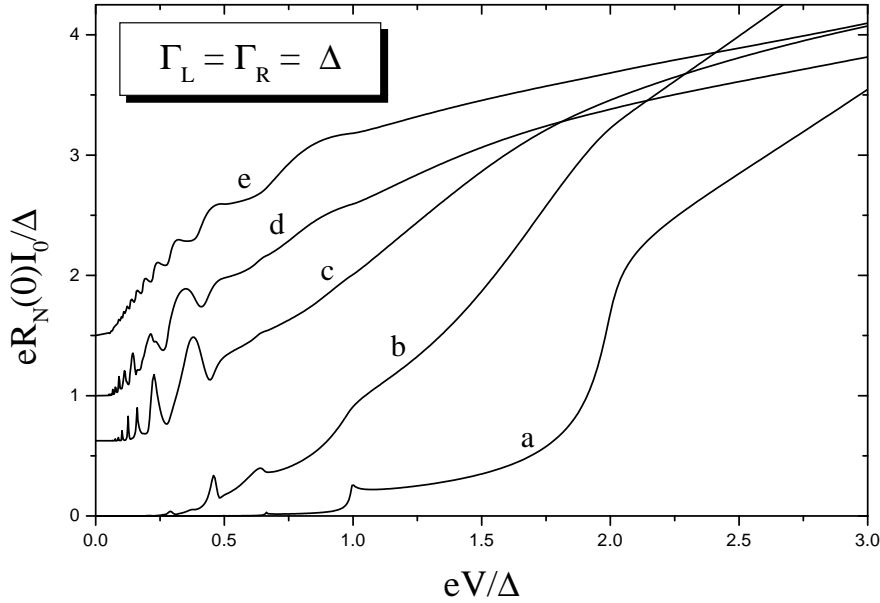
Figure 4.6: Zero-temperature I-V characteristics for different positions of the resonant level ϵ. (a) $\epsilon = 5\Delta$, (b) 2Δ, (c) Δ, (d) $\Delta/2$ and (e) 0. $R_N(0)$ is the normal resistance at the Fermi level. The curves (c), (d) and (e) have displaced for the sake of clarity.

Fig. 4.6 shows how the I-V characteristics evolve with the resonant level position ϵ. The tunneling rates are taken in this case as $\Gamma_L = \Gamma_R = \Delta$. As can be observed, when the level is far from the gap region (case a) the limit of energy independent transmission is recovered (see Fig. 2.6). As the resonant level approaches the gap region the subgap structure becomes progressively distorted with respect to the energy independent transmission case. While the structure corresponding to the opening of odd-order MAR processes is enhanced, the structure at $eV \sim 2\Delta/n$ with even n is suppressed. A detailed analysis of the I-V characteristics as a function of the resonant level position can be found in recent works [191, 192, 193].

As has been already mentioned, an ideal experimental setup to study the interplay between resonant tunneling and MAR's would be an *artificial atom* with

superconducting leads as represented in Fig. 4.1. In this type of structure, for a quantum dot area of $\sim (100nm)^2$, the mean level spacing would be around $2.7meV$ [194], which is much larger than the superconducting gap on the leads if these were made of Al ($\Delta_{Al} \sim 0.18meV$). On the other hand, the coupling to the leads could be given any desired value by varying the conductance of the two point contacts, and the charging energy could also in principle be changed by varying the different capacitances between the dot and the surrounding metallic leads and gates. Thus, the conditions for observing this regime could be attainable. In fact, a system of these characteristics would not be very different from the superconducting quantum point contacts developed by Takayanagi *et al.* [91].

4.5 Conclusions

In conclusion, in this chapter we have presented calculations for the electronic transport through discrete resonant levels coupled to superconducting leads. Firstly, we have analyzed the case of large dot charging energy and weak coupling with the electrodes. In this case the only contribution to the current comes from quasiparticle tunneling processes. The results that we have obtained naturally explain the I-V characteristics of the experiments in Al nanoparticles of Ref. [168].

The main part of this chapter has been devoted to the analysis of a situation in which the Coulomb blockade effect is absent. In this regime we have shown how the subgap structure is modified by the presence of a resonant transmission. One of the most remarkable features is the appearance of regions with negative conductance. Furthermore, we have shown that in the weak coupling limit the SGS can be described within a sequential picture for the multiple Andreev reflections. Finally, we have discussed the experimental conditions that should be met in order to observe this regime.

4.6 Future and open problems

With respect to the future and open problems related with the first part of the thesis, there are a lot of remaining challenges both from the experimental and the theoretical point of view. Let us first review some of the unsolved experimental problems.

Probably, the main experimental challenge in the superconducting electronic transport is the small bias voltage limit, and in particular the zero-voltage case. For instance, in the atomic contacts the critical current is smaller than the predicted one [74, 85, 86]. This discrepancy can be due to that in these experiments one does not measure the critical current strictly but the switching current, as we commented

in section 2.4.3. We expect that a similar analysis to the one developed in Ref. [141] for tunnel junctions gives us the solution of this problem.

With respect to the supercurrent-phase relation, the experiment of Koops *et al.* [138] showed for the first time a relation which deviated from the usual $I_S(\phi) \sim \sin \phi$. However, the agreement with the theory was not totally satisfactory, specially because they had not a method for determining the transmission distribution of the atomic contact. However, thanks to the channel spectroscopy introduced by Scheer *et al.* [143], we believe that one could now carry out a definitive comparison between experiment and theory.

Within the small bias voltage regime, an experimental determination of the linear conductance $G(\phi)$ is still lacking. As we commented in Chapter 2, this conductance could manifest in the analysis of the switching current or in a more direct way as in the experiment by Rifkin and Deaver [42].

Another pending issue is the direct observation of the Andreev bound states which carry the supercurrent in a superconducting contact. With respect to this point, in the Appendix D we propose a method for determining them by means of the analysis of the supercurrent under a microwave radiation. The coupling of the supercurrent to a microwave laser field gives rise to an induced current whose frequency dependence shows clearly the existence of the Andreev bound states (see Appendix D for details).

Another experimental challenge is the analysis of biased voltage contact under a laser radiation. Such radiation gives rise to the appearance of the well-known *Shapiro steps*. As we commented in section 2.4.2, in the case of a transmissive junctions would appear new steps with respect to the tunnel case. This is due to the possibility of multiple processes. On the other hand, this would be a way of revealing the ac current components and checking our predictions for such components.

With respect to the analysis of Chapter 3, the shot noise measure in an superconducting atomic contact is a nice experimental challenge and, in particular, the possibility of detecting the transfer of multiple charges associated with the Andreev reflections.

With respect to Chapter 4, it would be worthy to investigate experimentally situations in which the superconducting transport is modified by the presence of a resonant transmission, by charging effects or by electron correlations. In other words, it would be important to analyze the resonant tunneling, Coulomb blockade and Kondo effect in quantum dots coupled to superconducting leads. As we explained in previous sections, a semiconductor 2DEG is the ideal system to study these effects.

From the theoretical point of view there are a lot of remaining tasks. In the following paragraphs we shall remark some of the future projects which would be worthy to face.

In Chapter 2 we have developed a theory for the so called superconducting quan-

tum point contacts, where the constriction length is much smaller than the super-conducting coherence length. The following step would be to generalize the theory to the cases of contacts with arbitrary length, where the proximity effect play an essential role. Some steps toward this aim have already been done [195]. We also have started this projects by analyzing how the subharmonic gap structure is modified by the presence of a normal constriction whose length is comparable to the superconducting coherence length of the leads. This has been done in relation with the experiments in Al-Au-Al atomic contacts investigated by Scheer *et al.* [145, 146].

Within the analysis of SQPCs carried out in Chapter 2, there still remains the detailed study of the small bias voltage regime. In this case is difficult to satisfy experimentally the condition of constant voltage, as we have assumed throughout our analysis. Therefore, we must also study the case of a current biased contact.

It would be also interesting to analyze theoretically the Shapiro steps in a superconducting quantum point contact. We must still investigate how the ac current components manifest in such steps.

On the other hand, it would be also worthy to analyze how the subgap structure is modified by the presence of magnetism, for instance in a S-F-S quantum point contact, where F is a constriction of a ferromagnetic material. In this case the spin symmetry is broken and this modifies the Andreev reflections, because these processes couple electrons and holes with opposite spins.

In relation with the work presented in Chapter 4, there are two interesting future projects. First, it would be very interesting to analyze a situations where charging effect begin to modify the subharmonic structure. Secondly, the study of the Kondo effect in a quantum dot with at least a superconducting electrode would allow us to understand how electron correlations modify the superconducting transport. In principle, our Hamiltonian approach is well-adapted for these two projects and within our group there is great experience in this type of problems [110].

Finally, we also intend to take advantage of the experience acquired in the contacts of traditional superconductors for investigating the electronic transport in high temperature superconductors.

Part II

Electronic transport in atomic contacts

Chapter 5

Transport in atomic contacts: Introduction

During the present century they have been answered some of the fundamental questions about the elementary particles which form the matter. Although, we know that atoms are the basis of the solids since many decades ago, until recently it seemed a dream to be able to "see" the atoms or to manipulate them individually to form electronic devices. However, nowadays they are common practices in the nanotechnology laboratories all over the world. This great change is mainly due to the appearance in the eighties of the Scanning Tunneling Microscope (STM) [73]. This ingenious device consists of a metallic tip, attached to a piezoelectric, which approaches a surface also conducting. The distance between the tip and the surface is controlled by the piezo. When one applies a potential difference between the tip and the surface a current flows which allows us to obtain information on such surface. The most remarkable feature of this technique is that it permits to "see" the surface in situ, exploring defects, absorbates, etc. The STM was the first spectroscopic technique with spatial resolution which permitted to analyze atomic systems. Moreover, it opened the door to the manipulation of atoms, the design of atomic and molecular circuits, the study of mechanical properties at a nanometric scale and many other applications.

The STM and similar techniques obtain information on the systems investigated by means of a measure of the electrical current which flows through them. Thus, it is crucial to know how this current flows. So then, the objective of the part II of the thesis is the theoretical study of the electrical conduction through metallic atomic-size contacts. We are not concerned with the analysis of the Scanning Tunneling Microscope, whose theory is relatively well-established, but to know how the electronic transport takes place through metallic contacts with minimum sections of just a few atoms. Motivated by the questions that arose in relation with the experimental comparison of the superconducting I-V curves in atomic-size contacts

(see section 2.5.3), we endeavor to understand in these *atomic circuits* the relation between the electrical current and the quantum properties of the atoms forming such circuits.

This of the chapter is organized as follows. In section 5.1 we shall review some of the most important features of the electronic transport in atomic contacts and we shall emphasizing some of the open problems. Finally, section 5.2 is devoted to the presentation of our aims for the part II of thesis.

5.1   Historical review

We begin our historical review in the moment of the appearance of the Scanning Tunneling Microscope (STM) in 1981 [73]. The operation principle of the STM is rather simple as we commented in the introduction. It consists of a metallic tip which explores a surface typically at constant tunnel current (see Fig. 5.1). The displacements of the metallic tip given by the applied voltages to the piezos thus yield a topographic picture of the surface. The great STM resolution lies in the strong dependence of the tunnel current with the distance between the electrodes, i.e. between the metallic tip and the surface to be explored. This technique offered for the first time the possibility of determining the structure of a surface in real space, including non-periodic structures. Thus, it offers the possibility of observing in a direct way dislocations, defects, absorbates, etc, located on the surface.

The first quantitative theory of the STM was presented by Tersoff and Hamann in 1983 [196]. The main conclusion of this work was that the STM images at low voltages, or in short the current in the STM, is a measure of the sample local density of states at the Fermi level in the position of the tip. Then, an STM image is basically a spatial map of the surface electronic structure.

In the later years there appeared a great amount of experimental and theoretical works related with the STM. Let us mention here the theoretical works by Lang [197, 198] in which he analyzed the images of individual atoms absorbed in a metallic surface. His main conclusion was that the crucial parameter for determining the apparent height of an atom in a STM image at low voltages are the s and p densities of the absorbate at the Fermi energy.

Traditionally the STM has been used in the regime known as *tunnel regime*, in which the tip and the surface are kept apart, separated by a distance (~ 10 Å) which implies that the current depends exponentially on such a distance. In 1987 Gimzewski and Möller [199] analyzed the transition from tunnel regime to contact regime, in which the the tip and the surface "touch each other". These authors found that in this latter limit there are important corrections to the simple exponential behavior of the contact resistance as a function of the distance. Moreover, they found that the contact regime appears together with a mechanical instability which
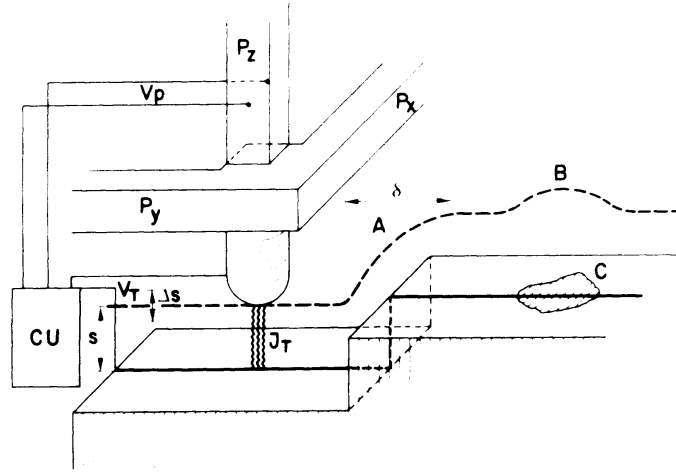
Figure 5.1: Operation principle of a Scanning Tunneling Microscope. The piezos P_x and P_y move the metallic tip M above the surface. The control unit applies an appropriate voltage V_p to the piezo P_z to have a constant tunnel current J_T at a given constant voltage V_T.

marks the transition between both regimes. Several authors, Lang [200] and Ferrer, Martín-Rodero and Flores [123] discussed this transition and found that at very short distances the current saturates at a certain value. In particular, Ferrer *et al.* [123] showed that in the case of one-atom contact (with only one orbital per atom) the resistance saturates at a constant value $h/2e^2 \sim 12.9k\Omega$, which is referred to as the *quantum resistance*.

Let us abandon for a moment the context of atomic contacts and speak about a fundamental phenomenon in our subsequent discussion. In 1988 there appeared two independent experimental works which investigated the conductance of a ballistic point contact defined on a two-dimensional electron gas (2DEG) of great mobility in heterostructures GaAs-AlGaAs [89, 90]. Both works showed that the low temperature conductance changed in steps quantized in units of $2e^2/h$ as the contact width was varied, controlled by a gate on top of the heterojunction (see Fig. 5.2).

Let us briefly explain this phenomenon known as *conductance quantization*. The appearance of conductance steps of height $2e^2/h$ can be understood with the Landauer formula for the low temperature conductance [95]. This formula tell us that the conductance of the system can be expressed as
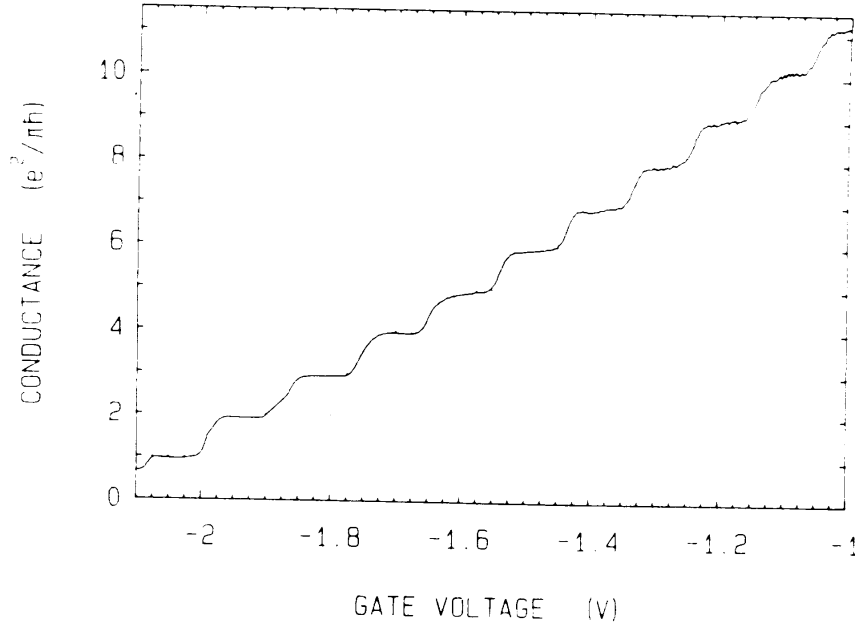
Figure 5.2: Conductance as a function of gate voltage in a point contact created in a GaAs-AlGaAS 2DEG [89]. Notice that the conductance exhibits plateaus at multiples of $2e^2/h$.

$$G = \frac{2e^2}{h} \sum_{i=1}^{N} T_i, \tag{5.1}$$

where T_i is the transmission probability of the i-th conducting channel and N is the number of conducting channels which contribute to the current. The width of these quantum point contacts is comparable to the Fermi wave length λ_F, which causes the quantization of the transversal momentum, giving rise to a discrete number of subbands contributing to the current. As the point contact width is continuously reduced, the number of conducting channel N reduces in a step-like way. This fact gives rise to the conductance pattern which can be seen in Fig. 5.2. Moreover, when the system is in the ballistic regime (i.e. there is no scattering with impurities), every channel has a perfect transmission and the step heights are equal to $2e^2/h$.

Let us go back to the atomic contacts. Since its invention the STM has provided images of surfaces, atoms and molecules with an unknown resolution. But the STM has also been used to modify surfaces, for instance positioning molecules [201] and

142

transferring an atom from the STM tip to the surface [202]. It is even more impressive the possibility which the STM offers of manipulating individual atoms with high precision [203, 204], permitting the fabrication of rudimentary structures. Thus, at the beginning of this decade the first steps toward the definite miniaturization of the electronic devices were given [205, 206]. Examples of atomic-size electronic devices are the atomic switches realized with the movement of an individual Xe atom [207], or the well-known quantum corrals [208].

The interest in the atomic-size contacts has not been exclusively restricted to the analysis of their electronic transport. Another aspect which has attracted the attention is the possibility of studying at an atomic scale mechanical properties like adhesion, contact formations, nanoindentation, separation, fracture, etc. From the experimental point of view the study of these properties has been possible due to the advent of the Atomic Force Microscope (AFM) [209], and from the theoretical point of view thanks to the molecular dynamics simulations [210, 211, 212]. Although we are not interested in studying the mechanical properties of atomic contacts, it is important to know a little about them because they determine the process of contact formation, defining the contact geometries which are finally reflected in the current through these systems.

The combination of the AFM with molecular dynamics simulation have showed that the process of a contact formation, by identing or pulling a tip over a surface, takes place in a series of elastic and plastic stages. During the elastic stages the atomic layers approach or are put apart keeping basically its crystalline structure. On the other hand, the plastic stages consist of sudden atomic rearrangements due to mechanical instabilities which give rise to abrupt changes in the contact section. Below, we shall comment the importance of these phenomena in the determination of the current, and in particular in relation with the conductance quantization in metallic contacts.

At the beginning of this decade arose another technique for creating atomic-size contacts. This is the technique of the *mechanically controllable breakjunctions* (MCB) [74], which has been widely described in the section 1.2.3. Due to the control in the breaking process in the breakjunctions it is possible to follow the evolution of the conductance as the contact section is changed. Fig. 5.3, taken from Ref. [83], shows two examples of the variation of the conductance G of the same Pt contact as a function of the voltage V_p in the piezoelectric, i.e. as a function of the diameter of the constriction. As can be seen, G changes in abrupt steps, in a similar way to the phenomenon of conductance quantization in semiconductor 2DEGs. Although the steps have the expected magnitude of the order of $2e^2/h$, a quantization as clear as in the semiconductor point contact is not found.

Experiments like the one mentioned in the previous paragraph were the starting point of a bitter discussion about the conductance quantization in metallic contacts,

143
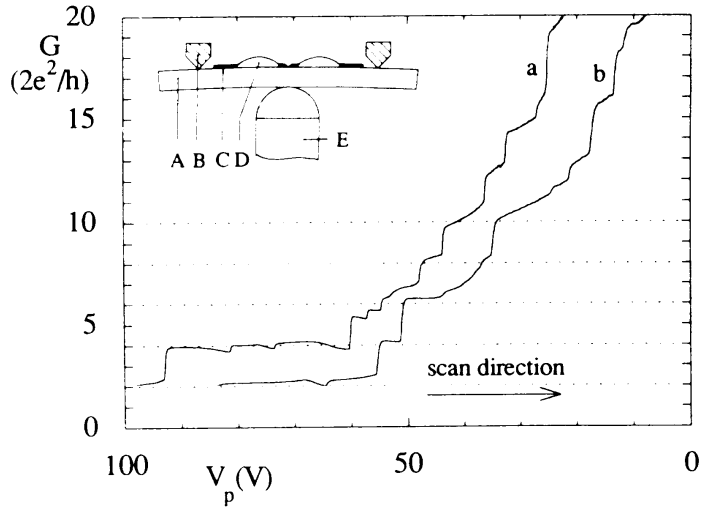
Figure 5.3: Evolution of the conductance of a Pt breakjunction as its section is decreased [83]. The heights of conductance steps are of the order of $2e^2/h$, but quantization is not observed.

which unfortunately has monopolized the discussion about the electronic transport in these systems. Early two explanation of the origin of the abrupt jumps in the conductance arose. The first one, identical to the one commented in the context of 2DEG, is based on the discrete variation of the number of conducting channel as the contact section varies continuously. The second explanation states that these jumps are related to the sudden atomic rearrangements which take place in the elongation o contraction of the contact. These explanations are based on two different pictures of the transport in these nanostructures. The first explanation of the origin of the conductance jumps is based on a transport picture based on the idea of free electrons flowing through a constriction. The second explanation is based on an atomistic picture of the electronic transport, in which the contact is described as a set of atoms through which the current flows. Next, we shall revise some of the main works which tried to clarify this transport phenomenon in atomic contacts.

Todorov and Sutton presented a work in which they combined a molecular dynamics simulation with a calculation of the conductance based on a tight-binding description of the contact [213]. Thus, they analyzed the conductance while the contact is elongated and they found that the contact section changes abruptly through a series of mechanical instabilities, which are reflected in step-like variation of the conductance in agreement with the experiments. In short, they claimed that the

conductance jumps are due to the atomic rearrangements that take place during the formation of the contact.

These abrupt conductance jumps were also observed in different experiments using STM. For instance, Agraït *et al.* [214] showed that in Au at low temperatures the last conductance plateaus before breaking the contact are reproducible and quantized in units of the quantum conductance $G_0 = 2e^2/h$. On the other hand, Pascual *et al.* [215] obtained similar results in Au contacts at room temperature. These latter authors attributed the conductance quantization to the quantization of the electron transversal momentum in the contact.

In an interesting work, Krans *et al.* [82] analyzed the conductance of breakjunctions during the elongation (or contraction) of the contacts for three different metals: Cu, Al and Pt. In this work they showed that the slopes of the conductance plateaus are characteristic of each metal and change from one metal to another [1]. Another interesting point of this work is that for the first time a histogram of the last conductance plateau was performed. The aim of these histograms is to investigate if some metals show a statistical tendency of conductance quantization. The histograms of Cu and Al showed that these metals have certain tendency to be quantized. However, Pt shows a conductance large than G_0 in its last plateau. This fact together with the different tendencies of the plateaus point out the importance of the electronic structure of each metal in the transport properties of these nanocontacts. In particular, the authors pointed out that the fact of having a conductance greater than G_0 in the Pt last plateau could be due to the fact that Pt is a transition metal and the d orbitals could provide additional channels for the current flow.

Another interesting work was done by Olesen *et al.* [216]. They presented conductance measurements at room temperature in point contacts formed between a STM tip and surfaces of Ni, Cu and Pt. With certain optimism they concluded that the conductance in these contacts is quantized in unit of G_0, presenting so the conductance quantization in metallic contact as an universal phenomenon. Naturally, the origin of the quantization was attributed to the quantization of the electron transversal momentum in a contact of a few atoms. This article was reply in a *comment* by Krans *et al.* [217] in which they argued that: "in irregular or atomically disordered atomic systems, where there are no well-defined transverse modes, one loses the notion of conductance channels. Conductance jumps may still occur, as a result, say, of atomic rearrangements, but these jumps can be of arbitrary size and are not a sign of conductance quantization". So, the discussion on the conductance steps went on and has arrived until nowadays.

A work that throws some light on the quantization problem was the one done by Krans and Ruitenbeek [218]. In this reference the authors analyzed the transition from semimetallic Sb contacts to vacuum tunnel junctions using mechanically

---

[1] We shall analyze the different tendencies of the conductance plateaus in Chapter 7.

controllable breakjunctions. They showed that the conductance of Sb atomic-size contacts is small compared to G_0 due to the large λ_F in a semimetal. Observation of subquantum conductance steps when varying the contact area of atomic dimensions gives clear experimental evidence for rearrangements of atoms building up the contact.

It seemed that the atomistic point of view of the transport in metallic contacts gathered strength. At that time an interesting questions was: is there any unambiguous evidence of conductance quantization in metallic contacts? The work done by Krans *et al.* [219] was devoted to the answer of this question. These authors observed a characteristic sequence of jumps in the evolution of the conductance upon stretching in Na breakjunctions. The concrete jump sequence which they observed was: $1G_0$, $3G_0$, $5G_0$, $6G_0$, ... (see Fig. 5.4). In this series the jumps in $2G_0$, $4G_0$ and $7G_0$ are absent. The authors claimed that the observed sequence has a natural explanation in terms of the conductance quantization in the contact. These jumps correspond to those that one would expect in a contact with cylindrical symmetry due to the degeneracy of certain modes in this geometry [220, 221, 222]. On the contrary, Cu contacts did not exhibit the same jump sequence, what was interpreted as that certain atomic configurations are preferred in this case [2]. The final conclusion of this interesting work was that in these experiments the conductance variation in metallic contacts of variable size is determined by the conductance quantization and by the discreteness of the contacts.

On the analysis of the conditions which favor the conductance quantization it is worth remarking two papers. In a theoretical work Bratkovsky *et al.* [224] combined molecular dynamics simulations with conductance calculations and concluded that the conductance quantization is favored at high temperatures. In the evolution of a contact in its process of formation, a high temperature implies that the atoms of the systems have a greater kinetic energy. Thus, the system has enough time to rearrange itself by minimizing the surface energy and giving rise to ordered compact structure. This absence of disorder is the cause which favors the quantization. This theoretical prediction was experimentally confirmed by Muller *et al.* [225]. These authors analyzed breakjunctions of Au and Cu at room temperature and found more horizontal plateaus than in the case of low temperatures, and a lot of them at integer multiples of G_0. However, they also found some deviations in the condition of quantization.

In what we have exposed so far, it is evident the relation between the transport properties and the mechanical ones. This relation was further clarify in a set of experiments in which a measure of the contact forces by means of an Atomic Force Microscope (AFM) and a measure of conductance were combined [226, 227, 228, 229,

---

[2]We now stress that this peculiar sequence of conductance steps are not observed in other metals, like for instance Au [223].
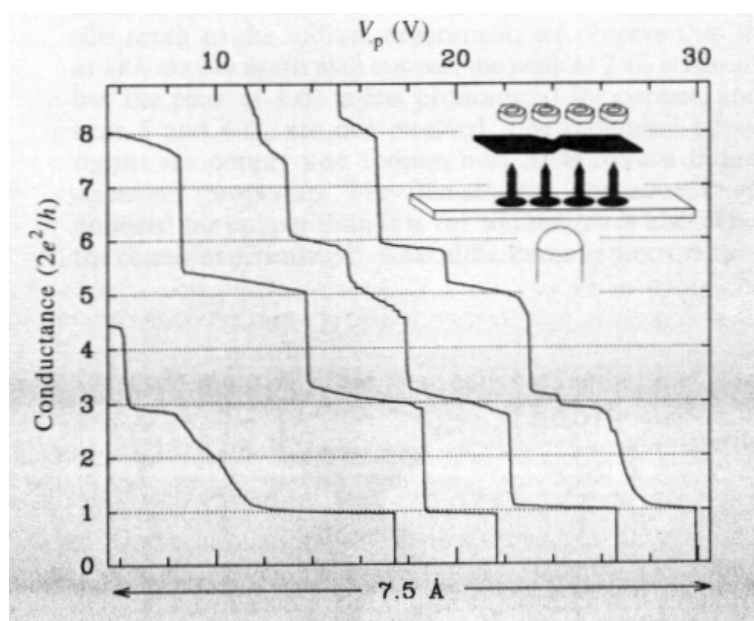
Figure 5.4: Evolution of the conductance in Na atomic-size contacts at 4.2 K [219]. The contact section is reduced by increasing the piezoelectric voltage.

230]. These experiments showed that the contact deformation takes place in a set of elastic and plastic stages in agreement with the molecular dynamics simulations. They stressed that every conductance jump corresponds to a jump in the forces, what was interpreted as the step-like variation of the conductance is always due to atomic rearrangements in the contact.

The first theoretical article that presented a simultaneous calculation of the conductance and the forces in an atomic contact was done by Todorov and Sutton [231]. In this work they showed by means of molecular dynamics simulation and tight-binding calculations of the conductance, that the jumps in both quantities coincide and are due to atomic rearrangement in the contact.

With the advent of these last works it seemed quite clear that the atomistic picture prevailed over the free electrons picture. However, both pictures are not incompatibles. For instance, Stafford *et al.* [232] have recently presented a work in which they developed an unified treatment of the cohesion and conduction properties in terms of the scattering matrix. Using a jellium-type approximation they presented a picture in which the conducting channels behave as delocalized chemical bonds which provide the metallic cohesion to the contact. At the same time, they showed a correlation between the conductance jumps and the force jumps. Several authors

have obtained similar results using similar approaches to this latter one [233, 234, 235]. Therefore, one can obtain similar results from different points of view about the electronic properties.

In the last paragraphes of this introduction to the electronic transport in atomic contacts, we would like to remark the importance of an essential factor to us. As it is clear from the experiments reviewed so far, there are evident differences between contacts of different metals, which in our opinion is a clear evidence of the relevance of the electronic structure in the transport properties of metallic nanocontacts. For this reason, we now concentrate in the influence of the contact *chemistry* on the current through these systems. To remind now the importance of the chemistry to somebody in the STM business is almost a sacrilege, because the usefulness of STM lies on the relation between the current and the electronic structure of the surfaces to be explored. However, in the context of *atomic circuits*, in which we are interested it is seem to have forgotten the importance of this item. This has been mainly due to the possible existence of the conductance quantization and its supposed universality, what of course would be much easier to understand within a picture of free electron circulating through a constriction whose width is comparable to the Fermi wave length of the system. Of course, there are notable exceptions between which we shall bring out someones in the next paragraphs.

Lang [236] generalized his ideas developed for the STM in order to analyze the case of atomic wires. The systems which he study consist of two semiinfinite metallic electrodes coupled to an atomic chain with an arbitrary number of atoms. The electrodes are describe with a jellium model within the framework of the density functional. For instance, he has calculated the resistance of Al wires with 1 to 3 atoms, and he found resistances between 6.6 and 9.0 $k\Omega$. But the relevant thing is that he stressed the importance of the contribution to the current of the s and p orbitals of Al, and showed how the electronic structure of individual atoms plays an essential role in the transport through atomic wires.

Another remarkable work on the importance of the contact electronic structure was done by Sirvent *et al.* [237]. In this work the authors analyzed experimentally atomic contacts of transition metals like Ni and Pt. They showed that these metals exhibit a last plateau before breaking the contact with conductance larger that G_0, while Au contacts are quantized. From the theoretical point of view they showed that the difference between transition metals and noble metals like gold is due to the contribution to the current of the d orbitals in the case of the transition metals.

Another interesting reference is the one by Yazdani *et al.* [238], in which the authors measured the resistance of wires consisting of one and two individual Xe atoms set in series using an STM. Both the measurements and the calculation based on the above mentioned Lang method yield a resistance of 10^5 Ohms for the case of one Xe atom and 10^7 Ohms for the case of two atoms. These resistances are much

larger than the quantum resistance ($\sim 12.9\ k\Omega$) because the conduction through the Xe atoms takes place through the tail of the $6s$ resonance of Xe, which lies very far from the Fermi level. Maybe, the most important thing in this work is the idea that the transport in these nanostructures can be understood in terms of the individual electronic states of the atoms.

In the last part of this section we shall comment the experiment which motivated the part II of this thesis, the experiment done by Scheer *et al.* [143] which we commented extensively in section 2.5 in relation with the superconducting transport. Here, we shall briefly remember this experiment and emphasize the consequences that it had for the normal transport in atomic contacts.

As in any mesoscopic structure, in an atomic contact the electrical transport takes place through independent *conducting channels* which are characterized by its transmission coefficient T_i and whose contribution to the total conductance G is $G_0 T_i$, where $G_0 = 2e^2/h$ is the quantum conductance [95]. In the metallic contacts only a few conducting channels contribute to the current. In the traditional experiments that we have described so far it is only obtained information on the contact total transmission $T = \sum_{i=1}^{N} T_i$ through the measure of the conductance G by using the relation $G = G_0 T$. It is evident that it would be very valuable to obtain information on the individual transmissions of the different channels. In their work Scheer *et al.* [143] showed that it is possible to measure the whole set $\{T_i\}$ in the case of superconducting materials (see Ref. [143] or section 2.5 for details). Hereafter we refer to the technique designed by Scheer *et al.*, which permits to obtain the transmission distribution, as *channel spectroscopy*.

As we commented in section 2.5, Scheer *et al.* analyzed the superconducting current-voltage characteristics of Al atomic-size contacts using microfabricated breakjunctions. From this experiment they obtained a set of fundamental conclusions with respect to the normal electronic transport in these contact, and we next remember some of them:

1. Even in cases in which $G < G_0$ several channels contributes to the current. In particular, in the Al last plateau before breaking the contact, where typically $G < G_0$, they found usually three channels and in some occasions two.

2. From the previous point it is deduced that one cannot even speak, at least in the Al case, about conductance quantization in the case of $G \sim G_0$, questioning the validity of conductance histograms to elucidate about the quantization [242].

3. The evolution of the conductance along a plateau arises from changes in several individual channels. This indicates that the channel transmissions are determined by the atomic configuration.

Several fundamental questions immediately arose from this work: what is the microscopic origin of the conducting channels in a metallic contact?, what properties determine the number and transmission of the conducting modes in a given metallic atomic-size contact? Our main aim for the part II of the thesis to answer these questions.

We finish this section recommending to the reader interested in a review of this topic the references [239, 240, 241].

5.2   Objective of the part II

As stated in the introduction, the aim of this part of the thesis is the theoretical study of the electrical current in metallic atomic-size circuits. To be exact, our aim is to answer the questions that we presented at the end of the previous section. Eventually, we want to find out the nature, number and transmission of the conducting channels in metallic atomic-size contacts.

As we commented in the historical review, the advances in nanofabrication techniques allow us to fuel the dream that electronic devices can be shrunk from the current micrometre-length scale all the way down to the single-atom or molecule scale. Nowadays we are attending to the first steps toward what is already known as *Molecular Electronics*. For instance, a single C_{60} molecule has been operated as an amplifier [243], and a single carbon nanotube has been used to make a room temperature transistor [244]. It seems that soon we will be able to design electronic circuits atom by atom. A prerequisite for successful design is a knowledge of the relationship between the macroscopic electrical characteristics of such circuits and the quantum properties of the individual atoms used as building blocks. Our objective is to study what determines the electrical properties, as the conductance, of atomic circuits. In order to obtain clear conclusions, we shall concentrate ourselves in the analysis of the simplest imaginable circuit: an one-atom contact between two metallic banks.

It is evident that in our way toward our aims we shall have to face some of the traditional questions of this field:

- What is the origin of the differences between contacts of different metals?

- What is the influence of the contact geometry on the conductance?

- What kind of atomic configurations are usually formed in these nanocontacts?

- In which situations one could expect conductance quantization?

- What are the simplest structures one can fabricate experimentally?, exist there and are stable the one-atom contacts?

Chapter 6

Microscopic origin of conducting channels in atomic contacts

6.1 Introduction

In this chapter we shall determine the transport properties of atomic-size contacts. Typically, we are interested in the current which flows through the contact. In the case of metallic contacts, in which the Ohm law is usually verified at the voltages we are interested in, the relevant quantity is the conductance or the resistance. In principle, in order to determine the resistance of these atomic circuits one should take into account different contributions: electron-phonon scattering, impurities, defects, etc. However, in a metallic atomic-size contact the main resistance source is the elastic scattering in the atomic neck walls. In particular, the number of transmitting modes is control basically by the narrowest part of the contact. One has a situation in which only a few conducting channels contribute to the current, a slight variation in this number may give rise to a resistance change of the order of $k\Omega$. Thus, it is quite clear the main source of resistance is concentrated in the neck region. Then, we shall concentrate in a suitable description of what happens in the neck region. Furthermore, at the typical temperatures of the experiments (1 K) the inelastic scattering length is of the order of 1 μm, so we can neglect inelastic effects.

For describing the electronic structure and the transport properties of atomic constrictions we shall use an atomic orbital basis. Moreover, the use of a semiempirical tight-binding description, as the one we follow, permits us to analyze the influence of different ingredients on the correct description of the transport properties. In particular, we believe that an adequate description needs at least the following three ingredients:

- **Chemistry:** when one revises the literature, as we did in the previous chapter,

one can see clear differences between contacts of different metals. For instance, the conductance quantization only is observed in simple metals like Na or in noble metals like Au, while it is not observed in metals like the transition ones. Another clear difference is the different behavior of the conductance plateaus upon elastic deformations. Furthermore, with the new technique introduced by Scheer *et al.* [143, 145, 146] it has been observed that contacts of different metals show different number of channels. All these facts unambiguously indicate that for the proper determination of the current one needs a suitable description of the contact electronic structure.

- **Geometry:** the histograms that one can find in the literature are not a proof of the conductance quantization [242], but a proof that the different atomic configurations give rise to different conductance values. For this reason we have to analyze the influence of the contact geometry on the conductance.

- **Charge neutrality:** in metals the screening length is of the order of interatomic distances, what implies that the local charge neutrality is approximately verified. In an atomic circuit the atoms of the neck region see an environment different from the one of bulk and one has to assure that the local charge neutrality condition is verified.

Finally, this chapter based on Refs. [147, 146] is organized as follows. In section 6.2 we shall describe our model for an atomic-size contact based on a semiempirical tight-binding description of the electronic structure. Section 6.3 is devoted to the expression of the current in terms of the microscopic quantities of the model. In section 6.4 we shall show the theoretical results for the transport through contacts of different metals: *sp*-like metals like Al and Pb, transition metals like Nb and simple and noble metals. Section 6.5 is devoted to the experimental results of Ref. [146] in which the direct connection between conducting channels in an one-atom contact and the valence orbitals of central atom is shown. We shall end this chapter in section 6.6 by summarizing the conclusions.

6.2   Tight-binding model for an atomic contact

As commented in the previous section, it seems reasonable to choose an atomic orbital basis for analyzing the electronic structure of an atomic-size system. This choice has been successfully used in the context of the Scanning Tunneling Microscope [123, 237, 245, 246]. Furthermore, the use of a local basis in combination with Green functions techniques provide an efficient way of obtaining the transport properties in terms of microscopic quantities [123, 237, 245, 247, 248]. In an atomic orbital basis the electronic Hamiltonian adopts the usual form

$$\hat{H} = \sum_{i\alpha,\sigma} \epsilon_{i\alpha} c_{i\alpha\sigma}^{\dagger} c_{i\alpha\sigma} + \sum_{i\alpha\neq j\beta,\sigma} t_{i\alpha,j\beta} c_{i\alpha,\sigma}^{\dagger} c_{j\beta,\sigma}, \qquad (6.1)$$

where i, j denote the atomic sites, α, β are the different atomic orbitals (the number of orbitals in each atom will be denoted by N_{orb}) and σ is the spin. We assume that the hopping elements $t_{i\alpha,j\beta}$ only connect first-neighboring atoms [1]. Thus, we must decide how to choose the Hamiltonian parameters, what type of contact we shall analyze, etc. The following paragraphs are devoted to the description of how we shall take into account the ingredients mentioned in the introduction of this chapter.

There exist different empirical procedures for determining the parameters of the tight-binding Hamiltonian (6.1) which are known to reproduce suitably the band structure of bulk materials [249, 250]. We shall use the parametrization proposed in Ref. [250] within the two centers Slater-Koster approximation [251]. Within this two centers approximation one only needs a reduced number of matrix elements between neighbors, for instance only four to describe sp bands, all hoppings can be determined projecting adequately these matrix elements (see Ref. [251]).

As a minimum basis for the description of the transport in each metal we choose the one formed for those orbitals which give a significant contribution to the density of states at the Fermi level. Thus, for the case of superconducting metals of the group III and IV, like Al or Pb, we only include the s and p orbitals, while for transition metals like Nb we have to include the d orbitals.

In an atomic contact the local environment in the neck region is very different to that of the bulk material and therefore the use of bulk parameters in the Hamiltonian requires some justification. In first place, the inhomogeneity of the contact geometry can produce large deviations from the approximate local charge neutrality that typical metallic elements must exhibit. Within the tight-binding approximation this effect can be corrected imposing local charge neutrality through a self-consistent variation of the diagonal energies $\epsilon_{i\alpha}$ [252]. As discussed below, this self-consistency in the neck region turns out to be crucial for the correct determination of the conducting channels. Regarding the hopping elements, $t_{i\alpha,j\beta}$, although we shall initially consider them as being equal to the bulk values in order to represent a neck geometry with bulk interatomic distances; we shall show that the results are robust with respect to fluctuations in the hopping elements induced by disorder in the atomic positions.

So far we have discussed two of the three ingredients that we mentioned in the introduction, namely, the chemistry of the contact and the importance of the charge neutrality condition. We shall now concentrate in the third one: the contact geometry. Indeed, this is the greatest problem that we face, because in a particular experiment the actual contact geometry is unknown. From the theoretical point

---

[1] This condition may easily relaxed.

of view one could determine the atomic positions by means of molecular dynamics simulations [210, 211, 212, 213]. However, for extracting conclusions as clear as possible about the nature of the conducting channels we shall adopt an *static* picture assuming a given geometry. To be precise, we shall concentrate in the analysis of the simplest contact, an one-atom contact like the one shown in Fig. 6.1. The existence of one-atom contacts has been pointed out since several years ago [214, 82]. However, there is no a conclusive proof of that the smallest contacts which are fabricated are actually one-atom contacts. As we show below, the combination of the theory which we present in this chapter together with recent experiments which use the channel spectroscopy technique gives a clear evidence that the one-atom contacts are stable and reproducible [146].

Even for an one-atom contact there exist many possibilities for its geometry. Fig. 6.1 shows the ideal geometry which we shall usually analyze. It consists of a close-packed fcc structure grown along the (111) direction (hereafter denoted as z direction), starting from a central atom. The neck region, which contains N atomic layers, is built starting from the central atom and choosing at each side the nearest-neighbors. This gives rise to a sequence: -6-3-1-3-6-, where each number indicates the number of atoms in the corresponding layer. Finally, this structure is connected to two semi-infinite crystals describing the metallic leads. The choice of the (111) direction is supported by molecular dynamics calculations which indicate that this direction is preferred. Even in cases when one starts from a different crystallographic direction, after stretching the contact close-packed structures tend to be formed (see for instance Ref. [212]). Of course, real contacts are not exactly like the one depicted in Fig. 6.1, so we have to study the effect of disorder in atomic positions and different crystallographic directions. Furthermore, by taking different values of N we can describe both cases of long and short necks.

6.3　Current and transmission in an atomic contact

In this section we determine the current through the atomic contact described in the previous section in terms of the microscopic quantities which appear in Hamiltonian (6.1). For the sake of clarity, the detailed derivation of the current expression for an atomic contact of arbitrary geometry is described in Appendix E. In this section we only give some indications of such derivation and we mainly concentrate in the understanding of the final result.

Our aim is to obtain an expression for the electrical current through an atomic contact due to a constant bias voltage applied between the leads. For this purpose, it is convenient the use of nonequilibrium Green function techniques [247]. In particular, we make use of the Keldysh formalism [119], described in Appendix A. This technique allows us to determine perturbatively the Green functions of a system *ar-*
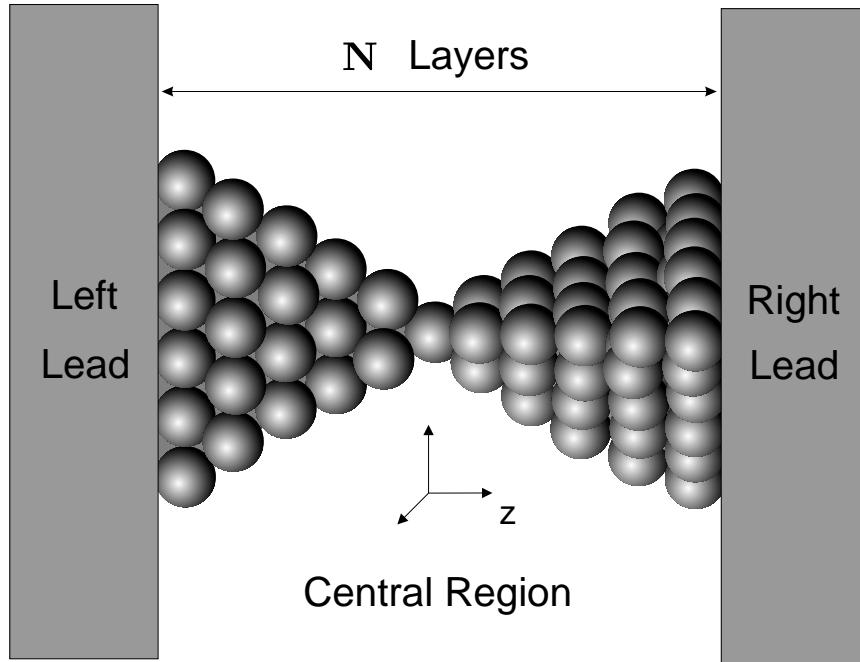
Figure 6.1: Idealized geometry for an one-atom contact (see text for description). The layers are numbered from 1 to N starting from the left lead.

bitrarily out of equilibrium. In our problem we follow a perturbative scheme in which we divide the system into three regions: the central region formed for the contact neck and the two leads or semi-infinite crystals (see Fig. 6.1). We treat the coupling between the central region and the leads as a perturbation. As this perturbation is one-electron we can carry out the perturbation expansion up to infinite order. Thus, it should be clear that this formalism permits us to obtain the exact solution of our atomic contact model.

Within this formalism the current can be written with an expression formally equivalent to that of scattering theory [95]. The current evaluated between the left lead and the central region is given by (see Appendix E and Ref. [253])

$$I = \frac{2e}{h} \int_{-\infty}^{\infty} T(E,V) \left[f_L(E) - f_R(E) \right] dE, \qquad (6.2)$$

where $f_{L,R}$ are the Fermi-distribution functions for the (left,right) leads and $T(E,V)$ is an energy and voltage dependent transmission probability, which can be written

in terms of the (retarded and advanced) Green functions of the system $\hat{G}^{r,a}(E)$ as [2]

$$T(E, V) = 4\text{Tr}\left[\text{Im}\hat{\Sigma}_L(E - e\frac{V}{2})\hat{G}^r_{1N}(E)\text{Im}\hat{\Sigma}_R(E + e\frac{V}{2})\hat{G}^a_{N1}(E)\right]. \tag{6.3}$$

In this expression $\hat{G}^r_{1N}$ and $\hat{G}^a_{N1}$ are matrices whose elements are the Green functions connecting the layer 1 and N, and $\hat{\Sigma}_{L,R}$ are the self-energy matrices describing the coupling of the central region to the leads. These matrices have a dimension equal to the number of orbitals in the first neck layer which is in contact with the left and right leads $(M_{L,R})$ and have a simple expression in terms of the Green functions of the uncoupled electrodes

$$\left(\hat{\Sigma}_{L,R}(E)\right)_{i\alpha,j\beta} = \sum_{k,l\in L,R\,;\,\gamma,\delta} t_{i\alpha,k\gamma}g^a_{k\gamma,l\delta}(E)t_{l\delta,j\beta}, \tag{6.4}$$

where the functions $g^a_{i\alpha,j\beta}$ are the advanced Green functions of the isolated semi-infinite crystals and can be evaluated numerically by standard decimation techniques [254].

In principle, the expression (6.2) gives the current for arbitrary bias voltage due to elastic processes. However, we are interested in the voltage range which is probed in the experiments with superconducting contacts, which is of the order of the gap parameter Δ (typically a few tenths of meV) [143]. For this bias range normal metallic systems behave Ohmically. Even when the atomic-size contacts exhibit resonances around E_F [252], their width will in general be much larger than Δ and the linearization of Eq. (6.2) is appropriate. In this linear regime the zero-temperature normal conductance can be expressed as

$$G = \frac{2e^2}{h}T(E_F, 0). \tag{6.5}$$

By using the cyclic property of the trace, G adopts the usual form of the Landauer formula

$$G = \frac{2e^2}{h}\text{Tr}\left[\hat{t}(E_F)\hat{t}^\dagger(E_F)\right], \tag{6.6}$$

where the transmission matrix $\hat{t}$ is defined as

$$\hat{t}(E) = 2\left[\text{Im}\hat{\Sigma}_L(E)\right]^{1/2}\hat{G}^r_{1N}(E)\left[\text{Im}\hat{\Sigma}_R(E)\right]^{1/2}. \tag{6.7}$$

---

[2]The Green functions $\hat{G}^{r,a}(E)$ are formally defined as $\hat{G}^{r,a}(E) = [E \pm i0^+ - \hat{H}]^{-1}$, where $\hat{H}$ is the Hamiltonian (6.1).

The existence of $(\text{Im}\hat{\Sigma})^{1/2}$ as a real matrix is warranted by $\text{Im}\hat{\Sigma}$ being positive definite. Moreover, $\hat{t}\hat{t}^{\dagger}$ is a hermitian matrix having M_L real eigenvalues, T_i, which are bounded by zero and one [3]. Associated with these eigenvalues there will be M_L eigenvectors, which in our model are linear combinations of the atomic orbitals in the layer which is in contact with the left lead. These eigenvectors define the way in which the atomic orbitals contribute to each conducting channel.

Summarizing, we have seen that the linear conductance can be expressed as a sum of independent contributions

$$G = \frac{2e^2}{h} \sum_{i=1}^{M_L} T_i, \tag{6.8}$$

where T_i are the eigenvalues of $\hat{t}\hat{t}^{\dagger}$ at the Fermi level. This formula together with the expression of the transmission (6.7) are the main technical results of this chapter. The expression of the conductance in terms of the channel transmissions allows us to study not only the total conductance but also the its decomposition into independent modes, what will help us to understand how the electrical current flows in atomic contacts of different metals. This will be the aim of the following section, but the rest of this section is devoted to the understanding of the previous expressions and we shall try to extract some conclusions using very simple arguments. To be precise, we shall try to get certain intuition about what is the influence of the different physical ingredients.

In first place, let us see how the previous expressions may help us to understand the role of the electronic structure in the electrical current. What we look for is a simple answer to the question: how the atomic orbitals participate in the conducting channels? In order to answer this question we go back to the analysis of Eq. (6.7). Although the dimension of $\hat{t}\hat{t}^{\dagger}$ can be arbitrarily large depending on the size of the central region, the actual number of conducting channels (those with a non-vanishing transmission) are limited by the number of orbitals in the narrowest section of the neck. In particular, we have N_{orb} channels in the case of a single-atom contact. This fact can be shown by the following simple argument. As the division between "central region" and leads is somewhat arbitrary, one could always redefine the leads for the geometry of Fig. 6.1 in such a way that the new central region would only consist of the central atom. Then, the new lead self-energy matrices $\hat{\Sigma}'_{L,R}$ would have a dimension of just N_{orb} and the new transmission matrix would only admit N_{orb} eigenmodes. Current conservation along each conducting channel ensures that the nonvanishing eigenvalues T_i and T'_i must be the same [4].

---

[3]All these properties can be deduced from the analytical properties of the Green functions.

[4]Furthermore, from the computational point of view it is more convenient to evaluate the transmission in the central atom, because there its dimension is minimum.

The above simple argument already allows an estimate of the maximum number of relevant conducting channels in an one-atom contact. Thus, for an sp-like metal like Al or Pb, this number should be typically four, while for a transition metal like Nb (having a negligible weight of p orbitals at E_F) this number would be of order six. As discussed below, this rough estimate should be taken as an upper bound. The actual number of conducting channels can be smaller as some of the channels can carry no current due to symmetry considerations [5].

We have just seen that the atomic orbitals control the number of channels, but what happens with the transmissions of such channels?, what is the relation between the density of states in the neck region and the transmissions? It is evident that the precise answers to these questions cannot be given until we do the detailed calculations for real contacts, but at least we can extract an idea about such answers by means of general considerations.

Following the argument of the previous paragraphs, one can write the conductance by means of Landauer formula (6.6) with the transmission evaluated at the central atom

$$\hat{t}(E) = 2 \left[\mathrm{Im} \hat{\Sigma}_L(E) \right]^{1/2} \hat{G}^r_{cc}(E) \left[\mathrm{Im} \hat{\Sigma}_R(E) \right]^{1/2} , \qquad (6.9)$$

where now the self-energies describe the coupling between the central atom and the electrodes and have a dimension equal to N_{orb}. On the other hand, $\hat{G}^r_{cc}$ is the retarded Green function at the central atom, which can be expressed in terms of the self-energies as

$$\hat{G}^r_{cc}(E) = \left[(E + i0^+)\hat{1} - \hat{\epsilon}_c - \hat{\Sigma}_L(E) - \hat{\Sigma}_R(E) \right]^{-1} , \qquad (6.10)$$

where $\hat{1}$ is the identy matrix and $\hat{\epsilon}_c$ is a diagonal matrix containing the atomic levels of the central atom.

In order to simplify the discussion let us now assume that we only have an orbital per atom with a level ϵ_0. In this case the self-energies and the Green function G^r_{cc}

---

[5]The fact that the maximum number of channels be N_{orb} is a consequence of working in a first-neighbors scheme. How is the maximum number of channels modified by the inclusion of interaction among further neighbors? Strictly, if we had coupling between atoms on the left and right of the central atom in the structure of Fig. 6.1, the actual number of channels would be the number of bonds which connect both electrodes, exceeding thus N_{orb}. However, we are only interested in those channels with a non-negligible transmission. A hopping element between second-neighbor atoms is typically an order of magnitude less than one between first-neighbor atoms. As the transmission probability (for a channel in the tunnel regime) is at least proportional to the hopping square, we have that the channels due second-neighbor couplings are usually two order of magnitude less than the ones we are considering. Moreover, in structures like the one shown in Fig. 6.1 the atoms on the left and right sides of the central atom are not even second-neighbors.

are complex scalar quantities, giving rise to only one channel. The local density of states at the central atom $\rho_c(E)$ is

$$
\begin{aligned}
\rho_c(E) &= -\frac{1}{\pi}\operatorname{Im}G_{cc}^r(E) \\
&= \frac{1}{\pi}\frac{\operatorname{Im}\left\{\Sigma_L(E)+\Sigma_R(E)\right\}}{\left[E-\epsilon_0-\operatorname{Re}\left\{\Sigma_L(E)+\Sigma_R(E)\right\}\right]^2+\left[\operatorname{Im}\left\{\Sigma_L(E)+\Sigma_R(E)\right\}\right]^2}
\end{aligned}
\tag{6.11}
$$

By defining the scattering rates $\Gamma_{L,R}(E)\equiv\operatorname{Im}\left\{\Sigma_{L,R}(E)\right\}$ and the effective level $\epsilon(E)\equiv\epsilon_0+\operatorname{Re}\left\{\Sigma_L(E)+\Sigma_R(E)\right\}$, we can write the density of states ρ_c as

$$
\rho_c(E)=\frac{1}{\pi}\frac{\Gamma_L+\Gamma_R}{(E-\epsilon)^2+(\Gamma_L+\Gamma_R)^2},
\tag{6.12}
$$

what looks like a Lorentzian, although we must keep in mind that both the scattering rates and the effective level depend on energy. Here we can see clearly the two effects that the couplings with the electrodes provoke on the central atom. First, they renormalize the atomic level position ϵ_0, and secondly the couplings provide a width $\Gamma_L+\Gamma_R$ to the bare level, which is typically of the order of several electronvolts.

On the other hand, one can see that the transmission probability $T(E)=tt^\dagger$ is given by a Breit-Wigner-type formula as

$$
T(E)=\frac{4\Gamma_L\Gamma_R}{(E-\epsilon)^2+(\Gamma_L+\Gamma_R)^2}.
\tag{6.13}
$$

This expression is quite similar to that one finds in the context of resonant tunneling through a single level. Anyway, one must keep in mind that here the "resonant tunneling" takes place through a level whose width is of several electronvolts. Thus, in the case of one orbital per site we see that the transmission and the density of states have a similar shape, as it is shown in Fig. 6.2 for the trivial case of energy-independent scattering rates ($\Gamma_{L,R}$). Let us remind that what really matters for the transport is the transmission probability at the Fermi level $T(E_F)$. Thus, in order to have a perfectly transmissive channel, the Fermi level should lie in the center of the "resonance", and moreover we should have a symmetric situation $\Gamma_L(E_F)=\Gamma_R(E_F)$ [6]. Thus, the fact of having a certain transmission depends on the Fermi level position E_F, which depends on the band occupation by means of the charge neutrality condition. This reveals the importance of this ingredient in our recipe. In particular, if one talks about conductance quantization, he should explain what the robust mechanism operates to make that the Fermi level lies in the center of the band. It is not difficult to figure out situations where the Fermi level lies far from

---

[6]This may seem a very restrictive condition, but let us remember that the resonances are very broad.

the resonance. An illustrative example is shown in the work done by Yazdani *et al.* in which they analyze the transport through individual atoms of Xe [238].
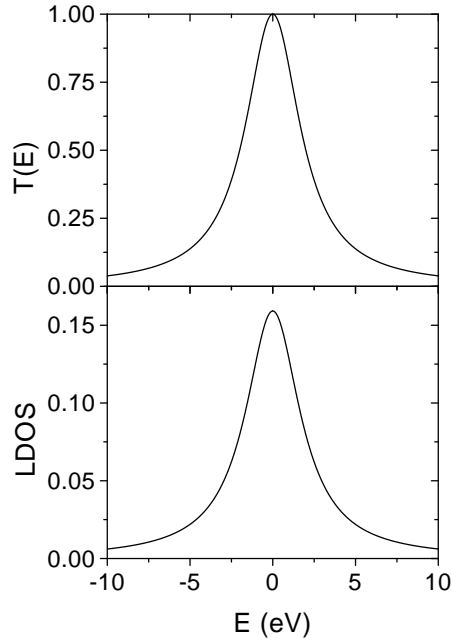
Figure 6.2: Academic example of one orbital per atom: transmission and local density of states (LDOS) at the central atom as a function of the energy. Parameters: $\Gamma_L = \Gamma_R = 1 \ eV$, $\epsilon = 0 \ eV$.

One should be careful and must not to go too far with the analogy between the transport through an one-atom contact and the resonant tunnel. The simple example of Fig. 6.2 may lead us to think that the current is exclusively controlled by the density of states at the central atom. However, in the expression of the transmission (Eq. (6.7)) one has information on the rest of the contact by means of the self-energies. Indeed, instead of *resonant tunneling* through the levels of the central atom, we have a *resonant tunneling* exploring the states of the neck region. In this sense one can say that we are doing atomic cluster spectroscopy. It will not always be so simple to do the correspondence between the density of states at the central atom and the transmission, but always this local density of states (LDOS) will help us to understand the conductance results.

The next question could be: what happens in the case of several orbitals per atom? The situation becomes more complex, but to get an idea let us consider the

following example which is totally academic. Let us assume two levels per atom ϵ_1 and ϵ_2. We assume that the self-energies $\hat{\Sigma}_{L,R}$ are identical and equal to

$$\hat{\Sigma}_{L,R} = i\Gamma \begin{pmatrix} 1 & 0 \\ 0 & 1 \end{pmatrix}, \tag{6.14}$$

where Γ is an energy-independent scattering rate. Thus, the problem is diagonal giving rise to two independent channels with transmission probabilities

$$T_{1,2}(E) = \frac{4\Gamma^2}{(E - \epsilon_{1,2})^2 + 4\Gamma^2}, \tag{6.15}$$

and the local density of states in the two orbitals of the central atom will be

$$\rho_{1,2}(E) = \frac{1}{\pi} \frac{2\Gamma}{(E - \epsilon_{1,2})^2 + 4\Gamma^2}. \tag{6.16}$$

Both expressions are represented in Fig. 6.3. If for instance we have an electron per atom and spin in the conduction band, the charge neutrality condition makes that the Fermi level lies where Fig. 6.3 shows. When we have a look at the transmission, we can see that the position of the Fermi level makes that the T_i have an intermediate value between 0 and 1.

Usually the electronic transport has been understood in terms of completely open channels or completely closed ones (transmission 1 or 0), specially in the context of two-dimensional electron gases. However, we see how in the atomic contacts the concept of semi-open channels with an intermediate transmission arises in a natural way. From the previous example it is easy to understand that in situations where there are several orbitals contributing to the current it is possible the appearance of channels with intermediate transmissions, even in absence of disorder. The reason is that in this case it seems rather difficult to satisfy the "resonant" condition for all channels at the same time. As we shall show in the next section, this is the situation that takes place in contacts made of *sp*-like metals like Al or Pb and transition metals like Nb. Thus, it seems rather complicated that in these metals the conductance quantization appears, leaving this possibility for the case of simple and noble metals.

The previous examples and arguments are not rigorous demonstrations and the definitive conclusions will come out with the calculations of real contacts. However, we hope that they serve to understand the results that will be obtained with the complete calculations.

In the same way we have qualitatively learnt about the importance of the orbital structure and the charge neutrality, we can now understand briefly what is the influence of the contact geometry. The geometry or local environment of the central atom determines the coupling and then the shape and width of the bands, as well as
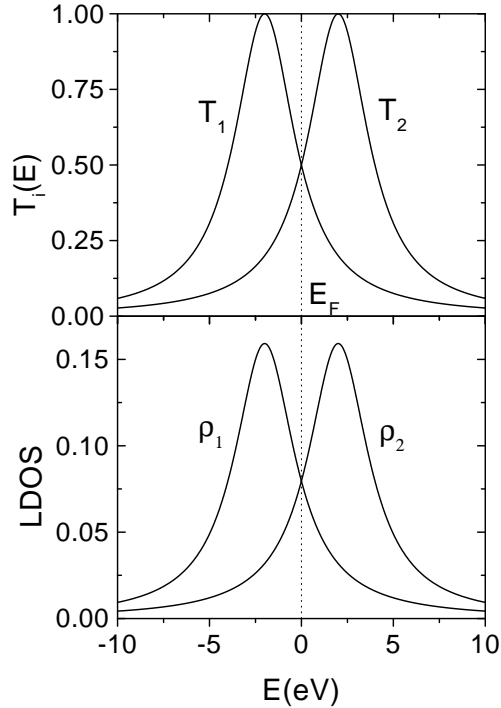
Figure 6.3: Academic example for the case of two orbitals per atom. The upper panel shows the transmissions as a function of the energy. Lower panel shows the densities of states for each orbital of the central atom. The Fermi level is indicated by a dashed line.

the central atom level positions. Furthermore, they control the atomic levels of the cluster.

Let us continue with some technical comments. One of the advantages of the use of Green functions is that one does not need the existence of ideal leads where the different channels are independents, as it is assumed in the scattering formalism. Here in principle, we are dealing with an infinite system in which if there is disorder we will never have a trivial decomposition of the modes.

Some authors have stated that in an atomic contact there are no well-defined channels due to the presence of disorder in the atomic positions. In a real atomic contact there is neither translational symmetry nor perfect crystal lattice symmetry. This implies that neither the linear momentum of the electron nor its crystal momentum are good quantum number, but this does not mean that one cannot di-

162

agonalize the problem, as we have shown here, describing the transport in terms of independent modes.
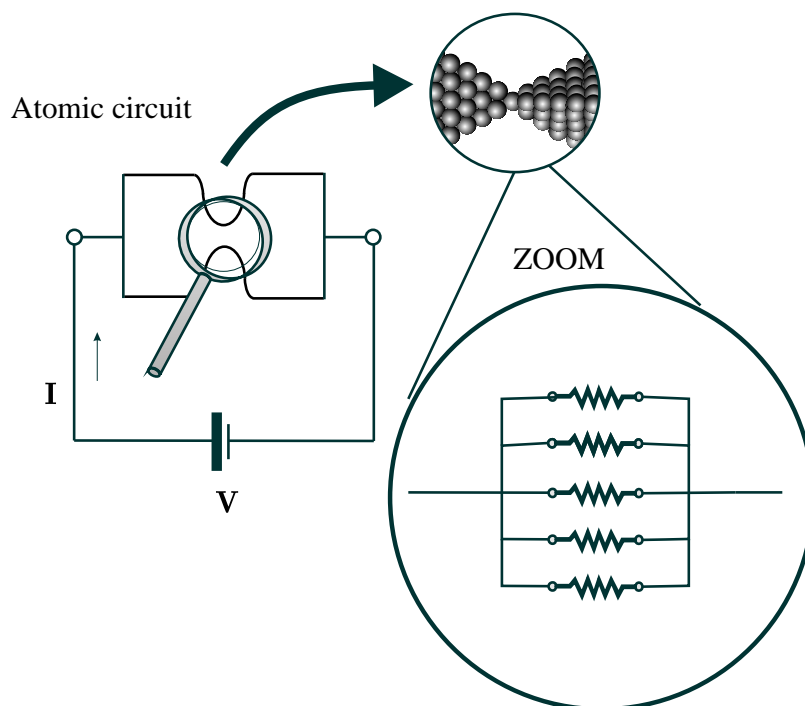
Figure 6.4: An one-atom metallic circuit may still have certain inner structure depending on its orbital structure. In this sense it can be viewed as a set of resistances associated in parallel.

Finally, let us summarize some of the ideas that we have discussed so far. Concentrating ourselves in the one-atom contact, we have seen that the valence orbitals of the central atom control the number of channels. Moreover, we have seen the relation between the local density of states and the transmission as well as some simple conclusions on the conductance quantization in certain metals. But to conclude, we would like to remark here the following idea. Usually, a single-atom contact has been seen as the most elementary circuit one can fabricate, assuming that an atom-contact can only sustain one channel with a resistance of $R_0 \sim 12.900\Omega$ (see Fig. 6.4). However, we have shown that when one looks at this contact in detail, this circuit has still an inner structure provided by the atomic orbitals. Thus, this contact can be represented as a set of resistances associated in parallel (see Fig. 6.4).

The number and nature of these resistances are determined by the valence orbitals of the metal. Moreover, the value of the individual resistances are not only determined by the valence orbitals of the central atom, but also by its local environment. Let us recall that the resistance of a quantum circuit like this is a non-local quantity, which depends on the systems at which is connected. Finally, our aim for the next section is to determine the number, nature and value of these resistances in parallel in the case of real contacts of different metals: *sp*-like metals, transition metals, etc.

6.4   Analysis of different metallic atomic-size contacts

In this section we shall analyze the theoretical results obtained with the model described in the previous sections. We shall cover a wide range of metals, investigating specially superconducting elements which allow us an experimental comparison. Thus, we shall study *sp*-like metals like Al and Pb, transition metals like Nb, and we end this section commenting the case of simple and noble metals.

6.4.1   *sp*-like metals: Al and Pb

First, we shall analyze *sp*-like metals of the group IIIA and IVA of the periodic table. As examples we take Al and Pb, two superconducting elements which permit an experimental comparison using the *channel spectroscopy* [143] (see section 6.5). Let us start by analyzing in detail the case of Al contacts which was the main motivation of this work [143].

As stated in section 6.2, for these metals we choose as a minimum basis that formed by the *s* and *p* orbitals. Moreover, we describe the *p* band with the basis formed by the orbitals p_x, p_y, p_z whose wave functions are real (see for instance Ref. [249]).

Al contacts

The atomic configuration of Al is $3s^2 3p^1$, what gives rise to a conduction *sp* band with three electrons per atom. Fig. 6.5 shows the Al bulk density of states decomposed in orbitals after Ref. [250]. As it can be observed, the $3s$ and $3p$ bands give the main contribution to the density of states at the Fermi level. The e_g and t_{2g} bands refer to the $3d$ bands, which have certain weight at the Fermi level but they are practically empty, and by the moment we do not include them in our minimum basis [7]. The levels $3s$ and $3p$ are separated by an energy of 7.7 eV.

---

[7]In chapter 7 we shall show that these *d* orbitals have certain influence in the value of the total conductance due to the hybridization with the *p* orbitals. However, their inclusion does not modify the main conclusions of this chapter.
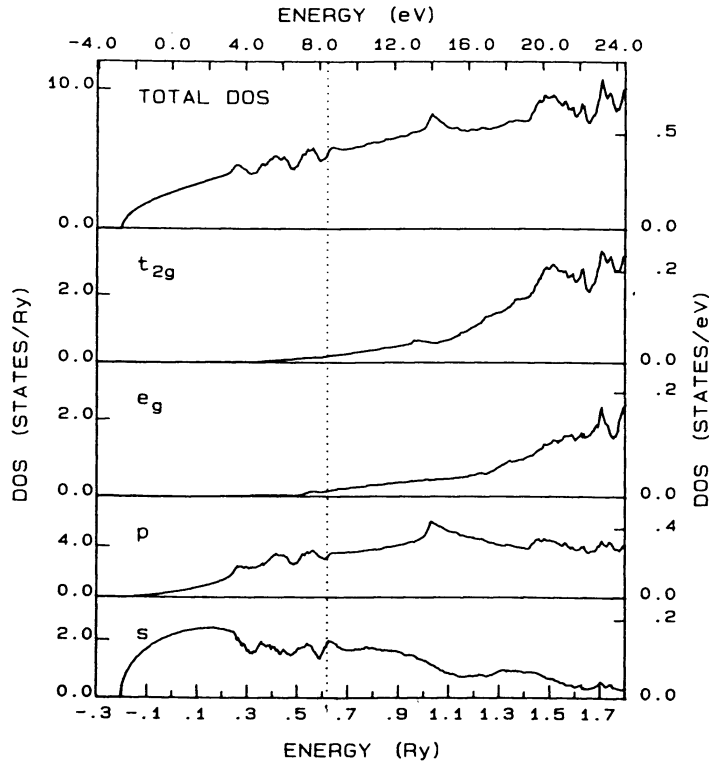
Figure 6.5: Al bulk density of states: the total one and the decomposition into orbitals [250]. The e_g and t_{2g} refer to the $3d$ bands.

While the simple argument discussed in section 6.3 predicts a maximum number of four channels for a one-atom contact, the self-consistent calculation for the ideal geometry of Fig. 6.1 yields only three channels with nonvanishing transmission. In order to be sure that the results are not a consequence of finite-size effects, we have analyzed contacts with different number of layer (N). We have found that although the contact transmission depends on its size, neither the number of channels nor their character depend on the system size. Thus for instance, in Fig. 6.6 we show the transmission eigenvalues as a function of energy for the ideal geometry (without disorder) for the case of a short neck ($N = 1$) and a long neck ($N \to \infty$) [8]. As it can

[8]The case $N \to \infty$ was done using a recursive method described in [255], which is specially adapted to efficiently calculate local quantities like the density of states in a given atom. This method permits us to include a large number of atomic layers. In particular, in Fig. 6.6 100 atomic layers ($> 10^5$ atoms) were introduced.

be observed, the transmission values change slightly, but there are certain features
that are common to both cases:
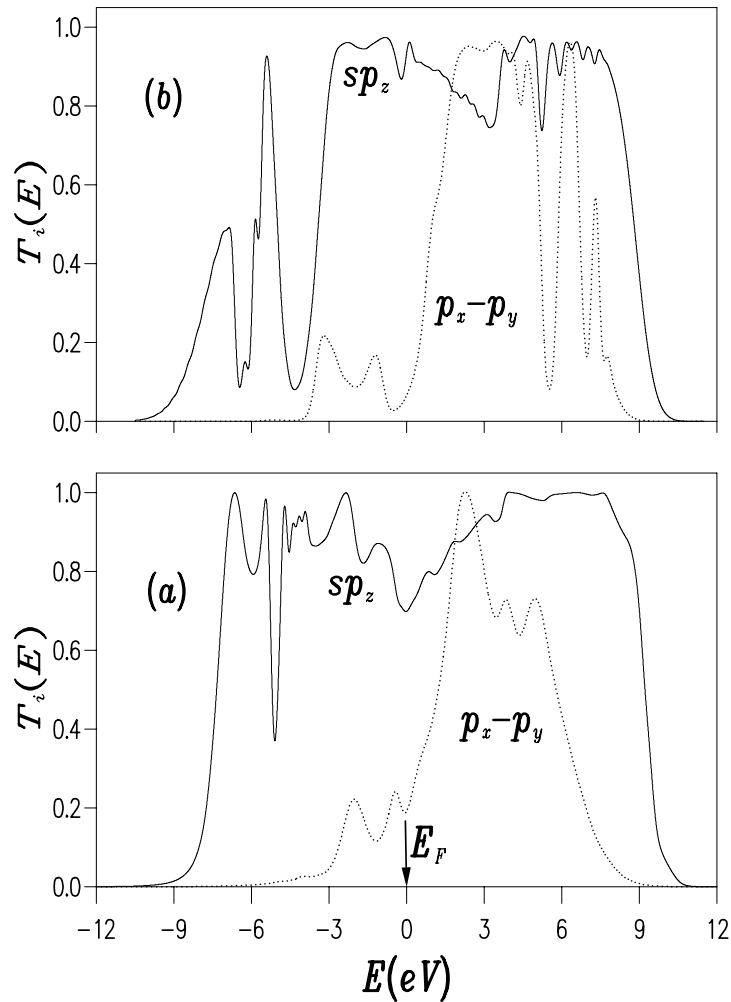
Figure 6.6: Transmission eigenvalues as a function of energy for Al one-atom contacts
in the two extreme cases: (a) short neck ($N = 1$) and (b) long neck ($N \to \infty$) (see
footnote 8). The solid curve corresponds to the nondegenerate sp_z mode and the
dotted curve corresponds to the twofold degenerate $p_x - p_y$ mode (see text).

1. There are three channels having a significant transmission around the Fermi

energy, the fourth one (not shown in Fig. 6.6) being almost closed for every energy.

2. The total transmission is close to one around the Fermi energy increasing to almost three at higher energies.

3. There is a nondegenerate mode which is widely open for almost every energy.

4. The second transmission eigenvalue is twofold degenerate and has a small value around the Fermi energy.

As commented in the previous section, the analysis of density of states may help us to understand better the results. Fig. 6.7 shows the local density of states (LDOS) at the central atom for the case of one atom between two surfaces, i.e. for the case of Fig. 6.6(a). Panel (a) shows the LDOS separated in the different orbitals and panel (b) shows a natural decomposition (as we shall see below) in a sp_z hybrid orbital and in a p_x or p_y orbital. Let us comment some interesting features of the LDOS at the central atom. As can be observed, there is a splitting between the p_z and $p_{x,y}$ orbitals, which is due to fact that the contact geometry breaks the symmetry of bulk material (let us remember that z is the direction of the contact axis). This fact gives rise to a p_z "effective level" with a lower energy, causing that the p_z band be hybridized with the s one forming a sp_z band. Moreover, the larger coupling between the central atom p_z orbital and its neighbors provokes that the p_z band be broader than the p_x and p_y bands. Another remarkable feature of the central atom LDOS is the degeneracy of the p_x and p_y bands. This is due to the rotational symmetry of the ideal geometry around the z axis. It is evident that this degeneracy will be broken by the introduction of disorder in the constriction. Finally, notice the position of the Fermi level. The charge neutrality condition tell us that we must locate three electrons in the central atom. This implies that the Fermi level lies at the beginning of the $p_{x,y}$ bands, what makes that the corresponding channels have a small transmission.

Let us next analyze the nature of the conducting channels. In the case of an one-atom contact we can classify the different modes according to the orbital character of the eigenvalues in the central atom (see Eq.(6.9)). Thus, every channel is a linear combination of the central atom orbitals as follows

$$|canal\ i\rangle = c_{s,i}|s\rangle_c + c_{p_x,i}|p_x\rangle_c + c_{p_y,i}|p_y\rangle_c + c_{p_z,i}|p_z\rangle_c, \qquad (6.17)$$

where $|\ \rangle_c$ indicates the corresponding orbital of the central atom. In order to illustrate the relative weight of the different orbitals in each mode, we show in Fig. 6.8 the modules square of the coefficients for each mode (case $N = 1$), normalized to the corresponding channel transmission. As can be observed in Fig. 6.8, the
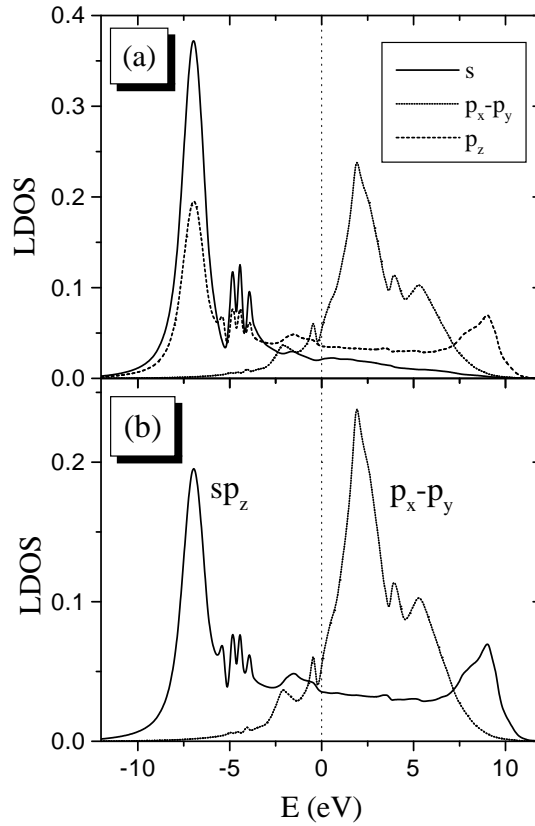
Figure 6.7: Local density of states (LDOS) at the central atom in an Al one-atom contact with $N = 1$. (a) LDOS decomposed into the four orbitals. (b) LDOS decomposed into sp_z and $p_{x,y}$ bands.

dominant mode is a combination of the s and p_z orbitals. For this reason we denote this mode as sp_z, as we did in Fig. 6.6. The second eigenvalue, which is twofold degenerate, lives in the subspace formed by p_x and p_y orbitals [9]. Hereafter we refer to this mode as $p_{x,y}$. The fourth channel, which is almost closed for every energy, is the antisymmetric combination of the s and p_z orbitals. In Appendix E we explain in detail the mathematical reason of this destructive interference. First, due to the contact geometry there is a splitting between the p_z and $p_x - p_y$ orbitals, causing

---

[9]As this mode is twofold degenerate, one can choose the character as it is shown in the figure.
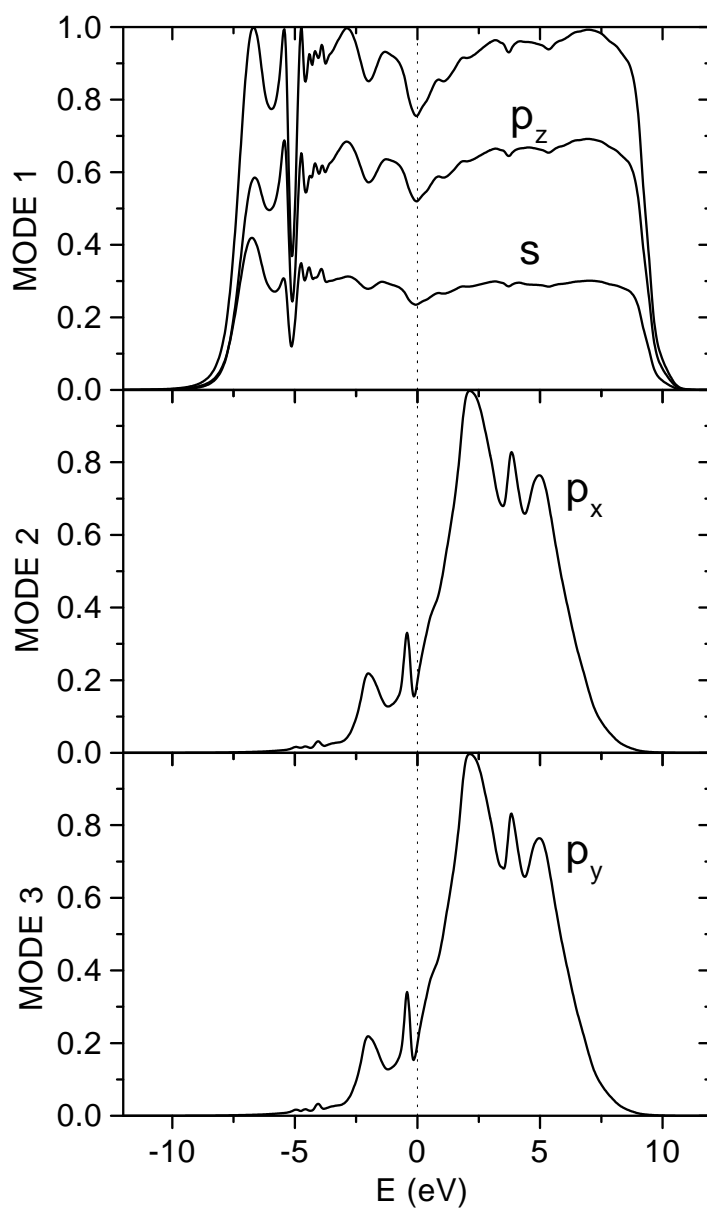
Figure 6.8: Orbital character of the conducting channels in an Al one-atom contact. The dominant mode (mode 1) is a combination of the s and p_z orbitals. The twofold degenerate mode (mode 2, mode 3) lives in the $p_x - p_y$ subspace.

that the problem of determining the transmission divides into two (2×2) problems. Thus, we have the $s - p_z$ subspace, where the fourth channels lies, and the $p_x - p_y$ subspace. As explained in Appendix E, the reason for having a vanishing eigenvalue in the $s - p_z$ subspace is that the hoppings connecting the central atom and the electrodes verify the approximate condition $t_{ss}t_{p_z p_z} \sim t_{sp_z}t_{p_z s}$, which is verified for almost all materials. Thus, we may say that this channel is closed due to a destructive interference due to the symmetry of the s and p_z orbitals.
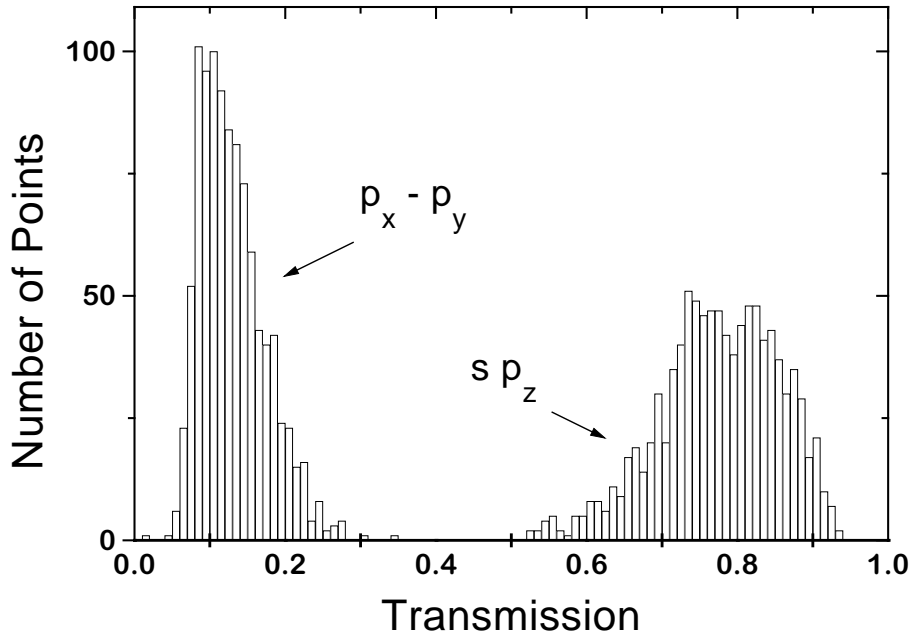
Figure 6.9: Typical distributions of the transmission eigenvalues for an Al one-atom contact when disorder in the atomic positions is included (the maximum fluctuation in the hopping parameters is of the order of 100% with respect to the bulk values, which corresponds to variations of the order of 20% in the interatomic distances). In this case the central region has 7 atomic layers. The two modes corresponding to the twofold degenerate eigenvalue in the idealized case exhibit a similar distribution.

The results shown so far are in a good agreement with the experimental findings of Scheer *et al.* [143] (see also Chapter 5). However, no real contact has exactly the ideal geometry that we have analyzed. The theoretical conclusions should be robust against the inclusion of disorder. We have studied this effect by introducing random fluctuations in the atomic positions of the idealized structure, assuming the distance

dependence on the hopping parameters as suggested by Harrison [249], which tell us that the s and p hoppings decay with the square of the distance between neighbors. Although there are certain features like the twofold degeneracy which, as expected, disappear with the inclusion of disorder, the gross features found for the ideal geometry are nevertheless robust. This fact is illustrated in the histograms shown in Fig. 6.9 for the individual transmissions. Although the channels are no longer sp_z and $p_{x,y}$ exactly, we still keep on denoting like this to indicate their approximate character. Furthermore, the p_x and p_y modes have similar distributions and we only show an histogram for them. As can be observed, the decomposition of the total transmission consists of a dominant channel with transmission between 0.6 and 0.9, and two more with small transmissions between 0.1 and 0.3. Maybe the most remarkable thing is that the fourth channel remains closed with a transmission $< 10^{-3}$. As we explain in Appendix E, the condition by means of which the antisymmetric sp_z channel remains closed is quite robust against the inclusion of disorder (see Appendix E). These predictions are consistent with the experimental results of Ref. [143] for the case of the Al last plateau.

Finally, we have checked that other factors, like the inclusion of second-neighbors hoppings or different crystallographic directions, do not modify the main conclusions about the number and nature of the conducting channels. This is an indication of that the channels are basically controlled by the central atom. The only difference that one finds is in the transmissions of the individual channels. For instance, we have found that the total transmission in a contact grown in the (100) direction tends to be greater that the one of a contact grown along the (111) direction. Thus, we can say that the local environment of the central atom mainly control the channel transmissions.

Pb contacts

After the analysis of Al contacts, one wonders how these results are generalized for the case of an arbitrary sp metal. From the analysis of the previous subsection one could conclude that the number of channels will be three for every sp-like metal, because this number only depends on the orbitals which play a role. Moreover, one would expect a similar classification for the channels: a sp_z channel and $p_{x,y}$ channels. On the other hand, the main change in the transmission can be due to the valence of the metal, since this will determine where the Fermi level lies. To confirm these impressions, we shall analyze the case of Pb, which has a different valence and is also a superconductor, allowing thus the experimental comparison.

Pb is a metal of the group IVA with an electronic structure $6s^2 6p^2$, which gives rise to a sp conduction band with four electrons per atom. Fig. 6.10 shows its bulk
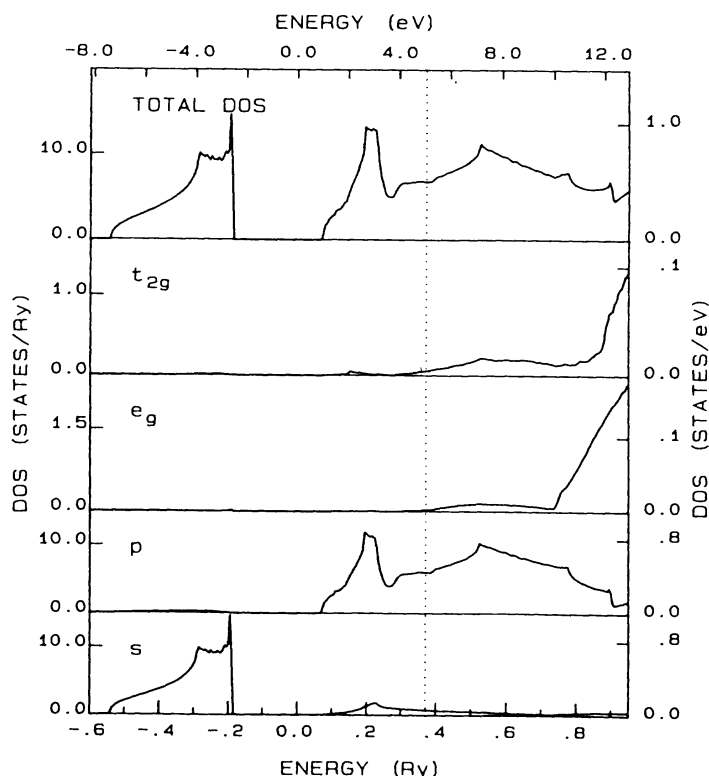
Figure 6.10: Pb bulk density of states: the total one and its decomposition into orbitals [250]. The bands e_g and t_{2g} refer to $6d$ bands.

density of states after Ref. [250] [10]. In its decomposition into orbitals we see that the main contributions around the Fermi level come from the s band and specially from the p one. On the other hand, the d bands are practically empty and do not play an important role. The $6s$ and $6p$ energy levels are separated 10 eV approximately in the bulk material.

Fig. 6.11 shows the local density of states at the central atom and the transmission as a function of energy for an Pb one-atom contact. The result corresponds to the ideal geometry of Fig. 6.1 with $N = 1$ [11]. With respect to the transmission,

---

[10]In this calculation of the Pb bulk density of states spin-orbit coupling has not been included. This effect can be relevant in the case of Pb.

[11]As in the Al case, this is a representative case of what happens for any number of layer in the neck contact.
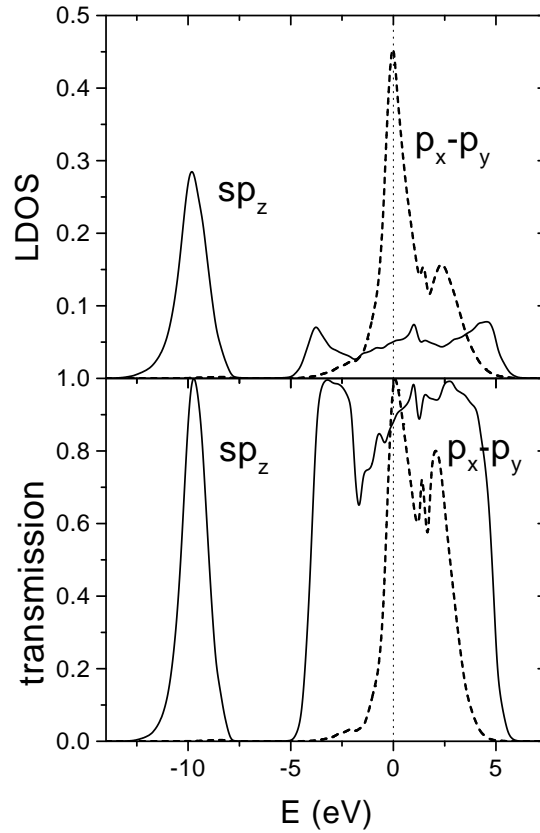
Figure 6.11: Local density of states at the central atom and transmission as a function of energy for a Pb one-atom contact. The LDOS has been decomposed into a sp_z band and a $p_x - p_y$ band. We find three transmission eigenvalues: one with sp_z character and a two-fold degenerate with $p_x - p_y$ character.

there are several remarkable features:

1. There are three channels with non-negligible transmission, the fourth one is almost closed for every energy ($T_4 < 10^{-3}$) and is not shown in Fig. 6.11.

2. The total transmission is ~ 2.8 around the Fermi level.

3. There is a mode which is open for a wide range of energies.

4. The second transmission eigenvalue is two-fold degenerate and is almost perfectly open around the Fermi level.

As it can be observed in Fig. 6.11, the energy dependence of both the density of states and the transmission is similar to the ones of Al case. This implies that the number of channels and basically their character are the same as in the Al case. However, there is an important difference. As in the Pb case there are four valence electrons, the Fermi level lies at higher energies than in the Al case. To be precise, the Fermi level lies around the center of the p bands where the three channels are almost perfectly open. This implies that the total conductance, in the case of Fig. 6.11, is of the order of 2.8. As we shall show in Chapter 7, the fact that the Fermi level lies in the center of p bands has also repercussions in the behavior of the Pb last conductance plateau, which exhibits a different tendency to the one of Al.

Fig. 6.12 shows the orbital character of the different channel in the same way we did in Fig. 6.8 for Al. As can be seen, the decomposition is similar to the one found for Al. We have a mode which is a combination of the s and p_z orbitals, and the two-fold degenerate lives in the subspace $p_x - p_y$. The fourth channel is a combination of the s and p_z orthogonal to the one of mode 1, and it remains almost closed for every energy for the reason explained in the Al case.

Thus, we have confirmed the conjecture that we did at the beginning of this subsection, in the sense that the number and nature of the channels only depend on the number and nature of the valence orbitals of the central atom.

6.4.2   Transition metals: Nb

As an example of transition metal we shall next study one-atom contact of Nb, a metal which is superconductor below 9.26 K, and in the next section we shall show an experimental comparison using the channel spectroscopy.

Nb is a transition metal whose atomic structure is $4d^4 5s^1$, with five valence electrons. Fig. 6.13 shows the bulk density of states [250]. As can be observed, the main contribution around the Fermi level come from the s and d bands. The p bands (coming from the $5p$ orbitals) is practically empty and we do not include them in the calculations. For describing the d bands we choose the basis formed by the orbitals d_{xy}, d_{yz}, d_{zx}, $d_{x^2-y^2}$ and d_{z^2}, whose wave functions are real (see for instance Ref. [249]).

As commented in section 6.3, in this case the maximum number of conducting channels is expected to be six due to the contribution of $5s$ and $4d$ orbitals. The idealized one-atom contact geometry yields in this case a total transmission between 2 and 3 depending on the number of layers in the central region. The channel decomposition shows that this total transmission is mainly built up from the contribution of five conducting channels, and in some occasions six depending on the size of the
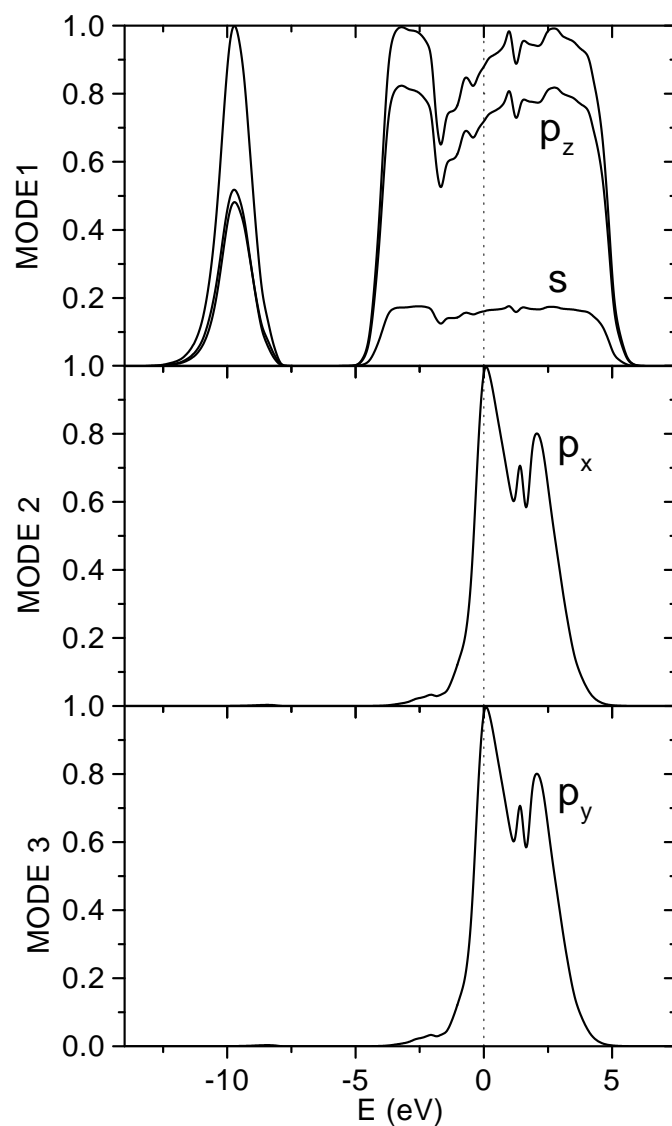
Figure 6.12: Orbital character of conducting channels in a Pb one-atom contact. The mode 1 is a combination of s and p_z orbitals and the two-fold degenerate mode (mode 2, mode 3) lives in the subspace $p_x - p_y$.

central region. Fig. 6.14 shows the transmission for the case of a long neck, obtained by means of the recursion method commented in footnote 8. We believe that this is
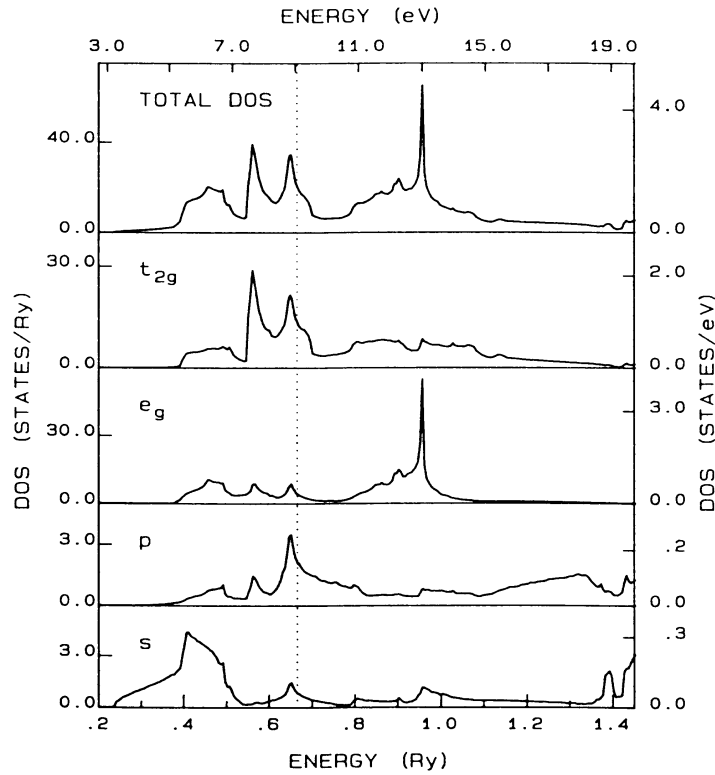
Figure 6.13: Nb bulk density of states: the total one and its decomposition into orbitals [250]. The bands e_g and t_{2g} refer to $4d$ bands.

the most representative situation. As can be observed, the d bands cause a strong energy dependence of the transmission eigenvalues, with typical energy scales of the order of 0.5 eV. The s and d_{z^2} hybridize strongly and give rise to the conducting channel with highest transmission around E_F (mode 1 in Fig. 6.14). The almost closed channel (mode 6 in Fig. 6.14) corresponds to the orthogonal combination of these two orbitals. There also appears a twofold degenerate channel with transmission ~ 0.7 and another twofold degenerate channel with transmission ~ 0.3 [12]. The total transmission is 2.5 for this case.

Let us analyze in more detail the origin of the transmission decomposition in

---

[12]This double degeneracy is due to the symmetry of the ideal geometry and it is also due to the fact of that we have not taken into account the splitting between the different d levels in order to simplify the analysis of the problem.
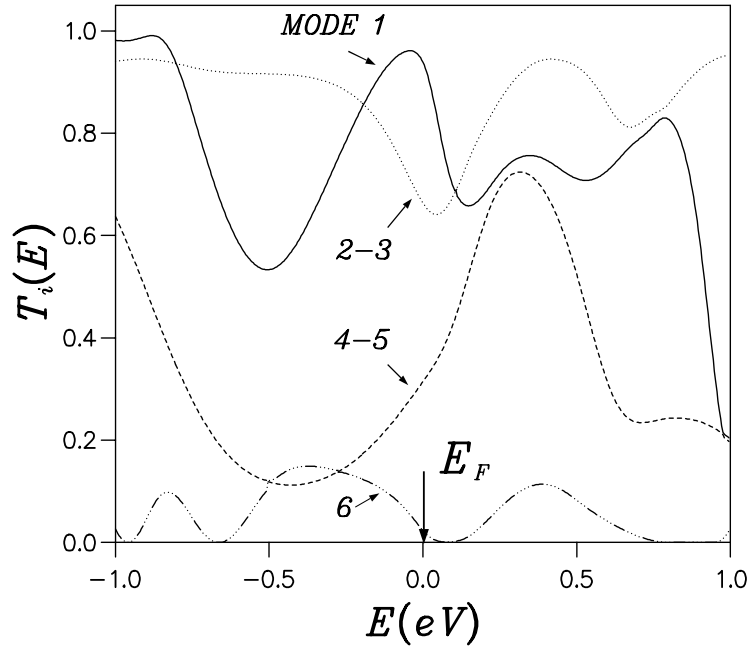
Figure 6.14: Transmission eigenvalues as a function of energy for a Nb one-atom contact for the long neck case ($N \to \infty$, see footnote 8). Notice the twofold degeneracy of modes 2-3 and 4-5.

the case of this transition metal. As usual the study of the density of states will help us for this purpose. Fig. 6.15(a) shows such density at the central atom for the case of the ideal geometry with $N = 1$, decomposed into the six orbital that we are considering. As one can see, there are two twofold degeneracies due to contact symmetry. This double degeneracy is reflected in the transmission, giving rise to two twofold degenerate modes, as can be observed in Fig. 6.15(b). It is evident that these degeneracies will disappear in a real contact due to the presence of disorder. As can be observed, for the case of one atom between two surfaces we have a non-negligible contribution of the sixth channel.

The symmetry of the orbitals controls again the nature of conducting channels. Fig. 6.16 shows the character of the modes defined as in the same way as for Al and Pb. We can see that the dominant channel is, as we said above, a combination of the s and d_{z^2} orbitals (mode 1 in Fig. 6.16). The orthogonal combination of these two orbitals gives rise to a channel with transmission ~ 0.3 at the Fermi level (mode 4 in Fig. 6.16). This is similar to the situation that takes place in sp-like metals for

177
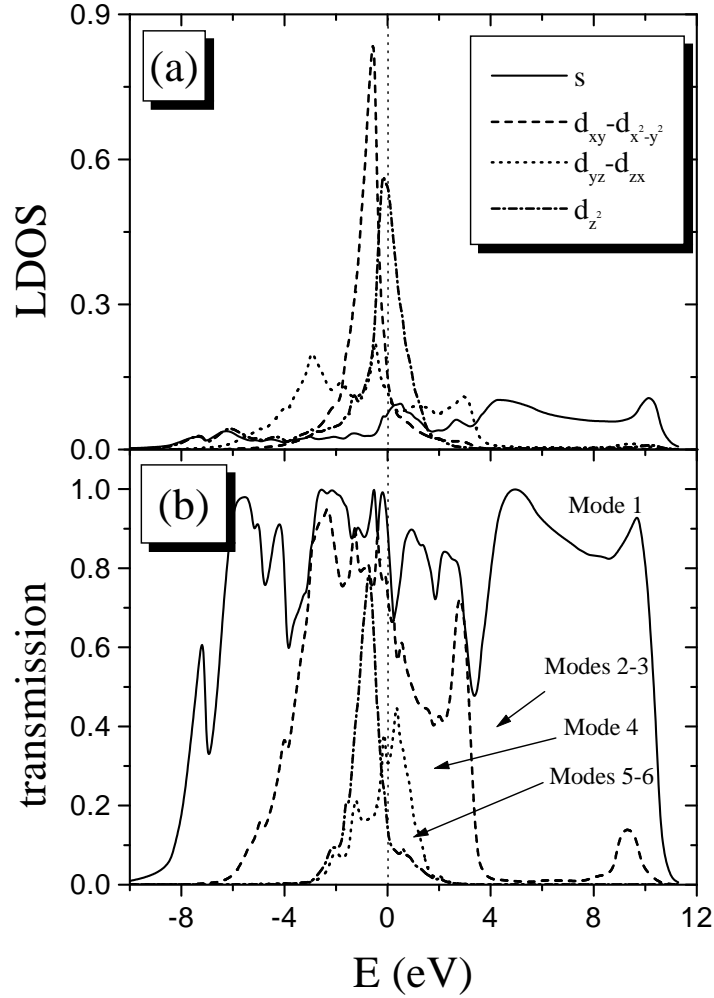
Figure 6.15: (a) Local density of states at the central atom and (b) transmission eigenvalues as a function of energy for a Nb one-atom contact for the short neck case ($N = 1$). Notice the degeneracy of modes 2-3 and 5-6. The Fermi level position is indicated by a vertical dashed line.

the dominant channel and the closed one. On the other hand, the two modes with transmission ~ 0.7 (modes 2 and 3 in Fig. 6.16) are combinations of the d_{xy} and d_{yz} orbitals, and d_{zx} and $d_{x^2-y^2}$. At the Fermi level they have a d_{yz} and d_{zx} character

respectively, what is similar to the decomposition in channels $p_x - p_y$ in the sp-like metals. Finally, the other two modes with transmission ~ 0.1 (mode 5 and 6 in Fig. 6.16) are the orthogonal combinations to the previous two modes, having at the Fermi level a character d_{xy} and $d_{x^2-y^2}$ respectively.

In summary, in the case of contacts of transition metals the d orbitals play a crucial role in the transport properties, providing additional conducting channels [237]. In general, this implies that in the context of atomic circuits the transition metals are better conductors than other types of metals, inverting the typical situation that takes place in macroscopic circuits. The contribution of the d orbitals provokes that the last plateau conductance in transition metal contacts be usually greater than the quantum [82, 237], thus there is no conductance quantization in this case.

6.4.3 Simple metals and noble metals

Our theory, as well as the experimental results that we shall show in the next section, show that atomic contacts of metals which have an important contribution from the p and d orbitals do not necessarily, even in the one-atom case, exhibit an integer number of perfectly transmitting modes. In other words, there is no conductance quantization neither in the sp-like metals nor in the transition metals.

This situation is at variance with that of simple metals like Na or noble metals like Au, Ag and Cu, in which the conductance exhibits certain tendency to adopt multiples of the quantum, specially in the last plateau where $G \sim G_0$ [214, 82, 216, 219, 223]. Traditionally, there is the extended belief that this case is well-understood. The free electron models obtain the conductance quantization in these metals *ad hoc* and some tight-binding calculations also show it [248]. But, it is difficult to find in the literature an argument explaining why the quantization is so robust, in the sense that is not affected by disorder and remains along the last plateau (which is completely flat). Within our model these metals are described simply with a s band with one electron per atom. Therefore, in this case we obtain a single conducting channel. But still one has to explain why this channel is usually completely open. A possible explanation has been pointed out in a recent paper by Levy Yeyati *et al.* [252]. In this work it is shown the possibility of the existence of resonances in the local density of states in contacts of monovalent metals. Due to the charge neutrality condition the Fermi level lies in the center of a resonance giving rise to a quantum conductance for the case of an one-atom contact. Moreover, this result is robust with the inclusion of disorder.

In the next chapter we shall analyze the different tendencies of the conductance plateaus under elastic deformations. In particular, we shall study the case of Au contacts, which shows a flat last conductance plateau. Thus, we postpone the results for a monovalent metal until that chapter. Let us say that the results that we shall show are in agreement with the ones obtained in Ref. [252].
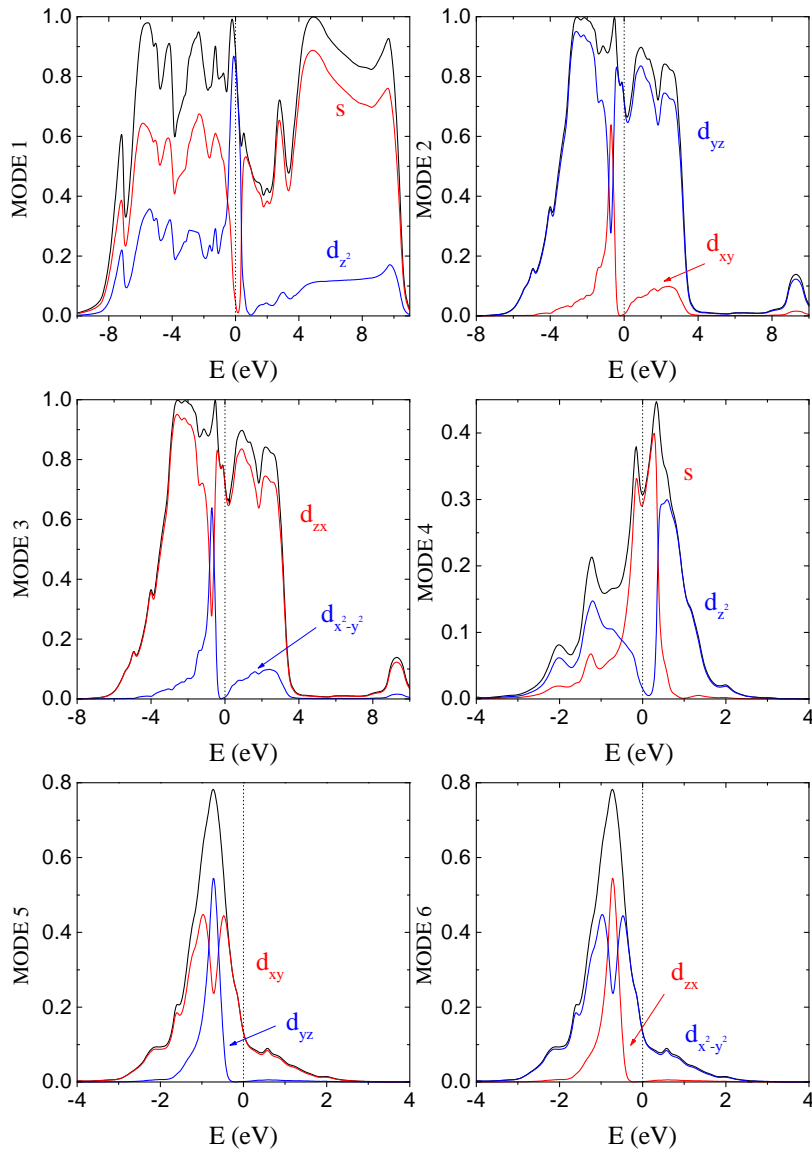
Figure 6.16: Orbital character of the channels for the Nb case of Fig. 6.15. The nature of each channel is indicated in each panel and the Fermi level position is indicated with a vertical dashed line.

6.5   The signature of the chemical valence in the electrical conduction through a single-atom contact

So far we have seen that the number of conducting channels in an one-atom contact is determined by the available valence orbitals, and thus varies for metals along the periodic table. These predictions were tested experimentally in a collaboration which gave rise to Ref. [146]. For this purpose we analyzed atomic-size constrictions of four elements (Pb, Al, Nb y Au), covering a broad range of valences and orbital structures. In order to obtain information on the individual channels we made used of the superconductivity through the channel spectroscopy [146]. This section is devoted to the description of the experimental results which were obtained in the mentioned work.

In this work [146], various experimental methods to achieve stable atomic-size contacts were used: a scanning tunneling microscope (STM) for the measurements on Pb [214], mechanically controllable break junctions for Nb [240], and lithographically fabricated versions of the latter [256] for Al and Au. Fig. 6.17 shows the typical development of the conductance G for the four metals as the contacts are stretched. The total conductance decreases by steps until the contact breaks. After that it decreases exponentially with distance, the signature of the tunnel regime. The stepheights are in the order of G_0, while the series of "plateaux" is different for each individual opening of the contact. It has been shown that the origin of the steps is in atomic rearrangements [230, 257, 213] which occur while the constriction is elongated. The typical value of G at which the contact breaks, the lengths of the plateaux, and the behavior within the plateaux are characteristic of each material. Pb shows plateaux with negative slope, and an almost continuous decrease of G between 3 G_0 and 1 G_0, where the contact usually breaks. Al has plateaux with positive slope, and breaks at around G_0 with a jump to $G < 0.1\ G_0$. Nb displays negatively inclined plateaux, smallest contacts with conductances between 2 G_0 and 1 G_0, and a jump to a tunneling conductance as high as $G \approx G_0$. For our lithographic Au samples we obtain less well defined plateaux. The last contact before break typically has a conductance between 0.3 G_0 and 0.6 G_0.

We can stop the elongation at any point and record the IVs. With the junction in the vacuum tunnel regime, the IV corresponds well to the one expected for a single channel as shown for Pb in curve (e) of Fig. 6.18. In the contact regime one observes IVs as depicted in curves (a) to (d) of the same figure. These curves were recorded on the same sample for different last plateaux before breaking. It is usually assumed that these smallest stable contacts are one-atom contacts [240]. As we shall show this analysis will give further support to this assumption. The occurrence of IVs with different sub-gap structure for the same total conductance (see Fig. 6.18) reveals the importance of the geometrical environment of the central atom for the conduction
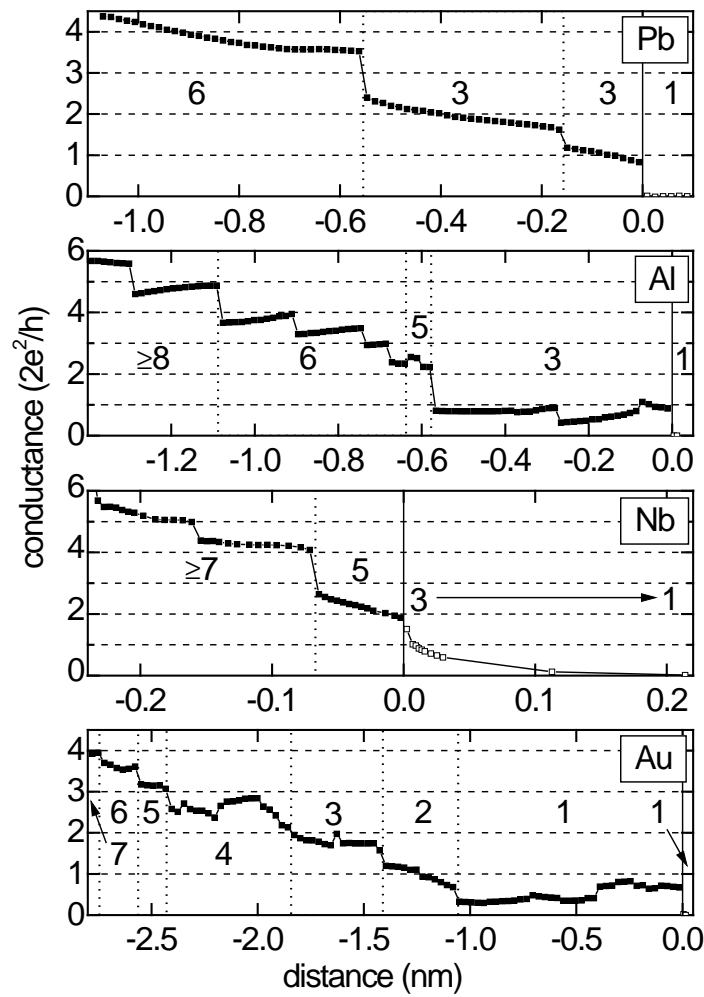
Figure 6.17: Typical conductance G as a function of distance, recorded in a continuous opening of the samples, for four different metals. The distribution of transmission values $\{T_n\}$ is establish by fitting the IVs recorded at each point. The data have been taken at a temperature of 1.5 K for Pb, below 100 mK for Al and Au and 1.6 K for Nb. The opening speeds were in all cases in the range 1-10 pm/s. The symbol " $\geq$ " means that only a lower bound for N could be determined. Plateaux corresponding to different N are separated by dotted vertical lines. The horizontal arrow indicates that N decreases in the tunnel regime. Filled symbols indicate contact regime, open symbols tunnel regime.

properties. In general, the IVs in the contact regime cannot be described by the single channel theory. We shall assume that the total current can be decomposed as

(see Chapter 2)

$$I(V) = \sum_{n=1}^{N} i(T_n, V) \tag{6.18}$$

where $i(T_n, V)$ is the current of channel n. The solid curves in Fig. 6.18 are fits to the experimental IVs using the previous expression, and the theoretical curves $i(T, V)$ calculated in Chapter 2 [112], with the set $\{T_n\}$ and the number of channels N as fitting parameters. Details of the analysis are given in [146].
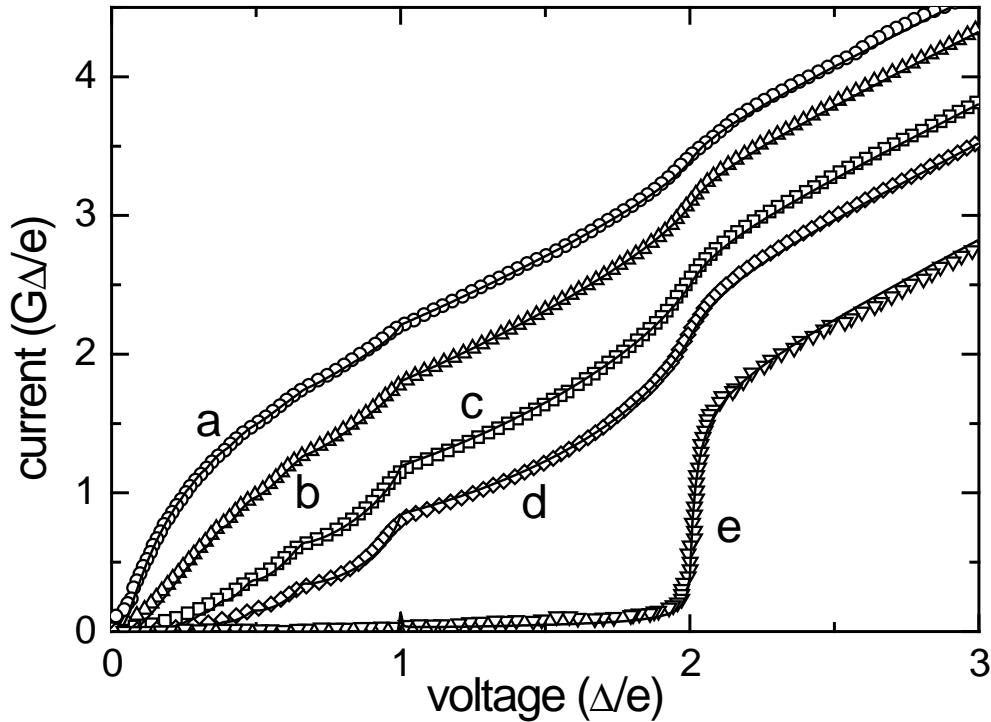
Figure 6.18: Measured current-voltage characteristics (plotting symbols) of five different configurations of a Pb sample at 1.5 K using STM, and best numerical fits (lines). Curves a-d have a very similar total transmission, close to 1.4; curve e has been taken in the tunnel regime. The individual channel transmissions obtained from the fits are: (a) $T_1 = 0.955$, $T_2 = 0.355$, $T_3 = 0.085$, $T_4 = 0.005$; (b) $T_1 = 0.89$, $T_2 = 0.36$, $T_3 = 0.145$, $T_4 = 0.005$; (c) $T_1 = 0.76$, $T_2 = 0.34$, $T_3 = 0.27$, $T_4 = 0.02$; (d) $T_1 = 0.65$, $T_2 = 0.34$, $T_3 = 0.29$, $T_4 = 0.12$; (e) $T = 0.026$. Voltage and current are in reduced units. The measured superconducting gap was $\Delta/e = 1.37$ mV.

For Pb it turns out that three or four channels contribute to the total current for

the smallest contacts. Despite the fact that more than two channels are available, G can be well below 2 G_0. For larger contacts with $G \geq 3$ G_0, we find six or more channels. The numbers N of channels we found at the different plateaus are indicated in Fig. 6.17. Only channels with a transmission larger than 1% of the total transmission are taken into account when determining N. Applying a similar analysis to different metals, we arrive at the important conclusion that the maximum number of channels N_{max} for the smallest contacts is characteristic for a given metal. In the IVs of Al smallest contacts we find typically the contributions of three channels, whereas for Nb we detect five channels. These results support the idea that N_{max} for one-atom contacts is limited by the number of valence orbitals of the central atom N_{orb}.

Our theoretical predictions are in good agreement with these experimental observations: smallest Pb contacts just before breaking most frequently have a G between 1 G_0 and 3 G_0. The decomposition usually results in three or four channels, where the T_n of the fourth one, if present, is usually smaller than 0.03. We neither find last plateaux before breaking with only one or two, nor with five channels. Typically the analysis of the last plateau yields one well transmitted mode with $T_n > 0.6$ and two smaller non-degenerate ones with $T_n \leq 0.4$. We attribute the lack of degeneracy and the smaller T_n's to an asymmetrical environment around the central atom in the experimental contacts.

In the previous section we already pointed out that there exists an agreement for Al in relation with the experiment of Ref. [143]. Again, in Fig. 6.17 one can see a last plateau with G just below G_0 distributed over three channels. The case of an Al atom sandwiched between two flat surfaces has already been treated with density functional [236] and other *ab initio* calculations [258], which predicted $G \simeq 2$ G_0.

Let us recall that for the case of Nb our calculation predicted a total conductance $G \simeq 2.5$ G_0 (see Fig. 6.14) decomposed in five channels, again in agreement with the experimental findings (see third panel of Fig. 6.17). The experimental determination of $\{T_n\}$ is less precise than for Pb and Al, because the quasiparticle density of states for Nb differs slightly from the one used for calculating the $i(T, V)$. (Deviations of the quasiparticle density of states from the case considered in the theory mostly affect the shape of the current steps around $V = 2\Delta/me$ but not the current values in between. Therefore the analysis with the unmodified density of states is still possible.) An additional difference from the Pb and Al case is observed in the tunnel regime: for Nb contacts just after breaking, three channels contribute to the tunnel current. With increasing distance between the electrodes, one channel becomes dominating.

The cases discussed so far correspond to superconducting elements having several valence orbitals per atom. A crucial test for the validity of our analysis would be provided by monovalent metals like Au and Na. As commented in the previous section, these metals can be described by a single s orbital, and the model predicts

a single channel with $T \simeq 1$ for an one-atom contact [252] in accordance with calculations based on molecular dynamics simulations [259]. As these monovalent metals are not superconducting, our method of characterizing channels is not directly applicable. However, a small piece of normal metal in good contact with a large piece of a superconductor develops a gap in its quasiparticle density of states [260]. The lithographic MCB technique allows for the fabrication of a constriction, where the central region consists of Au atoms, embedded in a superconducting Al environment. Using shadow evaporation through a suspended mask we evaporate 400 nm thick Al electrodes separated by 50 nm wide spacing, which is filled with a 20 nm thick Au layer deposited at a different angle under the same vacuum. The large asymmetry in thickness limits the influence of the normal metal on the quasiparticle density of states. As depicted in the lowermost panel of Fig. 6.17, we find indeed that the smallest Au contacts accommodate one single channel, contrary to the results for the sp-like and transition metals. However, we usually measure transmission values significantly below one. As for the other metals we interpret this reduced T with respect to the model predictions as arising from disorder in the contact. Our Au samples are presumably more prone to disorder because of the very small Au layer thickness. Considering that the accuracy in determining $\{T_n\}$ is limited also because of the slightly modified quasiparticle density of states, the single channel fit is still very satisfactory in the case of Au.

6.6   Conclusions

From the experimental results that we have shown in the previous section we draw the following conclusions. First, these results provide clear evidence that the smallest contacts produced by the different experimental techniques are indeed one-atom contacts, as the number of channels never exceeds the number of valence orbitals. We stress that in these experiments a single atom determines a macroscopic quantity, that is, the total conductance of the macroscopic circuit in which it is embedded. The current which an one-atom contact can sustain can be as large as $100\,\mu$A, corresponding to the very large current density of $10^{11}\,\mathrm{Acm}^{-2}$. This large current is carried by a small number of conducting channels.

On the other hand, the ensemble of the experimental and theoretical results show unambiguously that the conducting channels in an atomic contact are determined by the orbital electronic structure and the local atomic environment around the neck region. In particular, for the case of one-atom contacts the conducting channels are determined by the chemical nature of the central atom. As a simple rule, we could say that the number of active channels corresponds to the number of valence orbitals of such atom. For the case of an one-atom contact, the detailed calculations, in agreement with the experimental results, predict the presence of three conducting

channels for *sp*-like metals like Al or Pb. For transition metals like Nb, we expect the presence of five conducting modes due to the contribution of *d* orbitals. In the case of simple metals like Na or noble metals like Au, we expect the presence of a single conducting channel due to the contribution of the *s* band. These essential facts cannot be understood within a free electron model. Only a microscopic model that takes into account the atomic orbital structure as well as the local atomic geometry can fully explain the conduction properties of these contacts.

With respect to the conductance quantization, the results shown in this chapter indicate that this phenomenon does not take place in atomic contact of *sp*-like metals or transition metals due to the contribution of *p* and *d* orbitals respectively. As we have shown, in these contact there are channels with intermediate transmission, even in absence of disorder. The conductance quantization is thus reserved for simple metals or noble ones, where we have only the contribution of the *s* band.

Several authors have pointed out that the histograms are an indication of the statistical origin of the conductance quantization in metallic contacts [261, 262]. However, as we have shown in this chapter, even in the case of an one-atom of a *sp*-like metal or a transition metal we have always the contribution of several channels with intermediate transmissions. Thus, it seems difficult the appearance of integer multiples of the quantum conductance, and even the appearance of peaks in the histograms. Indeed, when one revises the literature this is precisely what happens in contacts of transition metals like Pt, Ni, Co, Ti o el Fe [82, 237, 263, 265], there is neither quantization nor peaks in the conductance histograms.

186

Chapter 7

Evolution of conducting channels under elastic deformation

7.1 Introduction

In recent experiments a combination of scanning tunneling microscopy (STM) and atomic force microscopy was used to study simultaneously the electrical and mechanical properties of atomic-size contacts [226, 227, 228, 229, 230]. In these experiments a metallic contact formed between tip and substrate is elongated or contracted. This deformation proceed in a sequence of elastic stages alternating with sudden atomic rearrangements [210, 211, 213]. During the elastic stages the conductance changes gradually resulting in gently sloped plateaus while the atomic rearrangements show as sharp conductance steps which are hysteretical. The conductance of the last plateau before rupture is of the order of one quantum of conductance, $G_0 = 2e^2/h$. As commented in the previous chapter, this last plateau corresponds to an one-atom contact.

As it was shown in section 6.5, the observed dependence of the conductance on elastic deformation varies from contact to contact but it is characteristic for a given metal. The first work which paid attention to the tendencies of the plateaus under elastic deformation of contacts of different metals was done by Krans $et\ al.$ [82], using breakjunctions. These author analyzed three metals: Cu, Al and Pt, finding that they presented different behaviors. Cu contacts exhibit negative sloped plateaus upon elongation, i.e. what one would expect naively. The last plateaus are rather flat, in particular the last one has a conductance $\sim 1G_0$. Surprisingly, Al contacts show positive inclined plateaus upon elongation, what means that the

conductance increases as one separates the electrodes. Finally, Pt is more irregular showing positive sloped plateaus upon elongation, except the last one which has a positive slope. The main conclusion of these experimental results, and of other like the ones presented in section 6.5, is that the observed dependence of the conductance on elastic deformation varies from contact to contact but it is characteristic for a given metal.

The aim of this chapter is to understand the tendencies of the plateaus appearing in metallic atomic-size contacts of different metals. For this purpose we shall study experimentally and theoretically the evolution of the conductance of metallic atomic-size contacts under elastic deformation. We concentrate ourselves in the last plateau where the contact is formed presumably by only one atom. We shall analyze contacts made of Au, Al and Pb which exhibit the three possible tendencies. This chapter is based on a work done in collaboration with G. Rubio, C. Untiedt y N. Agraït of The Low Temperature Laboratory of the Autonoma University of Madrid [148]. In this work we study from the experimental point of view these three types of contacts using a STM at low temperatures. We will show not only results for the total conductance but also its decomposition into eigenchannels using the *channel spectroscopy*. From the theoretical point of view we make use of the model presented in Chapter 6, adding the simulation of the elongation of the contact.

The elongation or stretching of the contact provide us an additional parameter which permits us to gain further insight into the transport properties of these nanocontacts. As we will show, the different tendencies reveal important aspects of the electronic and atomic structures of these contacts. Following the ideas exposed in Chapter 6, we shall show that the different tendencies can be naturally understood in terms of the different atomic orbital structures. Moreover, the possibility of analyzing the problem in terms of independent channels provides a further insight into the nature of this phenomenon.

The rest of this chapter is organized as follows. In section 7.2 we shall briefly describe the experimental results about the conductance of the last plateau for the three mentioned metals. Section 7.3 is devoted to describe the implementation of the elastic deformation in our model as well as the theoretical results obtained for the tendencies of the last plateau. In section 7.4 we shall make some comment and summarize the conclusions of this chapter. Finally, we will finish in section 7.5 with some comments about the future and open problems related to the topics treated in the second part of the thesis.

7.2 Experimental conductance evolution under elastic deformations

In Fig. 7.1 we show experimental results of last plateaus for three metals: Au, Al and Pb. In the case of Au, the plateaus are rather flat, specially the last one with a nearly constant conductance $\sim G_0$. In the case of Al, the conductance increases as the contact is stretched varying typically in the last plateau between 0.5 and $1G_0$, while for Pb this variation is in the opposite direction and within the range 3 to $1G_0$ for its last plateau. These experiments were conducted with a STM at low temperatures (4.2 K for Au and Al and 1.5 K for Pb). The detailed description of the set up and experimental procedure can be found in Ref. [266]. For the experiments with Al and Au, the conductance was obtained by measuring the current at a fixed voltage of 10 mV. In the case of Pb, since it was in the superconducting state, the conductance is given by the high-voltage differential conductance.

These are not the only experimental results that we are going to show. In the next section we shall also show the decomposition of conductance into eigenchannels in the case of Pb, which is the most interesting material.

7.3 Theoretical model and results for the elastic evolution of conductance

From the theoretical point of view we face this problem with the model described in the previous chapter. In particular, we shall study the evolution of conductance in the last plateau analyzing the case of one-atom contact. As we showed in Chapter 6, our model allows us to analyze not only the total conductance but also its decomposition into different channels, what will help us to understand the different tendencies of the three metals. Furthermore, in this chapter we pretend to give more quantitative, so that we shall increase the size of our basis and we will introduce new effects.

We now discuss how the effect of an elastic deformation can be studied within the formalism described in the previous chapter. A detailed description of the evolution of the ideal constriction geometry with a tensile stress requires knowledge of the force constants between every pair of atoms. However, when analyzing the elastic deformation on the last plateau it is reasonable to assume that the most important effect is due to the weakening of the coupling of the central atom. Thus, we simulate the elastic deformation by changing the distance between the central atom and its neighbors, as illustrated in Fig. 7.2. As shown below, this simple modelization is sufficient to account for the observed tendencies. The distance dependence of the hopping elements is well described by power laws provided that deformations are not larger than 5%-10% of the bulk interatomic distances. To be exact, Ref. [250]
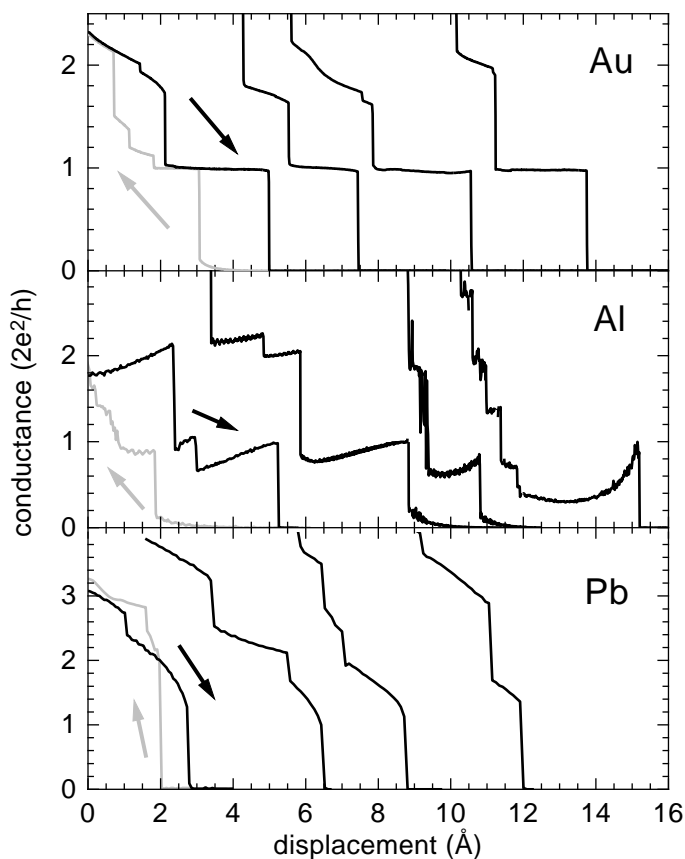
Figure 7.1: Evolution of conductance vs tip-sample displacement for several representative nanocontacts of Au, Al, and Pb in STM experiments. The black and grey curves correspond to elongation and contraction, respectively.

proposes the following decay law for a hopping $t_{ll'}$ between two orbitals of angular momentum l and l' separated by a distance d

$$t_{ll'} \sim \frac{1}{d^{(l+l'+1)}}. \tag{7.1}$$

Then, for instance hoppings t_{ss} decay as d^{-1}, hoppings t_{pp} as d^{-3}, t_{dd} as d^{-5}, t_{sp} as d^{-2}, etc. For larger deformation one would expect exponential decay of the hoppings

[267].
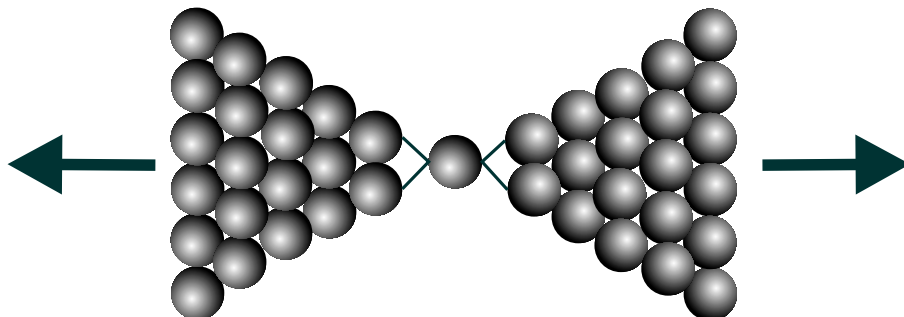
Figure 7.2: Schematical representation of the elongation model for an one-atom contact. In this model the elastic deformation is simulated by changing the distance between the central atom and its neighbors.

In order to study the last plateau conductance we shall analyze the one-atom contact shown in Fig. 6.1. Let us recall that this contact consists of N layer grown on a fcc lattice along the (111) direction (denoted as z direction), and this neck is finally connected to two perfect semiinfinite crystals which describe the reservoirs. The results that we present below have been obtained for a short neck model geometry ($N = 1$), i.e. one atom between two surfaces. Of course, we have verified that for longer necks and different elongation models similar results are obtained. Moreover, we shall comment what happens in different crystallographic directions to the (111), what will reveal the type of structures which are formed in these nanocontacts.

Figure 7.3 summarizes the results obtained for the evolution of the last plateau total conductance and its decomposition into individual channel contributions for the three metals considered. In this figure we show the conductance as a function of the distance between the central atom and its first neighbors d in units of their bulk interatomic distance d_0, from a stretched situation ($d < d_0$) to an elongated one [1]. Notice that both the approximate values of the total conductance as well as their variations upon elastic deformation are in good agreement with the experimental results of Fig. 7.1. To get a deeper insight into the observed trends it is convenient to analyze the evolution of the local density of states (LDOS) at the central atom and the individual channel transmissions as a function of the energy. Fig. 7.4 shows both quantities for the metals considered in the case where the contact is in equilibrium $d = d_0$. Fig. 7.4 show the same for a case where the contact is elongated ($d = 1.2d_0$).

Let us start commenting the case of Au which is a remaining task that we post-

---

[1]Notice that we cannot predict within our model when the contact breaks.
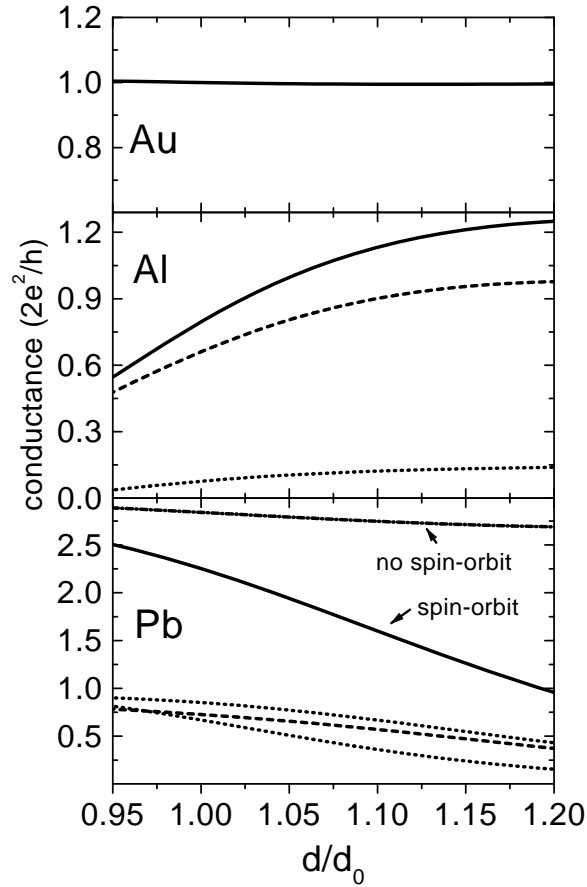
Figure 7.3: Calculated last plateau conductance (full line) and its decomposition for Au, Al and Pb as a function of the distance between the central atom and its first neighbors d in units of the equilibrium distance d_0. In the case of Au only one channel contributes to the conductance. For Al there are three channels (dotted and dashed lines), the one with lower transmission is two-fold degenerate. For Pb the total conductance for a case without spin-orbit coupling and with spin-orbit coupling are shown (see text), and the decomposition into three eigenchannels of the latter case.

poned in the previous chapter. The Au atomic configuration is $5d^{10}6s^1$, which gives rise to a conduction s band with one electron per atom. The d band is completely filled and we have checked that it does not play an important role in the transport properties. However, the $6p$ bands have a small weight at the Fermi level and we
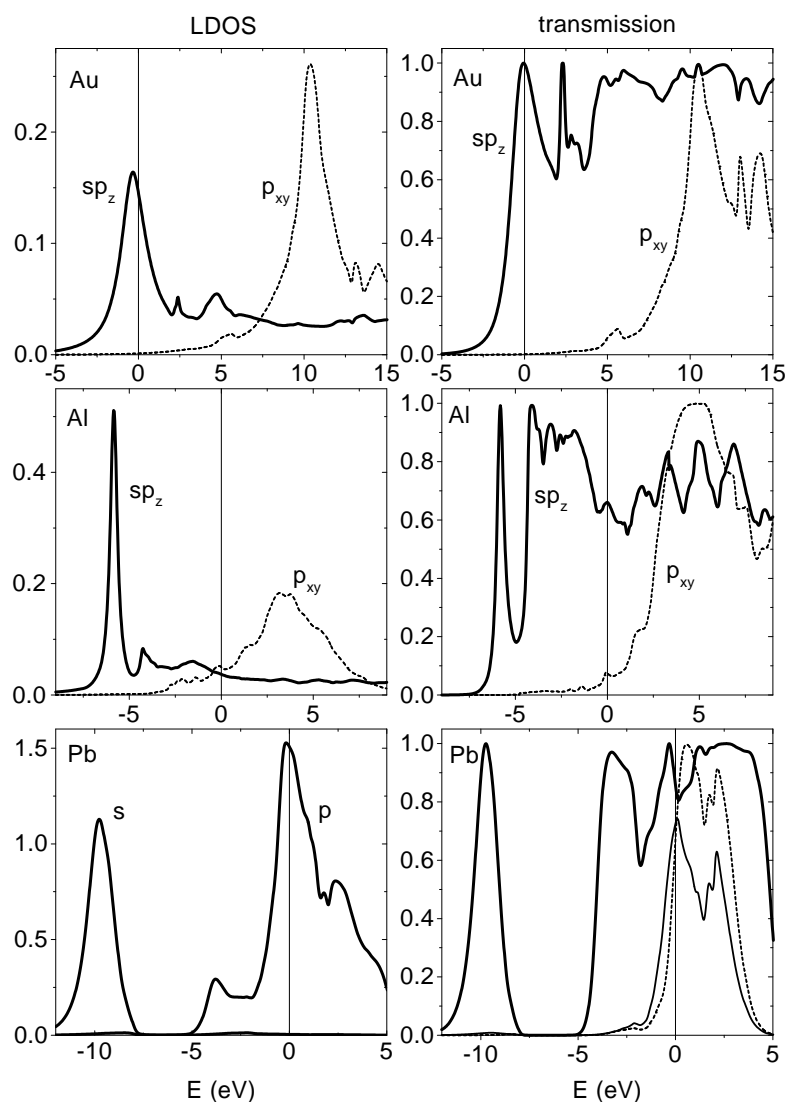
Figure 7.4: LDOS at the central atom and channel transmissions vs energy for the ideal geometry $(d = d_0)$ in Au, Al and Pb. In the case of Pb only the total s and p LDOS are shown. The character of the eigenchannels in this case is neither sp_z nor $p_{x,y}$ due to the spin-orbit coupling. The vertical lines indicate the position of the Fermi level.
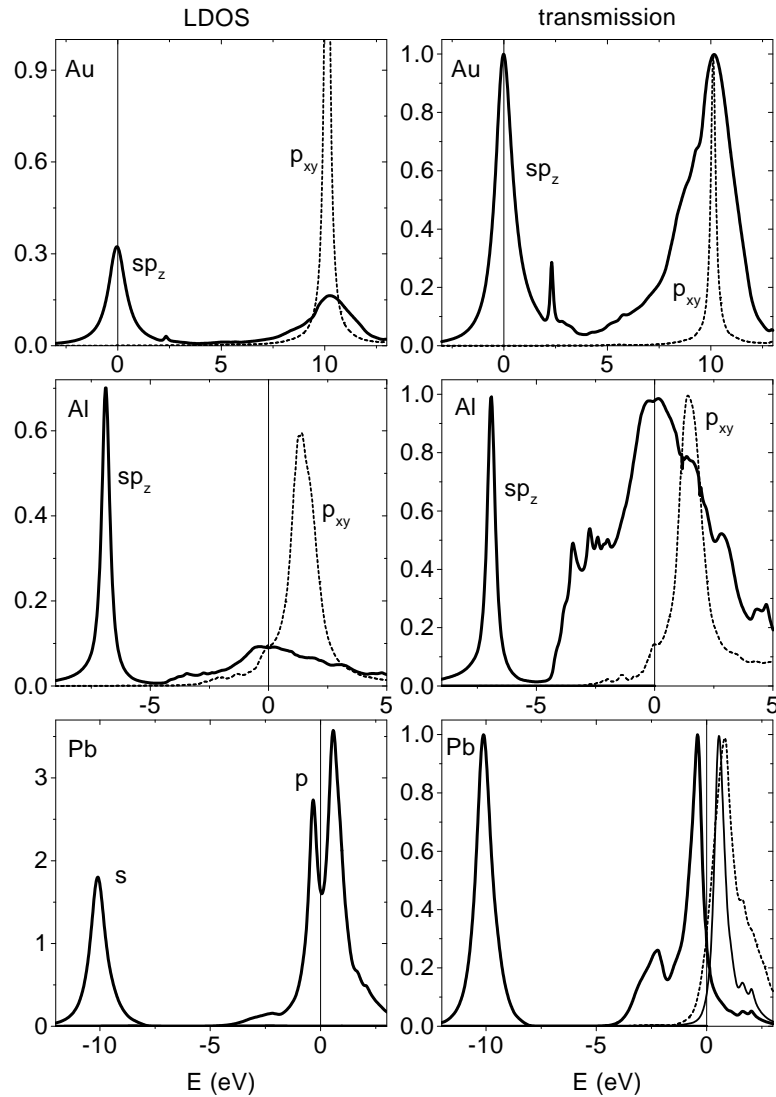
Figure 7.5: Same as Fig. 7.4 for a stretched contact ($d = 1.2d_0$).

have introduced them in the calculation to study their influence.

Our results predict the presence of a single relevant channel at the Fermi energy, whose contribution arise from the $6s$ orbital slightly hybridized with the $6p_z$. As can be observed in the top panel of Fig. 7.4, the local density of states at the central

atom and the transmission exhibit a resonance around the Fermi energy. In this case the charge neutrality condition pins the Fermi level at the center of the transmission resonance. This provides a strong mechanism accounting for the almost perfect conductance quantization for Au at the first plateau [252]. The effect of elastic deformation around this situation is to either broaden or narrow the resonance at the Fermi energy without modifying the value of the total conductance (see top panel of Fig. 7.5). Similar findings using a local density approximation for Au were reported by Brandbyge *et al.* [259].

As we already know, in the case of Al the $3s$ and $3p$ orbitals give the main contribution to the current. This time we have introduced the $3d$ orbitals which, although they are situated 9 eV above the p band center and therefore practically empty [250], they have certain influence in the total conductance value as we shall comment below. Although the relative position and shape of the s and p bands are similar to the case of Au, the Fermi level lies closer to the center of the p bands. Thus, as shown in Chapter 6, one finds three channels with non-negligible transmission: a widely open channel with sp_z character and two less transmissive ones with a p_x, p_y character. This splitting between p_z and p_{xy} bands (which are degenerate in the bulk) is due to the neck geometry which shifts the sp_z band into lower energies with respect to the center of $p_{x,y}$ bands (see middle panel in Fig. 7.4). As it was commented, the double degeneracy of the low transmissive channel is due to the symmetry of the ideal geometry and is broken when introducing disorder.

The inclusion of the d orbitals in the calculation does not modify the conclusions of the previous chapter relative to the number and character of conducting channels in Al one-atom contacts. However, they slightly reduce the total transmission value. For instance, we now have a conductance $\sim 0.8G_0$ for the perfect system ($d = d_0$). This effect is due to the hybridization between the p and d bands which somewhat shifts the p bands to higher energies reducing the transmission of the $sp_z$ channel with respect to what was found without d orbitals. In the case of Al, the bond weakening induced by stretching produces a narrowing of the sp_z and $p_{x,y}$ bands. This narrowing is more pronounced for the $p_{x,y}$ because of the faster decay of the t_{pp} hoppings (see Eq. (7.1)), and as a consequence the Fermi level tends to lie around the center of the sp_z transmission resonance. This is the reason why Al contacts usually break when the conductance is $\sim G_0$ [2]. As can be observed in middle panels of Figs. 7.3 and 7.5, the conductance at the maximum elongation is not exactly G_0. This is a consequence of while the sp_z is opened completely, the $p_{x,y}$ are not totally closed as probably happens (see Fig. 4 in Ref. [143]). This kind of deficiencies should be mend by a more sophisticated model where the self-consistency and the precise orbitals decay be determined in a more appropriate way.

The s and p orbitals also play the most important role in the case of Pb and the

---

[2]However, this does not explain why these contacts usually break just after reaching this point.

number of conducting channels is the same as for Al [3] However, Pb has an extra valence electron which moves the Fermi level to an energy region where both sp_z and $p_{x,y}$ channels are widely open. The calculated total conductance for the ideal geometry is $\sim 2.8G_0$. On the other hand, around the Fermi energy the sp_z has basically a p_z character, what makes that the three channels evolve in the same way upon stretching. This gives rise to a rather flat conductance plateau, as can be seen in Fig. 7.3 (lower panel without spin-orbit), which is at variance with the experimental finding (see Fig. 7.1). A much better agreement can be obtained by including the effect of spin-orbit coupling in the model calculations. This effect is known to play an important role in the adequate description of the Pb bulk band structure [268]. Within an atomic orbital basis, the spin-orbit coupling leads to an extra term in the Hamiltonian (6.1) of the form

$$\hat{H}_{so} = \lambda_{so} \sum_{i,\alpha\beta,\sigma\sigma'} \langle \alpha\sigma | \vec{L}\vec{S} | \beta\sigma' \rangle c_{i\alpha\sigma}^{\dagger} c_{i\beta\sigma'}, \qquad (7.2)$$

where $\vec{L}$ and $\vec{S}$ are the orbital and spin angular momentum operators respectively. The indexes α and β refer to p orbitals at the same lattice site with spin σ, σ' respectively. Typical values of spin-orbit coupling constant λ_{so} are of the order of 0.7 eV [268]. This spin-orbit term makes that neither the orbital angular momentum nor spin be good quantum numbers of the problem. In the new basis which diagonalizes the atomic problem, instead of p orbitals, we have the total angular momentum eigenstates $j = 1/2$ and $j = 3/2$, two-fold and four-fold degenerate respectively. In spectroscopy these orbitals are denoted as $p_{1/2}$ and $p_{3/2}$. The splitting between these two levels is $3\lambda_{so}/2$, and $p_{1/2}$ state has a lower energy. The evolution of the total conductance and its decomposition into eigenchannels including spin-orbit coupling is shown in Fig. 7.3 (lower panel). As can be observed in this figure, now not only the tendency is the correct one but also the conductance values are more adequate. For instance, for the ideal geometry $(d = d_0)$ one has $G \sim 2.25G_0$. In spite of introducing the spin-orbit coupling we keep on obtaining three channel (the transmission of the fourth one is of the order of 10^{-3}). However, the character of the channels change with respect to what we found in Chapter 6.

One can take advantage of the fact that Pb is in the superconducting state at the temperature at which the experiments were performed (1.5 K) to obtain the decomposition of the experimental conductance into eigenchannels using the *channel spectroscopy* introduced in Ref. [143]. Figure 7.6 shows a typical example of the evolution of the decomposition for Pb. As we can see there appear three channels whose evolution under elastic deformation is in agreement with the theoretical results that we have just commented.

---

[3]We have verified that the d orbitals in the case do not play an important role because they are farther than in the Al case.
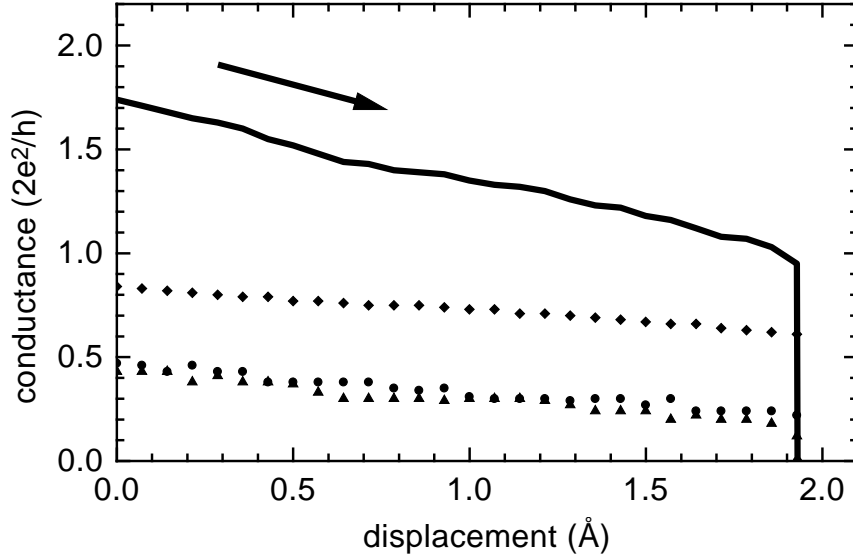
Figure 7.6: Experimental conductance for Pb and its decomposition into three different channels (represented as diamonds, dots, and triangles).

The pronounced decreased of the conductance can be understood by analyzing the LDOS at the central atom. For the ideal geometry (Fig. 7.4 lower panel) the Fermi level lies in the middle of the p band which does not exhibit any structure associated with the splitting of the atomic levels, since the broadening of central atom levels due to the coupling with electrodes is much greater than such splitting ($\sim 1\ eV$). However, the decomposition into sp_z and p_{xy} channels is no longer valid due to the spin-orbit coupling which also breaks the $p_{x,y}$ degeneracy. In the elongated contact (Fig. 7.5 lower panel) the splitting of the atomic levels manifests itself in the appearance of a doubled peaked structure at the p LDOS having a $p_{1/2}$ and a $p_{3/2}$ character. The Fermi level lies between these two peaks in order to approximately accommodate two electrons in the $p_{1/2}$ band. The double peaked structure is also present in the transmission as a function of energy explaining its pronounced decrease with elongation.

197

7.4   Comments and conclusions

The theoretical results presented so far have been obtain for a closed packed contact model grown along (111) direction. This seems the natural choice since (111) faces are known to be energetically favored in fcc metals. We have nevertheless also studied model geometries grown along other crystallographic directions like (100). As commented in Chapter 6, the number of channels and the approximate values of the total conductance are not dependent on the geometry choice. However, for the particular case of Al one finds a decrease in conductance upon stretching for the (100) case [269] at variance with the experimentally observed tendency. This result could indicate that in these nanocontacts compact structures tend to be formed.

In summary, in this chapter we have shown that the conducting channels in metallic one-atom contacts are in general neither completely open nor completely closed, which reflects in the variations of the conductance with strain. Conductance increases or decreases with strain depending on the electronic structure of the element.

The correct description of these transport properties requires going beyond the free-electron approximation. A good semiquantitative agreement has been achieved using a tight-binding model Hamiltonian based on fits to the bulk valence bands and a close packed model geometry with the addition of the charge neutrality condition. No special treatment is necessary for each metal indicating the power of our approach.

7.5   Future and open problems

With respect to the future, there are still many problems that we may analyze with our model. For instance, we can analyze other metals like the ones of the group IIB. In Fig. 7.7 we show preliminary results for Zn and Cd. These two metals have electronic structures Ar $3d^{10}4s^2$ and Kr $4d^{10}5s^2$ respectively. They are conducting material because the p band is hybridized with the s valence band [4]. These material are superconducting at low temperatures, which makes possible the experimental comparison. As can be seen in Fig. 7.7, both the local density of states at the central atom and the decomposition of the transmission into eigenchannels are similar to the ones of Al. Indeed, this is what one would expect since the transport takes place through the s and p bands. This preliminary results allow us to get some ideas about these metals, but we must still study in detail the influence of disorder or the d band, etc.

Another interesting case is the one of semimetals like Sb or Bi. As we commented in Chapter 5, Krans *et al.* [218] showed that a Sb atomic contact exhibits conductance plateaus below the quantum, which is probably due to the low density

---

[4]In the calculation of the Fig. 7.7 we have only included the s and p bands.
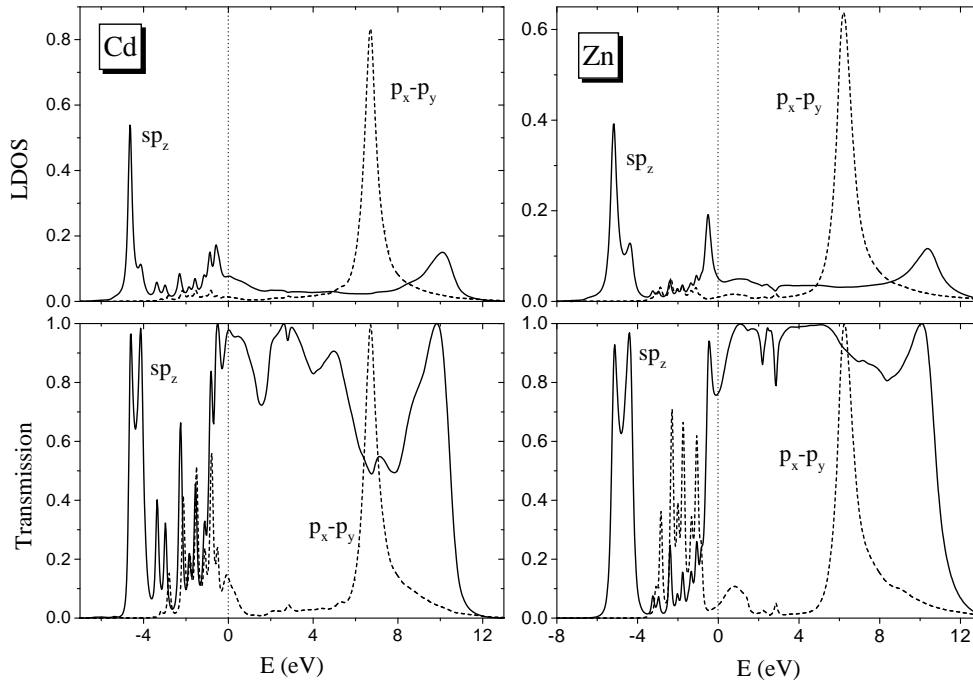
Figure 7.7: Local density of states and transmission as a function of energy for Cd and Zn one-atom contacts without disorder. In both cases the transmission has 3 eigenvalues with non-negligible transmissions. The dominant channel has a sp_z character. The second channel is two-fold degenerate with a small transmission at the Fermi level and has a sp_z character. The fourth channel is closed for the reason explained for the Al case. The density of states at the central atom is decomposed in two sp_z and $p_x - p_y$ bands. The position of the Fermi level is indicated as a vertical dotted line.

of states of a semimetal at the Fermi level. However, there have appeared a new work in which it is shown the possibility of conductance quantization in an atomic contact of Bi [264], which is at variance with results of other laboratories (C. Untiedt, private communication).

In principle, we can analyze semimetals with our theoretical model. However, in the case of semimetals the charge neutrality condition is not a very good approximation because of the large Fermi wave length. Anyway, the neutrality condition is always a first approximation in the self-consistent treatment of the electron-electron interaction. The analysis of semimetals is one of our remaining tasks.

Another interesting case is the one of ferromagnetic material as Fe, Co or Ni. In contacts of these metals the spin symmetry is broken and the channels split into spin up and spin down channels. As an example of a ferromagnetic case, in Fig. 7.8 we show preliminary results on Co one-atom contacts. It can be seen in this figure that there are spin up and spin down channels, and one can have funny situations like this, in which one has basically one channel for spin up due to the Co $4s$ orbital, and six channels for spin down due to the contribution of the $3d$ band. The analysis of contacts of ferromagnetic materials is one of challenges for the future both from the theoretical and experimental point of view.

In this work we have concentrated in the analysis of the simplest contact, an one-atom contact. Such contact corresponds to the last conductance plateau before breaking the contact. One of our aims is to extend the analysis to higher plateaus. In principle, our theoretical scheme is valid for analyzing contacts of arbitrary section, but our main problem is to determine the contact geometry. One of our aims is to combine our calculations of the transport properties with molecular dynamics simulations for determining the actual evolution of the contact geometry.

Of course, there are still several open problems in the context of metallic nanocontacts. For instance, what is the origin of the peculiar series of conductance steps in the case of simple metals [219]? (see Chapter 5), or in general, what is the origin of the peaks in the conductance histograms? As we pointed out in Chapter 5, the transport and mechanical properties are closely related. In our opinion the answers of the previous questions can be found in the mechanical properties of the contacts. It is very likely that certain atomic configurations are favored for energetic reasons, and this fact would be reflected in the patterns of the conductance evolution upon deformations. But this is only a speculation that would be interesting to explore in molecular dynamics simulations of the contact formations.

The following step in the study of electronic transport in nanocontacts could be the extension of our model to the case of molecular contacts. In the last years a growing attention has been paid to the investigation of the electrical current through individual molecules. Molecular circuits can be fabricated with the STM [270, 271, 272, 273] or with the breakjunction technique [274]. Recently several theoretical schemes have been developed for describing the transport in these circuits [270, 275, 276, 277, 278, 279], which use similar ideas to the ones we have presented here. Practically all theories make use of atomic orbital basis and Green functions techniques. The new ingredient, with respect to the atomic contacts, is the determination of the molecular levels and their coupling to the leads. The electronic structure of a molecule is usually determined with an extended Hückel method. The main conclusion of these theories is that the electrical current through contact of individual molecules is determined by individual molecular levels, in a similar way to what we have shown in these chapters for the case of atomic circuits.
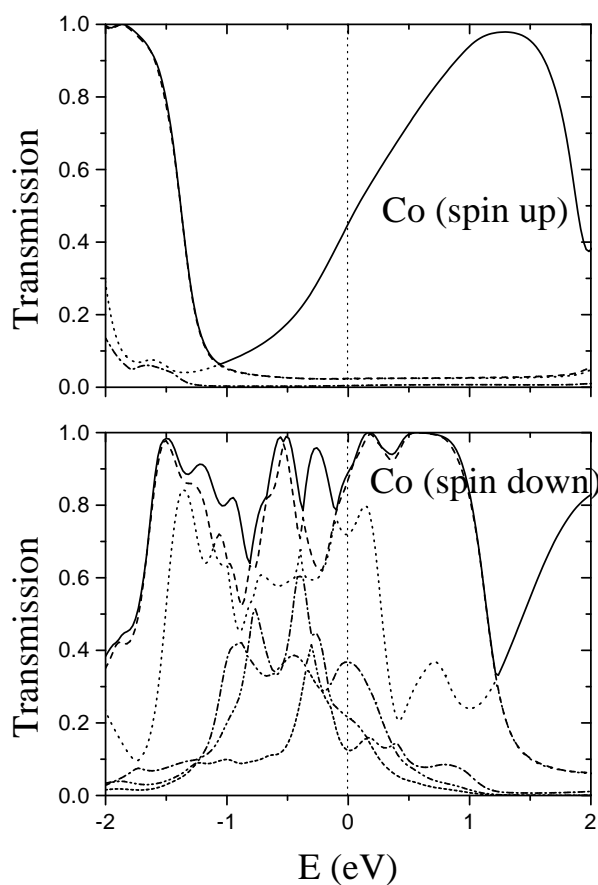
Figure 7.8: Transmission as a function of energy for a Co one-atom contact. The eigenvalues are separated in spin up and spin down due to the broken spin symmetry in a ferromagnetic material. The electronic structure of Co is Ar $3d^7 4s^2$. Around the Fermi level we find one channel with s character for spin up and 6 spin down channels due to the contribution of the d bands. The Fermi level is indicated with a vertical dotted line.

We have started answering some fundamental questions in the context of atomic and molecular circuits, but for the definitive success of the *molecular electronics* we should to answer other fundamental questions like:

- What type of atoms or molecules should we use, in order to integrate them in a macroscopic circuits and may realize millions of operations per second?

- What experimental techniques must we developed to incorporate the atoms or molecules with precision and rapidity?

Without any doubt we are in a crucial moment of the development of the nanoelectronics. Soon we shall know if the molecular electronics will be one of the technological revolutions of the next century, or if by the contrary it will remain as a mere academic curiosity.

Appendix A

Keldysh Formalism

This appendix is devoted to the study of non-equilibrium Green functions, in particular to the study of the Keldysh formalism [1]. Apart from the original paper, there exist excellent works devoted to this technique in the literature [2, 3, 4]. In spite of this, we have decided to include this appendix because this formalism is the basic tool of this thesis. We have tried to explain it didactically, in such a way that it be accessible for those who are familiar with the standard perturbation theory for the Green functions of a system in equilibrium [5, 6, 7].

In his original paper Keldysh developed a diagrammatic technique for calculating the Green functions of systems *arbitrarily* out of equilibrium [1]. This technique is a natural extension to the non-equilibrium case of the well-known diagrammatic theory that Feynman introduced in Quantum Field Theory [8]. The importance of the Keldysh formalism lies in that it allows us to go beyond of the usual linear response. Indeed, this technique provides us a quite general method for studying Non-equilibrium Statistical Mechanics from a perturbative point of view. Since its appearance it has been used in a great amount of different topics (see Ref. [4] and references therein). In particular, it has been applied to the study of electronic transport in many types of junctions (for instance see Ref. [9]).

This appendix is organized as follows: in section A.1 we lay the foundations of the Keldysh formalism. In section A.2 we describe the matrix representation of the non-equilibrium Green functions. In particular, we discuss some of the relations between the different Green functions which make this technique so useful. In section A.3 we briefly discuss the Feynman rules which govern the construction of the diagrams for the non-equilibrium case. Finally, we end with the references of this appendix.

A.1   The Keldysh contour

Let us consider a physical system represented by the time-independent Hamiltonian

$$\hat{H} = \hat{H}_0 + \hat{H}^i, \tag{A.1}$$

where $\hat{H}_0$ describes free particles and $\hat{H}^i$ the interaction between the particles.

In thermodynamic equilibrium, we describe the state of the system in the grand canonical ensemble by the density matrix

$$\hat{\rho} = \frac{1}{Z} e^{-\beta \hat{H}} \;\; ; \;\; Z = Tr\left[e^{-\beta \hat{H}}\right], \tag{A.2}$$

where $\beta = T^{-1}$ [1] and we measure the particle energies with respect to the chemical potential μ, i.e. $\hat{H}$ is indeed $\hat{H} - \mu \hat{N}$, where $\hat{N}$ is the particle number operator.

We are interested in how this system evolves when it is subjected to the action of a time-dependent perturbation $\hat{V}'(t)$ since an initial time t_0. For a latter time $t > t_0$, the system evolves governed by the Hamiltonian

$$\hat{\mathcal{H}}(t) = \hat{H} + \hat{V}'(t), \tag{A.3}$$

where $\hat{V}'(t) = 0$ for $t < t_0$. In order to describe the dynamics of the system we use the Heisenberg picture. In this representation the states are time-independent and the observables obey the equation of motion

$$i\frac{\partial}{\partial t}\hat{A}_{\mathcal{H}}(t) = \left[\hat{A}_{\mathcal{H}}(t), \hat{\mathcal{H}}(t)\right], \tag{A.4}$$

where the subindex $\mathcal{H}$ indicates Heisenberg picture. The average value of the operator $\hat{A}$ at a time t is given by

$$\langle \hat{A}(t)\rangle = Tr\left[\hat{\rho}_{\mathcal{H}}\hat{A}_{\mathcal{H}}(t)\right], \tag{A.5}$$

where let us recall that the density matrix in the Heisenberg picture does not depend on time.

In this appendix we are mainly concerned with the evolution of Green functions, as for instance the causal function

$$i\,G(1,1') = \langle \hat{T}\,\hat{\psi}_{\mathcal{H}}(1)\hat{\psi}_{\mathcal{H}}^{\dagger}(1')\rangle, \tag{A.6}$$

where $1 \equiv (\vec{x_1}, t_1)$, $1' \equiv (\vec{x_{1'}}, t_{1'})$, $\hat{\psi}_{\mathcal{H}}(1)$ and $\hat{\psi}_{\mathcal{H}}^{\dagger}(1')$ are field operators in the Heisenberg picture and $\hat{T}$ is the time-ordering operator

$$\hat{T}\,\hat{\psi}_{\mathcal{H}}(1)\hat{\psi}_{\mathcal{H}}^{\dagger}(1') \equiv \left\{ \begin{array}{ll} \hat{\psi}_{\mathcal{H}}(1)\hat{\psi}_{\mathcal{H}}^{\dagger}(1') & \text{if } t_1 > t_{1'} \\ \mp\hat{\psi}_{\mathcal{H}}^{\dagger}(1')\hat{\psi}_{\mathcal{H}}(1) & \text{if } t_1 \leq t_{1'}, \end{array} \right. \tag{A.7}$$

---

[1] We use throughout this appendix units $\hbar = k_B = 1$.

where the sign $-$ is for fermions and $+$ for bosons. From now on we shall only consider the case of fermions. In principle, from the knowledge of Green functions as the one in Eq. (A.6) every one-particle property may be derived.

As we mentioned in the introduction, the Keldysh formalism allows us to determine these Green functions using a perturbative technique. This technique is formally equivalent to the well-known expansions of Feynman [8] and Matsubara [10], and as they it is based on the Wick theorem [11]. This theorem states how a many-particle correlation may exactly be decomposed into sums and products of one-particle correlations. The most general proof of the Wick theorem is due to Danielewicz [12]. He showed that the Wick theorem holds if and only if the operators to be averaged are noninteracting and the initial density matrix is an one-particle density matrix. By noninteracting operators we mean operators in the Interaction picture with respect to a free Hamiltonian. Thus, if we want to use the Wick theorem for expanding the Green functions we find two problems. First, the initial density matrix $\hat{\rho}(t_0)$ given by Eq. (A.2) is a many-body density matrix. Secondly, in general the Hamiltonian $\hat{\mathcal{H}}(t)$ contains many-body contributions and therefore the corresponding time-development operator as well. The following paragraphs are devoted to the solution of both problems.

Let us start analyzing the second problem which is the central idea of this formalism. Our problem consists of studying the time-development of the Green function (A.6). For this purpose, if we want to make use of the Wick theorem, we must express it in terms of operators in the Interaction picture with respect to a free Hamiltonian $\hat{H}_0$. The relation between an operator $\hat{A}_{\mathcal{H}}$ in the Heisenberg picture and the corresponding $\hat{A}_{H_0}$ in the Interaction picture is given by

$$\hat{A}_{\mathcal{H}}(t) = \hat{S}(t_0, t)\hat{A}_{H_0}(t)\hat{S}(t, t_0), \tag{A.8}$$

where $\hat{S}$ is the time-development operator in the Interaction picture

$$\hat{S}(t, t_0) = e^{i\hat{H}_0 t} e^{-i\hat{\mathcal{H}}(t-t_0)} e^{-i\hat{H}_0 t_0}. \tag{A.9}$$

This time-development operator satisfies the following differential equation

$$i\frac{\partial}{\partial t}\hat{S}(t, t_0) = \hat{V}_{H_0}(t)\hat{S}(t, t_0), \tag{A.10}$$

where $\hat{V}_{H_0}(t)$ represents the interaction expressed in the Interaction picture. Here, the interaction $\hat{V}(t) = \hat{H}^i + \hat{V}'(t)$ includes the interaction between particles and the time-dependent potential.

The previous differential equation admits the formal solution

$$\hat{S}(t, t_0) = \hat{T}\exp\left(-i\int_{t_0}^{t} dt'\, \hat{V}_{H_0}(t')\right), \tag{A.11}$$

where $\hat{T}$ is the time-ordering operator. Using this result one can express Eq. (A.8) as

$$\hat{A}_{\mathcal{H}}(t) = \left[\tilde{T} \exp\left(i \int_{t_0}^{t} dt' \; \hat{V}_{H_0}(t') \right) \right] \hat{A}_{H_0}(t) \left[\hat{T} \exp\left(-i \int_{t_0}^{t} dt' \; \hat{V}_{H_0}(t') \right) \right], \quad \text{(A.12)}$$

where $\tilde{T}$ is the antiordering operator [2]

$$\tilde{T} \; \hat{A}(t_1)\hat{B}(t_2) \equiv \begin{cases} \hat{A}(t_1)\hat{B}(t_2) & \text{if } t_1 < t_2 \\ -\hat{B}(t_2)\hat{A}(t_1) & \text{if } t_1 \geq t_2. \end{cases} \quad \text{(A.13)}$$

One can conveniently compact the expression (A.12) making use of the so called **Keldysh contour**, which is shown in Fig. A.1 [13]. This contour runs on the upper branch (branch $+$) from $t_0 = t_0^+$ to t and on the lower branch (branch $-$) back to $t_0 = t_0^-$. Nevertheless, both branches are still lying on the real time. The vertical offset in Fig. A.1 is only a graphical method to demonstrate the different sense of ordering. On the branch $+$ the time ordering is chronological, whereas in the branch $-$ is antichronological.
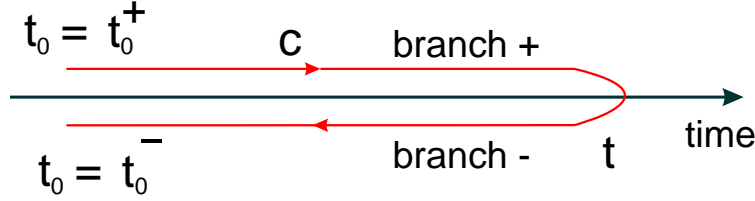
Figure A.1: c $\equiv$ Keldysh contour.

With this contour c the expression (A.12) reduces to

$$\hat{A}_{\mathcal{H}}(t) = \left\{ \hat{T}_c \exp\left(-i \int_c dt' \; \hat{V}_{H_0}(t') \right) \right\} \hat{A}_{H_0}(t), \quad \text{(A.14)}$$

where $\hat{T}_c$ is the time-ordering operator along the Keldysh contour and the integral runs along this contour. Defining the time-development operator on the Keldysh contour as

$$\hat{S}_c(t_2, t_1) = \hat{T}_c \exp\left(-i \int_{t_1}^{t_2} dt' \; \hat{V}_{H_0}(t') \right), \quad \text{(A.15)}$$

where $t_1, t_2 \in c$, finally we have

_____

[2] Let us recall that we only consider the case of fermions.

$$\hat{A}_{\mathcal{H}}(t) = \hat{T}_c \; \hat{S}_c(t_0^-, t_0^+) \; \hat{A}_{H_0}(t). \tag{A.16}$$

Using this results it is easy to convince oneself that the Green function (A.6) can be expressed in terms of noninteracting operators in the following way

$$i \, G(1, 1') = \langle \hat{T}_c \; \hat{S}_c(t_0^-, t_0^+) \; \hat{\psi}_{H_0}(1) \; \hat{\psi}_{H_0}^\dagger(1') \rangle. \tag{A.17}$$

Thus, we have solved our first problem.

There is still a problem. Namely, the averages of the type of Eq. (A.17) are still calculated with a many-body density matrix. Thus, if we want to use the Wick theorem we must expand the density matrix in terms of a free density matrix (non-interacting density matrix). The solution to this problem was found by Matsubara in his famous work on the finite temperature expansion [10]. Next, we explain this solution.

Let us analyze the exponential appearing in the density matrix (A.2). We may write it as

$$e^{-\beta \hat{H}} = e^{-\beta \hat{H}_0} e^{\beta \hat{H}_0} e^{-\beta \hat{H}}. \tag{A.18}$$

On the other hand, we can trivially extend the expression (A.9) for the time-development operator to the case of an imaginary time, thus

$$\hat{S}_{c'}(-i\beta, 0) = e^{\beta \hat{H}_0} e^{-\beta \hat{H}}, \tag{A.19}$$

where c' indicates that the time runs along the imaginary axis as it is shown in Fig. A.2.

Figure A.2: $c' \equiv$ Matsubara contour.

According to Eq. (A.11) $\hat{S}_{c'}(-i\beta, 0)$ can be expressed as

$$\hat{S}_{c'}(-i\beta, 0) = \hat{T}_{c'} \exp\left(-i \int_0^{-i\beta} dt' \, \hat{H}_{H_0}^i(t')\right), \tag{A.20}$$

where $\hat{H}_{H_0}^i$ is the interaction between particles in the Interaction picture, and $\hat{T}_{c'}$ orders along the Matsubara contour $c' = [0, -i\beta]$

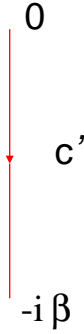$$\hat{T}_{c'} \, \hat{A}(t_1)\hat{B}(t_2) = \begin{cases} \hat{A}(t_1)\hat{B}(t_2) & \text{if } t_1 > t_2 \text{ in } c' \\ -\hat{B}(t_2)\hat{A}(t_1) & \text{if } t_1 \leq t_2 \text{ in } c' \end{cases}. \tag{A.21}$$

Inserting this into Eq. (A.18) we get

$$e^{-\beta \hat{H}} = e^{-\beta \hat{H}_0} \, \hat{S}_{c'}(-i\beta, 0). \tag{A.22}$$

On the other hand, the partition function can be written as

$$Z = Tr\left[e^{-\beta \hat{H}}\right] = Tr\left[e^{-\beta \hat{H}_0} \hat{S}_{c'}(-i\beta, 0)\right]. \tag{A.23}$$

So, we can then write the density matrix as follows

$$\hat{\rho} = \frac{e^{-\beta \hat{H}_0}\hat{S}_{c'}(-i\beta, 0)}{Tr\left[e^{-\beta \hat{H}_0}\hat{S}_{c'}(-i\beta, 0)\right]} = \frac{Z_0}{Z} \, \hat{\rho}_0 \, \hat{S}_{c'}(-i\beta, 0), \tag{A.24}$$

where $\hat{\rho}_0$ is the single-particle density matrix

$$\hat{\rho}_0 = \frac{e^{-\beta \hat{H}_0}}{Z_0} \quad ; \quad Z_0 = Tr\left[e^{-\beta \hat{H}_0}\right]. \tag{A.25}$$

Thus, we have solved our second problem, i.e. we have expanded $\hat{\rho}$ in terms of a free density matrix $\hat{\rho}_0$ and now we may use the Wick theorem.

Combining the results (A.24) and (A.17) we can write the Green function as

$$i \, G(1, 1') = \frac{Z_0}{Z} \langle \hat{S}_{c'}(-i\beta, 0) \, \hat{S}_c(t_0^-, t_0^+) \, \hat{\psi}_{H_0}(1) \, \hat{\psi}_{H_0}^\dagger(1')\rangle_0, \tag{A.26}$$

where $\langle \ \rangle_0$ indicates that the averages are calculated with $\hat{\rho}_0$.

The twofold expansion of the initial density matrix and the time-development operator may conveniently be combined to a single expansion. To this end we utilize the striking similarity between the treatment of the initial density matrix and the time-development operator, both of which are exponential functions. Following Wagner [14], we link the two contours c' and c together, $c^* \equiv c'c$ as illustrated in Fig. A.3 [15]. Moreover, we introduce a c^*-contour-ordering operator $\hat{T}_{c^*} \equiv \hat{T}_{c'}\hat{T}_c$. Hence, a point on c is always earlier than a point on c'.

Furthermore, we define a Heisenberg picture with respect to $\hat{H}_0$ along the contour and we extend the time-development operator to the c^* contour in the following way
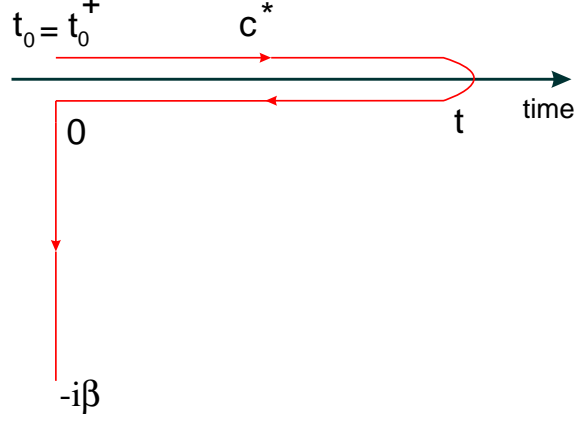
Figure A.3: Generalized contour c^*.

$$\hat{S}_{c^*} \equiv \hat{S}_{c^*}(-i\beta, t_0^+) \equiv \hat{S}_{c'}(-i\beta, 0)\, \hat{S}_c(t_0^-, t_0^+) = \hat{T}_{c^*} \exp\left(-i \int_{c^*} dt'\, K_{H_0}(t')\right), \quad \text{(A.27)}$$

where K_{H_0} is the perturbation in the Interaction picture

$$K_{H_0}(t') \equiv \begin{cases} \hat{V}(t') & t' \text{ in } c \\ \hat{H}^i(t') & t' \text{ in } c'. \end{cases} \quad \text{(A.28)}$$

With these definitions we can write Eq. (A.26) as

$$i\, G(1, 1') = \frac{Z_0}{Z} \langle \hat{T}_{c^*}\, \hat{S}_{c^*}\, \hat{\psi}_{H_0}(1)\, \hat{\psi}_{H_0}^\dagger(1')\rangle_0. \quad \text{(A.29)}$$

The crucial point is that this expression meet all requirements for the application of the Wick theorem to each of the terms in the expansion of $\hat{S}_{c^*}$. First, the average is taken over an one-particle density matrix $\hat{\rho}_0$ and secondly, all operators are given in an Interaction picture corresponding to a noninteracting system described by $\hat{H}_0$.

Let us summarize what we have obtained so far. In principle, with the theory we have developed so far we can describe the temporal evolution of a system initially in thermodynamical equilibrium, including the possible transient effects due to the initial correlations. However, in the Keldysh formalism one does not take into account transient effects or initial correlations. This can be achieved taking $t_0 \to -\infty$. Thus, if we assume that the Green functions decay rapidly as a function of the difference of times, we can neglect the contribution coming from the contour c'. A detailed

discussion about this point can be found in an excellent work by Mathias Wagner
(Ref. [14]). In this work Wagner developed a general formalism which permits to
take explicitly into account the initial correlations, and he showed that there appear
corrections to the Keldysh formalism due to such correlations. Thus, the study of
transient effects is out of the scope of the Keldysh formalism. Nevertheless, this
technique allows us to analyze systems out of equilibrium in which after certain time
a "stationary" situation is reached [3].

   Thus, if we neglect the initial correlations, the c^* contour reduces to the Keldysh
contour c, which now starts at $-\infty$ (see Fig. A.4).
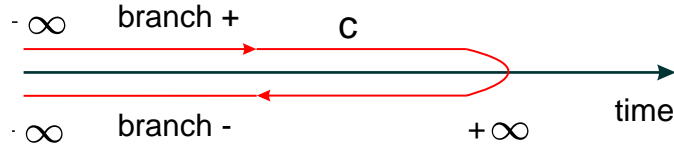
Figure A.4: The Keldysh contour.

   Furthermore, in the Keldysh formalism it is assumed that the interaction between
particles, $\hat{H}^i$, can be switched on adiabatically in such a way that the interaction
vanishes at $t \to -\infty$ and we can use $\hat{\rho}_0$ the initial density matrix. From now on, we
concentrate strictly in the Keldysh formalism as it is commonly used. It we take into
account the two mentioned simplifications, the Green function (A.29) now reduces
to

$$i\, G(1, 1') = \langle \hat{T}_c\, \hat{S}_c\, \hat{\psi}_{H_0}(1)\, \hat{\psi}^{\dagger}_{H_0}(1') \rangle_0, \qquad (A.30)$$

where c indicates the Keldysh contour of the Fig. A.4 and $\hat{S}_c \equiv \hat{S}_c(-\infty, -\infty)$. As
before, the Green function (A.30) is expressed in a suitable way for using the Wick
theorem in the expansion of $\hat{S}_c$ given by Eq. (A.15). However, it is easy to realize
that in this expansion other different Green functions will appear. Thus, we do not
get a closed equation for the Green function which we are analyzing. The reason
is the following: while the Green function temporal arguments t_1 and $t_{1'}$ lie in the
branch $+$, $\hat{S}_c$ has temporal arguments in both branches giving rise to functions with
the four possible pairings of the arguments on c. An elegant way of solving this
problem is to study a function which comprises all the functions occurring in the
expansion. This function is the so called *c-contour-ordered Green function*, which is
defined as

---

[3]The electronic transport problems that we analyze in thesis belong to this type of stationary
problems.

$$i\,G_c(1,1') \equiv \langle \hat{T}_c\,\hat{\psi}_{\mathcal{H}}(1)\hat{\psi}_{\mathcal{H}}^{\dagger}(1')\rangle = \begin{cases} \langle \hat{\psi}_{\mathcal{H}}(1)\hat{\psi}_{\mathcal{H}}^{\dagger}(1')\rangle & \text{if } t_1 > t_{1'} \text{ on } c \\ -\langle \hat{\psi}_{\mathcal{H}}^{\dagger}(1')\hat{\psi}_{\mathcal{H}}(1)\rangle & \text{if } t_1 \leq t_{1'} \text{ on } c \end{cases}, \quad \text{(A.31)}$$

where t_1 and $t_{1'}$ lie on the whole contour c and the operators are expressed in the Heisenberg picture. This function covers all possible pairings of the operators $\hat{\psi}_{\mathcal{H}}(1)$ and $\hat{\psi}_{\mathcal{H}}^{\dagger}(1')$ defined on c. For instance, if t_1 and $t_{1'}$ lie on the branch $+$, $G_c(1,1')$ reduces to the Green function (A.6).

Using Eq. (A.30) we have for G_c

$$i\,G_c(1,1') = \langle \hat{T}_c\,\hat{S}_c\,\hat{\psi}_{H_0}(1)\,\hat{\psi}_{H_0}^{\dagger}(1')\rangle_0. \quad \text{(A.32)}$$

It is evident that now the expansion of $\hat{S}_c$ leads to a closed equation for G_c. Due to the Wick theorem, every term in this expansion can be expressed as a sum of products of one-particle Green functions of the unperturbed system. The resulting terms in each order in the interaction may be described diagrammatically. It is easy to show, (see Ref. [1] for details) that the diagrammatic structure is identical to the one of the equilibrium case. In the same way, we have connected and disconnected diagrams, topologically distinct, etc. The only difference with the equilibrium expansion is the appearance of the integrations along the contour c instead of over the inverse of the temperature for the case of finite temperature, or over the real axis for the zero-temperature case.

As in the equilibrium case the expansion of the time-development operator $\hat{S}_c$ gives rise to an infinite geometrical series, where arises the concept of self-energy and the Green function G_c obeys a Dyson equation

$$G_c(1,1') = g_c(1,1') + \int_c dt_2 d\vec{x_2}\, dt_3 d\vec{x_3}\, g_c(1,2)\, \Sigma(2,3)\, G_c(3,1'), \quad \text{(A.33)}$$

where g_c is the unperturbed Green function and the self-energy Σ is as usual defined as a sum over all topologically distinct proper self-energy diagrams.

This is a closed equation for G_c which allows us to determine it, once the self-energy has been calculated. However, the Green functions in which we are interested in have not the form of G_c, but they have both temporal arguments defined in a concrete contour branch. Thus, for practical calculations it is more convenient to use a matrix representation for the c-contour-ordered Green function. This is the aim of the next section.

A.2 Matrix representation

As stated above, it is convenient to express the perturbative expansion in terms of Green functions defined on the real time axis. For this purpose we shall make use

of a matrix representation of the c-contour-ordered Green function. This function has two time arguments t_1 and $t_{1'}$ which can be placed on both Keldysh contour branches. There are four different possibilities to distribute these two parameter over the two branches. These four possibilities can be grouped in a (2×2) matrix

$$\hat{G}(1,1') = \begin{pmatrix} G^{+,+}(1,1') & G^{+,-}(1,1') \\ G^{-,+}(1,1') & G^{-,-}(1,1') \end{pmatrix}, \tag{A.34}$$

where the hat of $\hat{G}(1,1')$ indicates that it is a (2×2) matrix in the so called *Keldysh space*. The superindexes of the matrix elements denote the position of the time arguments on the contour. So, the left hand side superindex $\pm$ tell us that the argument t_1 lies in the branch $\pm$. The right superindex tell us the same for the argument $t_{1'}$. The matrix elements are determined according to the effect which has $\hat{T}_c$ on the product $\hat{\psi}(1)\hat{\psi}^\dagger(1')$ for each configuration of t_1, $t_{1'}$ on the contour c. Thus,[4]

$$i\, G^{+,+}(1,1') = \langle \hat{T}\, \hat{\psi}(1)\hat{\psi}^\dagger(1') \rangle = \begin{cases} \langle \hat{\psi}(1)\hat{\psi}^\dagger(1') \rangle = i\, G^{-,+}(1,1') & \text{if } t_1 > t_{1'} \\ -\langle \hat{\psi}^\dagger(1')\hat{\psi}(1) \rangle = i\, G^{+,-}(1,1') & \text{if } t_1 \leq t_{1'} \end{cases} \tag{A.35}$$

$$i\, G^{-,-}(1,1') = \langle \tilde{T}\, \hat{\psi}(1)\hat{\psi}^\dagger(1') \rangle = \begin{cases} \langle \hat{\psi}(1)\hat{\psi}^\dagger(1') \rangle = i\, G^{-,+}(1,1') & \text{if } t_1 < t_{1'} \\ -\langle \hat{\psi}^\dagger(1')\hat{\psi}(1) \rangle = i\, G^{+,-}(1,1') & \text{if } t_1 \geq t_{1'} \end{cases} \tag{A.36}$$

$$i\, G^{+,-}(1,1') = -\langle \hat{\psi}^\dagger(1')\hat{\psi}(1) \rangle \tag{A.37}$$

$$i\, G^{-,+}(1,1') = \langle \hat{\psi}(1)\hat{\psi}^\dagger(1') \rangle. \tag{A.38}$$

The function $G^{+,+}(1,1')$ is simply the causal (time-ordered) Green function (A.6). $G^{-,-}(1,1')$ is the antitime-ordered Green function. Finally, the non-diagonal elements have the order of the time arguments fixed, since they lie on different branches. The two functions are basically distribution functions which are incorporated to the perturbative expansion in this formalism.

In the same way the self-energy admits a similar matrix representation

$$\hat{\Sigma}(1,1') = \begin{pmatrix} \Sigma^{+,+}(1,1') & \Sigma^{+,-}(1,1') \\ \Sigma^{-,+}(1,1') & \Sigma^{-,-}(1,1') \end{pmatrix}, \tag{A.39}$$

where the matrix elements obey the relations

---

[4]We suppress the subindex $\mathcal{H}$ in the field operators to shorten the notation.

$$\Sigma^{+,+}(1,1') = \begin{cases} -\Sigma^{-,+}(1,1') & t_1 > t_{1'} \\ -\Sigma^{+,-}(1,1') & t_1 \leq t_{1'} \end{cases} \qquad (A.40)$$

$$\Sigma^{-,-}(1,1') = \begin{cases} -\Sigma^{-,+}(1,1') & t_1 < t_{1'} \\ -\Sigma^{+,-}(1,1') & t_1 \geq t_{1'}. \end{cases} \qquad (A.41)$$

It is easy to realize that within this matrix representation, the Dyson equation (A.33) admits a matrix representation in the Keldysh space given by

$$\hat{G}(1,1') = \hat{g}(1,1') + \int dt_2 d\vec{x_2} \ dt_3 d\vec{x_3} \ \hat{g}(1,2) \ \hat{\Sigma}(2,3) \ \hat{G}(3,1'), \qquad (A.42)$$

where now the time integration are along the real axis. Then, we finally arrive at a (2×2) matrix Dyson equation. As can be seen, the Keldysh formalism is formally identical to the equilibrium one, except that now every Green function becomes a (2×2) matrix in the Keldysh space. Thus, the only price that we have to pay for analyzing a non-equilibrium system is to handle with a greater number of Green functions. As can be observed in Eq. (A.42), the equation for the time-ordered Green function is coupled to the equation for $G^{+,-}$ and $G^{-,+}$, what is natural in a non-equilibrium problem since we must have an equation which describes the particle distribution in the system.

It is remarkable the elegance of this formalism summarized in the Dyson equation (A.42). It has a great resemblance with the Green functions formalism developed for studying phase transitions [16]. In general, when one analyzes a breaking symmetry the Green functions of the "normal" phase are coupled to new "anomalous" Green functions which are only non-zero in the new phase. Thus, a (2×2) matrix formalism arises, which is formally identical the normal case one. Typical examples are the superconducting transition, ferromagnetic transition, solid-gas transition, etc. The same happens in the case of the Keldysh formalism, what is easy to understand taking into account that we are handling with another breaking symmetry, namely the time breaking symmetry. Here, the "anomalous" Green functions are basically the nonequilibrium distribution functions.

The matrix structure can be further simplified. From the Eqs. (A.35-41) we can see that the different elements in the Keldysh space are non-independent. In particular, there exist the relations

$$G^{+,+} + G^{-,-} = G^{+,-} + G^{-,+} \qquad (A.43)$$

$$\Sigma^{+,+} + \Sigma^{-,-} = -\left(\Sigma^{+,-} + \Sigma^{-,+}\right). \qquad (A.44)$$

We can eliminate this redundancy by means of a canonical transformation [1] generated by

$$\hat{L} = \frac{1 - i\hat{\sigma}_y}{\sqrt{2}} \;\; ; \;\; \hat{\sigma}_y = \begin{pmatrix} 0 & -i \\ i & 0 \end{pmatrix} \tag{A.45}$$

We denote by $\check{G}$ the new (2×2) matrix generated by $\hat{L}$, then

$$\check{G} = \hat{L} \, \hat{G} \, \hat{L}^\dagger = \begin{pmatrix} 0 & G^a \\ G^r & G^K \end{pmatrix}, \tag{A.46}$$

where G^a is the advanced Green function.

$$\begin{aligned} G^a(1,1') &= G^{+,+}(1,1') - G^{-,+}(1,1') = G^{+,-}(1,1') - G^{-,-}(1,1') \\ &= i\Theta(t_{1'} - t_1)\langle [\hat{\psi}(1), \hat{\psi}^\dagger(1')]_+ \rangle, \end{aligned} \tag{A.47}$$

where $[\,,\,]_+$ represents the anticommutator and Θ is the step function which in this case selects times $t_{1'} > t_1$. On the other hand, G^r is the retarded Green function

$$\begin{aligned} G^r(1,1') &= G^{+,+}(1,1') - G^{+,-}(1,1') = G^{-,+}(1,1') - G^{-,-}(1,1') \\ &= -i\Theta(t_1 - t_{1'})\langle [\hat{\psi}(1), \hat{\psi}^\dagger(1')]_+ \rangle. \end{aligned} \tag{A.48}$$

Finally, G^K is the Keldysh function

$$\begin{aligned} G^K(1,1') &= G^{+,+}(1,1') + G^{+,-}(1,1') = G^{+,-}(1,1') + G^{-,+}(1,1') \\ &= -i\langle [\hat{\psi}(1), \hat{\psi}^\dagger(1')]_- \rangle, \end{aligned} \tag{A.49}$$

where $[\,,\,]_-$ is the commutator.

On the other hand, the self-energy is transformed as follows

$$\check{\Sigma} = \hat{L} \, \hat{\Sigma} \, \hat{L}^\dagger = \begin{pmatrix} \Sigma^K & \Sigma^r \\ \Sigma^a & 0 \end{pmatrix}, \tag{A.50}$$

where the following relations for the advanced, retarded and Keldysh self-energies hold

$$\Sigma^a = \Sigma^{+,+} + \Sigma^{-,+} = -\left(\Sigma^{-,-} + \Sigma^{+,-}\right) \tag{A.51}$$

$$\Sigma^r = \Sigma^{+,+} + \Sigma^{+,-} = -\left(\Sigma^{-,-} + \Sigma^{-,+}\right) \tag{A.52}$$

$$\Sigma^K = -\left(\Sigma^{+,+} + \Sigma^{-,-}\right) = \Sigma^{+,+} + \Sigma^{-,+} \tag{A.53}$$

$$\Sigma^{+,-} - \Sigma^{-,+} = \Sigma^r - \Sigma^a. \tag{A.54}$$

From the new matrix Dyson equation the following relations can be extracted: first, the advanced and retarded Green functions satisfy their own Dyson equations

$$G^a = g^a + g^a \Sigma^a G^a \tag{A.55}$$

$$G^r = g^r + g^r \Sigma^r G^r, \tag{A.56}$$

where integration over intermediate arguments is understood [5]. Secondly, the Keldysh function satisfies the following expression

$$G^K = g^K + g^K \Sigma^a G^a + g^r \Sigma^r G^K + g^r \Sigma^K G^a. \tag{A.57}$$

It is easy to convince oneself that the solution of this equation for G^K is

$$G^K = (1 + G^r \Sigma^r) g^K (1 + \Sigma^a G^a) + G^r \Sigma^K G^a. \tag{A.58}$$

Now, it is clear that the number of independent equation is indeed two, since G^r and G^a are hermite conjugated. The physical content of the functions $G^{r,a}$ and G^K is different, while $G^{r,a}$ basically give information on the states of the system, G^K informs on the occupation of those states.

We use more the function $G^{+,-}$ than the Keldysh function G^K. Thus, for ending this section we shall see how to express the function $G^{+,-}$ in terms of the advanced and retarded functions. Coming back to the original Keldysh space

$$\hat{G} = \hat{g} + \hat{L}^\dagger \, \check{g} \, \check{\Sigma} \, \check{G} \, \hat{L}. \tag{A.59}$$

Taking the element $(+, -)$ and making use of the relations (A.47-54), we obtain

$$G^{+,-} = g^{+,-} + g^{+,-} \Sigma^a G^a + g^r \Sigma^r G^{+,-} + g^r \Sigma^{+,-} G^a, \tag{A.60}$$

whose solution, as in the case of Eq. (A.57), is given by

$$G^{+,-} = (1 + G^r \Sigma^r) g^{+,-} (1 + \Sigma^a G^a) + G^r \Sigma^{+,-} G^a. \tag{A.61}$$

In the same way one obtains the following expression for $G^{-,+}$

$$G^{-,+} = (1 + G^r \Sigma^r) g^{-,+} (1 + \Sigma^a G^a) + G^r \Sigma^{-,+} G^a. \tag{A.62}$$

Eq. (A.61) for $G^{+,-}$ together with the Dyson equations (A.55-56) for the advanced and retarded functions form the set of equation that we have to solve in each concrete problem.

---

[5]We shall do the same for the rest of equations in this section in order to simplify the notation.

A.3   Feynman diagrams

Finally, in this section we briefly study how to build the Feynman diagrams in the Keldysh formalism, pointing out what are the main differences with the equilibrium case. Let us consider a simple example of a free electron system subjected to an external potential $V(\vec{x}, t)$ which constitutes the perturbation

$$\hat{V}(\vec{x}, t) = \int d\vec{x} \; \hat{\psi}^\dagger(\vec{x}, t) \; V(\vec{x}, t) \; \hat{\psi}(\vec{x}, t). \tag{A.63}$$

As stated in section A.1, the diagrammatic theory for the c-contour-ordered Green function is identical to the one for an ordinary Green function, except for the integrations along the Keldysh contour. The first order in the perturbative expansion of the Green function G_c is obtained from the expression (A.32) introducing the first order term in the expansion of $\hat{S}_c$ and applying the Wick theorem. This first order term $G_c^{(1)}$ is given by

$$G_c^{(1)}(1, 1') = \int d\vec{x}_2 \; \int_c dt_2 \; g_c(1, 2) \; V(2) \; g_c(2, 1'). \tag{A.64}$$

We are interested in the diagrammatic structure of each of the $\hat{G}$ elements in the Keldysh space. For obtaining them we decompose the integration along the contour into two integration along the real time axis

$$\int_c dt_2 = \int_{-\infty}^{\infty} dt_2 \; - \; \int_{-\infty}^{\infty} dt_2. \tag{A.65}$$

Splitting G_c (see Eq. (A.64)) into its components in the Keldysh space

$$G_{ij}^{(1)}(1, 1') = \int d\vec{x}_2 \int_{-\infty}^{\infty} dt_2 \; g_{ik}(1, 2) \; V_{kk'}(2) \; g_{k'j}(2, 1'), \tag{A.66}$$

where $i, j = +, -$, sum over repeated indexes is assumed and

$$V_{ij}(2) = V(2)(\hat{\sigma}_z)_{ij} \;\; ; \;\; \hat{\sigma}_z = \begin{pmatrix} 1 & 0 \\ 0 & -1 \end{pmatrix}. \tag{A.67}$$

For the sake of simplicity, we shall implicitly assume integrations over intermediate arguments. Thus, we can write down Eq. (A.66) as

$$\hat{G}^{(1)} = \hat{g} \; \hat{V} \; \hat{g}. \tag{A.68}$$

The only difference with the case of the corresponding equilibrium Green function is the appearance of $\hat{\sigma}_z$ in the perturbation. As in the equilibrium case the complete diagrammatic structure is the one shown in Fig. A.5. That is, the matrix Green function can be written as

$$\hat{G} = \hat{g} + \hat{g}\,\hat{V}\,\hat{G}. \tag{A.69}$$

This lead us to a self-energy

$$\hat{\Sigma} = \hat{V} = V\hat{\sigma}_z, \tag{A.70}$$

Thus, $\Sigma^{+,+} = -\Sigma^{-,-} = V$ and $\Sigma^{+,-} = \Sigma^{-,+} = 0$. Moreover, taking into account Eqs. (A.51-52) we have that $\Sigma^a = \Sigma^r = V$.
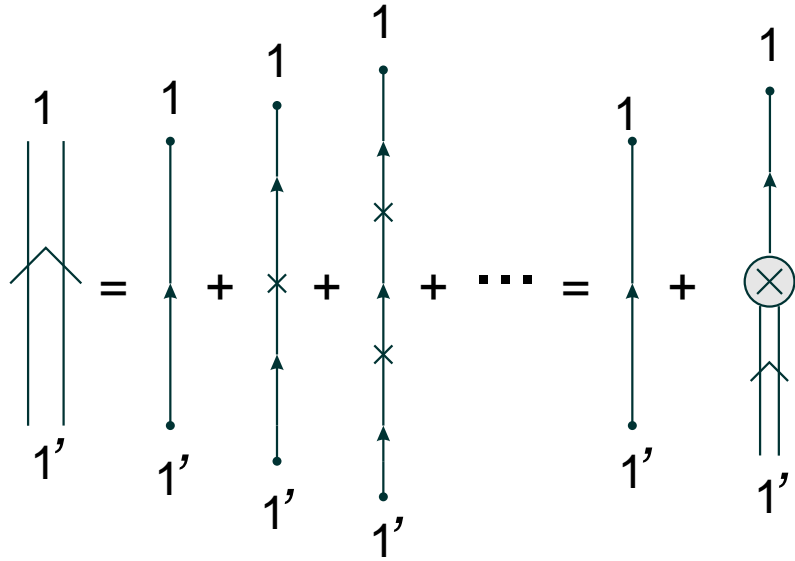
Figure A.5: Diagrammatic structure of a Green function in the case of an one-electron perturbation given by the external potential of Eq. (A.63).

As far as the perturbation is one-electron, the self-energies $\Sigma^{+,-}$ and $\Sigma^{-,+}$ vanish. These self-energies are associated to inelastic processes and then they will only be non-zero for many-body perturbations induced for example by an electron-electron interaction, electron-phonon interaction, etc. Finally, for the case of a two-body interaction, like the ones mentioned before, the diagrams are easily built following the same prescriptions that we have shown in this example.

Bibliography

[1] L.V. Keldysh, Zh. Ekps. Teor. Fiz. **47**, 1515 (1964) [Sov. Phys. JETP **20**, 1018 (1965)].

[2] D.F. Du Bois, *Nonequilibrium Quantum Statistical Mechanics of Plasma and Radiation*, in Lectures in Theoretical Physics Vol. IX C, edited by W.E. Brittin and A.D. Barut (Gordon and Breach, New York, 1967), p. 469.

[3] D.C. Langreth, in *Linear and Nonlinear Electron Transport in Solids*, edited by J.T. Devreese and V.E. van Doren, Vol. 17 of *Nato Advanced Study Institutes, Series B: Physics* (Plenum, New York, 1976).

[4] J. Rammer and H. Smith, Rev. Mod. Phys. **58**, 323 (1986).

[5] A.A. Abrikosov, L.P. Gorkov and I.E. Dzyaloshinski, *Methods of Quantum Field Theory in Statistical Physics*, Doover Publications, New York (1963).

[6] A.L. Fetter and J.D. Walecka, *Quantum Theory of Many-Particle Systems*, McGraw-Hill (1971).

[7] G.D. Mahan, *Many-Particle Physics*, Plenum Press (1990).

[8] R.P. Feynman, Phys. Rev. **76**, 749 (1949); *ibid.* **76**, 769 (1949).

[9] C. Caroli, R. Combescot, P. Nozieres, and D. Saint-James, J. Phys. C **4**, 916 (1971). C. Caroli, R. Combescot, D. Lederer, P. Nozieres, and D. Saint-James, J. Phys. C **4**, 2598 (1971). R. Combescot, J. Phys. C **4**, 2611 (1971). C. Caroli, R. Combescot, P. Nozieres, and D. Saint-James, J. Phys. C **5**, 21 (1972).

[10] T. Matsubara, Prog. Theor. Phys. **14**, 351 (1955).

[11] G.C. Wick, Phys. Rev. **80**, 268 (1950).

[12] P. Danielewicz, Ann. Phys. **152**, 239 (1984).

[13] Although nowadays this contour is known as Keldysh contour, indeed it was firstly introduced by J. Schwinger, J. Math. Phys. **2**, 407 (1961).

[14] M. Wagner, Phys. Rev. B **44**, 6104 (1991).

[15] This contour was originally introduced by Mills, R. Mills, *Propagators for Many-Particle Systems* (Gordon and Breach, New York, 1969).

[16] R.D. Mattuck and B. Johansson, Advances in Physics **17**, 509 (1968).

Appendix B

Calculation of the current in single channel N-N and N-S contacts

In this appendix we shall give the details of the calculation of the current in constant biased N-N and N-S single channel contacts using our Hamiltonian formalism.

As we explained in section 2.2, in these two cases the problem admits a stationary solution, so it is convenient to adopt a time-independent formulation based on the Hamiltonian (2.7). We assume that the left electrode is in normal state and the right one is either in normal or superconducting state. Moreover, we choose the energy origin at the right electrode chemical potential ($\mu_R = 0$). Let us remember that the current evaluated between the electrodes can be written in terms of the nonequilibrium Green functions $\hat{G}^{+-}$ (see section 2.2 for definition) as follows [1]

$$I(\tau) = \frac{2e}{\hbar} \left[\hat{t}\hat{G}_{RL}^{+-}(\tau,\tau) - \hat{t}^*\hat{G}_{LR}^{+-}(\tau,\tau) \right]_{11}, \tag{B.1}$$

where L and R denote the outermost sites of both electrodes, (1,1) indicates the corresponding element in the Nambu representation and the hopping $\hat{t}$ is given in this representation by the expression (2.14), being time-independent in the gauge which we have chosen.

As we commented in section 2.2, in order to solve this model we follow a perturbative scheme, based on the Keldysh formalism, in which we consider the electrode coupling term in the Hamiltonian (2.7) as a perturbation. Thus, it is easy to show that the self-energies of this problem have the form $\hat{\Sigma}_{LL}^{r,a} = \hat{\Sigma}_{RR}^{r,a} = 0$ and $\hat{\Sigma}_{LR}^{r,a} = (\hat{\Sigma}_{RL}^{r,a})^* = \hat{t}$.

---

[1] We assume that there exists spin symmetry and we only work in the electron space.

Due to the gauge choice that we have taken, the Green functions only depend on the difference of their temporal arguments. This permits us to write the current, after Fourier transforming, as follows

$$I = \frac{2e}{h} \int_{-\infty}^{\infty} d\omega \left[\hat{t} \hat{G}_{RL}^{+-}(\omega) - \hat{G}_{LR}^{+-}(\omega) \hat{t}^* \right]_{11}. \tag{B.2}$$

On the other hand, using their Dyson equations (see Appendix A) we can express the Green functions appearing in the current as

$$\begin{aligned}
\hat{G}_{LR}^{+-}(\omega) &= \hat{g}_{LL}^{+-}(\omega) \hat{t} \hat{G}_{RR}^{a}(\omega) + \hat{g}_{LL}^{r}(\omega) \hat{t} \hat{G}_{RR}^{+-}(\omega) \\
\hat{G}_{RL}^{+-}(\omega) &= \hat{G}_{RR}^{r}(\omega) \hat{t}^{\dagger} \hat{g}_{LL}^{+-}(\omega) + \hat{G}_{RR}^{+-}(\omega) \hat{t}^{\dagger} \hat{g}_{LL}^{a}(\omega),
\end{aligned} \tag{B.3}$$

where as usual $\hat{g}$ are the (retarded, advanced, etc) Green functions of the uncoupled electrodes, which are given by the expressions (2.16-17). On the other hand, $\hat{G}^{r,a}$ are the retarded and advanced Green functions of the perturbed system.

Introducing these expressions in the equation (B.2) and taking into account the general relation $\hat{G}^{a} - \hat{G}^{r} = \hat{G}^{+-} - \hat{G}^{-+}$, we can write the current as

$$I = \frac{2e}{h} |t|^2 \int_{-\infty}^{\infty} d\omega \left[g_{LL,11}^{+-}(\omega) G_{RR,11}^{-+}(\omega) - g_{LL,11}^{-+}(\omega) G_{RR,11}^{+-}(\omega) \right], \tag{B.4}$$

where let us remember that $\hat{g}^{+-}(\omega) = 2\pi i n_F(\omega)$ and $\hat{g}^{-+}(\omega) = -2\pi i \hat{\rho}(\omega)[1 - n_F(\omega)]$, where $\hat{\rho}(\omega) = (1/\pi) \mathrm{Im}[\hat{g}^{a}(\omega)]$ and $n_F(\omega)$ is the Fermi function.

What remains is to determine the perturbed Green functions $\hat{G}^{+-}$ and $\hat{G}^{-+}$. To do this we firstly express them in terms of advanced and retarded functions by means of the relation

$$\hat{G}^{(+-),(-+)}(\omega) = \left(\hat{I} + \hat{G}^{r}(\omega) \hat{\Sigma}^{r}(\omega) \right) \hat{g}^{(+-),(-+)}(\omega) \left(\hat{I} + \hat{\Sigma}^{a}(\omega) \hat{G}^{a}(\omega) \right). \tag{B.5}$$

If we take the (R,R) element in the previous expression we obtain

$$\hat{G}_{RR}^{(+-),(-+)} = \left(\hat{I} + \hat{G}_{RL}^{r} \hat{t} \right) \hat{g}_{RR}^{(+-),(-+)} \left(\hat{I} + \hat{t}^{\dagger} \hat{G}_{LR}^{a} \right) + \hat{G}_{RR}^{r} \hat{t}^{\dagger} \hat{g}_{LL}^{(+-),(-+)} \hat{t} \hat{G}_{RR}^{a}, \tag{B.6}$$

where we have not explicitly written the argument ω to make lighter the notation. Then, we take the (1,1) Nambu element in the latter expression having in mind that the left electrode is in the normal state, and thus, its Green functions $\hat{g}_{LL}$ are diagonal. Finally, we substitute in the current expression. Thus, we obtain that the current can be expressed as a sum of five terms: $I = \sum_{i=1}^{5} I_i$, where

$$I_1 = \frac{2e}{h}|t|^2 \int_{-\infty}^{\infty} d\omega \left(1 + G^r_{RL,11} t\right) \left(1 + t^* G^a_{LR,11}\right) \left\{g^{+-}_{LL,11} g^{-+}_{RR,11} - g^{-+}_{LL,11} g^{+-}_{RR,11}\right\}$$

$$I_2 = -\frac{2e}{h}|t|^2 \int_{-\infty}^{\infty} d\omega \, t \left(1 + G^r_{RL,11} t\right) G^a_{LR,21} \left\{g^{+-}_{LL,11} g^{-+}_{RR,12} - g^{-+}_{LL,11} g^{+-}_{RR,12}\right\}$$

$$I_3 = -\frac{2e}{h}|t|^2 \int_{-\infty}^{\infty} d\omega \, t^* G^r_{RL,12} \left(1 + t^* G^a_{LR,11}\right) \left\{g^{+-}_{LL,11} g^{-+}_{RR,21} - g^{-+}_{LL,11} g^{+-}_{RR,21}\right\}$$

$$I_4 = \frac{2e}{h}|t|^4 \int_{-\infty}^{\infty} d\omega \, G^r_{RL,12} G^a_{LR,21} \left\{g^{+-}_{LL,11} g^{-+}_{RR,22} - g^{-+}_{LL,11} g^{+-}_{RR,22}\right\}$$

$$I_5 = \frac{2e}{h}|t|^4 \int_{-\infty}^{\infty} d\omega \, G^r_{RR,12} G^a_{RR,21} \left\{g^{+-}_{LL,11} g^{-+}_{LL,22} - g^{-+}_{LL,11} g^{+-}_{LL,22}\right\} \tag{B.7}$$

The different perturbed Green functions $\hat{G}^{r,a}$ which appear in the previous expression can be determined using their Dyson equations:

$$\hat{G}^{r,a}(\omega) = \hat{g}^{r,a}(\omega) + \hat{g}^{r,a}(\omega)\hat{\Sigma}^{r,a}(\omega)\hat{G}^{r,a}(\omega), \tag{B.8}$$

just taking the corresponding sites and Nambu elements. Moreover, relations like $\hat{G}^a_{AB}(\omega) = \hat{G}^{r\dagger}_{BA}(\omega)$ can be deduced, and they allows us to simplify the expression of the current and to reduce the number of Green functions to be determined.

In the N-N case, i.e. when the right electrode is in the normal state, only the first term in the current expression survives. Then, the normal current adopts the form

$$I_{NN} = \frac{2e}{h}|t|^2 \int_{-\infty}^{\infty} d\omega \, |1 + G^r_{RL,11} t|^2 \left\{g^{+-}_{LL,11} g^{-+}_{RR,11} - g^{-+}_{LL,11} g^{+-}_{RR,11}\right\}. \tag{B.9}$$

From the Dyson equation (B.8), assuming that the R electrode is in normal state, one can obtain

$$G^r_{RL,11} = \frac{g^r_{RR,11} t^* g^r_{LL,11}}{1 - g^r_{RR,11} t^* g^r_{LL,11} t}. \tag{B.10}$$

Finally, we introduce this expression in the current and we express the functions $g^{(+-),(-+)}$ in terms of the density of states and Fermi functions of both electrodes. So, we can write the current I_{NN} as in the scattering formalism

$$I_{NN} = \frac{2e}{h} \int_{-\infty}^{\infty} T(\omega, V) \left[n_F(\omega - eV) - n_F(\omega)\right] d\omega, \tag{B.11}$$

where $T(\omega, V)$ is an energy and voltage dependent transmission coefficient given by [2]

---

[2]In the following expression we have suppressed the Nambu indexes because we are in the normal case.

$$T(\omega, V) = \frac{4\pi^2 |t|^2 \rho_{LL}(\omega - eV)\rho_{RR}(\omega)}{|1 - t^2 g_{LL}(\omega - eV)g_{RR}(\omega)|^2}, \qquad (B.12)$$

where now we have explicitly written the voltage dependence (let us remember that we had taken the right electrode chemical potential as the energy origin).

In principle, this expression is valid for an arbitrary voltage. If the system is in the linear regime we can assume that the density of states is energy independent in an interval around the Fermi level. Thus, in this range the normal Green functions are given by $g_{LL}^a = g_{RR}^a = i/W$, where W is an energy scale related to the density of states at the Fermi level: $\rho(\epsilon_F) = 1/(\pi W)$. So, in the ohmic regime the transmission probability becomes energy independent, adopting the form

$$T(\omega, V) \simeq \frac{4t^2/W^2}{(1 + t^2/W^2)^2} \equiv \alpha. \qquad (B.13)$$

The zero temperature normal linear conductance will be given by the expression $G_{NN} = (2e^2/h)\alpha$, which is nothing but the Landauer formulae for a single channel contact.

If the right electrode (R) is in superconducting state, the current is given by the full equation (B.7). If we assume electron-hole symmetry, the terms I_2 and I_3 give the same contribution. On the oter hand, I_5 is just the Andreev term, which we have denoted as I_A in Chapter 2. Thus, it is easy to realize that the expression (B.7) reduces to the expression (2.26) for the N-S current. In order to calculate this I_{NS} current one has to determine the different perturbed Green functions by solving the Dyson equations (B.8). Moreover, let us remember that the Green functions of the uncoupled electrodes are given by Eq. (2.16). Thus, after some elementary algebra one may obtain the results that we showed in section 2.3 for the N-S case.

Appendix C

Calculation of the current in a single channel S-S contact

In this appendix we shall describe the algorithm for determining the current in a constant voltage biased single channel S-S contact. We shall start analyzing the general case, then we shall concentrate in several limits, in which analytical results can be obtained, like the large voltage limit, the perfect transmission case and the small bias voltage regime ($eV \ll \Delta$).

C.1 General algorithm

As it was explained in section 2.2, in the case of a S-S contact it is convenient to do a gauge choice in which the voltage appears as a phase factor in the hopping element which connects the electrodes. Thus, we describe a single channel S-S contact by the Hamiltonian

$$\hat{H}(\tau) = \hat{H}_L + \hat{H}_R + \sum_\sigma \left(t e^{i\phi(\tau)/2} c^\dagger_{L\sigma} c_{R\sigma} + t^* e^{-i\phi(\tau)/2} c^\dagger_{R\sigma} c_{L\sigma} \right), \qquad \text{(C.1)}$$

where $H_{L,R}$ are the BCS Hamiltonians for the isolated electrodes, in the coupling term L and R stand for the outermost sites of each electrode and $\phi(\tau) = \phi_0 + 2eV\tau/\hbar$ is the time dependent superconducting phase.

Within this model the total current through the system evaluated between the electrodes is given by

$$I(\tau) = \frac{ie}{\hbar} \sum_\sigma (t e^{i\phi(\tau)/2} < c^\dagger_{L\sigma}(\tau) c_{R\sigma}(\tau) > - t^* e^{-i\phi(\tau)/2} < c^\dagger_{R\sigma}(\tau) c_{L\sigma}(\tau) >). \quad \text{(C.2)}$$

We write the expectation values appearing in the current in terms of the Keldysh Green functions $\hat{G}^{+-}$ (see section 2.2 for definition), then

$$I(\tau) = \frac{e}{\hbar} \, \text{Tr} \left[\hat{\sigma}_z \left(\hat{t}(\tau) \hat{G}_{RL}^{+-}(\tau,\tau) - \hat{G}_{LR}^{+-}(\tau,\tau) \hat{t}^{\dagger}(\tau) \right) \right], \qquad \text{(C.3)}$$

where $\hat{\sigma}_z$ is the corresponding Pauli matrix, Tr denotes the trace in the Nambu space and $\hat{t}$ is the time dependent hopping that in the mentioned matrix representation is written as

$$\hat{t} = \begin{pmatrix} te^{i\phi(\tau)/2} & 0 \\ 0 & -t^* e^{-i\phi(\tau)/2} \end{pmatrix}. \qquad \text{(C.4)}$$

As we said in section 2.4, we analyze this problem in terms of the renormalized hoppings. So, the following step is to express the current in terms of the dressed hoppings and the Green functions of the uncoupled electrodes. As usual we follow a perturbative scheme in which we consider the coupling term in the Hamiltonian (C.1) as a perturbation. Thus, the self-energies of this problem have the form $\hat{\Sigma}_{LL}^{r,a} = \hat{\Sigma}_{RR}^{r,a} = 0$ and $\hat{\Sigma}_{LR}^{r,a} = (\hat{\Sigma}_{RL}^{r,a})^* = \hat{t}$. Within this scheme, we make use of the Dyson equations fulfilled by the Green functions appearing in the current to express them as (see Appendix A)

$$\hat{G}_{LR}^{+-}(\tau,\tau) = \int d\tau_1 \left\{ \hat{g}_{LL}^{+-}(\tau-\tau_1) \hat{t}(\tau_1) \hat{G}_{RR}^{a}(\tau_1,\tau) + \hat{g}_{LL}^{r}(\tau-\tau_1) \hat{t}(\tau_1) \hat{G}_{RR}^{+-}(\tau_1,\tau) \right\}$$

$$\hat{G}_{RL}^{+-}(\tau,\tau) = \int d\tau_1 \left\{ \hat{G}_{RR}^{r}(\tau,\tau_1) \hat{t}^{\dagger}(\tau_1) \hat{g}_{LL}^{+-}(\tau_1-\tau) + \right.$$
$$\left. \hat{G}_{RR}^{+-}(\tau,\tau_1) \hat{t}^{\dagger}(\tau_1) \hat{g}_{LL}^{a}(\tau_1-\tau) \right\}, \qquad \text{(C.5)}$$

where $\hat{g}$ represent the (retarded, advanced, etc) Green functions of the uncoupled electrodes, which are given by the expressions (2.16-17). On the other hand, $\hat{G}^{r,a}$ are the retarded and advanced Green functions which verify their own Dyson equations:

$$\hat{G}^{r,a}(\tau,\tau') = \hat{g}^{r,a}(\tau-\tau') + \int d\tau_1 \, \hat{g}^{r,a}(\tau-\tau_1) \hat{\Sigma}^{r,a}(\tau_1) \hat{G}^{r,a}(\tau_1,\tau'). \qquad \text{(C.6)}$$

Next, we define the renormalized hoppings in terms of which we will finally express the current. Such hoppings are defined in terms of the Green functions as

$$\hat{T}_{LR}^{a,r}(\tau,\tau') = \hat{t}(\tau)\delta(\tau-\tau') + \hat{t}(\tau) \, \hat{G}_{RL}^{a,r}(\tau,\tau') \, \hat{t}(\tau')$$
$$\hat{T}_{RL}^{a,r}(\tau,\tau') = \hat{t}(\tau)^{\dagger}\delta(\tau-\tau') + \hat{t}^{\dagger}(\tau) \, \hat{G}_{LR}^{a,r}(\tau,\tau') \, \hat{t}^{\dagger}(\tau'). \qquad \text{(C.7)}$$

Taking into account the Dyson equation (C.6) and the definition of the dressed hoppings, it is easy to realize that there exist relations like

$$\hat{G}_{RR}^{r,a}\,\hat{t}^\dagger = \hat{g}_{RR}^{r,a}\,\hat{T}_{RL}^{r,a} \quad ; \quad \hat{G}_{LL}^{r,a}\,\hat{t} = \hat{g}_{LL}^{r,a}\,\hat{T}_{LR}^{r,a}$$
$$\hat{t}\,\hat{G}_{RR}^{r,a} = \hat{T}_{LR}^{r,a}\,\hat{g}_{RR}^{r,a} \quad ; \quad \hat{t}^\dagger\,\hat{G}_{LL}^{r,a} = \hat{T}_{RL}^{r,a}\,\hat{g}_{LL}^{r,a}, \tag{C.8}$$

where integration over intermediate arguments is understood, as we will do from now on, except if we say explicitly the contrary.

In order to achieve our aim of expressing the current in terms of the renormalized hoppings, we write the Green function $\hat{G}_{RR}^{+-}$, which appears in Eq. (C.5), in terms of the retarded and advanced Green functions. To do this we make use of the relation

$$\hat{G}_{RR}^{+-} = \left(\hat{1} + \hat{G}_{RL}^r \hat{t}\right)\,\hat{g}_{RR}^{+-}\,\left(\hat{1} + \hat{t}^\dagger \hat{G}_{LR}^a\right) + \hat{G}_{RR}^r \hat{t}^\dagger \hat{g}_{LL}^{+-} \hat{t} \hat{G}_{RR}^a. \tag{C.9}$$

Now, we introduce this relation in the expression (C.5) and substitute in the current expression. Taking into account the definition of the renormalized hoppings and the relations of Eq. (C.8), it is easy to check that the current can be written as follows

$$I(\tau) = \frac{e}{\hbar}\,\text{Tr}\left[\hat{\sigma}_z\left(\hat{T}_{LR}^r \hat{g}_{RR}^{+-}\hat{T}_{RL}^a \hat{g}_{LL}^a - \hat{g}_{LL}^r \hat{T}_{LR}^r \hat{g}_{RR}^{+-}\hat{T}_{RL}^a \right.\right.$$
$$\left.\left. +\hat{g}_{RR}^r \hat{T}_{RL}^r \hat{g}_{LL}^{+-}\hat{T}_{LR}^a - \hat{T}_{RL}^r \hat{g}_{LL}^{+-}\hat{T}_{LR}^a \hat{g}_{RR}^a\right)\right], \tag{C.10}$$

where again there is an implicit integration over intermediate temporal arguments.

Once we have expressed the current in terms of the dressed hoppings, it only remains to determine them. It is easy to realize that these hoppings verify their own Dyson equations. If we introduce the Green functions Dyson equation in the definition of the renormalized hoppings and make use of relations (C.8), we arrive at the following Dyson equation

$$\hat{T}_{LR}^{a,r}(\tau,\tau') = \hat{t}(\tau)\delta(\tau - \tau') +$$
$$\int d\tau_1 d\tau_2\,\hat{t}(\tau)\hat{g}_{RR}^{a,r}(\tau - \tau_1)\hat{t}^\dagger(\tau_1)\hat{g}_{LL}^{a,r}(\tau_1 - \tau_2)\hat{T}_{LR}^{a,r}(\tau_2,\tau')$$
$$\hat{T}_{RL}^{a,r}(\tau,\tau') = \hat{t}^\dagger(\tau)\delta(\tau - \tau') +$$
$$\int d\tau_1 d\tau_2\,\hat{t}(\tau)^\dagger \hat{g}_{LL}^{a,r}(\tau - \tau_1)\hat{t}(\tau_1)\hat{g}_{RR}^{a,r}(\tau_1 - \tau_2)\hat{T}_{RL}^{a,r}(\tau_2,\tau'), \tag{C.11}$$

where we have explicitly written the time integration for the sake of clarity.

As usual, in order to solve these equations is more convenient to pass to the frequency space where they become algebraic equations. Thus, we Fourier transform the hoppings with respect to the temporal arguments

$$\hat{T}(\tau, \tau') = \frac{1}{2\pi} \int d\omega \int d\omega' \, e^{-i\omega\tau} e^{i\omega'\tau'} \, \hat{T}(\omega, \omega'). \tag{C.12}$$

Indeed, both frequencies are not independent. It is easy to convince oneself that the renormalized hoppings admit a Fourier expansion of the form

$$\hat{T}(\tau, \tau') = \frac{1}{2\pi} \sum_n e^{in\phi(\tau')/2} \int d\omega \, e^{i\omega(\tau-\tau')}\hat{T}(\omega, \omega + n\omega_0/2), \tag{C.13}$$

where $\omega_0 = 2eV/\hbar$ and $\phi(\tau)$ is the time-dependent superconducting phase difference. One can see that this is true by checking that the Dyson equations (C.11) admit solutions of the previous form.

Taking into account the latter expression one can write the current as

$$I(\tau) = \sum_{m=-\infty}^{\infty} I_m e^{im\phi(\tau)}, \tag{C.14}$$

where the different Fourier current components can be expressed in terms of the Fourier components of the dressed hoppings $\hat{T}_{nm}(\omega) \equiv \hat{T}(\omega + n\omega_0/2, \omega + m\omega_0/2)$ as follows

$$
\begin{aligned}
I_m \;=\; & \frac{e}{h} \int d\omega \sum_n \text{Tr} \Big[\hat{\sigma}_z \Big(\hat{T}^r_{LR,0n} \hat{g}^{+-}_{RR,nn} \hat{T}^a_{RL,nm} \hat{g}^a_{LL,mm} - \hat{g}^r_{LL,00} \hat{T}^r_{LR,0n} \hat{g}^{+-}_{RR,nn} \hat{T}^a_{RL,nm} \\
& + \hat{g}^r_{RR,00} \hat{T}^r_{RL,0n} \hat{g}^{+-}_{LL,nn} \hat{T}^a_{LR,nm} - \hat{T}^r_{RL,0n} \hat{g}^{+-}_{LL,nn} \hat{T}^a_{LR,nm} \hat{g}^a_{RR,mm} \Big) \Big] .
\end{aligned}
\tag{C.15}
$$

Using the Dyson equations of the renormalized hoppings it can be shown that the general relation $\hat{T}^{a,r}_{RL,nm}(\omega) = \hat{T}^{r,a\dagger}_{LR,mn}(\omega)$ holds. Thus, we can express the current only in terms of the hoppings $\hat{T}^{a,r}_{LR,nm}$. In order to simplify the notation we denote these latter hoppings as $\hat{T}^{a,r}_{nm}$. So, we can write the current components for a symmetric junction as

$$
\begin{aligned}
I_m \;=\; & \frac{e}{h} \int d\omega \sum_n \text{Tr} \Big[\hat{\sigma}_z \Big(\hat{T}^r_{0n} \hat{g}^{+-}_{nn} \hat{T}^{r\dagger}_{mn} \hat{g}^a_{mm} - \hat{g}^r_{00} \hat{T}^r_{0n} \hat{g}^{+-}_{nn} \hat{T}^{r\dagger}_{mn} \\
& + \hat{g}^r_{00} \hat{T}^{a\dagger}_{n0} \hat{g}^{+-}_{nn} \hat{T}^a_{nm} - \hat{T}^{a\dagger}_{n0} \hat{g}^{+-}_{nn} \hat{T}^a_{nm} \hat{g}^a_{mm} \Big) \Big] ,
\end{aligned}
\tag{C.16}
$$

where we have got rid of the site indexes L and R in the Green functions of the uncoupled electrodes because we shall only deal with a symmetric junction.

Now, we have reduced the problem of the current calculation to the evaluation of the hopping Fourier components, $\hat{T}_{nm}(\omega)$. As it can be seen from de Dyson equations (C.11), these components fulfill the following set of algebraic linear equations

$$\hat{T}_{nm} = \hat{t}_{nm} + \hat{\epsilon}_n \hat{T}_{nm} + \hat{V}_{n,n-2} \hat{T}_{n-2,m} + \hat{V}_{n,n+2} \hat{T}_{n+2,m}, \qquad \text{(C.17)}$$

where the matrix coefficients $\hat{\epsilon}_n$ and $\hat{V}_{nm}$ can be expressed in terms of the Green functions of the uncoupled electrodes, given by Eq. (2.16), as

$$\hat{\epsilon}_n = t^2 \begin{pmatrix} g_{n+1} g_n & g_{n+1} f_n \\ g_{n-1} f_n & g_{n-1} g_n \end{pmatrix}$$

$$\hat{V}_{n,n+2} = -t^2 f_{n+1} \begin{pmatrix} f_{n+2} & g_{n+2} \\ 0 & 0 \end{pmatrix}$$

$$\hat{V}_{n,n-2} = -t^2 f_{n-1} \begin{pmatrix} 0 & 0 \\ g_{n-2} & f_{n-2} \end{pmatrix}, \qquad \text{(C.18)}$$

where we have used the notation $g(\omega) \equiv g_{11}(\omega) = g_{22}(\omega)$ and $f(\omega) \equiv g_{12}(\omega) = g_{21}(\omega)$, due to the electron-hole symmetry. Moreover, in the above equations the shorthand notation $g_n = g(\omega + n\omega_0/2)$ has been used.

As commented in section 2.4, the linear equations (C.17) are analogous to those describing a tight-binding chain with nearest-neighbor hopping parameters $\hat{V}_{n,n+2}$ and $\hat{V}_{n,n-2}$. A solution can then be obtained by standard recursive techniques. It is straightforward to show that the following recursive relations between the coefficients $\hat{T}_{nm}$ hold:

$$\begin{aligned} \hat{T}_{n+2,m}(\omega) &= \hat{z}^+ [\omega + (n-1)\omega_0] \, \hat{T}_{nm}(\omega), & n \geq 1 \\ \hat{T}_{n-2,m}(\omega) &= \hat{z}^- [\omega + (n+1)\omega_0] \, \hat{T}_{nm}(\omega), & n \leq -1, \end{aligned} \qquad \text{(C.19)}$$

where the transfer matrix $\hat{z}^{\pm}(\omega)$ satisfies the equation

$$\hat{z}^{\pm}(\omega) = \left[\hat{I} - \hat{\epsilon}_{\pm 3} - \hat{V}_{\pm 3, \pm 5} \hat{z}^{\pm}(\omega \pm \omega_0) \right]^{-1}. \qquad \text{(C.20)}$$

One can see from the previous equation that $\hat{z}^+(\omega)$ and $\hat{z}^-(\omega)$ are related by $\hat{z}^-(\omega, V) = \hat{\sigma}_x \hat{z}^-(\omega, -V) \hat{\sigma}_x$, where $\hat{\sigma}_x$ is the corresponding Pauli matrix.

By virtue of the relation $\hat{T}_{nm}(\omega) = \hat{T}_{n-m,0}(\omega + m\omega_0/2)$, one can write the current components given by Eq. (C.16) in terms of $\hat{T}_{n0}(\omega) \equiv \hat{T}_n$. Using recursive relation (C.19) the calculation of the components $\hat{T}_n$ can be reduced to a closed system for the coefficients $\hat{T}_1$ and $\hat{T}_{-1}$:

$$\begin{aligned} \left[\hat{I} - \hat{\epsilon}_1 - \hat{V}_{13} \hat{z}^+(\omega) \right] \hat{T}_1 &= \hat{t}_{10} + \hat{V}_{1,-1} \hat{T}_{-1} \\ \left[\hat{I} - \hat{\epsilon}_{-1} - \hat{V}_{-1,-3} \hat{z}^-(\omega) \right] \hat{T}_{-1} &= \hat{t}_{-10} + \hat{V}_{-1,1} \hat{T}_1. \end{aligned} \qquad \text{(C.21)}$$

The remaining task is the calculation of the transfer matrix $\hat{z}^+(\omega)$. It can be shown that the solution of Eq. (C.20) is a diagonal matrix whose elements can be expressed in terms of a scalar function $\lambda^+(\omega)$

$$\hat{z}^+(\omega) = -t^2 \begin{pmatrix} f_2 f_3 \frac{\delta_0^+ \delta_1^+}{\lambda_0^+ \lambda_1^+} & 0 \\ 0 & f_1 f_2 \frac{\delta_{-1}^+ \delta_0^+}{\lambda_0^+ \lambda_1^+} \end{pmatrix}, \tag{C.22}$$

where $\lambda_n^+ = \lambda^+(\omega + n\omega_0/2)$ and $\delta_n^+ = (\lambda_n^+ - g_{n+2})/t^2 f_{n+2}^2$. The function $\lambda^+(\omega)$ satisfies the following equation

$$\lambda_0^+ = g_2 + (t^2/W^2)\lambda_1^+ + t^2 g_2 \lambda_0^+ \lambda_1^+. \tag{C.23}$$

In principle, this expression gives rise to a infinite quadratic system, which will be truncated depending on the voltage and transmission. For arbitrary bias voltage, this system can only be solve numerically. However, as we will show below, it is possible to obtain analytical solutions in special cases like $\omega_0 \to 0$, $\omega_0 \to \infty$ and the perfect transmission case.

Once $\hat{z}^+(\omega)$ has been determined one can calculate the coefficients $\hat{T}_1$ and $\hat{T}_{-1}$ from Eq. (C.21)

$$\hat{T}_1 = \frac{-t}{1 - t^2 \lambda_2^- \lambda_{-1}^+} \begin{pmatrix} t^4 f_0 f_1 \delta_2^- \delta_{-1}^+ & t^2 f_1 \delta_{-1}^+ \\ t^2 f_0 \delta_2^- & 1 \end{pmatrix} \tag{C.24}$$

$$\hat{T}_{-1}(\omega, V) = -\hat{\sigma}_x \hat{T}_1(\omega, -V)\hat{\sigma}_x, \tag{C.25}$$

where $\lambda_n^-(\omega, V) = \lambda_n^+(\omega, -V)$ and $\delta_n^-(\omega, V) = \delta_n^+(\omega, -V)$. The rest of the coefficients $\hat{T}_n$ can be calculated from Eqs. (C.19):

$$\hat{T}_{2n+1} = \left[\prod_{i=1}^{n} \hat{z}^+(\omega + (i-1)\omega_0)\right]\hat{T}_1, \qquad n > 0$$

$$\hat{T}_{-n} = -\hat{\sigma}_x \hat{T}_n(\omega, -V)\hat{\sigma}_x, \qquad n > 0. \tag{C.26}$$

We finish the discussion about the general algorithm dividing the current into its dissipative, I_D, and nondissipative part, I_S,

$$I_D(\tau) = I_0 + \sum_{m>0}\left\{I_m^D \cos m\phi(\tau)\right\}$$

$$I_S(\tau) = \sum_{m>0}\left\{I_m^S \sin m\phi(\tau)\right\}, \tag{C.27}$$

where I_0 is the dc component, $I_m^D \equiv I_m + I_{-m}$ are the dissipative components and $I_m^S \equiv i(I_m - I_{-m})$ are the nondissipative components.

In the case of a symmetric junction it can be shown that the relation $\hat{T}_{LR,nm}^r = -\hat{\sigma}_x \hat{T}_{m-n}^a(\omega + n\omega_0)\hat{\sigma}_x$ holds, where we have used the new notation in the right hand side of the equation. This expression permits us, after some algebra, to write the current components as

$$I_0 = -\frac{4e}{h} \int_{-\infty}^{\infty} d\omega \sum_{n=odd} \text{Re} \left\{ \text{Tr} \left(\hat{\sigma}_z \hat{T}_n^{a\dagger}(\omega) \hat{g}_n^{+-} \hat{T}_n^a(\omega) \hat{g}_0^a \right) \right\} \qquad (C.28)$$

$$I_m^D = -\frac{4e}{h} \int_{-\infty}^{\infty} d\omega \sum_{n=odd} \text{Re} \left\{ \text{Tr} \left(\hat{\sigma}_z \left[\hat{T}_{n+m}^{a\dagger}(\omega - m\omega_0/2) + \hat{T}_{n-m}^{a\dagger}(\omega + m\omega_0/2) \right] \right.\right.$$
$$\left.\left. \hat{g}_n^{+-} \hat{T}_n^a(\omega) \hat{g}_0^a \right) \right\} \qquad (C.29)$$

$$I_m^S = \frac{4e}{h} \int_{-\infty}^{\infty} d\omega \sum_{n=odd} \text{Im} \left\{ \text{Tr} \left(\hat{\sigma}_z \left[\hat{T}_{n+m}^{a\dagger}(\omega - m\omega_0/2) - \hat{T}_{n-m}^{a\dagger}(\omega + m\omega_0/2) \right] \right.\right.$$
$$\left.\left. \hat{g}_n^{+-} \hat{T}_n^a(\omega) \hat{g}_0^a \right) \right\}. \qquad (C.30)$$

So far, we have describe the general algorithm. In the next sections we shall concentrate in some limiting cases where analytical results can be obtained.

C.2   Excess current

In this section we give the details on the evaluation of the excess current in a S-S junction. In the limit $eV/\Delta \to \infty$ only the dc current component I_0 survives. The infinite summation over n in Eq. (C.28) can be truncated in this case neglecting the $|n| > 1$ terms. This is justified as the product $f_n f_{n+1}$ are negligible in this limit leading to a vanishing transfer matrix $\hat{z}^{\pm}(\omega)$. Physically, this is equivalent to neglecting multiple Andreev processes for $eV/\Delta \gg 1$. Then, Eq. (C.28) reduces to

$$I_0 = -\frac{4e}{h} \int_{-\infty}^{\infty} d\omega \sum_{n=-1,1} \text{Re} \left\{ \text{Tr} \left(\hat{\sigma}_z \hat{T}_n^{a\dagger}(\omega) \hat{g}_n^{+-} \hat{T}_n^a(\omega) \hat{g}_0^a \right) \right\} \qquad (C.31)$$

where now

$$\hat{T}_1 \sim \frac{-t}{1 - t^2 \lambda_2^- \lambda_{-1}^+} \begin{pmatrix} 0 & t^2 f_1 \delta_{-1}^+ \\ t^2 f_0 \delta_2^- & 1 \end{pmatrix}$$
$$\hat{T}_{-1}(\omega, V) = -\hat{\sigma}_x \hat{T}_1(\omega, -V) \hat{\sigma}_x.$$

On the other hand, when neglecting contributions of order Δ/eV Eq. (C.23) simply yields $\lambda_n^+ \sim (g_{n+2} + it^2/W^3)/(1 - it^2 g_{n+2}/W)$. Carrying this solution to the current and after some trivial algebra, we obtain the results $I_{exc}^{SS} = 2I_{exc}^{NS}$ for the excess current at zero temperature and any value of the transmission coefficient.

C.3 Dc current for $\alpha = 1$

This section is devoted to the analysis of the dc current in the perfect transmission case, whose results were commented in section 2.4.1.

The case $\alpha = 1$ is reached when the condition $t = W$ (see Eq. (2.25)) takes place. This implies that Eq. (C.23) admits a simple solution: $\lambda_n = i/t$ (we refer to the advanced parameter). This solution makes that the transfer matrix $\hat{z}^+(\omega)$ adopts a very simple form:

$$\hat{z}^+(\omega) = \begin{pmatrix} a_2 a_3 & 0 \\ 0 & a_1 a_2 \end{pmatrix}, \tag{C.32}$$

where $a(\omega)$ is the probability amplitude of an Andreev reflection in a N-S interfase with perfect transmission and it is given by $a \equiv (i - g^a)/f^a$, what yields an energy dependence given by Eq. (2.48). Moreover, we have used the shorthand notation $a_n = a(\omega + neV)$.

On the other hand, the hopping Fourier components adopt the expressions

$$\hat{T}_1^a = -\frac{t}{2} \begin{pmatrix} a_0 a_1 & a_1 \\ a_0 & 1 \end{pmatrix},$$

$$\hat{T}_{2n+1}^a = -\frac{t}{2} \left[\prod_{i=1}^{2n} a_i \right] \begin{pmatrix} a_0 a_{2n+1} & a_{2n+1} \\ a_0 & 1 \end{pmatrix}, \qquad n > 0. \tag{C.33}$$

If we introduce these expressions in Eq. (C.28) for the dc current, we obtain the expression (2.47) after elementary algebra.

One of the main features of the dc current at perfect transmission is its saturation at zero voltage. In order to obtain the saturation value is convenient to regroup the series appearing in Eq. (2.47) to write the dc current as follows

$$I_0 = \frac{2e}{h} \int_{-\infty}^{\infty} d\omega \sum_{n=-\infty}^{\infty} R_n(\omega) \left\{ n_F(\omega + (n - 1/2)eV) - n_F(\omega + (n + 1/2)eV) \right\}, \tag{C.34}$$

where n_F is the Fermi function and R_n is the probability of a multiple Andreev reflection for perfect transmission given by $R_n = \prod_{i=1}^{n} |a_{i-1/2}|^2$ for $n > 0$, $R_0 = 1$

and $R_{-n} = \prod_{i=1}^{n} |a_{-i+1/2}|^2$ con $n > 0$. When the bias voltage tends to zero at zero temperature, the integrand in the previous expression tends to one inside the gap and zero outside. This is just a consequence of having a probability equal to one inside the gap for the multiple Andreev reflections. Then, the saturation value of the dc current at zero voltage is $I_0 = (4e/h)\Delta$.

C.4 Small bias voltage limit

In this section we give the main steps in the analytical calculation of the current components in the limit $eV/\Delta \to 0$, commented in section 2.4.3.

C.4.1 Linear regime ($\eta \gg eV$)

Let us start analyzing the linear regime case which takes place when the relaxation energy η is greater than the voltage. In this case η becomes the natural cut-off of the Andreev reflections, giving rise to a linear regime which we are going to study now.

The small voltage response can be straightforwardly derived from Eqs. (C.28-30) by expanding the Fermi functions appearing in $\hat{g}^{+-}$ up to first order in eV: $n_F(\omega + n\omega_0/2) \sim n_F(\omega) - (\beta/8)n\omega_0 \text{sech}^2(\beta\omega/2)$, where β is the inverse of the temperature, and evalutating the rest of these expressions at $eV = 0$. The current components can be written as

$$I_0 = \frac{2e^2}{h}\beta V \int_{-\infty}^{\infty} d\omega \, \text{sech}^2(\frac{\beta\omega}{2}) \sum_{n=odd>0} n\text{Re}\left\{\text{Tr}\left(\hat{\sigma}_z \hat{T}_n^{a\dagger}(\hat{g}_0^a - \hat{g}_0^r)\hat{T}_n^a \hat{g}_0^a\right)\right\} \quad (C.35)$$

$$I_m^D = \frac{2e^2}{h}\beta V \int_{-\infty}^{\infty} d\omega \, \text{sech}^2(\frac{\beta\omega}{2}) \sum_{n=odd>0} n\text{Re}\left\{\text{Tr}\left(\hat{\sigma}_z \left[\hat{T}_{n+m}^{a\dagger} + \hat{T}_{n-m}^{a\dagger}\right](\hat{g}_0^a - \hat{g}_0^r)\hat{T}_n^a \hat{g}_0^a\right)\right\}$$
$$(C.36)$$

$$I_m^S = \frac{8e}{h} \int_{-\infty}^{\infty} d\omega \, n_F(\omega) \sum_{n=odd>0} \text{Im}\left\{\text{Tr}\left(\hat{\sigma}_z \left[\hat{T}_{n+m}^{a\dagger} - \hat{T}_{n-m}^{a\dagger}\right](\hat{g}_0^a - \hat{g}_0^r)\hat{T}_n^a \hat{g}_0^a\right)\right\}.$$
$$(C.37)$$

Thus, the dissipative contribution, I_D, goes to zero as $I_D(\phi) \sim G(\phi)V$, $G(\phi)$ being the phase-dependent linear conductance, while the supercurrent part $I_S(\phi)$, tends to a finite value at $V = 0$.

In the zero-voltage limit the coefficients $\hat{T}_n$ adopt a simple form. The transfer matrix $\hat{z}^{\pm}(\omega)$ becomes a scalar function: $\hat{z}^+(\omega) = \hat{z}^-(\omega) \equiv z(\omega)\hat{I}$; with $z(\omega) = -t^2 f\delta^2/\lambda^2$, where $\lambda^+(\omega) = \lambda^-(\omega) \equiv \lambda(\omega)$ satisfies the simple quadratic equation

$$t^2 g(\omega)\lambda^2(\omega) - (1 - \frac{t^2}{W^2})\lambda(w) + g(\omega) = 0. \tag{C.38}$$

The physical solution of this equation for $\eta = 0$ is [1]

$$\lambda = \frac{e^{i\varphi_\lambda(\omega)}}{t}, \qquad \Delta\sqrt{1-\alpha} \le |\omega| \le \Delta, \tag{C.39}$$

where

$$\varphi_\lambda(\omega) = \arcsin\left(\frac{1}{\sqrt{\alpha}|\omega|}\sqrt{\omega^2 - (1-\alpha)\Delta^2}\right). \tag{C.40}$$

As we see λ is just a phase factor in the indicated energy range. Due to this fact, this range will be the most important one in this problem because, as we will show below, in this interval the Andreev bound states move giving the most important contribution to the current in the weakly damped regime.

Finally, the coefficients $\hat{T}_n$ adopt the form

$$\hat{T}_1(\omega) = \frac{-t}{1 - t^2\lambda^2}\begin{pmatrix} t^4 f^2 \delta^2 & t^2 f\delta \\ t^2 f\delta & 1 \end{pmatrix} \tag{C.41}$$

$$\hat{T}_{2n+1}(\omega) = z^n(\omega)\hat{T}_1(\omega), \qquad n \ge 0. \tag{C.42}$$

Due to these simple recursive relations, the series appearing in the current components become geometrical series, which can be summed up without difficulty. In the weakly damped case, $\eta/\alpha\Delta \ll 1$, these summations lead to analytical expressions for the dissipative and nondissipative parts of the current. By solving Eq. (C.38) up to corrections of order $\eta/\alpha\Delta$ one obtains

$$z(\omega) = e^{i\varphi(\omega)} - \frac{4\omega\eta}{\alpha\Delta^2}\left[i + \cotg(\varphi(\omega))\right], \qquad \Delta\sqrt{1-\alpha} \le |\omega| \le \Delta, \tag{C.43}$$

where

$$\varphi(\omega) = \arcsin\left(\frac{2}{\alpha\Delta^2}\sqrt{\Delta^2 - \omega^2}\sqrt{\omega^2 - (1-\alpha)\Delta^2}\right). \tag{C.44}$$

The summation of the geometrical series appearing in the current components yields

---

[1]This solution refers to the advanced parameter, i.e. considering that the Green functions appearing in Eq. (C.38) are advanced. Let us recall that we are expressing the current in terms of advanced hoppings.

$$I_0 = \frac{2e^2}{h}\beta V \int_{-\infty}^{\infty} d\omega \, \text{sech}^2(\frac{\beta\omega}{2})\text{Re}\left\{A(\omega)\right\} \frac{1+|z|^2}{(1-|z|^2)^2} \qquad (C.45)$$

$$I_m^D = \frac{2e^2}{h}\beta V \int_{-\infty}^{\infty} d\omega \, \text{sech}^2(\frac{\beta\omega}{2})\text{Re}\left\{A(\omega)\left[(z^m + (z^*)^m)\frac{1+|z|^2}{(1-|z|^2)^2} + \frac{2mz^m}{1-|z|^2}\right]\right\}$$
$$(C.46)$$

$$I_m^S = \frac{8e}{h}\int_{-\infty}^{\infty} d\omega \, n_F(\omega)\text{Im}\left\{A(\omega)\frac{(z^*)^m - z^m}{1-|z|^2}\right\}, \qquad (C.47)$$

where $A(\omega) \equiv \text{Tr}[\hat{\sigma}_z \hat{T}_1^{a\dagger}(\hat{g}^a - \hat{g}^r)\hat{T}_1^a \hat{g}^a]$. This expression is valid for arbitrary η within the linear regime and allows us to identify the two subregimes we spoke about in section 2.4.3. It can be noticed that in the weakly damped limit ($\eta \ll \alpha\Delta$) the integrands in the previous expressions go like $1/\eta$ and the energy interval $\Delta\sqrt{1-\alpha} \leq |\omega| \leq \Delta$ gives the main contribution to the current. On the other hand, in the strongly damped case ($\eta \gg \alpha\Delta$) an important contribution to the current comes from the continuous band. This is illustrated in Fig. 2.15 where the current density for the dc component is shown for different values of η.

Finally, we sum up all the current components to obtain the total contribution to the dissipative and nondissipative parts. When carrying out these sums, the current densities become singular at the condition $\varphi(\omega) = \phi$. This condiction is satisfied for $\omega = \omega_S = \pm\Delta\sqrt{1 - \alpha\sin^2(\phi/2)}$, i.e. at the Andreev bound state energy levels. In the weakly damped regime these sums lead us to

$$I_D(\phi) = \frac{e^2\alpha^2\Delta^4}{8\eta h}\beta V \int_{-\infty}^{\infty} d\omega \, \text{sech}^2(\frac{\beta\omega}{2})\frac{\sin^2 \varphi(\omega)}{\omega} \times$$
$$\text{Im}\left\{\frac{1}{(\omega - |\omega_S| - i\eta)(\omega + |\omega_S| - i\eta)}\right\} \quad (C.48)$$

$$I_S(\phi) = -\frac{2e}{h}\alpha\Delta^2\sin\phi \int_{-\infty}^{\infty} d\omega \, n_F(\omega)\text{Im}\left\{\frac{1}{(\omega - |\omega_S| - i\eta)(\omega + |\omega_S| - i\eta)}\right\}. \quad (C.49)$$

All the contributions to the current come from the poles at the Andreev bound states, what makes the evaluation of these integrals quite simple. Eqs. (C.48-49) yield the expressions (2.55-56) for the supercurrent and phase-dependent linear conductance.

C.4.2 Nonlinear regime ($\eta \ll eV$)

When $\eta < eV$ there is no a linear regime. In this subsection we give technical details about this case which has been analyzed by Averin and Bardas [130].

First, making use of the relation $\hat{T}_{-n}(\omega, V) = -\hat{\sigma}_x \hat{T}_n(\omega, -V)\hat{\sigma}_x$, we can rewrite the current components (Eqs. (C.28-30)) as

$$
I_0 = \frac{4e}{h} \int_{-\infty}^{\infty} d\omega \tanh\left(\frac{\beta\omega}{2}\right) \sum_{n=odd>0} \mathrm{Re}\left\{ \mathrm{Tr}\left(\hat{\sigma}_z \hat{T}_n^{a\dagger}(\omega - n\omega_0/2)(\hat{g}_0^a - \hat{g}_0^r) \times \right.\right.
$$
$$
\left.\left. \hat{T}_n^a(\omega - n\omega_0/2)\hat{g}_{-n}^a \right) \right\}
$$

$$
I_m^D = \frac{4e}{h} \int_{-\infty}^{\infty} d\omega \tanh\left(\frac{\beta\omega}{2}\right) \sum_{n=odd>0} \mathrm{Re}\left\{ \mathrm{Tr}\left(\hat{\sigma}_z \times \right.\right.
$$
$$
\left.\left. \left[\hat{T}_{n+m}^{a\dagger}(\omega - n\omega_0/2) + \hat{T}_{n-m}^{a\dagger}(\omega - n\omega_0/2)\right] (\hat{g}_0^a - \hat{g}_0^r)\hat{T}_n^a(\omega - n\omega_0/2)\hat{g}_{-n}^a \right) \right\}
$$

$$
I_m^S = -\frac{4e}{h} \int_{-\infty}^{\infty} d\omega \tanh\left(\frac{\beta\omega}{2}\right) \sum_{n=odd>0} \mathrm{Im}\left\{ \mathrm{Tr}\left(\hat{\sigma}_z \times \right.\right.
$$
$$
\left.\left. \left[\hat{T}_{n+m}^{a\dagger}(\omega - n\omega_0/2) - \hat{T}_{n-m}^{a\dagger}(\omega - n\omega_0/2)\right] (\hat{g}_0^a - \hat{g}_0^r)\hat{T}_n^a(\omega - n\omega_0/2)\hat{g}_{-n}^a \right) \right\}. \quad (C.50)
$$

In the limit $eV \to 0$ the solution of Eq. (C.23) is $\lambda_n^+ = \lambda[\omega + (n+2)\omega_0/2]$, where $\lambda(\omega)$ satisfies the quadratic equation (C.38). The coefficients $\hat{T}_n$ ($n > 0$) can then generated starting from $\hat{T}_1$ and using the transfer matrix $\hat{z}^+(\omega)$. These quantities are obtained from Eqs. (C.22) and (C.24) making use of the $eV \to 0$ solution for λ_n^+.

For the nonlinear regime analytical results can only be obtained for perfect transmission. In this case, as it was shown above, we have $\lambda_n^+ = i/t$, what yields the expression (C.33) for the hopping components. As discussed in Ref. [130], when written as in Eq. (C.50), the main contribution to the current in this limit comes from a small energy range around the gap edges. Moreover, one can see that when $eV \to 0$ the nondissipative components vanish, while the nondissipative ones tend to finite values. Evaluation of the integrals appearing in Eq. (C.50) leads to expression (2.57) for the total dissipative current I_D.

Appendix D

Josephson current and microwave radiation: Detection of the Andreev bound states

As discussed in Chapter 2, the Andreev states play a central role in the adiabatic dynamics of an SQPC at low bias voltage. From the theoretical point of view nobody doubts about their existence, however there is no yet a direct experimental evidence of it. The aim of this appendix is to propose a method for the direct detection of the Andreev states in a Josephson junction at zero bias voltage. Considering that the typical subgap energies are in the microwave range, it seems natural to propose using microwave radiation for a direct detection of these bound states. This possibility has been suggested in a previous work by us [280] and in Ref. [281].

In order to analyze the effect of a microwave radiation on the dc Josephson current we shall study the single channel model introduced in section 2.2. We shall describe the laser field by a classic vector potential $\vec{A}(\vec{r}, \tau) = \vec{A}_0(\vec{r}) \cos(\omega_r \tau)$, which means neglecting quantum fluctuations in the photon field. The precise distribution of the electromagnetic field around the junction interface is dependent on materials and geometry, and its direct calculation is a complicated problem. However, for a wide range of frequencies we may assume that the field intensity is maximum in the interfase region and we can neglect the effect of the field penetrating inside the electrodes.

In the presence of a laser field the Hamiltonian (2.8) for a single channel Josephson junction is modified by an extra contribution given by

$$\delta \hat{H} = -\frac{1}{c} \int d^3r \; \vec{J}(\vec{r}) \; \delta \vec{A}(\vec{r}) \tag{D.1}$$

where $\vec{J}(\vec{r})$ is the current density in the junction.

Within the previous assumptions the field can be introduced as a phase factor modulating the hopping which connects the electrodes in Hamiltonian (2.8) as follows [128]

$$t(\tau) = t e^{i(\phi_0 + \alpha_0 \cos \omega_r \tau)},$$ (D.2)

where ϕ_0 is the superconducting phase difference across the junction, ω_r is the microwave frequency and $\alpha_0 = eV_{opt}/(\hbar \omega_r)$, V_{opt} being the optical voltage induced by the field across the constriction. The parameter α_0 measures the strength of the coupling with the external field.
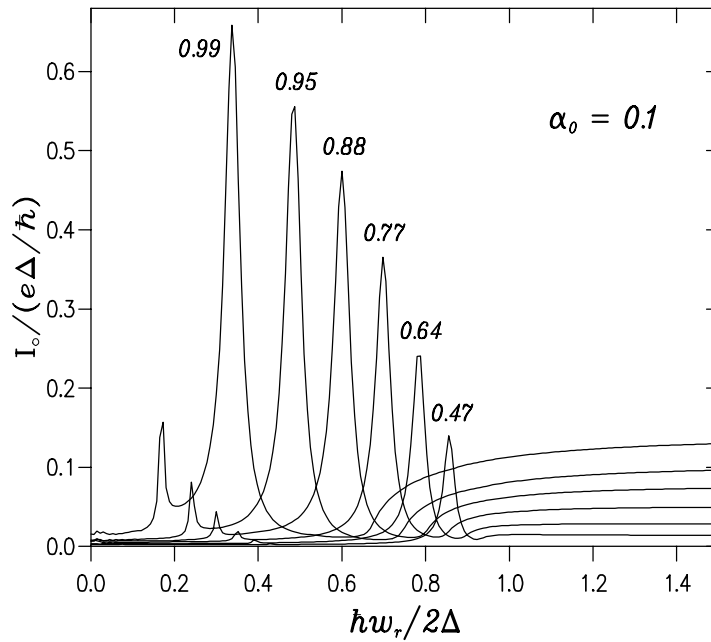
Figure D.1: Induced dc current in a SQPC under microwave radiation for different normal transmissions in the limit of weak coupling ($\alpha_0 = 0.1$).

The time-dependent hopping can be expanded as

$$t(\tau) = t \sum_n i^n J_n(\alpha_0) e^{in\omega_r \tau},$$ (D.3)

where J_n is the n-order Bessel function. For small coupling one can keep the lowest order terms in Eq. (D.3) and obtain some analytical results [280]. In the general case, the model Hamiltonian can be viewed, according to Eq. (D.3), as a superposition of

processes where an arbitrary number of energy quanta $\hbar\omega_r$ are absorbed or emitted. As the temporal dependence of each term in Eq. (D.3) is formally equivalent to that in the constant voltage case, the generalization of the algorithm discussed in Chapter 2 to the present case is straightforward.
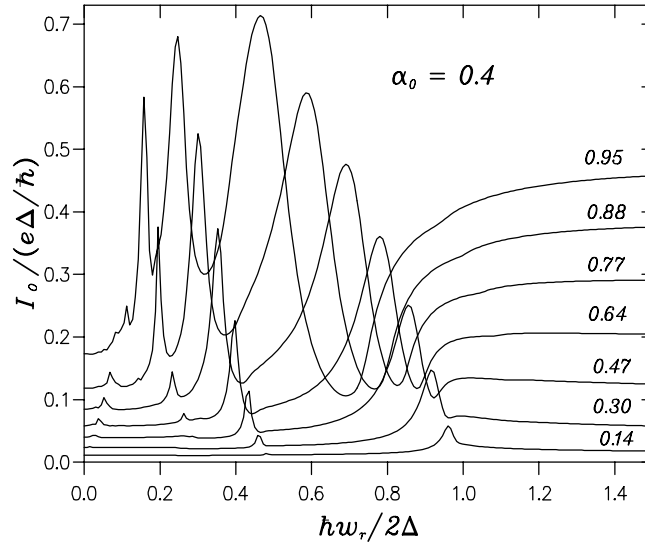

Figure D.2: The same as in Fig. D.1 for $\alpha_0 = 0.4$.

Fig. D.1 shows the induced dc current [1] as a function of the microwave frequency for the case of low coupling constant ($\alpha_0 = 0.1$). All the results correspond to the situation in which the contact is carrying the maximum supercurrent. In this weak coupling limit the induced current is mainly due to the excitation from the lower to the upper Andreev state, which carries a negative current, i.e. opposite to the supercurrent. As a consequence the induced current exhibits a maximum for the resonant condition $\omega_r = 2\epsilon(\phi)$, where $\epsilon(\phi) = \Delta\sqrt{1 - T\sin^2(\phi/2)}$ is the position of the Andreev state inside the gap. For low transmission this feature becomes the Riedel peak at $\omega_r = 2\Delta$ [20]. At resonances, the induced current can be of the same order as the critical supercurrent. One can also notice a second satellite peak around $\epsilon(\phi)$ associated with two-photon processes and a continuous band above $\Delta + \epsilon(\phi)$.

When the coupling constant α_0 increases the contribution of higher order processes becomes progressively more important, as illustrated in Figs. D.2 and D.3, giving rise to a greater number of resonances in the region $\omega_r < 2\Delta$. Finally, for

---

[1]The induced dc current is defined as $I_0(\phi, \omega_r) \equiv I_S(\phi) - I(\phi, \omega_r)$, where $I_S(\phi)$ is the supercurrent without radiation and $I(\phi, \omega_r)$ is the total dc current in the presence of the laser radiation.

$\alpha_0 > 1$ the resonant condition for the excitation of the upper Andreev state can no longer be resolved.
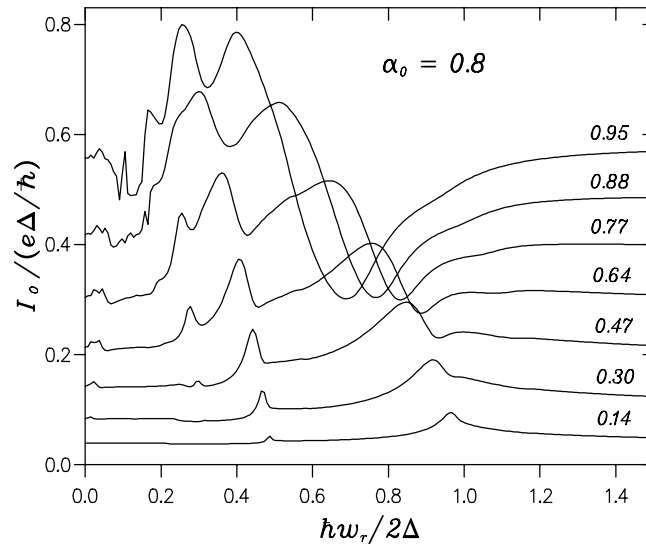

Figure D.3: The same as in Fig. D.1 for $\alpha_0 = 0.8$.

Finally, we have shown in this appendix that the analysis of the dc Josephson current under a non very high microwave radiation ($\alpha_0 \sim 0.1 - 0.5$) would allow to reveal the Andreev bound states responsibles of the supercurrent.

Appendix E

Current in an atomic contact

This appendix is devoted to the analysis of several technical issues related to the calculation of the current and transmission in a metallic atomic-size contact. In section E.1 we shall deduce the current expression in these systems, and in section E.2 we shall analyze the problem of why the fourth channel in the sp-like metals is closed.

E.1 Expression of the current through an atomic contact

First, we face the problem of the calculation of the elastic current in an atomic contact with arbitrary geometry in terms of its microscopic parameters.

Let us consider an atomic contact with arbitrary geometry like the one depicted in Fig. E.1. In this contact we distinguish three different parts: the reservoirs L and R, with their respective chemical potentials, and a central region formed by N atomic layers [1] numbered as indicated in the figure, which can contain an arbitrary constriction. In principle, the reservoirs L and R can have an arbitrary shape and we assume that they provide a region where the temperature and the chemical potential are constants. This separation of the contact in these three subsystems is somewhat arbitrary and one can play with that.

As explained in Chapter 6, we describe an atomic contact with the following electronic tight-binding Hamiltonian:

$$\hat{H} = \sum_{i\alpha,\sigma} \epsilon_{i\alpha} c^{\dagger}_{i\alpha\sigma} c_{i\alpha\sigma} + \sum_{i\alpha\neq j\beta,\sigma} t_{i\alpha,j\beta} c^{\dagger}_{i\alpha,\sigma} c_{j\beta,\sigma}, \tag{E.1}$$

---

[1] The existence of ordered layers is not necessary. In the picture is shown like this to make easy their numbering.
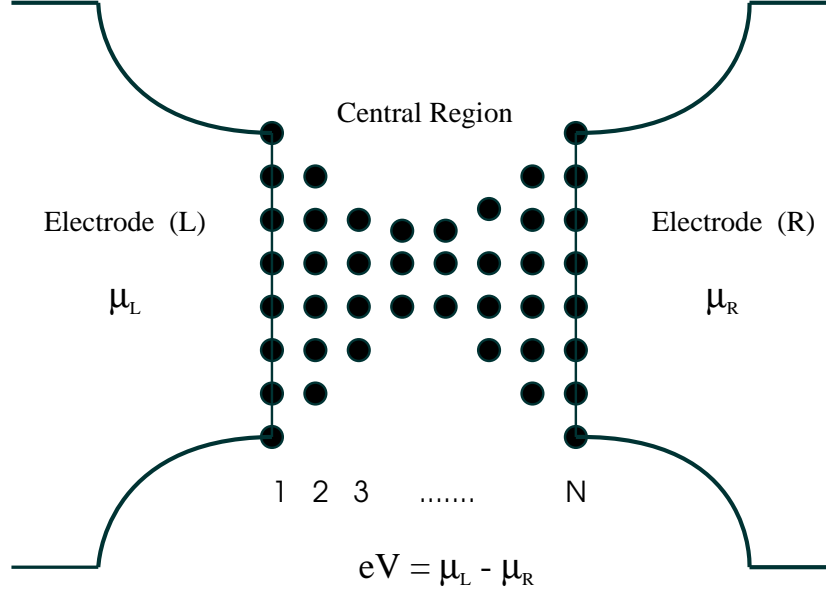
Figure E.1: Schematical representation of an atomic contact. We distinguish three parts: a central region and two leads.

where i, j run over the atomic sites and α, β denote the different atomic orbitals (the number of orbitals in each site is denoted by N_{orb}). We assume that the hopping elements only connect nearest-neighbor atoms.

Our aim is to determine the current through the contact induced by a constant bias voltage, $eV = \mu_L - \mu_R$. Let us start evaluating the current at the interfase between the left lead L and the layer 1, which in the tight-binding representation adopts the form

$$I = \frac{ie}{\hbar} \sum_{i \in L; j \in 1; \alpha, \beta, \sigma} \left\{ t_{i\alpha, j\beta} \langle \hat{c}^\dagger_{i\alpha, \sigma} \hat{c}_{j\beta, \sigma} \rangle \ - \ t_{j\beta, i\alpha} \langle \hat{c}^\dagger_{j\beta, \sigma} \hat{c}_{i\alpha, \sigma} \rangle \right\} , \qquad (E.2)$$

where i runs over the atoms of the left electrode which are connected with the atoms in the layer 1, and j runs over the atoms of the layer 1. The indexes α and β indicate the different atomic orbitals.

As stated in Chapter 6, to calculate the current we make use of nonequilibrium Green functions techniques, the so called Keldysh formalism which is described in detail in Appendix A. We can express the expectation values appearing in the current

expression in terms of the Keldysh Green functions $\hat{G}^{+-}$. These functions give information on the distribution function of the system, and in an atomic basis have the following form

$$G_{i\alpha,j\beta}^{+-;\sigma\sigma'}(\tau,\tau') = i\langle \hat{c}_{j\beta,\sigma'}^{\dagger}(\tau')\hat{c}_{i\alpha,\sigma}(\tau)\rangle. \qquad (\text{E.3})$$

Using this expression one can write the current as

$$I = \frac{e}{\hbar} \sum_{i\in L; j\in 1; \alpha,\beta,\sigma} \left\{ t_{i\alpha,j\beta}G_{j\beta,i\alpha}^{+-;\sigma\sigma}(\tau,\tau) \;-\; t_{j\beta,i\alpha}G_{i\alpha,j\beta}^{+-;\sigma\sigma}(\tau,\tau) \right\}. \qquad (\text{E.4})$$

The current can be expressed in a more compact way by defining the hopping matrix $\hat{t}_{L1}$ y $\hat{t}_{1L}$ whose elements are given by

$$\begin{aligned} (\hat{t}_{L1})_{i\alpha,j\beta} &= t_{i\alpha,j\beta} \;\; \text{con } i \in L; \; j \in 1 \\ (\hat{t}_{1L})_{i\alpha,j\beta} &= t_{i\alpha,j\beta} \;\; \text{con } i \in 1; \; j \in L. \end{aligned} \qquad (\text{E.5})$$

In the same way, similar matrix can be defined for the Green function G^{+-}. Then, one can express the current as

$$I = \frac{2e}{\hbar}\text{Tr}\left\{ \hat{G}_{1L}^{+-}(\tau,\tau)\hat{t}_{L1} \;-\; \hat{t}_{1L}\hat{G}_{L1}^{+-}(\tau,\tau) \right\}, \qquad (\text{E.6})$$

where Tr denotes the trace over orbitals in layer 1. The prefactor 2 comes from the sum over spins, since we are not going to consider any magnetic situation, and we can thus suppressed the superindex σ in the Green functions.

The different Green functions only depend on the difference of temporal arguments, what makes that the problem admit a stationary solution. This fact allow us to Fourier transform with respect to the difference of the temporal argument and expressing the current as

$$I = \frac{2e}{h} \int_{-\infty}^{\infty} dE \; \text{Tr}\left\{ \hat{G}_{1L}^{+-}(E)\hat{t}_{L1} \;-\; \hat{t}_{1L}\hat{G}_{L1}^{+-}(E) \right\}. \qquad (\text{E.7})$$

As we can see, the current is expressed in terms of the trace of a matrix whose dimension is $M_1 \times N_{orb}$, where M_1 is the number of atoms in the layer 1. Then, in principle there are $M_1 \times N_{orb}$ entry channels. The problem has been now reduced to the determination of the functions G^{+-} in terms of the hoppings and energy levels of the Hamiltonian (E.1). We shall calculate these functions considering the coupling term between the electrodes and the central region as a perturbation. Then, starting from the Green functions for the three isolated systems we shall determine the corresponding functions for the whole system. With this choice, the self-energies of the problem are the hopping matrix defined in Eq. (E.5) and the equivalent one for the interfase between the layer N and the right electrode.

We make use of the Dyson equation in Keldysh space to write the functions G^{+-} as follows [2]

$$\begin{aligned}
\hat{G}^{+-}_{L1} &= \hat{g}^{+-}_{LL}\hat{t}_{L1}\hat{G}^{a}_{11} + \hat{g}^{r}_{LL}\hat{t}_{L1}\hat{G}^{+-}_{11} \\
\hat{G}^{+-}_{1L} &= \hat{G}^{+-}_{11}\hat{t}_{1L}\hat{g}^{a}_{LL} + \hat{G}^{r}_{11}\hat{t}_{1L}\hat{g}^{+-}_{LL},
\end{aligned}$$ (E.8)

where $g^{r,a}$ are the (retarded, advanced) Green functions of the corresponding uncoupled subsystems. Introducing this equation in the current expression and making use of the relation $\hat{G}^{+-} - \hat{G}^{-+} = \hat{G}^{a} - \hat{G}^{r}$ we obtain

$$I = \frac{2e}{h}\int_{-\infty}^{\infty}dE\,\mathrm{Tr}\left\{\hat{G}^{-+}_{11}\hat{t}_{1L}\hat{g}^{+-}_{LL}\hat{t}_{L1} - \hat{G}^{+-}_{11}\hat{t}_{1L}\hat{g}^{-+}_{LL}\hat{t}_{L1}\right\}.$$ (E.9)

Then, we determine $\hat{G}^{(+-)(-+)}$ by means of the relation

$$\hat{G}^{(+-)(-+)} = \left(\hat{1} + \hat{G}^{r}\hat{t}\right)\hat{g}^{(+-)(-+)}\left(\hat{1} + \hat{t}\hat{G}^{a}\right)$$ (E.10)

Taking the element (1,1) (referred to the layer 1) we obtain

$$\hat{G}^{(+-)(-+)}_{11} = \hat{G}^{r}_{11}\hat{t}_{1L}\hat{g}^{(+-)(-+)}_{LL}\hat{t}_{L1}\hat{G}^{a}_{11} + \hat{G}^{r}_{1N}\hat{t}_{NR}\hat{g}^{(+-)(-+)}_{RR}\hat{t}_{RN}\hat{G}^{a}_{N1}.$$ (E.11)

Sustitution of this equation in the expression of the current yields

$$\begin{aligned}
I &= \frac{2e}{h}\int_{-\infty}^{\infty}dE\,\mathrm{Tr}\left\{\hat{G}^{r}_{1N}\hat{t}_{NR}\hat{g}^{-+}_{RR}\hat{t}_{RN}\hat{G}^{a}_{N1}\hat{t}_{1L}\hat{g}^{+-}_{LL}\hat{t}_{L1} - \right. \\
&\qquad\qquad \left. \hat{G}^{r}_{1N}\hat{t}_{NR}\hat{g}^{+-}_{RR}\hat{t}_{RN}\hat{G}^{a}_{N1}\hat{t}_{1L}\hat{g}^{-+}_{LL}\hat{t}_{L1}\right\}.
\end{aligned}$$ (E.12)

Let us recall that the unperturbed functions g^{+-} y g^{-+} satisfy the relations:

$$\begin{aligned}
\hat{g}^{+-} &= (\hat{g}^{a} - \hat{g}^{r})\,f = 2i\,\mathrm{Im}\{\hat{g}^{a}\}\,f \\
\hat{g}^{-+} &= (\hat{g}^{a} - \hat{g}^{r})\,(f-1) = 2i\,\mathrm{Im}\{\hat{g}^{a}\}\,(f-1),
\end{aligned}$$ (E.13)

where f is the Fermi function. Thus, the current can be expressed as

$$I = \frac{8e}{h}\int_{-\infty}^{\infty}dE\,\mathrm{Tr}\left\{\hat{G}^{r}_{1N}\hat{t}_{NR}\mathrm{Im}\{\hat{g}^{a}_{RR}\}\hat{t}_{RN}\hat{G}^{a}_{N1}\hat{t}_{1L}\mathrm{Im}\{\hat{g}^{a}_{LL}\}\hat{t}_{L1}\right\}[f_{L} - f_{R}].$$ (E.14)

One can further simplify the current expression noticing that the following self-energies appear in the previous expression:

---

[2]We do not write the argument E explicitly. Moreover, since there are no inelastic processes involved in this model, the self-energies Σ^{+-} associated with them vanish.

$$\hat{\Sigma}_L = \hat{t}_{1L}\hat{g}^a_{LL}\hat{t}_{L1}$$
$$\hat{\Sigma}_R = \hat{t}_{NR}\hat{g}^a_{RR}\hat{t}_{RN}, \tag{E.15}$$

These self-energies describe the coupling between the reservoirs and the central region. The current is expressed in terms of these self-energies as

$$I = \frac{2e}{h} \int_{-\infty}^{\infty} dE\, T(E,V)\,[f_L - f_R], \tag{E.16}$$

where $T(E,V)$ is an energy and voltage dependent total transmission probability given by

$$T(E,V) \equiv 4\mathrm{Tr}\left[\hat{G}^r_{1N}\mathrm{Im}\left\{\hat{\Sigma}_R\right\}\hat{G}^a_{N1}\mathrm{Im}\left\{\hat{\Sigma}_L\right\}\right]. \tag{E.17}$$

One can further symmetrize this expression by using the cyclic property of the trace and write $T(E,V) = \hat{t}(E,V)\hat{t}^\dagger(E,V)$, where

$$\hat{t}(E,V) \equiv 2\mathrm{Im}\left\{\hat{\Sigma}_L\right\}^{1/2}\hat{G}^r_{1N}\mathrm{Im}\left\{\hat{\Sigma}_R\right\}^{1/2} \tag{E.18}$$

is the transmission matrix of the system. The existence of $(\mathrm{Im}\hat{\Sigma})^{1/2}$ as a real matrix is warranted by $\mathrm{Im}\hat{\Sigma}$ being positive definite.

Finally, the current adopts the form

$$I = \frac{2e}{h} \int_{-\infty}^{\infty} dE\, \mathrm{Tr}\left\{\hat{t}(E,V)\hat{t}^\dagger(E,V)\right\}[f_L - f_R], \tag{E.19}$$

valid for arbitrary bias voltage. In the linear regime this expression is simplified giving a zero-temperature conductance given by the Landauer formula

$$G = \frac{2e^2}{h}\mathrm{Tr}\left\{\hat{t}(E_F,0)\hat{t}^\dagger(E_F,0)\right\} = \frac{2e^2}{h}\sum_{i=1}^{M_1 \times N_{orb}} T_i, \tag{E.20}$$

where T_i are the eigenvalues of $\hat{t}\hat{t}^\dagger$ at the Fermi level. As one can see, in principle the number of channel would be $M_1 \times N_{orb}$, which is the dimension of the matrix $\hat{t}\hat{t}^\dagger$ evaluated in layer 1. But as we stated at the beginning of this appendix, the separation in three subsystems in somewhat arbitrary and one can evaluate the current in any point. Thus, it is evident that the actual number of channels is controlled by the narrowest part of the constriction. So, in the case of an one-atom contact analyzed in chapters 6 and 7, the number of channels is the number of orbitals of the central atom, and the transmission evaluated in the central atom can be expressed as

$$\hat{t}(E) \equiv 2\mathrm{Im}\left\{\hat{\Sigma}_L\right\}^{1/2}\hat{G}^r_{cc}\mathrm{Im}\left\{\hat{\Sigma}_R\right\}^{1/2}, \tag{E.21}$$

where $\hat{G}_{cc}$ is the Green function of the central atom and now the self-energies describe the coupling between the central atom and the rest of the system. Then, the transmission evaluated at the central atom is a matrix whose dimension is $(N_{orb} \times N_{orb})$, i.e. the actual number of channels is N_{orb}. Using the analytical properties of the Green functions, it can be shown that the whole spectrum of the transmission matrix is conserved from layer to layer, giving rise to the same channels in any case. Thus, it is convenient from the computational point of view to evaluate the transmission at the central atom, where its dimension is minimum.

To end this section we shall briefly comment some details about the calculation of the Green functions of the system. As we have seen, the calculation of the transmission is reduced to determine the different retarded and advanced Green functions of the system in equilibrium [3]. These functions are formally defined as $\hat{G}^{r,a} = \left[E\hat{1} \pm i0^+ - \hat{H} \right]^{-1}$. In particular, for the one-atom contact it is easy to show, following the perturbative scheme indicated above, that the central atom Green function is given by $\hat{G}^a_{cc} = \hat{G}^{r\dagger}_{cc} = \left[E\hat{1} - i0^+ - \hat{H}_0 - \hat{\Sigma}_L - \hat{\Sigma}_R \right]^{-1}$, where $\hat{H}_0$ is the Hamiltonian of the central atom, i.e. it is a diagonal matrix which contains the atomic levels. On the other hand, the self-energies correspond to the ones of Eq. (E.15), which describe the left and right electrodes starting from the central atom.

The self-energies are determined in terms of the Green functions of the uncoupled electrodes. As commented in chapter 6, the system that we study consist of a central neck of arbitrary length finally connected to two perfect semiinfinite crystals, which represent the electrodes. The Green functions of a infinite surface can be determined with arbitrary precision by means of standard recursive methods, like the ones described in Ref. [254]. The idea behind these methods is to determine the Green functions of a plane, transforming to a Bloch basis which diagonalizes the problem, and then connecting the different planes with interplane hoppings. This converts the problem in a one dimensional problem, like the one of a tight-binding linear chain, easily solvable by means of recursion.

E.2   Fourth channel in sp-like metal contacts

This subsection is devoted to the analysis of why the fourth channel in sp like metals one-atom contacts is closed for all energies. Fig. E.2 shows the transmission of such channel as a function of energy for the Al one-atom contact of Fig. 6.6(a).

First of all, due to the splitting between the p_z and $p_x - p_y$ central atom levels, provoked by the contact geometry, the problem is separated in two subspaces: the $s - p_z$ subspace and the $p_x - p_y$ subspace. This converts the problem of the analysis

---

[3]The readers who want to learn more about the techniques used for determining the Green function of a tight-binding system are encouraged to consult Ref. [122].
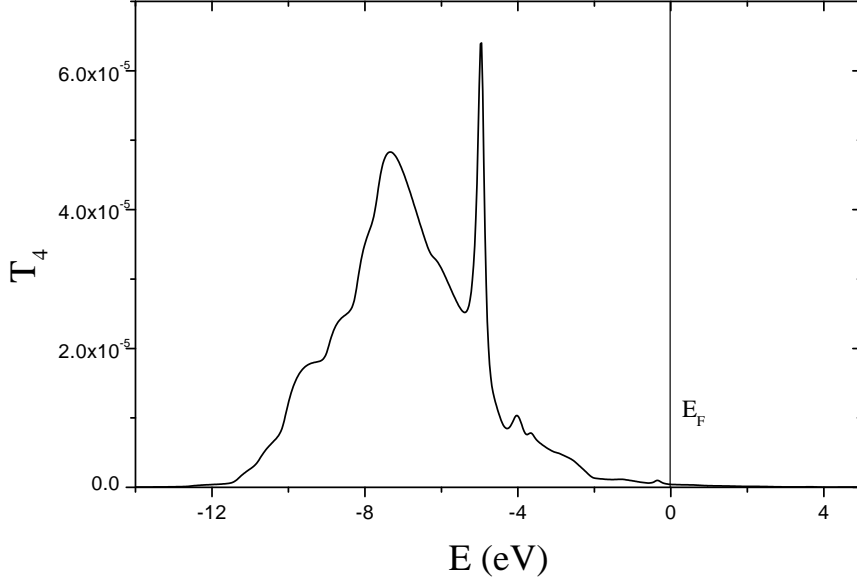
Figure E.2: Transmission of the fourth channel as a function of energy for an Al one-atom contact ($N = 1$).

of the transmission in two (2×2) problems. As we are interested in what happens to the fourth channel, which is a combination of the s and p_z central atom orbitals, we shall concentrate in the first subspace.

In the subspace $s - p_z$ the transmission evaluated at the central atom is a (2×2) matrix given by Eq. (E.21), where

$$\text{Im}\left\{\hat{\Sigma}_L\right\} \equiv \hat{\Gamma}_L = \begin{pmatrix} \Gamma_{ss}^L & \Gamma_{sp_z}^L \\ \Gamma_{p_zs}^L & \Gamma_{p_zp_z}^L \end{pmatrix} \quad (\text{E.22})$$

is the matrix scattering rate which describes the coupling between the central atom and the left electrode in the sp_z subspace. On the other hand, $\text{Im}\left\{\hat{\Sigma}_R\right\} \equiv \hat{\Gamma}_R$ is given by a similar expression. In order to have a vanishing eigenvalue of the matrix $\hat{t}\hat{t}^\dagger$ it is sufficient that one of the scattering rate matrix has a vanishing determinant. This determinant is zero if the following condition holds: [4]

$$\Gamma_{ss}\Gamma_{p_zp_z} = \Gamma_{sp_z}\Gamma_{p_zs}, \quad (\text{E.23})$$

---

[4]Let us recall that $\hat{\Gamma}$ is a positive definite matrix, what makes that $\Gamma_{ss}\Gamma_{p_zp_z} \geq \Gamma_{sp_z}\Gamma_{p_zs}$.

where we have suppressed the indexes L and R because no matter what electrode we are referring. Let us recall that these rates are given by the expression $\hat{\Gamma}_L = \hat{t}_{cL}\text{Im}\left\{\hat{g}^a_{LL}\right\}\hat{t}_{Lc}$, where $\hat{t}_{cL}$ is the hopping matrix which connects the central atom and the left hand side electrode, like the one in Eq. (E.5). It is easy to convince oneself that in order to verify the condition (E.23) it is sufficient that the hopping connecting the central atom and its neighbors satisfy the relation

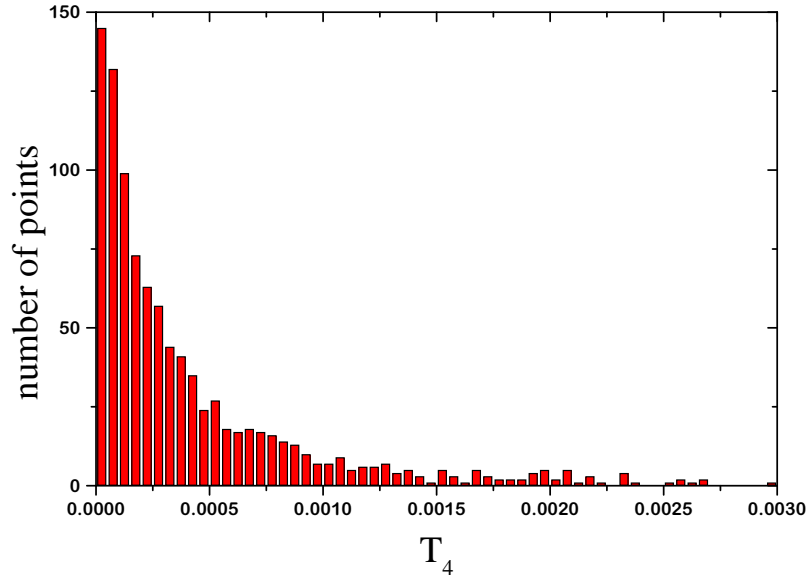$$t_{ss}t_{p_z p_z} = t_{sp_z}t_{p_z s}. \tag{E.24}$$

Figure E.3: Histogram of the fourth channel for the Al one-atom contact of Fig. 6.9.

It is worth noticing that the hoppings we are considering are projections of the matrix elements $V_{ss\sigma}$, $V_{pp\sigma}$ and $V_{sp\sigma}$. For any metal the relation $V_{ss\sigma}V_{pp\sigma} \sim V_{sp\sigma}$ is approximately verified, so that the condition (E.24) holds approximately for the considered geometries and so does the condition (E.23).

It is important to remark that in order to have a vanishing eigenvalue of $\hat{t}\hat{t}^\dagger$ it is only necessary that the condition (E.23) be verified approximately. Great deviations of this condition are necessary for having a non-negligible transmission for this channel, what explains why it is closed even in presence of disorder due to the symmetry of the orbitals (s y p_z) involved. This is illustrated in Fig. E.3 where the histogram of the fourth of the Al one-atom contact corresponding to Fig. 6.9 is shown. As it

can be seen large random deviations of the hoppings are not enough for opening this channel at the Fermi level.

Bibliography

[1] H.K. Onnes, Leiden Comm. **1206**, 1226 (1911), Suppl. **34** (1913).

[2] J. Bardeen, L.N. Cooper, and J.R. Schrieffer, Phys. Rev. **108**, 1175 (1957).

[3] J.H. Hinken, *Superconductor Electronics*, Springer-Verlag Berlin (1989).

[4] *Superconducting Devices*, edited by S.T. Ruggiero and D.A. Rudman, Academic Press, Inc. (1990).

[5] Y. Imry, in *Directions in Condensed Matter Physics*, Vol. 1 (G. Grinstein and G. Mazenko, eds.), World Scientific, Singapore, (1986).

[6] *Mesoscopic Quantum Physics*, E. Akkermans, G. Montamboux, J.-L. Pichard, and Zinn-Justin, eds. (North-Holland, Amsterdam, 1995).

[7] S. Datta, *Electronic Transport in Mesoscopic Systems* (Cambridge University Press, Cambridge, 1995).

[8] *Mesoscopic Electron Transport*, ed. by L.L. Sohn, L.P. Kouwenhoven, and G. Schön, NATO ASI Series E, Vol.345 (Kluwer Academic Publishing, Dordrecht, 1997).

[9] Y. Imry, *Introduction to Mesoscopic Physics*, Oxford University Press, New York (1998).

[10] I. Giaever, Phys. Rev. Lett. **5**, 147 (1960).

[11] J. Bardeen, Phys. Rev. Lett. **6**, 57 (1961).

[12] M.H. Cohen, L.M. Falicov, and J.C. Phillips, Phys. Rev. Lett. **8**, 316 (1962).

[13] J. Nicol, S. Shapiro and P.H. Smith, Phys. Rev. Lett. **5**, 461 (1960).

[14] I. Giaever, Phys. Rev. Lett. **5**, 464 (1960).

[15] D.H. Douglass, Jr., Phys. Rev. Lett. **7**, 14 (1961).

[16] A.H. Dayem and R.J. Martin, Rev. Lett. **8**, 246 (1962).

[17] I. Giaever, H.R. Hart, Jr., and K. Magerle, Phys. Rev. **126**, 941 (1962).

[18] B.D. Josephson, Phys. Lett. **1**, 251 (1962).

[19] V. Ambegaokar and A. Baratoff, Phys. Rev. Lett. **10**, 486 (1963), errata: Phys. Rev. Lett. **11**, 104 (1963).

[20] E. Riedel, Z. Naturforsch **19A**, 1634 (1964).

[21] A. Barone and G. Paterno, *Physics and Applications of the Josephson Effect* (Wiley, New York, 1982).

[22] E.L. Wolf, *Principles of Electron Tunneling Spectroscopy* (Oxford University Press, New York, 1985).

[23] P.W. Anderson and J.M. Rowell, Phys. Rev. Lett. **10**, 230 (1963).

[24] B.D. Josephson, Rev. Mod. Phys. **36**, 216 (1964). B.D. Josephson, Adv. Phys. **14**, 419 (1965).

[25] J.M. Rowell, Phys. Rev. Lett. **11**, 200 (1963).

[26] M.D. Fiske, Rev. Mod. Phys. **36**, 221 (1964).

[27] S. Shapiro, Phys. Rev. Lett. **11**, 80 (1963). S. Shapiro, A.R. Janus and S. Hally, Rev. Mod. Phys. **36**, 223 (1964).

[28] I. Giaever, Phys. Rev. Lett. **14**, 904 (1965).

[29] I.K. Yanson, V.M. Svistunov and I.M. Dimitrenko, Zh. Eksp. Teor. Fiz. **48**, 976 (1965) [Soviet Phys. JETP **21**, 650 (1965)].

[30] B.N. Taylor and E. Burstein, Phys. Rev. Lett. **10**, 14 (1963).

[31] C.J. Adkins, Phil. Mag. **8**, 1051 (1963); Rev. Mod. Phys. **36**, 211 (1964).

[32] I.K. Yanson, V.M. Svistunov, and I.M. Dmitrenko, Sov. Phys. JETP **20**, 1404 (1965).

[33] S.M. Marcus, Phys. Letters **19**, 623 (1966); **20**, 236 (1966).

[34] J.R. Schrieffer and J.W. Wilkins, Phys. Rev. Lett. **10**, 17 (1963).

[35] J.M. Rowell and W.L. Feldmann, Phys. Rev. **172**, 393 (1968).

[36] N.R. Werthamer, Phys. Rev. **147**, 255 (1966).

[37] M. Tinkham, *Introduction to Superconductivity*, McGraw-Hill, New York (1996).

[38] N.F. Pedersen, T.F. Finnegan, and D.N. Langenberg, Phys. Rev. B **6**, 4151 (1972).

[39] C.M. Falco, W.H. Parker, and S.E. Trullinger, Phys. Rev. Lett. **31** 933 (1973).

[40] D.A. Vincent and B.S Deaver, Jr., Phys. Rev. Lett. **32**, 212 (1974).

[41] M. Nisenoff and S. Wolf, Phys. Rev. B **12**, 1712 (1975).

[42] R. Rifkin and B.S Deaver, Jr., Phys. Rev. B **13**, 3894 (1976).

[43] N.F. Pedersen, O.H. Soerensen, and J. Mygind, Phys. Rev. B **18**, 3221 (1978).

[44] B.S Deaver, Jr., B.G. Boone and R. Rifkin, Phys. Letters **57A**, 186 (1976).

[45] A.B. Zorin, I.K. Kulik, K.K. Likharev and J.R. Schrieffer, Fiz. Nizk. Temp. **5**, 1138 (1979) [Engl. Transl., Sov. J. Low Temp. Phys. **5**, 537 (1979)].

[46] I.O. Kulik and I.K. Yanson, *Josephson Effect in Superconducting Tunnel Structures* (Nauka, Moscow) [Keter Press, Jerusalem (1972)].

[47] L. Solymar, *Superconducting Tunneling and Aplications* (Chapman and Hall, London, 1972).

[48] R.D. Parks, *Superconductivity*, Marcel Dekker, INC. (New York, 1969).

[49] J. Clarke, Am. J. Phys., **38**, 1071 (1970).

[50] J.R. Waldram, Rep. Prog. Phys. **39**, 751 (1976).

[51] P.W. Anderson and A.H. Dayem, Phys. Rev. Lett. **13**, 195 (1964).

[52] P.G. de Gennes, Rev. Mod. Phys. **36**, 225 (1964).

[53] J.E. Zimmerman and A.H. Silver, Phys. Rev. **141**, 367 (1966).

[54] I.O. Kulik and A.N. Omelyanchuk, Fiz. Nizk. Temp. **3**, 945 (1977). [Engl. Transl., Sov. J. Low. Temp. Phys. **3**, 459 (1977)]

[55] K.K. Likharev, Rev. Mod. Phys. **51**, 101 (1979).

[56] P.E. Gregers-Hansen, E. Hendricks, M.T. Levinsen and G.R. Pickett, Phys. Rev. Lett. **31**, 524 (1973).

[57] O. Hoffmann Soerensen, B. Kofoed, N.F. Pedersen and S. Shapiro, Rev. de Phys. Appl. **9**, 153 (1974).

[58] M. Octavio, W.J. Skocpol and M. Tinkham, IEEE Trans. MAG-13, 739 (1977).

[59] K. Flensberg and J.B. Hansen, Phys. Rev. B **40**, 8693 (1989).

[60] M. Octavio, W.J. Skocpol and M. Tinkham, Phys. Rev. B **17**, 159 (1978).

[61] Yu. Ya. Divin and F. Ya. Nad', Sov. J. Low Temp. Phys. **4**, 520 (1978); JETP Lett. **29**, 517 (1979).

[62] T.M. Klapwijk, G.E. Blonder and M. Tinkham, Physica B **109&110**, 1657 (1982).

[63] G.E. Blonder, M. Tinkham, and T.M. Klapwijk, Phys. Rev. B **25**, 4515 (1982).

[64] M. Octavio, G.E. Blonder, M. Tinkham, and T.M. Klapwijk, Phys. Rev. B **27**, 6739 (1983).

[65] A.F. Andreev, Sov. Phys. JETP **19**, 1228 (1964).

[66] P.G. de Gennes, *Superconductivity of Metals and Alloys*, (W.A. Benjamin, New York, 1966).

[67] G.E. Blonder and M. Tinkham, Phys. Rev. B **27**, 112 (1983).

[68] K. Flensberg, J.B. Hansen and M. Octavio, Phys. Rev. B **38**, 8707 (1988).

[69] G.B. Arnold, Phys. Rev. B **17**, 3576 (1978).

[70] G.B. Arnold, J. Low Temp. Phys. **59**, 143 (1985).

[71] G.B. Arnold, J. Low Temp. Phys. **68**, 1 (1987).

[72] C.W.J. Beenakker and H. van Houten, *Quantum Transport in Semiconductor Nanostructures* in Solid State Physics Vol. 44, 1 (1991).

[73] G. Binnig, H. Rohrer, Ch. Gerber and E. Weibel, Appl. Phys. Lett. **40**, 178 (1982); *ibid.*, Phys. Rev. Lett. **49**, 57 (1982); *ibid.*, Physica B **109-110**, 2075 (1982).

[74] C.J. Muller, J.M. van Ruitenbeek and L.J. de Jongh, Physica C **191**, 485 (1992).

[75] C.W.J. Beenakker, in *Proceedings of the 14th Taniguchi International Symposium on Transport Phenomena in Mesoscopic Systems* edited by Fukuyama and T. Ando (Springer, Berlin, 1992).

[76] T.M. Klapwijk, Physica B **197**, 481 (1994).

[77] C.W.J. Beenakker, in *Mesoscopic Quantum Physics*, E. Akkermans, G. Montamboux, J.-L. Pichard, and Zinn-Justin, eds. (North-Holland, Amsterdam, 1995).

[78] *Mesoscopic Superconductivity*, Proc. of the NATO-ARW, F.W.J. Hekking, G. Schön, D.V. Averin, eds. (North-Holland, Amsterdam, 1995).

[79] C. Lambert and R. Raimondi, J. Phys.: Condens. Matter **10**, 901 (1998).

[80] M.C. Koops, *Thesis*, University of Leiden (The Netherlands) in 1996.

[81] J. Moreland and J.W. Ekin, J. Appl. Phys. **58**, 3888 (1985); J. Moreland and P.K. Hansma, Rev. Sci. Instrum. **55**, 399 (1984).

[82] J.M. Krans, C.J. Muller, I.K. Yanson, Th.M. Govaert, R. Hesper, and J.M. van Ruitenbeek, Phys. Rev. B **48**, 14271 (1993).

[83] C.J. Muller, J.M. van Ruitenbeek, and L.J. de Jongh, Phys. Rev. Lett. **69**, 140 (1992).

[84] C.J. Muller, J.M. van Ruitenbeek, C.W.J. Beenakker and R. de Bruyn Ouboter, Physica B **189**, 225 (1993).

[85] N. van der Post, E.T. Peters, I.K. Yanson, and J.M. van Ruitenbeek, Phys. Rev. Lett. **73**, 2611 (1994).

[86] B.J. Vleeming, C.J. Muller, M.C. Koops, and R. de Bruyn Ouboter, Phys. Rev. B **50**, 16741 (1994).

[87] J.G. Rodrigo, N. Agraït and S. Vieira, Phys. Rev. B **50**, 374 (1994).

[88] J.G. Rodrigo, N. Agraït, C. Sirvent and S. Vieira, Phys. Rev. B **50**, 12788 (1994).

[89] B.J. van Wees, H. van Houten, C.W.J. Beenakker, J.G. Williamson, L.P. Kouwenhoven, D. van der Marel, and C.T. Foxon, Phys. Rev. Lett. **60**, 848 (1988).

[90] D.A. Wharam, T.J. Thornton, R. Newbury, M. Pepper, H. Ahmed, J.E.F. Frost, D.G. Hasko, D.C. Peacock, D.A. Ritchie, and G.A.C. Jones, J. Phys. C **21**, L209 (1988).

[91] H. Takayanagi, T. Akazaki and J. Nitta, Phys. Rev. Lett. **75**, 3533 (1995).

[92] C.L. Foden, N. Rando, A. van Dordrecht, A. Peacock, J. lumley and C. Pereira, Phys. Rev. B **47**, 3316 (1993).

[93] R. Cristiano, L. Frunzio, R. Monaco, C. Nappi, and S. Pagano, Phys. Rev. B **49**, 429 (1994).

[94] A.W. Kleinsasser, R. E. Miller, W.H. Mallison and G.B. Arnold, Phys. Rev. Lett. **72**, 1738 (1994).

[95] R. Landauer, IBM J. Res. Develop. **1**, 223 (1957); Philos. Mag. **21**, 863 (1970).

[96] A. Furusaki, H. Takayanagi and M. Tsukada, Phys. Rev. Lett. **67**, 132 (1991).

[97] C.W.J. Beenakker, Phys. Rev. Lett. **67**, 3836 (1991).

[98] C.J. Lambert, J. Phys. Condens. Matter **3**, 6579 (1991).

[99] C.W.J. Beenakker, Phys. Rev. B **46**, 12841 (1992).

[100] K.D. Usadel, Phys. Rev. Lett. **25**, 507 (1970).

[101] A. Schmid, in *Nonequilibrium Superconductivity, Phonons and Kapitza Boundaries*, edited by K.E. Gray (Plenum Press, New York, 1981).

[102] J. Rammer and H. Smith, Rev. Mod. Phys. **58**, 323 (1986).

[103] A.I. Larkin and Yu.N. Ovchinikov, in *Nonequilibrium Superconductivity*, edited by D.N. Langenberg and A.I. Larkin (North-Holland, Amsterdam, 1986).

[104] S. Guéron, *Thesis*, CEA Saclay (France) in 1997.

[105] Yu. V. Nazarov, Phys. Rev. Lett. **73**, 1420 (1994).

[106] W.M. van Huffelen, T.M. Klapwijk, D.R. Heslinga, M.J. de Boer, and N. van der Post, Phys. Rev. B **47**, 5170 (1993).

[107] M. Büttiker, Phys. Rev. Lett. **57**, 1761 (1986).

[108] A. Martín-Rodero, F. J. García-Vidal and A. Levy Yeyati, Phys. Rev. Lett. **72**, 554 (1994).

[109] A. Levy Yeyati, A. Martín-Rodero, F. J. García-Vidal, Phys. Rev. B **51**, 3743 (1995).

[110] A. Levy Yeyati, A. Martín-Rodero and F. Flores, Phys. Rev. Lett. **71**, 2991 (1993).

[111] A. Martín-Rodero, A. Levy Yeyati, and J.C. Cuevas, Physica B **218**, 126 (1996); A. Levy Yeyati, A. Martín-Rodero, and J.C. Cuevas, J. Phys.: Condens. Matter **8**, 449 (1996).

[112] J.C. Cuevas, A. Martín-Rodero and A. Levy Yeyati, Phys. Rev. B **54**, 7366 (1996).

[113] L.P. Gorkov, Sov. Phys. JETP **7**, 505 (1958).

[114] J.R. Schrieffer, *Theory of Superconductivity*, W.A. Benjamin, Inc., New York, (1964).

[115] N.N. Bogoliubov, Sov. Phys. JETP **7**, 41 (1958).

[116] J. Ferrer, A. Martín-Rodero and F. Flores, Phys. Rev. B **39**, 11320 (1989).

[117] M.Yu. Kupriyanov and V.F. Lukichev, Fiz. Nizk. Temp. **8**, 1045 (1982) [Sov. J. Low Temp. Phys. **8**, 526 (1982)]; A.A. Zubkov and M.Yu. Kupriyanov, Fiz. Nizk. Temp. **9**, 548 (1983) [Sov. J. Low Temp. Phys. **9**, 279 (1983)].

[118] D. Rogovin and D.J. Scalapino, Annals of Physics **86**, 1 (1974).

[119] L.V. Keldysh, Sov. Phys. JETP **20**, 1018 (1965).

[120] Y. Nambu, Phys. Rev. **117**, 648 (1960).

[121] S.B. Kaplan et al., Phys. Rev. B **14**, 4854 (1976).

[122] E.N. Economou, *Green's Functions in Quantum Physics*, Springer-Verlag, (1990).

[123] J. Ferrer, A. Martín-Rodero, and F. Flores, Phys. Rev. B **38**, 10113 (1988).

[124] Y.A. Genenko and Y.A. Ivanchenko, Theor. Math. Phys. **69**, 1056 (1986).

[125] J. Sánchez-Cañizares and F. Sols, Phys. Rev. B **55**, 531 (1997).

[126] L.E. Hasselberg, J. Phys. F **3**, 1438 (1973); L.E. Hasselberg, M.T. Levinsen, and M.R. Samuelsen, Phys. Rev. B **9**, 3757 (1974).

[127] A.V. Zaitsev, Zh. Eksp. Teor. Fiz. **78**, 221 (1980) [Sov. Phys. JETP **51**, 111 (1980).

[128] A. Levy Yeyati and F. Flores, Phys. Rev. B **44**, 9020 (1991); J. Phys: Condensed Matter **4**, 7341 (1992).

[129] E.N. Bratus, V.S. Shumeiko, and G. Wendin, Phys. Rev. Lett. **74**, 2110 (1995).

[130] D. Averin and A. Bardas, Phys. Rev. Lett. **75**, 1831 (1995).

[131] U. Gunsenheimer and A.D. Zaikin, Phys. Rev. B **50**, 6317 (1994).

[132] M. Hurd, S. Datta and P.F. Bagwell, Phys. Rev. B **54**, 6557 (1996).

[133] E.N. Bratus, V.S. Shumeiko, E.V. Bezuglyi and G. Wendin, Phys. Rev. B **55**, 12666 (1997).

[134] A. Furusaki and M. Tsukada, Physica B **165+166**, 967 (1990).

[135] W. Haberkorn, H. Knauer, and J. Richter, Phys. Status Solidi **47**, K161 (1978).

[136] A.V. Zaitsev, Sov. Phys. JETP **59**, 1015 (1984).

[137] J. Ferrer, *Thesis*, Universidad Autónoma de Madrid (1991).

[138] M.C. Koops, G.V. van Duyneveldt, and R. de Bruyn Ouboter, Phys. Rev. Lett. **77**, 2542 (1996).

[139] H.B. Callen and T.W. Welton, Phys. Rev. **83**, 34 (1951).

[140] A. Martín-Rodero, A. Levy Yeyati and F.J. García-Vidal, Phys. Rev. B (RC), **53**, 8891 (1996).

[141] D. Vion, M. Götz, P. Joyez, D. Esteve, and M.H. Devoret, Phys. Rev. Lett. **77**, 3435 (1996).

[142] M. Büttiker, in: *Superconducting Quantum Interference Devices and their Application* (Walter de Gruyter, Berlin, 1985).

[143] E. Scheer, P. Joyez, D. Esteve, C. Urbina and M.H. Devoret, Phys. Rev. Lett. **78**, 3535 (1997).

[144] A. Bardas and D.V. Averin, Phys. Rev. B **56**, R8518 (1997).

[145] E. Scheer, P. Joyez, D. Esteve, C. Urbina and M.H. Devoret, Superlattices and Microstructures **24** (1998).

[146] E. Scheer, N. Agraït, J.C. Cuevas, A. Levy Yeyati, B. Ludoph, A. Martín-Rodero, G. Rubio, J.M. van Ruitenbeek and C. Urbina, Nature **394**, 154 (1998).

[147] J.C. Cuevas, A. Levy Yeyati and A. Martín-Rodero, Phys. Rev. Lett. **80**, 1066 (1998).

[148] J.C. Cuevas, A. Levy Yeyati, A. Martín-Rodero, G. Rubio, C. Untiedt and N. Agraït, Phys. Rev. Lett. **81**, 2990 (1998).

[149] For a recent review, see M.J.M. de Jong and C.W.J. Beenakker, in: *Mesoscopic Electron Transport*, ed. by L.L. Sohn, L.P. Kouwenhoven, and G. Schön, NATO ASI Series E, Vol.345 (Kluwer Academic Publishing, Dordrecht, 1997).

[150] W. Schottky, Ann. Phys. (Leipzig) **57**, 541 (1918).

[151] L. Saminadayar, D.C. Glattli, Y. Lin and B. Etienne, Phys. Rev. Lett. **79**, 2526 (1997).

[152] R. de-Picciotto, M. Reznikov, M. Heiblum, V. Umansky, G. Bunin and D. Mahalu, Nature **389**, 162 (1997).

[153] V.A. Khlus, Sov. Phys. JETP **66**, 1243 (1987).

[154] M.J.M. de Jong and C.W.J. Beenakker, Phys. Rev. B **49**, 16070 (1994).

[155] B.A. Muzykantskii and D.E. Khmelnitskii, Phys. Rev. B **50**, 3982 (1994).

[156] M.P. Anantram and S. Datta, Phys. Rev. B **53**, 16390 (1996).

[157] T. Martin, Physics Letters A **220**, 137 (1996).

[158] P. Dieleman, H.G. Bukkems, T.M. Klapwijk, M. Schicke and K.H. Gundlach, Phys. Rev. Lett. **79**, 3486 (1997).

[159] J.P. Hessling, V.S. Shumeiko, Yu. M. Galperin and G. Wendin, Europhys. Lett. **34**, 49 (1996).

[160] D.V. Averin and H.T. Imam, Phys. Rev. Lett. **76**, 3814, (1996).

[161] G.B. Lesovik JETP Lett. **49**, 592 (1989).

[162] B. Yurke and G.P. Kochanski, Phys. Rev. B **41**, 8184 (1990).

[163] M. Büttiker, Phys. Rev. Lett. **65**, 2901 (1990).

[164] Th. Martin and R, Landauer, Phys. Rev. B **45**, 1742 (1992).

[165] M. Büttiker, Phys. Rev. B **46**, 12485 (1992).

[166] L.S. Levitov and G.B. Lesovik, JETP Lett. **58**, 230 (1993).

[167] M.A. Kastner, Rev. Mod. Phys. **64**, 849 (1992); M. A. Kastner, Phys. Today **46**, No. 1, 24 (1993).

[168] D.C. Ralph, C.T. Black, and M. Tinkham, Phys. Rev. Lett. **74**, 3241 (1995).

[169] C.T. Black, D.C. Ralph, and M. Tinkham, Phys. Rev. Lett. **76**, 688 (1996).

[170] A. Levy Yeyati, J.C. Cuevas, A. López-Dávalos, and A. Martín-Rodero, Phys. Rev. B **55**, R6317 (1997).

[171] M.T. Tuominen, J.M. Hergenrother, T.S. Tighe, and M. Tinkham, Phys. Rev. Lett. **69**, 1997 (1992).

[172] P. Lafarge, P. Joyez, D. Esteve, C. Urbina, and M.H. Devoret, Phys. Rev. Lett. **70**, 994 (1993).

[173] T.M. Eiles, J.M. Martinis, and M.H. Devoret, Phys. Rev. Lett. **70**, 1862 (1993).

[174] M.T. Tuominen, J.M. Hergenrother, T.S. Tighe, and M. Tinkham, Phys. Rev. B **47**, 11599 (1993).

[175] D.V. Averin and Yu. V. Nazarov, Phys. Rev. Lett. **69**, 1993 (1992).

[176] F.W.J. Hekking, L.I. Glazman, K.A. Matveev, and R.I. Shekhter, Phys. Rev. Lett. **70**, 4138 (1993).

[177] K.A. Matveev, M. Gisselfält, L.I. Glazman, M. Jonson, and R.I. Shekhter, Phys. Rev. Lett. **70**, 2940 (1993).

[178] F.W.J. Hekking and Yu. V. Nazarov, Phys. Rev. Lett. **71**, 1625 (1993).

[179] J.M. Hergenrother, M.T. Tuominen, and M. Tinkham, Phys. Rev. Lett. **72**, 1742 (1994).

[180] L.I. Glazman and K.A. Matveev, JETP Lett. **49**, 659 (1989).

[181] V.A. Khlus, A.V. Dyomin and A.L. Zazunov, Physcia C **214**, 413 (1993).

[182] C.W.J. Beenakker and H. van Houten, *Single Electron Tunneling and Mesoscopic Devices*, (Springer, Berlin, 1992).

[183] P.W. Anderson, Phys. Rev. **124**, 41 (1961).

[184] S. Hershfield *et al.* Phys. Rev. Lett. **67**, 3720 (1991).

[185] Y. Meir *et al.* Phys. Rev. Lett. **70**, 2601 (1993).

[186] C.A. Stafford and S. Das Sarma, Phys. Rev. Lett. **72**, 3590 (1994).

[187] D.V. Averin and A.N. Korotkov, J. Low Temp. Phys. **80**, 173 (1990).

[188] D.V. Averin, A.N. Korotkov, and K.K. Likharev Phys. Rev. B **44**, 6199 (1991).

[189] C.W.J. Beenakker, Phys. Rev. B **44** , 1646 (1991).

[190] C.B. Whan and T.P. Orlando, Phys. Rev. B **54**, R5255 (1996).

[191] G. Johansson, V.S. Shumeiko, G. Wendin and K.N. Bratus, Physica C **293**, 77 (1997).

[192] G. Johansson, *Thesis*, Chalmers, Göteborg University (Sweden) in 1998.

[193] G. Johansson, V.S. Shumeiko, K.N. Bratus and G. Wendin, cond-mat 9807240.

[194] H. van Houten et al., in *Single Charge Tunneling*, edited by H. Grabert and M.H. Devoret (Plenum, New York, 1992).

[195] A.V. Zaitsev and D.V. Averin, Phys. Rev. Lett. **80**, 3602 (1998).

[196] J. Tersoff and D.R. Hamann, Phys. Rev. Lett. **50**, 1998 (1983).

[197] N.D. Lang, Phys. Rev. Lett. **56**, 1164 (1986).

[198] N.D. Lang, Phys. Rev. Lett. **58**, 45 (1987).

[199] J.K. Gimzewski and R. Möller, Phys. Rev. B **36**, 1284 (1987).

[200] N.D. Lang, Phys. Rev. B **36**, 8173 (1987).

[201] J.S. Foster, J.E. Frommer and P.C. Arnett, Nature **331**, 324 (1988).

[202] R.S. Becker, J.A. Golovchenko and B.S. Swartzentruber, Nature **325**, 419 (1987).

[203] D.M. Eigler and E.K. Schweizer, Nature **344**, 524 (1990).

[204] J.A. Stroscio and D.M. Eigler, Science **254**, 1319 (1991).

[205] I.W. Lyo and P. Avouris, Science **245**, 1369 (1989).

[206] P. Bedrossion, D.M. Chen, K. Mortensen and J.A. Golovchenko, Nature **342**, 258 (1989).

[207] D.M. Eigler, C.P. Lutz and W.E. Rudge, Nature **352**, 600 (1991).

[208] M.F. Crommie, C.P. Lutz and D.M. Eigler, Science **262**, 218 (1993).

[209] G. Binning, C.F. Quate and Ch. Gerber, Phys. Rev. Lett. **56**, 930 (1986).

[210] U. Landman, W.D. Luedtke, N.A. Burnham, and R.J. Colton, Science **248**, 454 (1990).

[211] A.P. Sutton and J. B. Pethica, J. Phys.: Condens. Matter **2**, 5317 (1990).

[212] R.M. Lynden-Bell, Science **263**, 1704 (1994).

[213] T.N. Todorov and A.P. Sutton, Phys. Rev. Lett. **70**, 2138 (1993).

[214] N. Agraït, J.G. Rodrigo, and S. Vieira, Phys. Rev. B **47**, 12345 (1993).

[215] J.I. Pascual, J. Méndez, J. Gómez-Herrero, A.M. Baró, N. García and V.T. Binh, Phys. Rev. Lett. **71**, 1852 (1993).

[216] L. Olesen, E. Laegsgaard, I. Stensgaard, F. Besenbacher, J. Schiotz, P. Stoltze, K.W. Jacobsen, and J.K. Norskov, Phys. Rev. Lett. **72**, 2251 (1994).

[217] J.M. Krans, C.J. Muller, N. van der Post, F.R. Postma, A.P. Sutton, T.N. Todorov, and J.M. van Ruitenbeek, Phys. Rev. Lett. **74**, 2146 (1995).

[218] J.M. Krans and J.M. van Ruitenbeek, Phys. Rev. B **50**, 17659 (1994).

[219] J.M. Krans, J.M. van Ruitenbeek, V.V. Fisun, I.K. Yanson and L.J. de Jongh, Nature **375**, 767 (1995).

[220] E.N. Bogachek, A.N. Zagoskin and I.O. Kulik, Soviet J. Low Temp. Phys. **16**, 796 (1990).

[221] J.A. Torres, J.I. Pascual and J.J. Sáenz, Phys. Rev. B **49**, 16581 (1994).

[222] J.A. Torres and J.J. Sáenz, Phys. Rev. Lett. **77**, 2245 (1996).

[223] J.L. Costa-Krämer, N. García, P. García-Mochales and P.A. Serena, Surface Science **342**, L1144 (1995).

[224] A.M. Bratkovsky, A.P. Sutton and T.N. Todorov, Phys. Rev. B **52**, 5036 (1995).

[225] C.J. Muller, J.M. Krans, T.N. Todorov and M.A. Reed, Phys. Rev. B **53**, 1022 (1996).

[226] N. Agraït, J.G. Rodrigo, G. Rubio, C. Sirvent and S. Vieira, Thin Solid Films **253**, 199 (1994).

[227] N. Agraït, G. Rubio and S. Vieira, Phys. Rev. Lett. **74**, 3995 (1995).

[228] A. Stalder and U. Dürig, Appl. Phys. Lett. **68**, 637 (1996).

[229] A. Stalder and U. Dürig, J. Vac. Sci. Technol. B **14**, 1259 (1996).

[230] G. Rubio, N. Agraït and S. Vieira, Phys. Rev. Lett. **76**, 2302 (1996).

[231] T.N. Todorov and A.P. Sutton, Phys. Rev. B **54**, 14234 (1996).

[232] C.A. Stafford, D. Baeriswyl and J. Bürki, Phys. Rev. Lett. **79**, 2863 (1997).

[233] J.M. van Ruitenbeek, M.H. Devoret, D. Esteve, and C. Urbina, Phys. Rev. B **56**, 12566 (1997).

[234] C. Yannouleas, E.N. Bogachek and U. Landman, Phys. Rev. B **57**, 4872 (1998).

[235] S. Blom, H. Olin, J.L. Kosta-Krämer, N. García, M. Jonson, P.A. Serena, and R.I. Shekhter, Phys. Rev. B **57**, 8830 (1998).

[236] N.D. Lang, Phys. Rev. B **52**, 5335 (1995).

[237] C. Sirvent, J.G. Rodrigo, S. Vieira, L. Jurczyszyn, N. Mingo and F. Flores, Phys. Rev. B **53**, 16086 (1996).

[238] A. Yazdani, D.M. Eigler and N.D. Lang, Science **272**, 1921 (1996).

[239] A.P. Sutton, Current Opinion in Solid State & Material Science **1**, 827 (1996).

[240] J.M. van Ruitenbeek, in *Mesoscopic Electron Transport*, NATO-ASI Series E: Appl. Sci., Vol. 345 (eds. L.L. Sohn, L.P. Kouwenhoven, G. Schön), p. 549, (Kluwer Academic Publishers, 1997).

[241] *Nanowires*, edited by P.A. Serena and N. García (Kluwer, Dordrecht,1997).

[242] A.I. Yanson and J.M. van Ruitenbeek, Phys. Rev. Lett. **79**, 2157 (1997).

[243] C. Joachim and J.M. Gimzewski, Chem. Phys. Lett. **265**, 353 (1997).

[244] S.J. Tans, A.R.M. Verschueren and C. Dekker, Nature **393**, 49 (1998).

[245] P. Sautet and C. Joachim, Chem. Phys. Lett. **185**, 23 (1991).

[246] Natalio Mingo, *Thesis*, Universidad Autónoma de Madrid (Spain), in 1997.

[247] C. Caroli, R. Combescot, P. Nozieres, and D. Saint-James, J. Phys. C **4**, 916 (1971). C. Caroli, R. Combescot, D. Lederer, P. Nozieres, and D. Saint-James, J. Phys. C **4**, 2598 (1971). R. Combescot, J. Phys. C **4**, 2611 (1971). C. Caroli, R. Combescot, P. Nozieres, and D. Saint-James, J. Phys. C **5**, 21 (1972).

[248] T.N. Todorov *et al.* J. Phys. Condens. Matter **5**, 2389 (1993).

[249] W.A. Harrison, *Electronic Structure and the Properties of Solids* (Freeman, San Francisco, 1980).

[250] D.A. Papaconstantopoulos, *Handbook of the band structure of elemental solids*, Plenum Press, New York (1986).

[251] J.C. Slater and G.F. Koster, Phys. Rev. **94**, 1498 (1954).

[252] A. Levy Yeyati, A. Martín-Rodero and F. Flores, Phys. Rev. B **56**, 10369 (1997).

[253] A. Levy Yeyati, Phys. Rev. B **45**, 14189 (1992).

[254] F. Guinea *et al.*, Phys. Rev. B **28**, 4397 (1982).

[255] R. Haydock, V. Heine and M.J. Kelly, J. Phys. C **5**, 2485 (1972).

[256] J.M van Ruitenbeek *et al.*, Rev. Sci. Instrum. **67**, 108 (1996).

[257] U. Landman, W.D. Luedtke, B.E. Salisbury and R.L. Whetten, Phys. Rev. Lett. **77**, 1362 (1996).

[258] C.C. Wan, J.L. Mozos, G. Taraschi, J. Wang and H. Guo, Appl. Phys. Lett. **71**, 419 (1997).

[259] M. Brandbyge, M.R. Sorensen and K.W. Jacobsen, Phys. Rev. B **56**, 10369 (1997).

[260] W. Belzig, C. Bruder and G. Schön, Phys. Rev. B **54**, 9443 (1996).

[261] P. García-Mochales and P.A. Serena, Phys. Rev. Lett. **79**, 2316 (1997).

[262] E. Bascones, G. Gómez-Santos, and J.J. Sáenz, Phys. Rev. B **57**, 2541 (1998).

[263] J.L. Costa-Krämer, N. García and H. Olin, Phys. Rev. Lett. **78**, 4990 (1997).

[264] J.L. Costa-Krämer, Phys. Rev. B **55**, R4875 (1997).

[265] K. Hansen, E. Laegsgaard, I. Stensgaard, and F. Besenbacher, Phys. Rev. B **56**, 2208 (1997).

[266] C. Untiedt, G. Rubio, S.Vieira, and N. Agra´ït, Phys. Rev. B **56**, 2154 (1997).

[267] F. Flores *et al.*, Nuovo Cimento **10**, 303 (1988).

[268] K. Würde, A. Mazur, and J. Pollmann, Phys. Rev. B **49**, 7679 (1994).

[269] D. Sánchez-Portal *et al.*, Phys. Rev. Lett. **79**, 4198 (1997).

[270] C. Joachim, J.K. Gimzewski, R.R. Schlittler, and C. Chavy, Phys. Rev. Lett. **74**, 2102 (1995).

[271] C. Joachim and J.K. Gimzewski, Europhys. Lett. **30**, 409 (1995).

[272] L.A. Bumm *et al.*, Science **271**, 1705 (1996).

[273] R.P. Andres *et al.*, Science **272**, 1323 (1996).

[274] M.A. Reed, C. Zhou, C.J. Muller, T.P. Burgin, and J.M. Tour, Science **278**, 252 (1997).

[275] M. Kemp, A. Roitberg, V. Mujica, T. Wanta, and M.A. Ratner, J. Phys. Chem. **100**, 8349 (1996); V. Mujica, M. Kemp, A. Roitberg, and M.A. Ratner, J. Chem. Phys. **104**, 7296 (1996).

[276] C. Joachim and J.F. Vinuesa, Europhys. Lett. **33**, 635 (1996), and references therein.

[277] M.P. Samanta, W. Tian, S. Datta, J.I. Henderson, and C.P. Kubiak, Phys. Rev. B **53**, R7626 (1996).

[278] C.P. Tsu and R.A. Marcus, J. Chem. Phys. **106**, 584 (1997).

[279] S. Datta *et al.*, Phys. Rev. Lett. **79**, 2530 (1997).

[280] A. Levy Yeyati, J.C. Cuevas and A. Martin-Rodero, in *Photons and Local Probes*, edited by O. Marti and R. Müller (Kluwer Academic, Dordrecht, 1995).

[281] V.S. Shumeiko, G. Wendin and E.N. Bratus, Phys. Rev. B **48**, 13129 (1993).